

© 2009 by Kyungsoo Park

POTENTIAL-BASED FRACTURE MECHANICS USING COHESIVE ZONE
AND VIRTUAL INTERNAL BOND MODELING

BY

KYOUNGSOO PARK

B.S., Hanyang University, 2003

M.S., University of Illinois at Urbana-Champaign, 2005

DISSERTATION

Submitted in partial fulfillment of the requirements
for the degree of Doctor of Philosophy in Civil Engineering
in the Graduate College of the
University of Illinois at Urbana-Champaign, 2009

Urbana, Illinois

Doctoral Committee:

Professor Glaucio H. Paulino, Chair and Director of Research
Associate Professor Jeffery R. Roesler, Co-Director of Research
Assistant Professor C. Armando Duarte
Professor Robert B. Haber
Professor Yonggang Huang, Northwestern University
Associate Professor Karel Matous, University of Notre Dame
Assistant Professor Spandan Maiti, Michigan Technological University

Abstract

The characterization of nonlinear constitutive relationships along fracture surfaces is a fundamental issue in mixed-mode cohesive fracture simulations. A generalized potential-based constitutive theory of mixed-mode fracture is proposed in conjunction with physical quantities such as fracture energy, cohesive strength and shape of cohesive interactions. The potential-based model is verified and validated by investigating quasi-static fracture, dynamic fracture, branching and fragmentation. For quasi-static fracture problems, intrinsic cohesive surface element approaches are utilized to investigate microstructural particle/debonding process within a multiscale approach. Macroscopic constitutive relationship of materials with microstructure is estimated by means of an integrated approach involving micromechanics and the computational model. For dynamic fracture, branching and fragmentation problems, extrinsic cohesive surface element approaches are employed, which allow adaptive insertion of cohesive surface elements whenever and wherever they are needed. Nodal perturbation and edge-swap operators are used to reduce mesh bias and to improve crack path geometry represented by a finite element mesh. Adaptive mesh refinement and coarsening schemes are systematically developed in conjunction with edge-split and vertex-removal operators to reduce computational cost. Computational results demonstrate that the potential-based constitutive model with such adaptive operators leads to an effective and efficient computational framework to simulate physical phenomena associated with fracture. In addition, the virtual internal bond model is utilized for the investigation of quasi-brittle material fracture behavior. All the computational models have been developed in conjunction with verification and/or validation procedures.

To my family

Acknowledgments

I would like to express my sincere gratitude to my advisor Professor Glaucio H. Paulino. This thesis would not have been possible without his direction, support and enthusiasm. I am also indebted to my co-advisor Professor Jeffery R. Roesler for his invaluable suggestions and encouragement.

I am grateful to Professor Yonggang Huang for his kind advice and insightful comments, and he has been a source of inspiration. Our collaboration resulted in Chapter 5 of this thesis and a joint paper. I would like to thank to committee members, C. Armando Duarte, Robert B. Haber, Karel Matous and Spandan Maiti for their constructive remarks and suggestions. In addition, I owe many thanks to Professor Waldemar Celes for his feedback and hands-on help.

I benefited from discussions with my colleagues, Duc Ngo and Rodrigo Espinha, about micromechanics and topological data structure. I am beholden to my group members, Matthew C. Walters, Alok Sutradhar, Zhengyu Zhang, Seong-Hyeok Song, Eshan V. Dave, Bin Shen, Huiming Yin, Shun Wang, Chau H. Le, Tam Nguyen, Cameron Talischi, Lauren Stromberg, Arun L. Gain, Sofie Leon and Tomas Zegard. The discussions that we had were enjoyable and valuable.

I can not express enough appreciation to my parents and wonderful sister for their perpetual support and trust. Finally, I would like to express my deepest thanks to my lovely wife, Younhee Ko. She has always been supportive of me, and I treasure the time that she and I have spent together.

Table of Contents

List of Tables	ix
List of Figures	x
Chapter 1 Introduction	1
1.1 Cohesive Fracture Model	1
1.2 Cohesive Constitutive Relationships	3
1.2.1 Non-Potential-Based Models	3
1.2.2 Potential-Based Models	4
1.3 Computational Methods	6
1.3.1 Intrinsic versus Extrinsic Cohesive Models	6
1.3.2 Enrichment Function Based Approach: GFEM/X-FEM	8
1.3.3 Finite Elements with Embedded Discontinuities	9
1.3.4 Microplane Model	9
1.3.5 Atomistic/Continuum Coupling	10
1.3.6 Virtual Internal Bond Model	10
1.3.7 Peridynamics	11
1.3.8 Other Methods	11
1.3.9 Present Approach	12
1.4 Research Objective and Thesis Organization	12
Chapter 2 Virtual Internal Pair-Bond Model for Quasi-Brittle Materials	14
2.1 Introduction	14
2.2 Virtual Internal Bond (VIB) Model Formulation	15
2.2.1 Strain Energy Function in the VIB Model	16
2.2.2 Constitutive Relation	17
2.2.3 Virtual Bond Density Potential	18
2.2.4 Computational Implementation	19
2.3 Virtual Internal Pair-Bond (VIPB) Model	19
2.4 Determination of Material Properties	22
2.4.1 Elastic Properties at Infinitesimal Strains	22
2.4.2 Fracture Properties and Mesh Size Dependences	23
2.5 Verification – Fracture Properties and Element-Size Dependence	25
2.5.1 Pure Tension Test	26

2.5.2	Double Cantilever Beam (DCB) Test	27
2.6	Validation	30
2.6.1	Three-Point Bending (TPB) Tests of Plain Concrete	31
2.6.2	On Size Effect	33
2.6.3	TPB Test of Fiber Reinforced Concrete (FRC)	34
2.7	Conclusions	35
Chapter 3 PPR: Unified Potential-Based Cohesive Model of Mixed-Mode Fracture		37
3.1	Previous Potentials for Cohesive Fracture	37
3.1.1	Needleman, 1987	38
3.1.2	Needleman, 1990	40
3.1.3	Beltz and Rice, 1991	41
3.1.4	Xu and Needleman, 1993	44
3.1.5	Limitations of the Exponential Potential	46
3.2	PPR: Unified Potential-Based Constitutive Model	48
3.2.1	Definition of the Unified Potential for Mixed-Mode Fracture	48
3.2.2	Cohesive Interaction (Softening) Region	53
3.2.3	Extension to the Extrinsic Cohesive Zone Model	54
3.2.4	Remarks	57
3.3	Path Dependence of Work-of-Separation	58
3.3.1	Proportional Separation	58
3.3.2	Non-Proportional Separation	62
3.4	Mixed-Mode Fracture Verification	66
3.5	Concluding Remarks	70
Chapter 4 Implementation of the PPR Potential-Based Cohesive Model		71
4.1	Finite Element Formulation	71
4.2	Time Integration	72
4.3	Topological Data Structure	74
4.3.1	Client-Server Approach	75
4.3.2	API and Callback functions	76
4.4	Unloading and Reloading Relationships	77
4.4.1	Coupled Unloading/Reloading Model	78
4.4.2	Uncoupled Unloading/Reloading Model	80
4.4.3	Remarks	82
4.5	Constitutive Relationships	84
4.5.1	Determination of Cohesive Interaction Region	84
4.5.2	Cohesive Traction Vector and Tangent Matrix	84
4.6	Verification of Cohesive Elements	88

Chapter 5	Microstructural Particle/Matrix Debonding Process by the PPR Potential-Based Model	91
5.1	Introduction	91
5.2	Constitutive Behavior of Composites with Particle/Matrix Interface Debonding	93
5.2.1	Hydrostatic Tension Stress State	94
5.2.2	Extended Mori-Tanaka Method under Hydrostatic Tension	95
5.2.3	Extended Mori-Tanaka Method under Equi-biaxial Tension	97
5.3	PPR: Potential-Based Cohesive Model for Interface Debonding	97
5.4	Micromechanics Investigation of the PPR Model	99
5.4.1	Effect of Particle Size	100
5.4.2	Effect of Particle Volume Fraction	101
5.4.3	Effect of Cohesive Energy	102
5.4.4	Effect of Cohesive Strength	103
5.5	Theoretical and Computational Investigation of Materials with Microstructure Accounting for Particle/Matrix Interface Debonding	104
5.5.1	Particle/Matrix Debonding Process	106
5.5.2	Effect of Microstructure Size	110
5.5.3	Effect of Particle Elastic Modulus	111
5.5.4	Effect of Fracture Energy and Particle Size	112
5.5.5	Effect of Cohesive Strength and Particle Size	113
5.5.6	Remarks	114
5.6	Case Study: Determination of the PPR Cohesive Relation	114
5.7	Concluding Remarks	118
Chapter 6	Adaptive Dynamic Cohesive Fracture Simulation Using Nodal Perturbation and Edge-Swap Operators	119
6.1	Introduction	119
6.2	Toward Unstructured Geometry – Nodal Perturbation (NP)	124
6.2.1	Crack Length Convergence	126
6.2.2	Crack Angle Convergence	129
6.3	Toward Unstructured Topology – Edge Swap (ES)	131
6.3.1	Crack Length Convergence	131
6.3.2	Crack Angle Convergence	133
6.4	Computational Quantification of Isoperimetric Property	134
6.5	Nodal Perturbation and Edge Swap Algorithm	138
6.6	Numerical Examples	140
6.6.1	Compact Compression Specimen (CCS) Test	140
6.6.2	Microbranching Experiments	143
6.6.3	Fragmentation Simulations	150
6.7	Some Remarks on 4k and Pinwheel Meshes	154
6.8	Concluding Remarks	155

Chapter 7 Adaptive Mesh Refinement and Coarsening for Cohesive Dynamic Fracture	157
7.1 Introduction	157
7.2 Adaptive Mesh Refinement	159
7.2.1 Mesh Refinement Schemes	159
7.2.2 Refinement Criterion and Interpolation of New Nodes	162
7.3 Adaptive Mesh Coarsening	165
7.3.1 Mesh Coarsening Schemes	166
7.3.2 Coarsening Criterion and Local Update	168
7.4 Numerical Examples	170
7.4.1 Predefined Crack Path Problem: Mode I Fracture	170
7.4.2 Mixed-Mode Crack Propagation	180
7.4.3 Crack Branching Problem	188
7.5 Concluding Remarks	193
Chapter 8 Conclusions and Future Work	195
8.1 Concluding Remarks	195
8.2 Suggestions for Future Work	198
Appendix A User-defined element (UEL) subroutine of ABAQUS for the PPR potential-based cohesive zone model	201
Appendix B User-defined material (UMAT) subroutine of ABAQUS for the virtual internal pair-bond (VIPB) model	210
References	215
Curriculum Vitae	231

List of Tables

2.1	Relationship between the VIB element size and the fracture energy. . .	26
2.2	Elastic and fracture parameters of concrete beam experiments by Roesler et al. (2007b).	31
2.3	Material properties and the constants in the bond density potential for each size of beam in the VIB (single-bond) model with the localization zone size of 0.5 mm.	33
2.4	The constants in each bond density potential for the VIPB (pair-bond) model with the localization zone size of 0.5 mm.	33
2.5	Elastic and fracture parameters of plain concrete (Roesler et al., 2007a). . .	35
3.1	Potentials for cohesive fracture.	38
3.2	Fracture parameters for the unified potential-based model (PPR). . .	58
3.3	Fracture parameters for the model by Xu and Needleman (1993). . .	58
3.4	Geometry of the MMB test specimen.	67
4.1	Comparison between the coupled unloading/reloading and the uncoupled unloading/reloading.	83
5.1	Properties of high explosive material PBX9501.	118
6.1	Geometrical and topological considerations for cohesive zone model simulations.	120
6.2	ρ -path deviation ratio (dev_ρ) and Hausdorff distance ($H(p, q)$) with respect to the number of elements.	136
7.1	Numbers of nodes and elements, and relative error of the total energy with respect to the coarsening error levels (e_{4k}).	179
7.2	Computational cost comparison for the mixed-mode crack propagation. . .	184
7.3	Computational cost comparison for the crack branching problem. . .	189

List of Figures

1.1	Types of fracture process behavior (Bazant and Planas, 1998).	2
1.2	Schematics of the cohesive zone model.	3
1.3	(a) Shape of a general atomistic potential (Ψ) and (b) its derivative (Ψ').	5
1.4	Schematics of the intrinsic cohesive zone model.	7
1.5	Schematics of the extrinsic cohesive zone model.	8
2.1	Schematic illustration of the original VIB model.	16
2.2	Schematic illustration of the VIPB model: (a) the relationship between stress and bond length from the pair-bond potential ($\Psi = \Psi_1 + \Psi_2$); (b) the relationship from the steep short-range potential (Ψ_1) and (c) the relationship from the shallow long-range potential (Ψ_2).	20
2.3	Bilinear Softening model for concrete where f'_t is the tensile strength, G_f is the initial fracture energy, G_F is the total fracture energy, β_k is the strength ratio at the kink point, w_1 is the horizontal axis intercept of the initial descending line, w_k is the crack opening width at the kink point, and w_f is the final crack opening width – see Park (2005); Park et al. (2008a).	21
2.4	J -integral contours (a) for an arbitrary path and (b) for a path of the localization zone.	24
2.5	Numerical simulation result of a pure tension test using the VIB model with different domain sizes ($W = 1$ m and 0.5 m). The loading is performed with displacement control (δ).	26
2.6	Comparison between the VIB (single-bond) model and the VIPB (pair-bond) model with the localization zone size of $W = h_L = 0.5$ mm. The loading is performed with displacement control (δ).	27
2.7	(a) The geometry of the DCB test; (b) mesh detail around initial notch with the element size varying from 0.5 mm (localization zone) to 2 mm (outer region); (c) normal stress, σ_{yy} , distribution under the deformed shape.	28
2.8	Numerical simulation results of the DCB test using the VIB and the VIPB models with the localization zone size of, (a) $h_L = 0.5$ mm and (b) $h_L = 0.25$ mm.	29
2.9	Specimen geometry of a three-point bending (TPB) tests.	30

2.10	Comparison of load-CMOD curves with experimental results: (a) specimen size $D = 63$ mm, (b) specimen size $D = 150$ mm and (c) specimen size $D = 250$ mm.	32
2.11	Size effect for three-point bending (TPB) fracture test configuration.	34
2.12	Prediction of load-CMOD curves of FRC beam tests compared with experimental data.	35
3.1	Needleman (1987) potential (Ψ) and its gradients (T_n, T_t) with respect to separations (Δ_n, Δ_t); $\phi_n = 100$ N/m, $\sigma_{\max} = 30$ MPa, and $\alpha_s = 10$	39
3.2	Needleman (1990) potential and its gradients; $\phi_n = 100$ N/m, and $\sigma_{\max} = 30$ MPa.	40
3.3	Beltz and Rice (1991) generalized exponential-periodic potential and its gradients; $\phi_n = 2\gamma_s = 100$ N/m, $\phi_t = \gamma_{us} = 200$ N/m, $\sigma_{\max} = 30$ MPa, $\tau_{\max} = 40$ MPa, and $r = 0$	43
3.4	Xu and Needleman (1993) exponential potential and its gradients; $\phi_n = 100$ N/m, $\phi_t = 200$ N/m, $\sigma_{\max} = 30$ MPa, $\tau_{\max} = 40$ MPa, and $r = 0$	45
3.5	Xu and Needleman (1993) exponential potential and its gradients; $\phi_n = 200$ N/m, $\phi_t = 100$ N/m, $\sigma_{\max} = 30$ MPa, $\tau_{\max} = 40$ MPa, and $r = 0$	47
3.6	Fracture boundary conditions for the unified mixed-mode potential.	49
3.7	Unified mixed-mode potential (PPR) and its gradients for the intrinsic cohesive zone model with $\phi_n = 100$ N/m, $\phi_t = 200$ N/m, $\sigma_{\max} = 40$ MPa, $\tau_{\max} = 30$ MPa, $\alpha = 5$, $\beta = 1.3$, $\lambda_n = 0.1$, and $\lambda_t = 0.2$	52
3.8	Description of each cohesive interaction (T_n, T_t) region defined by the final crack opening widths (δ_n, δ_t) and the conjugate final crack opening widths ($\bar{\delta}_n, \bar{\delta}_t$); (a) T_n versus ($\delta_n, \bar{\delta}_t$) space; (b) T_t versus ($\bar{\delta}_n, \delta_t$) space.	53
3.9	Proposed potential and its gradients for the extrinsic cohesive zone model with $\phi_n = 100$ N/m, $\phi_t = 200$ N/m, $\sigma_{\max} = 40$ MPa, $\tau_{\max} = 30$ MPa, $\alpha = 5$, and $\beta = 1.3$	56
3.10	Proportional separation path (Δ_r) with the separation angle (θ).	59
3.11	The PPR potential-based model: (a) work-of-separation, (b) work done by the normal traction, and (c) work done by the tangential traction with respect to the change of the proportional angle, θ	60
3.12	Xu and Needleman (1993) exponential potential: (a) work-of-separation, (b) work done by the normal traction, and (c) work done by the tangential traction with respect to the change of the proportional angle, θ	61
3.13	Two arbitrary separation paths for the material debonding process; (a) non-proportional Path 1 ; (b) non-proportional Path 2	62
3.14	The PPR potential-based model: variation of the work-of-separation for the case of $\phi_n < \phi_t$ ($\phi_n = 100$ N/m, $\phi_t = 200$ N/m); (a) non-proportional Path 1 ; (b) non-proportional Path 2	63

3.15	The PPR potential-based model: variation of the work-of-separation for the case of $\phi_n > \phi_t$ ($\phi_n = 200$ N/m, $\phi_t = 100$ N/m); (a) non-proportional Path 1 ; (b) non-proportional Path 2	64
3.16	Xu and Needleman (1993) exponential potential: variation of the work-of-separation for the case of $\phi_n < \phi_t$ ($\phi_n = 100$ N/m, $\phi_t = 200$ N/m and $r = 0.5$); (a) non-proportional Path 1 ; (b) non-proportional Path 2	65
3.17	Xu and Needleman (1993) exponential potential: variation of the work-of-separation for the case of $\phi_n > \phi_t$ ($\phi_n = 200$ N/m, $\phi_t = 100$ N/m and $r = 0.5$); (a) non-proportional Path 1 ; (b) non-proportional Path 2	65
3.18	Mixed-mode bending test.	66
3.19	Comparison between the analytical solutions and the numerical simulation results considering the same fracture energy ($\phi_n = \phi_t = 1$ N/mm).	68
3.20	Comparison between the analytical solutions and the numerical simulation results considering different fracture energies ($\phi_n = 1$ N/mm, $\phi_t = 2$ N/mm) (a) $\sigma_{\max} = 10$ MPa and (b) $\sigma_{\max} = 20$ MPa.	69
4.1	Client-server architecture.	75
4.2	One-dimensional cohesive law and its unloading/reloading paths.	77
4.3	Schematics of the coupled unloading/reloading model: (a) normal interaction and (b) tangential interaction.	79
4.4	Comparison between the softening relationships obtained by the potential and the coupled unloading/reloading relationship with the maximum loading history index of $\eta_{\max} = \sqrt{0.3\delta_n^2 + 0.2\delta_t^2}$	80
4.5	Schematics of the uncoupled unloading/reloading model: (a) normal interaction and (b) tangential interaction.	81
4.6	Comparison between the softening relationships obtained by the potential and the coupled unloading/reloading relationship with the maximum loading history indices of $\eta_{\max} = 0.3\delta_n$ and $\eta_{t\max} = 0.2\delta_t$	82
4.7	Cohesive fracture separations along the local coordinate system (a) two-dimensions (Δ_1, Δ_2) and (b) three-dimensions ($\Delta_1, \Delta_2, \Delta_3$).	88
4.8	Geometry of (a) pure mode I, and (b) pure mode II simulation.	89
4.9	Computational result of the pure mode I test.	89
4.10	Computational result of the pure mode II test.	90
5.1	(a) Spherical particle under hydrostatic tension stress state, and (b) cylindrical particle under equi-biaxial tension stress state.	96
5.2	Illustrative intrinsic cohesive relation of normal interface debonding.	98
5.3	Stress versus strain curve of the material ($a = 100\mu\text{m}$).	100
5.4	Effect of particle size (a) on the constitutive relation ($f = 0.6$).	100
5.5	Effect of particle volume fraction (f) on the constitutive relation in the case of fine particles ($a = 100\mu\text{m}$).	101
5.6	Effect of particle volume fraction (f) on the constitutive relation in the case of coarse particles ($a = 2\text{ mm}$).	101

5.7	Effect of cohesive energy (ϕ_n) on the constitutive relation with volume fraction $f = 0.6$: (a) $a = 100 \mu m$, and (b) $a = 2 \text{ mm}$	102
5.8	Effect of cohesive strength (σ_{\max}) on the constitutive relation with volume fraction $f = 0.6$: (a) $a = 100 \mu m$, and (b) $a = 2 \text{ mm}$	103
5.9	(a) Geometry of the square unit cell (size b) with particle of radius a , and (b) boundary conditions for the computational modeling.	104
5.10	(a) Finite element mesh of the unit cell, and (b) zoom of the mesh along the interface between particle ($a = 2 \text{ mm}$) and matrix.	105
5.11	Computational results displaying macroscopic strain versus strain along the horizontal and vertical directions with cohesive strength of (a) 15 MPa, and (b) 25 MPa.	107
5.12	Particle/matrix debonding process for softening behavior (Figure 5.11(a)) at the stage of (a) point A, (b) point B, (c) point C, and (d) point D.	108
5.13	Particle/matrix debonding process for snap-back behavior (Figure 5.11(b)) at the stage of (a) point A, (b) point B, (c) point C, (d) point D, (e) point E, and (f) point F.	109
5.14	Effect of the particle size (a) on the constitutive relationship.	110
5.15	Effect of the ratio of elastic modulus on the constitutive relationship.	111
5.16	Effect of the fracture energy (ϕ_n) on the constitutive relationship with particle size of (a) $100 \mu m$, and (b) 2 mm	112
5.17	Effect of the cohesive strength (σ_{\max}) on the constitutive relationship with particle size of (a) $100 \mu m$, and (b) 2 mm	113
5.18	Case study: macroscopic cohesive relation of the high explosive material PBX 9501 (Tan et al., 2005b).	115
6.1	Discrepancy between a mathematical path (thick dashed line) and a discrete path (thick solid line). The aspect ratio of the rectangular domain is $1 : 2.11$	121
6.2	(a) Crack path test, and (b) error between the <i>mathematical</i> length (\overline{OP}) and the <i>discrete length</i> represented by the $4k$ structured mesh. The maximum error occurs at $x = \sqrt{2} - 1$ (angle $\angle COP = 67.5^\circ$).	122
6.3	Schematic description of a potential zigzag pattern.	123
6.4	Effect of the nodal perturbation (NP) factor on a finite element mesh: (a) NP = 0.0 (unperturbed), (b) NP = 0.1, (c) NP = 0.2, and (d) NP = 0.3.	124
6.5	Mesh quality estimation: (a) histogram and (b) Lo's parameter for each element considering NP = 0.3. Notice that all 6400 elements in the unperturbed mesh (NP = 0.0) have Lo's parameter of 0.866.	125
6.6	Error with respect to (a) nodal perturbation (NP) factor considering 10×24 mesh grid, and (b) element size considering the nodal perturbation factor of 0.3.	127
6.7	Error with respect to the nodal perturbation (NP) factor along the 45° direction.	128

6.8	Representative results of crack angle convergence for (a) nodal perturbation factor of 0.0 (NP = 0.0), and (b) nodal perturbation factor of 0.3 (NP = 0.3).	129
6.9	Number of appearances of geometrically obtained angles (θ_{FE}) for given nodal perturbation (NP) factors.	130
6.10	Three successive mesh instances showing a schematic description of the edge-swap (ES) operator.	131
6.11	Error with respect to (a) the nodal perturbation factor and (b) element size in conjunction with the edge-swap operator.	132
6.12	Number of appearances of geometrically obtained angles (θ_{FE}) with respect to the nodal perturbation (NP) factor in conjunction with the edge-swap (ES) operator.	133
6.13	Examples of each mesh type: (a) Type I, (b) Type II, (c) Type III, and (d) Type IV.	135
6.14	(a) Illustration of the parameter ρ in the rectangular domain, and (b) constraint for the set of vertices (p, q) related to the parameter ρ . . .	135
6.15	Quantification of the isoperimetric property in conjunction with (a) the ρ -path deviation ratio, and (b) the Hausdorff distance.	137
6.16	Location of the mid-point in the edge-swap operator: (a) 4k structured mesh, and (b) 4k perturbed mesh.	139
6.17	Geometry of compact compression specimen tests and its boundary condition.	140
6.18	Finite element mesh of the compact compression specimen.	141
6.19	Crack path of CCS simulation results.	142
6.20	Observation of microbranching experiment: (a) crack velocity (v), (b) fractured surface, and (c) crack patterns with respect to different crack speeds ($v \sim 300m/s < v_c$, $v \sim 400m/s \sim v_c$, $v \sim 600m/s > v_c$). Figure is reproduced from Figure 4 of Sharon and Fineberg (1996). .	144
6.21	Schematics of geometry and boundary conditions for the microbranching experiments.	144
6.22	Branching patterns with respect to different initial strains: (a) $\epsilon_0 = 0.01$, (b) $\epsilon_0 = 0.012$, and (c) $\epsilon_0 = 0.015$ for the 4k mesh grid of 192×48	145
6.23	Microbranching evolution with respect to time: (a) $2\mu s$, (b) $8\mu s$, (c) $14\mu s$, and (d) $20\mu s$	146
6.24	Crack velocity versus time and averaged velocity for initial strains (ϵ_0) of 0.01, 0.012 and 0.015 with the 4k mesh grid of 192×48	147
6.25	Branching patterns with respect to different initial strains: (a) $\epsilon_0 = 0.01$, (b) $\epsilon_0 = 0.012$, and (c) $\epsilon_0 = 0.015$ for the 4k mesh grid of 256×64	148
6.26	Crack velocity versus time and averaged velocity for initial strains (ϵ_0) of 0.010, 0.012 and 0.015 with the 4k mesh grid of 256×64	148
6.27	Three consecutive simulations for the initial strain of 0.015 with the edge-swap operator.	149

6.28	Three consecutive simulations for the initial strain of 0.015 without the edge-swap operator.	149
6.29	Energy evolution with respect to the time for $\epsilon_0 = 0.015$	150
6.30	(a) Geometry of a thick cylinder, and (b) applied impact pressure with respect to time.	151
6.31	Fragmentation patterns of three consecutive computational results with the nodal perturbation factor of 0.3.	152
6.32	Fragmentation procedure with respect to time: (a) 26 μs , (b) 37 μs , (c) 39 μs , (d) 47 μs , (e) 54 μs , and (f) 64 μs	153
6.33	Comparison by mapping edges of pinwheel-based mesh into edges of 4k structured mesh.	154
6.34	Comparison between a set of pinwheel tiles and a 4k mesh.	154
6.35	Comparison by mapping edges of 4k structured mesh into edges of pinwheel-based mesh with additional dashed-red edges.	155
7.1	(a) Sample initial non-deformed mesh, and (b) local nodal incidences of triangles of a region of the mesh.	159
7.2	Local mesh patterns for which edge splits are allowed: (a) mesh around an interior edge (b) boundary edge.	160
7.3	Recursive edge split procedure; (a) request for an edge-split along the edge with a dashed line, (b) split edges to create an allowable pattern, and (c) split edge along the dashed edge.	160
7.4	Edge split along a cohesive surface element.	161
7.5	Example of the edge-split operation and computed edge depth.	161
7.6	Sequence of edge-split operations along the dashed edges.	162
7.7	Three refinement steps executed inside a circular region: (a) level 1, (b) level 2, and (c) level 3.	163
7.8	Example of the edge-split operations.	163
7.9	Interpolation scheme for new nodes.	164
7.10	(a) Physical coordinate system, and (b) mapped coordinate system.	165
7.11	Vertex-removal operator for mesh coarsening: (a) interior vertex-removal and (b) boundary vertex-removal.	166
7.12	Sequence of vertex-removal operations in shaded 4k patches.	167
7.13	(a) Original 4k patch, and (b) coarsened 4k patch.	168
7.14	Schematics of geometry and boundary condition.	170
7.15	Mode I fracture problem: (a) Extrinsic cohesive zone model with predefined path, and (b) intrinsic cohesive zone model with predefined cohesive surface elements.	171
7.16	Convergence of crack tip location with respect to the time increment: (a) element size of 20 μm , and (b) element size of 10 μm	172
7.17	The contribution of $\Delta t^2/8(\ddot{\mathbf{u}}_{n+1} - \ddot{\mathbf{u}}_n)^T \mathbf{M}(\ddot{\mathbf{u}}_{n+1} + \ddot{\mathbf{u}}_n)$ with respect to the time increments.	173
7.18	Convergence of crack tip location with respect to the element size.	173
7.19	Cohesive process zone size versus time with respect to mesh refinement.	174

7.20	(a) Finite element mesh with uniform element size of $5\mu\text{m}$, and (b) finite element mesh with local refinement around crack tip and the size of $5\mu\text{m}$	175
7.21	Deformed shape with finite element mesh at $t = 0.2\mu\text{s}$ (a) uniform 400×40 mesh grid, and (b) 100×10 mesh grid with adaptive local mesh refinement.	176
7.22	Strain energy at $t = 0.2\mu\text{s}$ (a) 400×40 mesh grid, and (b) 100×10 mesh grid with the AMR.	176
7.23	Energy evolution with respect to the time for the uniform mesh refinement (black lines) and the AMR (red lines).	177
7.24	Total energy variation with respect to time for different coarsening error level of e_{4k}	178
7.25	Energy evolution with respect to the time for the uniform mesh refinement (black lines) and the adaptive mesh refinement & coarsening (AMRC) (red lines).	179
7.26	(a) Geometry and boundary condition of a doubly notched specimen, and (b) its symmetry domain for finite element analysis.	180
7.27	Finite element discretization for the adaptive mesh refinement and coarsening (a) at the initial time step, (b) at time $t = 55\mu\text{s}$ and (c) at time $t = 77.5\mu\text{s}$, and (d) strain energy density at time $t = 77.5\mu\text{s}$. . .	182
7.28	Finite element discretization without employing the symmetry boundary conditions (a) at the initial time step, and (b) at time $t = 77.5\mu\text{s}$. . .	183
7.29	Finite element discretization at time $t = 77.5\mu\text{s}$ for (a) the uniform mesh refinement, and (b) the adaptive mesh refinement.	184
7.30	(a) Crack path, and (b) crack velocity for the uniform mesh refinement, the adaptive mesh refinement, and the adaptive mesh refinement & coarsening.	185
7.31	(a) Crack path, and (b) crack velocity for different sizes of the coarse mesh grid.	186
7.32	Energy evolution with respect to time for (a) adaptive mesh refinement, and (b) adaptive mesh refinement and coarsening.	187
7.33	Geometry of a branching problem.	188
7.34	Comparison of crack patterns and finite element meshes (a) uniformly refined mesh, (b) adaptive mesh refinement, and (c) adaptive mesh refinement and coarsening.	189
7.35	Crack velocity for the uniform mesh refinement, the adaptive mesh refinement, and the adaptive mesh refinement & coarsening.	190
7.36	Vertical stress distribution with respect to time: (a) $10\mu\text{s}$, (b) $13\mu\text{s}$, (c) $16\mu\text{s}$, (d) $19\mu\text{s}$, (e) $22\mu\text{s}$, (f) $25\mu\text{s}$, (g) $28\mu\text{s}$ and (h) $31\mu\text{s}$. . .	191
7.37	Crack branching at different time steps: (a) time = $20\mu\text{s}$, (b) time = $40\mu\text{s}$, and (c) time = $60\mu\text{s}$	192
7.38	Zoom of the finite element mesh at time $60\mu\text{s}$	193
8.1	Parallel runtime performance.	199

Chapter 1

Introduction

The collapse and failure of infrastructure, for example bridges, aircraft, oil tankers and nuclear power plants, result in significant casualties and property damage, and adversely influence the local economy. In order to prevent such disasters, it is necessary to understand and predict deformation and failure mechanisms of structures. To this end, not only are appropriate physical theories and robust computational techniques needed, but they should also be verified and validated. This thesis focuses on the characterization of cohesive fracture behavior derived from a potential-based model and on the computational simulation of failure phenomenon including quasi-static fracture, dynamic fracture, microbranching and fragmentation. In this chapter, fracture process of materials is briefly described in conjunction with the size of the nonlinear zone, and the concept of the cohesive zone model is explained. Next, two types of the constitutive relationships for the cohesive zone model are presented, i.e. non-potential-based models and potential-based models. Several computational methods representing the cohesive zone model are reviewed. Finally, the scope of the current work and the thesis organization are described.

1.1 Cohesive Fracture Model

Fracture process behavior is generally classified on the basis of the size of the nonlinear fracture process zone (Bazant and Planas, 1998). In front of a crack tip, the *fracture process zone*, or the nonlinear softening zone, characterizes the progressive softening behavior (the gray area in Figure 1.1). The outer region of this zone (the black area in Figure 1.1) is named the *nonlinear hardening zone* which represents inelasticity. For the first behavior type (Figure 1.1(a)), both the fracture process zone and the nonlinear hardening zone are relatively small. Brittle materials such as glass, PMMA, brittle ceramics and brittle metal, show this type of fracture process behavior. The next type of behavior (Figure 1.1(b)) possesses the large nonlinear hardening zone and the small fracture process zone due to the plastic yielding. For instance, elasto-

plastic fracture mechanics can be utilized in this case. Ductile materials (e.g. ductile metals) fall into the second behavior type. The third type of behavior (Figure 1.1(c)) illustrates the progressive damage with material softening along the fracture process zone. While the nonlinear hardening zone might be negligible for this type, the relatively large fracture process zone significantly influences the stress redistribution. Because of the relatively large fracture process zone, the strength of a structure depends not only on the strength of a material but also on the size of a structure, which is associated to the size effect (Bazant, 1999). This behavior, called quasi-brittle, is found in concrete, rock, ice, paper, stiff clay, etc.

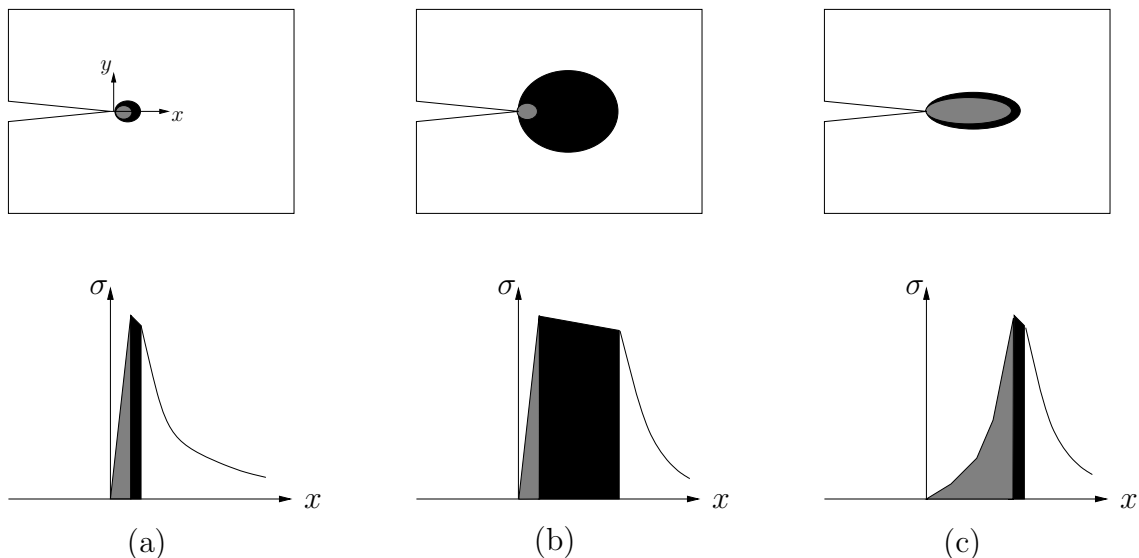


Figure 1.1: Types of fracture process behavior (Bazant and Planas, 1998).

Nonlinear fracture process behavior such as void growth and microcrack formation can be approximated by the cohesive zone model (e.g. Barenblatt, 1959; Dugdale, 1960). The fracture process of the cohesive zone model generally consists of four stages (Figure 1.2). The first stage (Stage I) represents general continuum material behavior without fracture. The next stage (Stage II) is the initiation of a crack when a certain criterion is met, for example, maximum hoop stress (Ergodan and Sih, 1963), maximum hoop strain (Anderson et al., 1971), minimum strain energy density (Sih, 1974), or loss of ellipticity (Hill, 1962). The third stage describes the evolution of the failure, which is governed by the nonlinear cohesive relationship or the softening curve, i.e. the relation between the cohesive tractions (T_n , T_t) and crack opening widths (Δ_n , Δ_t) across the fracture surface (Stage III). Because the cohesive relationship defines the characteristic of the fracture process zone, the shape of the softening curve depends on the material fracture process behavior. For example, a

linear softening model is utilized for brittle materials (Camacho and Ortiz, 1996), while a trapezoidal shape is employed to describe an elastic-plastic solid (Tvergaard and Hutchinson, 1992). For quasi-brittle materials like concrete, a bilinear softening model is widely utilized (Bazant and Planas, 1998; Park et al., 2008a). The final stage (Stage IV) defines failure when the crack opening width reaches the final crack opening width (e.g. δ_n). Stage IV represents the new surfaces created by the fracture process, which have no traction (no load bearing capacity).

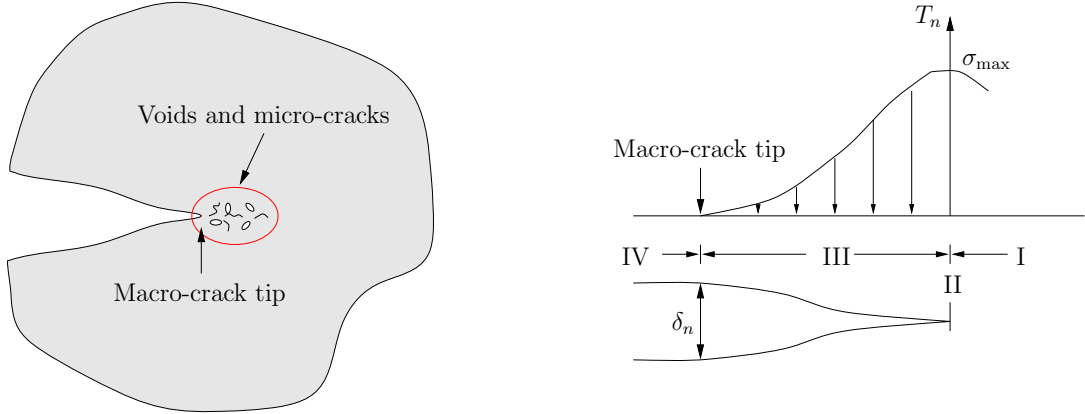


Figure 1.2: Schematics of the cohesive zone model.

1.2 Cohesive Constitutive Relationships

In the cohesive zone model, the fundamental issue for simulation of failure mechanisms is the characterization of cohesive interactions along the fracture surface. The cohesive constitutive relationship can be classified by either *non-potential-based models* (e.g. Geubelle and Baylor, 1998; Yang and Thouless, 2001; Camanho and Davila, 2002; Zhang and Paulino, 2005; van den Bosch et al., 2006) or *potential-based models* (e.g. Needleman, 1987; Beltz and Rice, 1991; Tvergaard and Hutchinson, 1993; Xu and Needleman, 1993).

1.2.1 Non-Potential-Based Models

Non-potential-based models are relatively simple to develop cohesive interactions because a symmetric system is not required. For instance, Yang and Thouless (2001) utilized trapezoidal shaped traction-separation relationships to simulate mixed-mode fracture of plastically deforming adhesive joints. Zhang and Paulino (2005) utilized a traction-based bilinear cohesive zone model for the analysis of homogeneous and

functionally graded materials (FGMs) undergoing dynamic failure. Shim et al. (2006) extended the traction-based model to the displacement-based bilinear cohesive zone model in order to investigate J resistant behavior of TiB/Ti FGM in conjunction with the domain integral. In addition, van den Bosch et al. (2006) proposed an alternative exponential cohesive relationship, and assessed the work-of-separation under mixed-mode conditions. However, the main limitation of a non-potential-based model is that one does not account for all possible separation or loading paths of crack growth in a domain. Therefore, non-potential-based models may provide non-physical cohesive interactions (e.g. positive stiffness in a softening region) under certain mixed-mode fracture conditions, although they can capture physical fracture behavior for known crack path problems (e.g. mode I fracture or inter-layer delamination). Thus, such models may converge to a wrong solution. Moreover, the tangential stiffness leads to the unsymmetric condition, which increases computational cost when solving the underlying linear system of governing equations.

1.2.2 Potential-Based Models

A potential function is associated with physical field quantities as a function of position at the continuum or atomistic level (e.g. gravity, strain energy, magnetic energy, electric energy). In a continuum setting, strain-energy functions allow the determination of stresses and the stiffness distributions in a solid. For isotropic and incompressible materials, the general strain-energy function can be deduced from the linear relationship between shear and traction (Mooney, 1940). At the atomistic level, pair potentials are mostly utilized to represent the particle debonding process as a function of an atomic distance (ℓ) such as the Lennard-Jones potential. The general shape of atomistic potentials (Girifalco and Weizer, 1959) is shown in Figure 1.3(a). A potential function must have a minimum at some point because the interaction force, i.e. the derivative of the potential, must be attractive at large distances, and repulsive at smaller distances. The work to complete dissociation (Ψ_0) of an interaction should be finite, which corresponds to the area under the interaction force curve (Figure 1.3(b)). When the distance between particles becomes critical (ℓ_{cr}), the interaction reaches a limit point. The potential (Ψ) has a convex shape ($\Psi'' > 0$) before the limit, and a concave shape ($\Psi'' < 0$) after the limit point.

Due to the physical nature of a potential, the first derivative of the fracture energy potential (Ψ) provides the traction (cohesive interactions) over fracture surfaces, and its second derivative provides the constitutive relationship (material tangential mod-

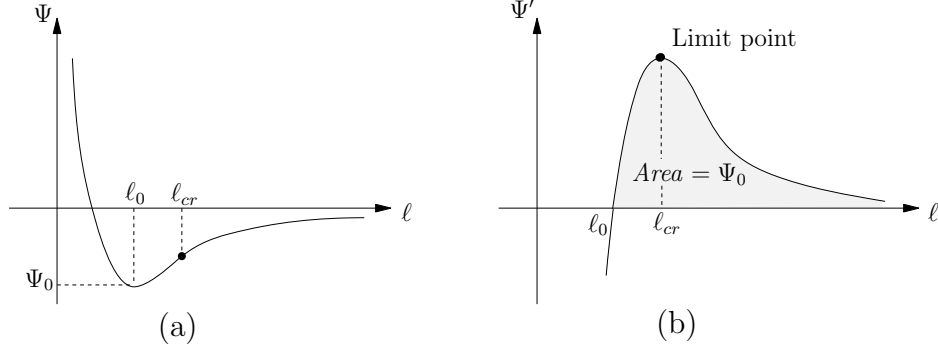


Figure 1.3: (a) Shape of a general atomistic potential (Ψ) and (b) its derivative (Ψ').

ulus). A single potential function, therefore, characterizes the physical fracture behavior. Previously, Tvergaard and Hutchinson (1993) developed the one-dimensional traction potential,

$$\Psi = \delta_n \int_0^\lambda \sigma(\lambda') d\lambda' , \quad (1.1)$$

which has been utilized to simulate interfacial fracture. The mode-mixity is considered by an effective displacement (λ) expressed as

$$\lambda = \sqrt{(\Delta_n/\delta_n)^2 + (\Delta_t/\delta_t)^2} \quad (1.2)$$

where Δ_n and Δ_t are normal and tangential separations over the fracture surface, respectively, and δ_n and δ_t are characteristic length scales which are related to the fracture energy and the cohesive strength. The function $\sigma(\lambda)$ represents a traction-separation relationship.

Although the one-dimensional potential model captures fracture behavior by changing the shape of the softening curve, the model can not have different fracture energies in modes I and II (Tvergaard and Hutchinson, 1993). However, most materials have different fracture energies with respect to the loading mode (Anderson, 1995). Several researchers have demonstrated the variation of the fracture energy from mode I fracture to mode II fracture through mixed-mode fracture specimen testing (Banks-Sills and Bortman, 1986) and delamination testing (Reeder and Crews Jr., 1990; Benzeggagh and Kenane, 1996). Carpinteri et al. (1989) demonstrated that mixed-mode fracture energy increased by about 30% over the mode I fracture energy for concrete. Zhu et al. (2009) obtained traction-separation relationships for mode I and mode II fracture of adhesive, and illustrated that the mode II fracture energy is approximately two times greater than the mode I fracture energy. Due to the relatively high fracture energy in mode II, a structure may have higher loading capacity under certain

loading conditions. Therefore, a potential function, which captures different fracture energies, is necessary for the simulation of the mixed-mode fracture. This is one of the contributions of the present work.

There are several potential functions that describe different fracture modes for cohesive fracture. Needleman (1987) proposed a polynomial function-based potential to simulate void nucleation by debonding. In order to account for large shear displacements, Needleman (1990) developed the exponential-periodic potential. Later, the exponential-periodic potential was generalized by Beltz and Rice (1991). The normal interaction is described by the exponential expression based on the atomistic potential by Rose et al. (1981), while the tangential interaction employs a periodic function due to the periodic dependence of the underlying material lattice (Rice, 1992). In order to consider shear failure relation, Xu and Needleman (1993) proposed the exponential potential for both normal and tangential cohesive interactions. The limitations of these potentials are discussed in detail in Chapter 3.

1.3 Computational Methods

Based on the concept of the cohesive zone model, the nonlinear fracture process zone has been approximated by various computational methods. For example, Hillerborg et al. (1976) combined the cohesive zone model with the finite element method (FEM) for the analysis of quasi-brittle materials (e.g. concrete) through an equivalent nodal force that corresponds to the linear traction-separation relationship. Ingraffea et al. (1984) introduced tension softening elements to consider the bond-slip in reinforced concrete. In this section, several computational methods such as intrinsic cohesive surface element approach, extrinsic cohesive surface element approach, enrichment function-based approach, embedded discontinuities, microplane model, atomistic/continuum coupling model, virtual internal bond model, peridynamics, and other methods are briefly reviewed.

1.3.1 Intrinsic versus Extrinsic Cohesive Models

In the cohesive surface element approach, the nonlinear cohesive traction separation relationship is represented by cohesive surface elements, while continuum deformation is described by volumetric (or bulk) elements. Cohesive surface elements are inserted between two volumetric elements, which result in the discontinuity of displacement field, and represent the constitutive relationship of cohesive fracture. Cohesive surface

elements can be inserted either before or during computational simulation. The former approach requires a cohesive surface network within the potential crack path domain (Xu and Needleman, 1994), as shown in Figure 1.4. This approach leads to the *intrinsic cohesive zone model*. The traction-separation relationship (e.g. $T_n - \Delta_n$) of the intrinsic cohesive zone model includes an initial elastic range in which separation is between zero and critical (e.g. δ_{nc} in Figure 1.4). When separation is critical (e.g. $\Delta_n = \delta_{nc}$), the cohesive traction reaches the cohesive strength (σ_{\max}) which corresponds to the onset of a crack initiation. In this case, a crack propagation criterion is incorporated with the constitutive relation. The initial elastic range can provide significant artificial compliance, especially when cohesive surface elements are inserted in a large domain (Klein et al., 2001). However, the main advantage of the intrinsic cohesive zone model is that the model can be easily integrated with a standard finite element analysis software. Because of its simplicity, intrinsic cohesive zone models have been utilized for a wide range of materials such as FGMs (Zhang and Paulino, 2005), plain concrete (Park, 2005; Roesler et al., 2007b), and asphalt concrete (Song et al., 2006).

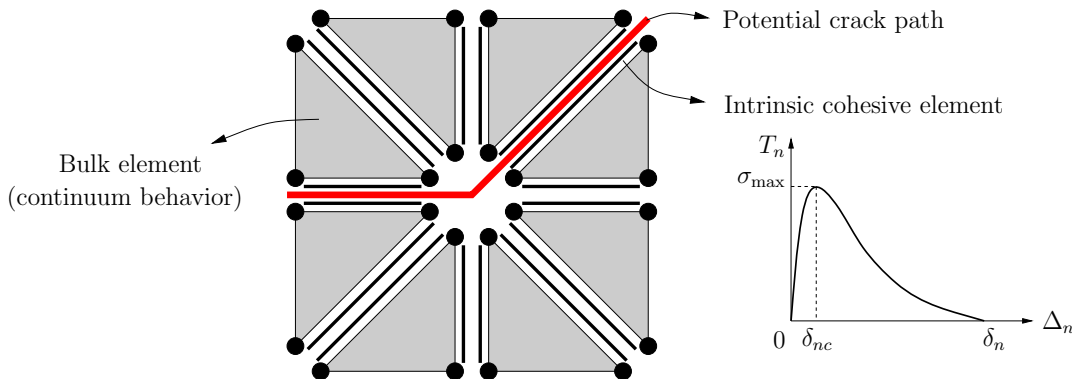


Figure 1.4: Schematics of the intrinsic cohesive zone model.

On the other hand, cohesive surface elements can be adaptively inserted during computational simulation whenever and wherever they are necessary (Camacho and Ortiz, 1996), as shown in Figure 1.5. This approach leads to the *extrinsic cohesive zone model*. The insertion of cohesive elements results in the duplication of nodes and the change of local element connectivity. Because of such modifications during computation, an efficient and robust topological data structure is generally necessary in the extrinsic cohesive zone model (Celes et al., 2005a; Paulino et al., 2008). The constitutive relationship of the extrinsic cohesive zone model excludes the elastic range (i.e. no artificial compliance), and thus provides a finite traction value at

the zero separation. This model requires an external criterion for the insertion of cohesive surface elements. Camacho and Ortiz (1996) introduced the initially rigid linear cohesive relation, and Ortiz and Pandolfi (1999) extended the linear cohesive relationship to finite-deformation irreversible cohesive interaction in three dimensions. Based on the linear cohesive interaction, Zhou et al. (2005) investigated fragmentation process in conjunction with strain rate and initial defects distribution, and Zhang et al. (2007) simulated microbranching instability experiments. In addition, Falk et al. (2001) demonstrated that computational results with the extrinsic cohesive zone model can be different from the results with the intrinsic cohesive zone model. Papoulia et al. (2003, 2006) addressed time continuity at the time of cohesive surface element activation, and error in representing cracks with finite element meshes.

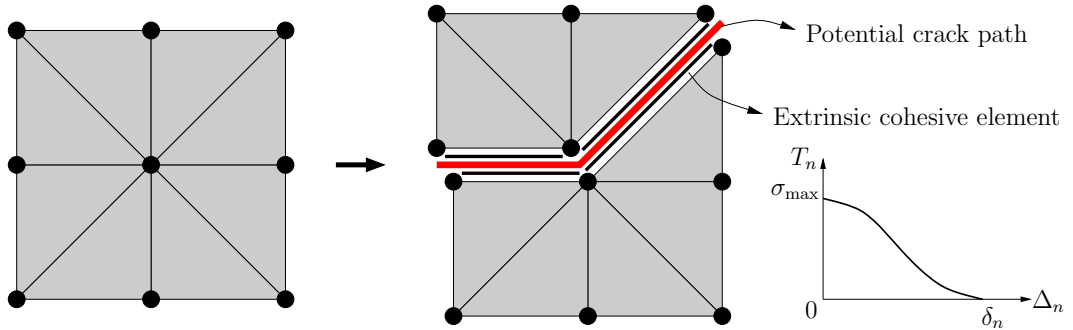


Figure 1.5: Schematics of the extrinsic cohesive zone model.

1.3.2 Enrichment Function Based Approach: GFEM/X-FEM

A crack in a domain is represented by a set of shape functions in the FEM. Then, the standard finite element shape functions are generalized/extended by introducing custom-built enrichment functions using the partition of unity methodology (Babuska and Melenk, 1997; Duarte and Oden, 1996). Accordingly, the resulting method is named either generalized FEM (GFEM) (Duarte et al., 2000) or extended FEM (X-FEM) (Daux et al., 2000) in the technical literature. Wells and Sluys (2001) and Moes and Belytschko (2002) utilized a Heaviside function to represent cohesive crack growth. Note that a node whose support (or cloud) has a crack is enriched by a Heaviside function. Duarte et al. (2007) represented through-the-thickness three-dimensional Y-shaped branch cracks for arbitrary background finite element meshes with high-order enrichment functions. However, non-polynomial enrichment functions lead to additional computational costs in numerical integration (Park et al.,

2009b). In addition, calculations based on a level-set discontinuity tracking method (Belytschko et al., 2003) have difficulties in representing complicated crack patterns, for example, micro-crack branching that exists around a major crack in dynamic fracture problems (Song and Belytschko, 2009). According to Bishop (2009), computational modeling of arbitrary three-dimensional intersecting cracks becomes untenable when crack branching and crack coalescence occurs.

1.3.3 Finite Elements with Embedded Discontinuities

Discontinuity is introduced at the element level, which leads to either a *weak discontinuity* or a *strong discontinuity*. A weak discontinuity provides discontinuous strain fields and continuous displacement fields, while a strong discontinuity results in both strain and displacement discontinuity within the element level. A weak discontinuity like strain localization is introduced, for instance, by enriching strain fields (Ortiz et al., 1987) or by imposing traction continuity and compatibility within an element (Belytschko et al., 1988). A strong discontinuity is considered by continuum type constitutive relationships in conjunction with the Dirac distribution (Simo et al., 1993). Discontinuities introduced in finite elements lead to additional parameters (or degrees of freedom), and these additional degrees of freedom are eliminated by condensation on the element level (Jirasek, 2000). Linder and Armero (2007, 2009) utilized finite elements with embedded strong discontinuities for simulation of quasi-static fracture, and extended the embedded discontinuities to so-called “T-shaped” discontinuities for dynamic branching problems. Maiti et al. (2009) replaced an element with an internal discontinuity due to cohesive fracture by two superimposed elements with a combination of original and imaginary nodes.

1.3.4 Microplane Model

A microplane model integrates elastic and fracture (or softening) behaviors in the constitutive relation. The constitutive relationships of the microplane model are characterized by stresses and strains on planes of various orientations within a material, called the microplanes (Bazant, 1984; Jirasek and Bazant, 1995). This idea is originated from the slip theory of plasticity (Taylor, 1938; Batdorf and Budiansky, 1949), which is used for capturing strain hardening behavior. For the investigation of tensile softening material behavior like concrete, Bazant and Oh (1985) considered normal microplane stress, which was a function of normal strain on a microplane,

and obtained a tangent stiffness by using the principle of virtual work. In order to represent wide range of Poisson's ratio, normal deviatoric and volumetric strains and shear strain on microplanes were introduced by Bazant and Prat (1988). Because the microplane model by Bazant and Prat (1988) can lead to large lateral strains under large tensile strains, Bazant et al. (1996) incorporated the concept of stress-strain boundaries. Carol and Bazant (1997) demonstrated the relationship between microplane elasto-plasticity and a classical macroscopic elasto plastic formulation. The microplane model is further improved in conjunction with work-conjugate deviatoric stress (Bazant et al., 2000) and traction-separation relationships of cohesive fracture (Bazant and Caner, 2005).

1.3.5 Atomistic/Continuum Coupling

Continuum deformation and failure are analyzed in conjunction with atomic-scale models. In order to couple atomistic and continuum deformation, Tadmor et al. (1996) proposed the quasi-continuum method by adopting the Cauchy-Born rule. Miller et al. (1998) utilized the quasi-continuum method to investigate the competition between simple cleavage and crack-tip dislocation emission. Shilkrot et al. (2002) combined the quasi-continuum method with continuum defect models like the discrete dislocation method. Alternatively, Liu et al. (2008) modified the Cauchy-Born rule to account for kinematics of surface separation by introducing a discontinuous Cauchy-Born rule, which resulted in the estimation of the cohesive traction-separation relationships based on atomistic information. Li et al. (2008) used the generalized mathematical homogenization theory to obtain continuum descriptions from molecular dynamics equations.

1.3.6 Virtual Internal Bond Model

Macroscopic cohesive fracture is represented by connecting an atomistic potential to a macroscopic continuum potential through multi-scaling techniques. Gao and Klein (1998) developed the virtual internal bond (VIB) model, which integrates the macroscopic view of cohesive surfaces and the atomistic view of cohesive bonding between discrete particles. While the cohesive zone model separates fracture and elastic behaviors into cohesive surface elements and volumetric (or bulk) elements, respectively; the VIB model represents both elastic and fracture behavior within the framework of continuum mechanics via the Cauchy-Born rule (Born, 1940; Klein et al., 2001). Gao

and Ji (2003) implemented the VIB modeling in nanomaterials demonstrating transition of fracture mechanisms from classical linear elastic fracture mechanics (LEFM) to homogeneous failure near the theoretical strength of solids. Thiagarajan et al. (2004) have investigated dynamic fracture behavior for a brittle material under impact loading using the VIB model. Moreover, the model was modified by Volokh and Gao (2005) to account for two independent linear elastic constants. The VIB model is further extended to consider two different fracture energies in this study.

1.3.7 Peridynamics

The peridynamics theory (Silling, 2000) is developed to represent discontinuities (e.g. a crack) as a result of deformation. In peridynamics, damage is associated with a pairwise force function that allows bonds to break. Computational implementation of peridynamics incorporates existing computational methods such as the meshless method (Silling and Askari, 2005), the FEM (Macek and Silling, 2007), and molecular dynamics (Parks et al., 2008). Gerstle et al. (2007) generalized the peridynamic model by adding pairwise peridynamic moments, named as the micropolar peridynamic model, because the original peridynamic model suffered from representing a Poisson's ratio other than 0.25 (Silling, 1998). Bobaru (2007) utilized the peridynamic method to analyze the effect of van der Waals forces on mechanical properties of nanofiber networks, and Kilic et al. (2009) investigated damage progression of center-cracked composite laminates with different fiber orientations.

1.3.8 Other Methods

The space-time FEM is developed on the basis of the discontinuous Galerkin method (Hughes and Hulbert, 1988). The method is applied to fracture problems, for example, oxidation-driven fracture (Carranza et al., 1998), and elasto-dynamic cohesive fracture (Huang and Costanzo, 2004). Furthermore, the concept of the space-time FEM is extended to the space-time discontinuous Galerkin method, which supports fully unstructured space-time meshes and discontinuous basis functions across inter-element boundaries (Abedi et al., 2006). Alternatively, Abraham et al. (1994) employed molecular dynamic simulations with parallel computing to investigate the dynamic instability of a crack tip. Fago et al. (2004) integrated the density functional theory with macroscopic finite element calculation by using the Cauchy-Born hypothesis. Fan and Fish (2008) introduced a refined local patch to describe failure mode,

and embedded the local patch into the coarse grid by using the partition of unity method, named as the *rs*-method. Matous et al. (2008) developed a multiscale cohesive failure model of heterogeneous adhesives in conjunction with a computational homogenization scheme, and Kulkarni et al. (2009) used the multiscale cohesive failure model to examine macroscopic failure response of heterogeneous adhesives. Song and Belytschko (2009) introduced a set of discrete crack segment to represent complicated two-dimensional dynamic fracture patterns.

1.3.9 Present Approach

In this study, potential-based cohesive zone and virtual internal bond models are utilized. For the computational investigation of dynamic fracture, branching and fragmentation, the extrinsic cohesive zone model is implemented in conjunction with a topological data structure, nodal perturbation and edge-swap operator. In order to achieve efficient computation, adaptive mesh refinement and coarsening schemes are introduced in dynamic fracture and branching problems. Notice that the extrinsic cohesive zone model is capable of representing spontaneous crack initiation, propagation, branching and fragmentation within a framework of the FEM. For quasi-static crack propagation problems, the intrinsic cohesive zone model is implemented in commercial software as a user element subroutine, while the virtual internal bond model is also implemented as a user material subroutine.

1.4 Research Objective and Thesis Organization

The objective of this thesis is to investigate crack propagation phenomena through the development of a novel potential-based constitutive model in conjunction with robust and efficient computational methods. A unified potential-based cohesive model of mixed-mode fracture is proposed for the constitutive relationship of the fracture surface. The proposed model is verified and validated through investigations of quasi-static fracture, dynamic fracture, microbranching and fragmentation. In addition, the virtual internal bond model is employed to investigate fracture behavior of quasi-brittle materials including the size effect.

The thesis is organized as follows. In the subsequent chapter, the original virtual internal bond model is extended to the virtual internal pair bond (VIPB) model in order to represent a relatively large fracture process zone in quasi-brittle materials like concrete. The VIPB model accounts for two different fracture energies associating

a short range potential and a long range potential. Next, a potential-based cohesive zone model, named as the PPR (Park-Paulino-Roesler) model, is developed in Chapter 3. The PPR model is based on physical fracture parameters such as fracture energy, cohesive strength and shape of softening curve in order to be applicable to a wide range of material softening behavior. Chapter 4 explains the implementation of the PPR potential-based model including the unloading/reloading relationships. Then, the PPR model is utilized for the investigation of both quasi-static fracture (Chapter 5) and dynamic fracture (Chapters 6 and 7) phenomena. Chapter 5 focuses on particle/matrix interfacial fracture, i.e quasi-static, to obtain macroscopic constitutive relationships of materials with microstructure. This multiscale investigation is integrated with micromechanics and a finite element-based cohesive zone model. Chapters 6 and 7 explore dynamic fracture, microbranching and fragmentation problems associating with adaptive topological operators. Chapter 6 proposes the use of nodal perturbation and/or edge-swap operators in dynamic fracture simulation in order to obtain realistic crack patterns. Adaptive mesh refinement and coarsening (AMR & C) schemes for cohesive fracture are developed in Chapter 7, which significantly reduce computational cost. Adaptive mesh refinement is based on a sequence of edge-split operators, while adaptive mesh coarsening is performed by utilizing edge-collapse (or vertex-removal) operators. The convergence and consistency of computational results are addressed. Finally, Chapter 8 summarizes major contribution of this thesis, and provides possible research areas for future work.

Chapter 2

Virtual Internal Pair-Bond Model for Quasi-Brittle Materials

The present multiscale investigation employs the initial and total fracture energy through a virtual internal pair-bond (VIPB) model. The proposed VIPB model is an extension of the traditional virtual internal bond (VIB) model. Two different types of potentials, a steep short-range potential and a shallow long-range potential, are employed to describe the initial and the total fracture energies, respectively. The Morse potential function is modified for the virtual bond potential so that it is independent of specific length scales associated with the lattice geometry. This feature is incorporated in the VIPB model, which uses both fracture energies and cohesive strength. With respect to the discretization by finite elements, the element size dependence is addressed in conjunction with the J -integral. Parameters in the VIPB model are evaluated by computational simulations of a pure tension test in conjunction with measured fracture parameters. The VIPB model is validated by predicting load versus crack mouth opening displacement curves for geometrically similar specimens, and the measured size effect. Finally, an example involving fiber-reinforced concrete is provided, which demonstrates the advantage of the VIPB model over the usual VIB model.

2.1 Introduction

Interpreting structural behavior such as maximum load-bearing capacity is a relevant issue for structures containing quasi-brittle materials, especially concrete, because of their relatively large fracture process zone. The relatively large fracture process zone present in concrete results in the strength of a concrete beam in a laboratory-sized specimen being different from the strength of a concrete beam in an actual structure. This behavior is typically associated to the size effect (Bazant and Planas, 1998; Bazant, 1999, 2000). In order to characterize the relatively large fracture process zone in quasi-brittle materials, two different fracture energies, the initial fracture energy and the total fracture energy, are introduced by employing the concept of the

equivalent elastic crack model (Bazant and Planas, 1998; Shah et al., 1995). Roesler et al. (2007b) and Park (2005) have shown that both energies are essential to characterize concrete fracture behavior. For computational simulation of fracture behavior for quasi-brittle materials, the virtual internal bond (VIB) model is employed, among several computational methods discussed in Chapter 1. The VIB model integrates the macroscopic view of cohesive surfaces and the atomistic view of cohesive bonding between discrete particles (Gao and Klein, 1998).

In order to consider two fracture energies, a virtual internal pair-bond (VIPB) model is proposed, which accounts for the relatively large fracture process zone and the size effect for quasi-brittle materials. Additionally, a modified Morse potential is utilized so that it is independent of any lattice parameter. The VIPB model thus characterizes essential macroscopic fracture parameters, i.e. fracture energies (initial and total) and cohesive strength of the material.

This chapter is organized as follows. In the following section, the traditional VIB model formulation and a modified Morse potential function are presented for quasi-brittle materials. Next, the concept of the VIPB model is described in conjunction with two distinct fracture energies. Section 2.4 explains the determination of material properties including element size dependences, and Sections 2.5 and 2.6 address verification and validation, respectively. Finally, the key findings of the present work are summarized.

2.2 Virtual Internal Bond (VIB) Model Formulation

The VIB model (Gao and Klein, 1998; Klein and Gao, 1998) describes the continuum behavior based on the microscopic interactions between particles within the concept of homogenization, as shown in Figure 2.1. The microscopic behavior is connected to the macroscopic behavior by the Cauchy-Born rule, which results in the strain energy function (Tadmor et al., 1996). The VIB model represents both elastic and fracture behavior within the framework of continuum mechanics by using the macroscopic strain energy function. In this section, the VIB model formulation is reviewed, and a modified Morse bonding potential function, which represents the microscopic interactions between particles, is proposed.

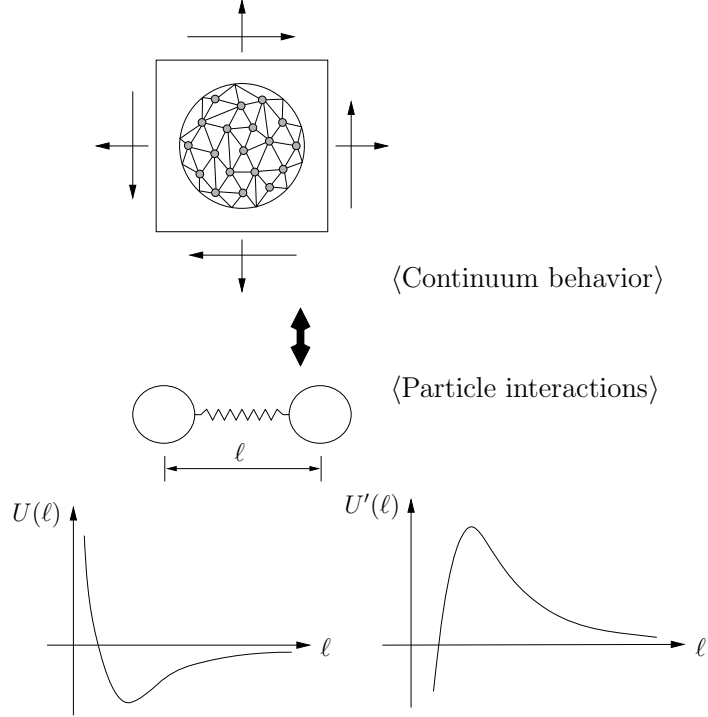


Figure 2.1: Schematic illustration of the original VIB model.

2.2.1 Strain Energy Function in the VIB Model

The strain energy function in the VIB model is characterized by the bonding potential function via the Cauchy-Born rule. The Cauchy-Born rule is essentially a multiscale assumption to connect atomistic behavior in the micro length scale with continuum behavior in the macro length scale. Under this assumption, continuum behavior can be described by a single mapping function (i.e. deformation gradient \mathbf{F}),

$$\mathbf{F} = \frac{\partial \mathbf{x}}{\partial \mathbf{X}}, \quad (2.1)$$

from the undeformed configuration (Lagrangian coordinates, $\mathbf{X} = X_I$) to the deformed configuration (Eulerian coordinates, $\mathbf{x} = x_i$). Therefore, the bonding potential $U(\ell)$ is defined by a deformed virtual bond length ℓ along a bond direction $\boldsymbol{\xi}$,

$$\ell = \ell_0 \sqrt{\boldsymbol{\xi} \cdot \mathbf{F}^T \mathbf{F} \boldsymbol{\xi}}, \quad (2.2)$$

where ℓ_0 is an undeformed virtual bond length. Based on the bonding potential, the strain energy function (Φ) is represented by the summation of the bonding potential

with a bond density \mathcal{D}_Ω over domain Ω ,

$$\Phi = \int U(\ell(\mathbf{F}))\mathcal{D}_\Omega d\Omega . \quad (2.3)$$

If the bond direction $\boldsymbol{\xi}$ is specified by a three dimensional spherical coordinate system, the strain energy function (2.3) is expressed by

$$\Phi = \langle U(\ell) \rangle , \quad (2.4)$$

where

$$\langle \dots \rangle = \int_0^{2\pi} \int_0^\pi \int_0^{\ell_0} \dots \mathcal{D}_\Omega(\phi, \theta, \ell_0) \sin \theta d\ell_0 d\theta d\phi , \quad (2.5)$$

and the bond direction vector is given as $\boldsymbol{\xi} = (\sin \theta \cos \phi, \sin \theta \sin \phi, \cos \theta)$.

For a two dimensional plane stress problem, the strain energy function is expressed by

$$\Phi = \langle U(\ell) \rangle = \int_0^{2\pi} \int_0^{\ell_0} U(\ell)\mathcal{D}_\Omega(\phi, \ell_0)d\ell_0 d\phi \quad (2.6)$$

and the bond direction vector is selected as $\boldsymbol{\xi} = (\cos \phi, \sin \phi)$.

In this study, a two dimensional constant bond density function, $\mathcal{D}_\Omega = \mathcal{D}_0$, is considered, which illustrates an isotropic solid, and has the same initial bond length (ℓ_0) over the domain. The constant bond density function simplifies the strain energy function to

$$\Phi = \langle U(\ell) \rangle = \mathcal{D}_0 \int_0^{2\pi} U(\ell)d\phi , \quad (2.7)$$

which is also suitable for numerical investigation of fracture properties.

2.2.2 Constitutive Relation

From the determination of the strain energy function (2.7), the constitutive relation is formulated on the basis of continuum mechanics. The Lagrangian strain \mathbf{E} and the 2nd Piola-Kirchhoff stress tensor \mathbf{S} are used for computing the stress and the material modulus. The derivative of the strain energy with respect to the Lagrangian strain provides the second Piola-Kirchhoff stress,

$$S_{IJ} = \frac{\partial \Phi}{\partial E_{IJ}} = \left\langle \ell_0^2 \frac{U'(\ell)}{\ell} \xi_I \xi_J \right\rangle . \quad (2.8)$$

Similarly, the material tangent modulus is obtained by the second derivative of the strain energy function with respect to the Lagrangian strain,

$$C_{IJKL} = \frac{\partial^2 \Phi}{\partial E_{IJ} \partial E_{KL}} = \left\langle \ell_0^4 \left(\frac{U''(\ell)}{\ell^2} - \frac{U'(\ell)}{\ell^3} \right) \xi_I \xi_J \xi_K \xi_L \right\rangle , \quad (2.9)$$

which satisfies the Cauchy symmetry,

$$C_{IJKL} = C_{IKJL} , \quad (2.10)$$

in addition to the usual major and minor symmetries of elasticity. Because of these symmetries, only one elastic property is necessary. Therefore, the Cauchy symmetry is satisfied by the fourth order isotropic elasticity tensor whose Lamé parameters (μ , λ) are the same (Thiagarajan et al., 2004). Additionally, the VIB (or VIPB) model is hyperelastic and does not account for dissipation (unloading path is the same as the loading path).

2.2.3 Virtual Bond Density Potential

The focus of the VIB model is the determination of the virtual bond potential ($U(\ell)$) and the bond density function (\mathcal{D}_0), which describe both elastic behavior and fracture behavior. The bond density potential Ψ is defined as the bond potential multiplied by a bond density function,

$$\Psi(\ell) = \mathcal{D}_0 U(\ell) . \quad (2.11)$$

Previous researchers (e.g. Gao and Klein, 1998; Klein and Gao, 1998; Zhang et al., 2002; Klein et al., 2001; Nguyen et al., 2004; Thiagarajan et al., 2004) have employed a two-parameter (A , B) phenomenological cohesive law,

$$\Psi'(\ell) = \mathcal{D}_0 U'(\ell) = A(\ell - \ell_0) e^{-(\ell - \ell_0)/B} , \quad (2.12)$$

for the bond density potential in the VIB model implementation. The constant A is related to the initial Young's modulus while the constant B can be determined by the cohesive strength or by the fracture energy. Thus, this potential function can only characterize two material parameters: the initial elastic property and one fracture property.

In this study, the generalized Morse function (Morse, 1929; Girifalco and Weizer, 1959; Milstein, 1973) is modified to represent the bond density potential and to char-

acterize three macroscopic material parameters, specifically initial elastic modulus, fracture energy and cohesive strength. The modified Morse potential function is proposed herein as

$$\Psi(\ell) = \mathcal{D}_0 U(\ell) = \frac{\mathcal{D}}{m-1} \left[e^{-m\alpha(\ell/\ell_0-1)} - m e^{-\alpha(\ell/\ell_0-1)} \right] . \quad (2.13)$$

The two exponents (m, α) in the potential function can characterize two fracture parameters: the cohesive strength and the fracture energy. The parameter \mathcal{D} is associated with one elastic property, i.e. Young's modulus. Furthermore, the potential function is independent of the lattice parameter (ℓ_0) because the particle distance (ℓ) is normalized with respect to the lattice parameter (ℓ_0), which is not the case in the original Morse potential.

2.2.4 Computational Implementation

Numerical simulations of the VIB (or VIPB) model can be implemented by using a commercial software, e.g. ABAQUS, with the application of the user material (UMAT) subroutine (see Appendix B). If the software uses the Cauchy stress ($\boldsymbol{\sigma}$) rather than the 2nd Piola-Kirchhoff stress (\mathbf{S}) for the stress update scheme, then one must transform the 2nd Piola-Kirchhoff stress into the Cauchy stress with the known relationship (see, for example, Belytschko et al. (2000)),

$$\boldsymbol{\sigma} = \frac{1}{\det(\mathbf{F})} \mathbf{F} \mathbf{S} \mathbf{F}^T . \quad (2.14)$$

2.3 Virtual Internal Pair-Bond (VIPB) Model

The fracture energy and the cohesive strength are basic quantities to describe material fracture behavior. For quasi-brittle materials, especially concrete, two different energies are necessary for explaining the size effect (Bazant and Becq-Giraudon, 2002). The initial fracture energy (G_f) is size independent and is based primarily on the peak load. The other quantity is the total fracture energy (G_F), which is specimen size dependent. The proposed virtual internal pair-bond (VIPB) model considers both fracture energies in order to capture the measured size effect (Park et al., 2008b).

In the VIPB model, two bonding density potentials are connected between two particles, as shown in Figure 2.2(a). One step short-range potential, $\Psi_1(\ell)$, Figure

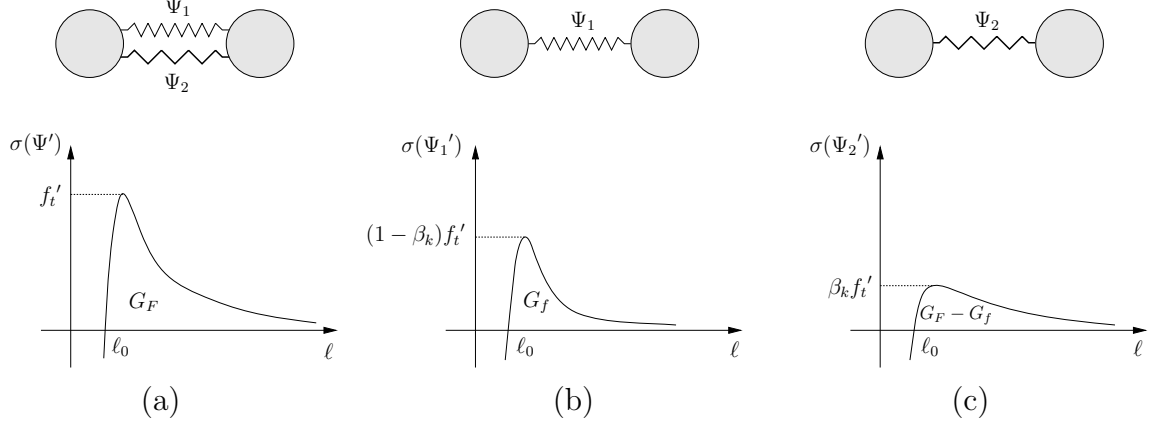


Figure 2.2: Schematic illustration of the VIPB model: (a) the relationship between stress and bond length from the pair-bond potential ($\Psi = \Psi_1 + \Psi_2$); (b) the relationship from the steep short-range potential (Ψ_1) and (c) the relationship from the shallow long-range potential (Ψ_2).

2.2(b), is related to the initial fracture energy, and a longer-range shallower potential, $\Psi_2(\ell)$, Figure 2.2(c), is associated with the difference between the initial fracture energy and the total fracture energy. The summation of each potential represents the bond density potential function of the VIPB model as illustrated in Figure 2.2(a),

$$\Psi(\ell) = \Psi_1(\ell) + \Psi_2(\ell) , \quad (2.15)$$

where

$$\Psi_i(\ell) = \frac{\mathcal{D}_i}{m_i - 1} [e^{-m_i \alpha_i (\ell/\ell_0 - 1)} - m_i e^{-\alpha_i (\ell/\ell_0 - 1)}] \quad (i = 1, 2) . \quad (2.16)$$

In this model, one bond density potential (Ψ_1), represented by G_f , is independent of the size so that the VIPB model characterizes the size effect. Another bond density potential (Ψ_2), described by $(G_F - G_f)$, depends on the specimen size to satisfy the size dependence of the total fracture energy.

Each potential function contains three unknown constants (\mathcal{D}_i , m_i and α_i) which can be determined by an elastic property (elastic modulus), and fracture properties (fracture energy and cohesive strength). The elastic and fracture properties are defined in each of the respective bond density potential function (Ψ_1 and Ψ_2). The fracture energy is separated into G_f and $(G_F - G_f)$, as previously discussed.

The cohesive strength of the steep short-range potential is assumed then to be $(1 - \beta_k)f'_t$, while that of the longer-range shallower potential is assumed to be $\beta_k f'_t$, as shown in Figure 2.2(b) and (c). The strength ratio (β_k) of the two potentials can be defined as the kink point stress ratio in the bilinear softening model described

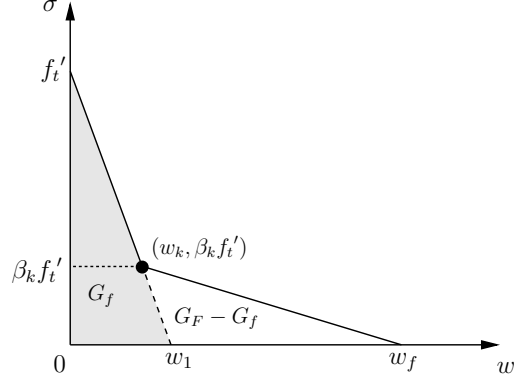


Figure 2.3: Bilinear Softening model for concrete where f'_t is the tensile strength, G_f is the initial fracture energy, G_F is the total fracture energy, β_k is the strength ratio at the kink point, w_1 is the horizontal axis intercept of the initial descending line, w_k is the crack opening width at the kink point, and w_f is the final crack opening width – see Park (2005); Park et al. (2008a).

in Figure 2.3 (Park, 2005; Park et al., 2008a). Because the kink point in the bilinear softening model is related to a post-peak load behavior, the long-range potential characterizes a post-peak load behavior in the VIPB model. The initial elastic modulus of each potential is determined under the assumption of linear elasticity at small strain. The elastic modulus of the pair-bond potential model is the summation of each potential, $E = E_1 + E_2$, because the bonds are connected in parallel. Each elastic modulus can, therefore, be defined by the same ratio as the cohesive strength for each potential.

The concept of the VIPB model is extended to characterize material responses of fiber reinforced concrete (FRC). Fracture mechanisms of FRC generally consist of aggregate bridging and fiber bridging zones (Anderson, 1995; van Mier, 1996). The aggregate bridging zone describes the crack branching and interlocking which result from the weak interface between the aggregates and cement matrix. The fiber bridging zone represents the effect of fibers on the stress transfer at larger opening displacements. The aggregate bridging zone is illustrated by the steep short-range potential while the fiber bridging zone is described by the shallow long-range potential. The steep short-range potential (Ψ_1) is associated with the total fracture energy of plain concrete, and the shallow long-range potential (Ψ_2) is related to the difference between the total fracture energy of plain concrete (G_F) and the total fracture energy of FRC (G_{FRC}).

2.4 Determination of Material Properties

Since the proposed VIPB model is based on the same framework of continuum mechanics as the VIB model, elastic and fracture properties are investigated in conjunction with the traditional VIB model. In the VIB model, elastic properties are examined at the state of infinitesimal strain while fracture properties are evaluated with respect to element size dependences (Klein and Gao, 1998). Therefore, previous studies provide the basis for the material properties to be used in both the VIB model and the VIPB model.

2.4.1 Elastic Properties at Infinitesimal Strains

Elastic material properties of the VIB (or VIPB) model can be evaluated at the state of small strain by defining the material tangent modulus in two different ways (Gao and Klein, 1998). Either the strain energy function of the VIB (or VIPB) model or the linear elastic strain energy function represents the material tangent modulus. For the calculation of the material tangent modulus, the linearized strain is utilized because strain at the elastic range is infinitesimal.

First, the material tangent modulus is calculated by the strain energy function (2.4) of the VIB (or VIPB) model. Assuming infinitesimal strain, and taking a Taylor series expansion of the strain energy function and its second derivative with respect to the linearized strain, one obtains the material tangent modulus,

$$C_{ijkl} = \frac{4\pi}{15} \ell_0^2 \Psi''(\ell_0) (\delta_{ij}\delta_{kl} + \delta_{ik}\delta_{jl} + \delta_{il}\delta_{kj}) , \quad (2.17)$$

described by a bond density potential function, $\Psi(\ell)$, of the VIB (or VIPB) model.

Alternatively, the elastic modulus can be also obtained by the theory of linear elasticity. Since the strain is assumed to be linear, the strain energy function is quadratic. Taking the second derivative with respect to the linearized strain, one obtains the material tangent modulus, as expected

$$C_{ijkl} = \lambda \delta_{ij}\delta_{kl} + \mu (\delta_{ik}\delta_{jl} + \delta_{il}\delta_{kj}) . \quad (2.18)$$

From the Cauchy symmetry relation (2.10), the two Lamé parameters are assumed to be the same ($\lambda = \mu$) in the material tangent modulus. As a result, equating (2.17) and (2.18) results in the relationship between the shear modulus and the bond density

potential function,

$$\mu = \frac{4\pi}{15} \ell_0^2 \Psi''(\ell_0) , \quad (2.19)$$

for a three dimensional problem. The elastic properties are also represented by the Poisson's ratio (ν) and Young's modulus (E) whose relationships are

$$\nu = \frac{1}{4} \quad \text{and} \quad E = \frac{2\pi}{3} \ell_0^2 \Psi''(\ell_0) . \quad (2.20)$$

Moreover, for two dimensional plane stress problems, the relationship between the shear modulus and the bond density potential energy function is

$$\mu = \frac{\pi}{4} \ell_0^2 \Psi''(\ell_0) , \quad (2.21)$$

and Hooke's law leads to

$$\nu = \frac{1}{3} \quad \text{and} \quad E = \frac{2\pi}{3} \ell_0^2 \Psi''(\ell_0) . \quad (2.22)$$

The initial Young's modulus has been formed to correlate with the bond density potential (2.11), under the Cauchy symmetry condition ($\lambda = \mu$). Therefore, a constant \mathcal{D}_i ($i = 1, 2$), in the bond density potential is determined from the relationship between the Young's modulus and the bond density potential function (2.20 and 2.22) of the VIPB model. Substitution of (2.16) into (2.22) leads to

$$\mathcal{D}_i = \frac{3E_i}{2\pi m_i \alpha_i^2} \quad (i = 1, 2) , \quad (2.23)$$

which provides the closed form of the bond density function in terms of the elastic modulus and the two exponents (m_i, α_i) in the bond density potential. The exponents (m_i, α_i) can be associated with two fracture properties of materials, i.e. the fracture energy and the cohesive strength.

2.4.2 Fracture Properties and Mesh Size Dependences

The essential fracture parameters for mode I fracture are cohesive strength and fracture energy. These experimental fracture properties are utilized to estimate the two exponents (m_i, α_i) in the bond density potential through numerical simulations, e.g., the pure tension test (as discussed in the next section). In the simulation of a pure tension example, the numerical cohesive strength is assumed to be the peak stress in the pure tension test, while the numerical fracture energy is obtained from the area

under the stress-displacement curve in the simulation. The two exponents (m_i, α_i) in the bond potential can then be determined by curve fitting; the two numerical fracture parameters (strength and fracture energy) obtained by a pure tension simulation coincide with known material properties from experiments.

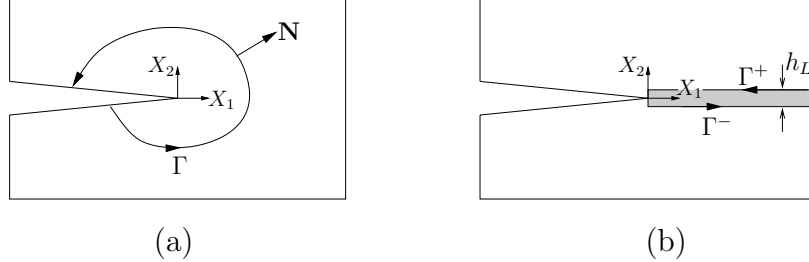


Figure 2.4: J -integral contours (a) for an arbitrary path and (b) for a path of the localization zone.

In the VIB (or VIPB) model, the fracture energy depends on the element size (Klein et al., 2001), which can be explained by the path independent J -integral (Rice, 1968b),

$$J = \int_{\Gamma} (U_0 \delta_{IJ} - P_{iJ} F_{iI}) N_J d\Gamma, \quad (2.24)$$

where Γ is a contour in the undeformed configuration surrounding the crack tip, U_0 is the strain energy density, \mathbf{P} is the 1st Piola-Kirchhoff stress, and \mathbf{N} is the outward normal to the contour, as shown in Figure 2.4(a). Because of path independence, a contour is selected along the upper and lower bound (Γ^+ and Γ^-) of the localization zone (h_L) where stress softening occurs (Figure 2.4(b)) for a mode I loading (Klein and Gao, 1998). The contour results in the symmetric stress and displacement field, and then one obtains J for mode I,

$$J = h_L \int_1^{\infty} P_{22} d\lambda_2 = G_I, \quad (2.25)$$

where λ_2 is stretch along the X_2 direction. Therefore, the J -integral introduces a length scale (h_L) which is proportional to the fracture energy in the VIB (or VIPB) model. Because of this relationship, one should consider a length scale (e.g. localization zone size) for the simulation of the VIB (or VIPB) model. Furthermore, the relationship provides guidance for verification studies and for determination of fracture parameters, discussed in the next section.

In summary, cohesive strength and fracture energy are considered in conjunction with the localization zone size to determine the exponents (α_i, m_i) in the bond density potential. First, one selects the localization zone size. Next, the exponents

are calibrated by numerical simulation, e.g. the pure tension test, which provides two numerical fracture parameters (cohesive strength and fracture energy) which are consistent with expected values of experiments.

2.5 Verification – Fracture Properties and Element-Size Dependence

The fracture behavior of the VIB (or VIPB) model is analyzed by performing both the pure tension and the double cantilever beam (DCB) tests. Because numerical simulations of the pure tension example are associated with the measured cohesive strength and the fracture energy, the simulations lead to determine the two exponents (m_i and α_i) with respect to the localization zone size (h_L). Additionally, the DCB test verifies the relationship between the fracture energy and the size of the localization zone, h_L , derived from the J -integral. Moreover, in order to illustrate that the localization zone size is proportional to the fracture energy obtained by the numerical simulations of the DCB example, each numerical test has two different FEA mesh sizes for the localization zone where the VIB (or VIPB) element is defined. The main difference between the pure tension and the DCB examples is that the localization zone is taken as the entire domain in the former example, while it is taken as a (single element) strip in the latter example.

The determination of the bond density potential for the VIB model correlates with three measured concrete material properties: the Young’s modulus ($E = 32$ GPa), the cohesive strength ($f_t' = 4.15$ MPa), and the reference fracture energy ($G_{F0} = 164$ N/m). The bond density potentials for the VIPB model are associated with additional measured fracture parameters, i.e. initial fracture energy ($G_f = 56.6$ N/m), and the strength ratio ($\beta_k = 0.34$).

Since the fracture energy (G_F) depends on the localization zone size (h_L) related to the VIB (or VIPB) element size, the reference fracture energy (G_{F0}) is defined at a reference localization zone size ($h_{L0} = 0.5$ mm). As shown in Table 2.1, if the size of the localization zone (h_L) grows in the FEA mesh, the numerical result of the fracture energy (G_F) also increases with the same ratio as that of the localization zone,

$$G_F = G_{F0} \frac{h_L}{h_{L0}} . \quad (2.26)$$

This relationship follows from expression (2.25), derived for the J -integral.

Table 2.1: Relationship between the VIB element size and the fracture energy.

	VIB element size (h_L) (m)	Total fracture energy	
		G_F - h_L relation (2.26) (N/m)	Computational results (N/m)
Pure tension	1	328000	328302
	0.5	164000	164311
DCB	$h_{L0} = 0.0005$	$G_{F0} = 164$	164
	0.00025	82	82

2.5.1 Pure Tension Test

The pure tension numerical simulation has a square (W by W) domain, elongated at the top under displacement control. The numerical results for two different plate sizes ($W = 1$ m and 0.5 m) are provided in Figure 2.5. The peak stress of the plate corresponds to the cohesive strength of 4.15 MPa. For the evaluation of the macroscopic numerical fracture energy, one calculates the area under the stress-displacement curve up to 40% elongation (chosen arbitrarily) of the virtual bond length (ℓ) with respect to the undeformed virtual bond length (ℓ_0). The calculated numerical fracture energy almost coincides with the analytical expression in (2.26), as shown in Table 2.1. Nu-

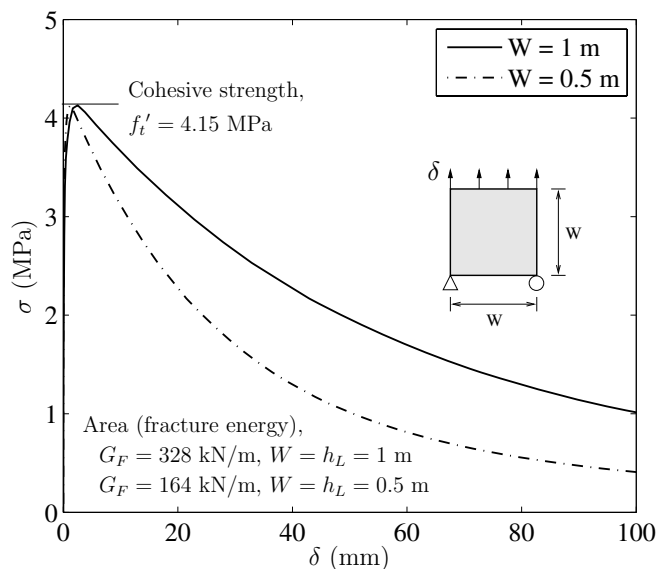


Figure 2.5: Numerical simulation result of a pure tension test using the VIB model with different domain sizes ($W = 1$ m and 0.5 m). The loading is performed with displacement control (δ).

merically, the area under the curve of the 1 m by 1 m plate is nearly twice that of the 0.5 m by 0.5 m plate. The bigger plate has twice the localization length of the smaller one. These numerical results illustrate that the fracture energy is proportional to the localization zone size in the VIB (or VIPB) model.

In addition, the VIPB (pair-bond potential) model is compared to the VIB (single bond potential) model in Figure 2.6, displaying results of the pure tension test with a localization zone size of 0.5 mm. The VIPB model results are indicated by a solid line for the stress-displacement curve, while the VIB model results are given by a dotted line. Each potential (Ψ_1 , Ψ_2) for the VIPB model is represented by dashed lines. Both the VIB and the VIPB model have the same fracture energy and cohesive strength, but exhibit different post-peak load behavior. The different post-peak load behavior influences the maximum load capacity of structures containing quasi-brittle materials.

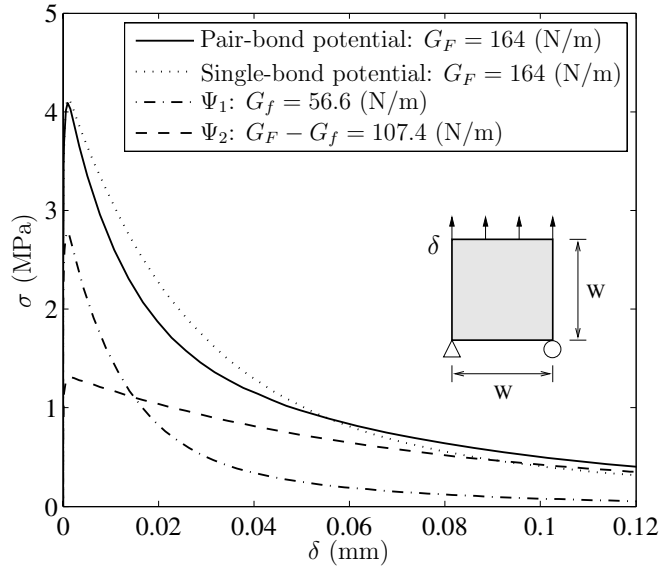


Figure 2.6: Comparison between the VIB (single-bond) model and the VIPB (pair-bond) model with the localization zone size of $W = h_L = 0.5$ mm. The loading is performed with displacement control (δ).

2.5.2 Double Cantilever Beam (DCB) Test

The geometry of the DCB test is described in Figure 2.7(a). It has initial notch (a_0) of 0.1 m, height ($2h$) of 0.1 m, and length (L) of 1 m. The DCB mesh detail around the crack tip (boxed area in Figure 2.7(a)) is shown in Figure 2.7(b), and

the localization zone is defined by the VIB (or VIPB) element along the direction of crack propagation. Material properties are also the same as in the pure tension test

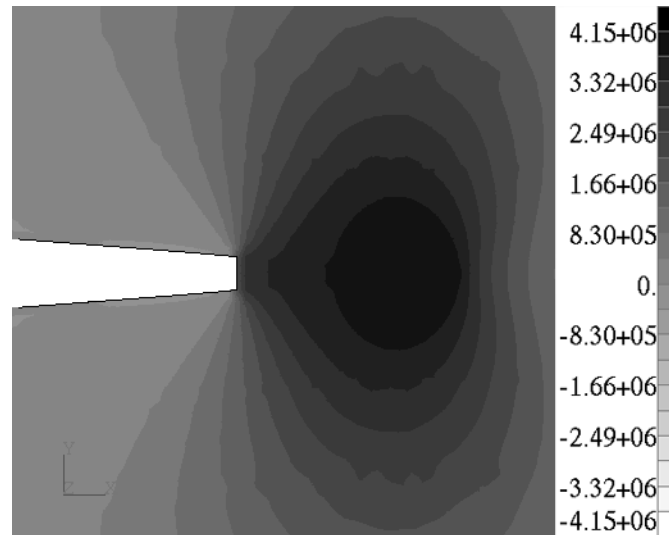
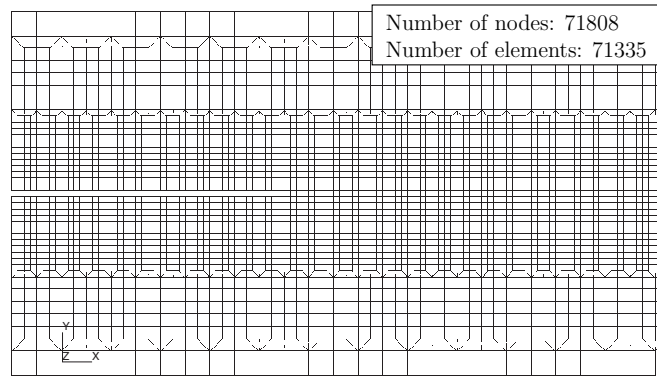
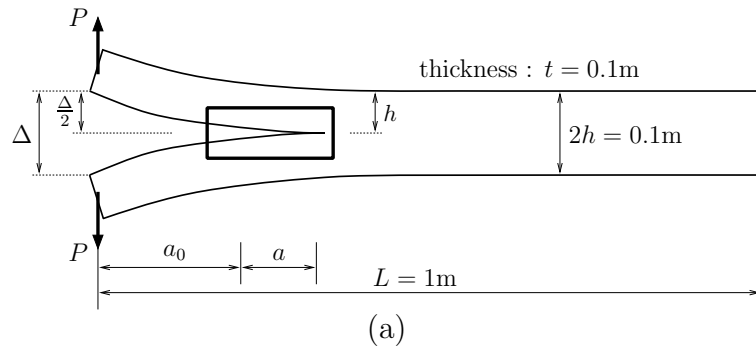
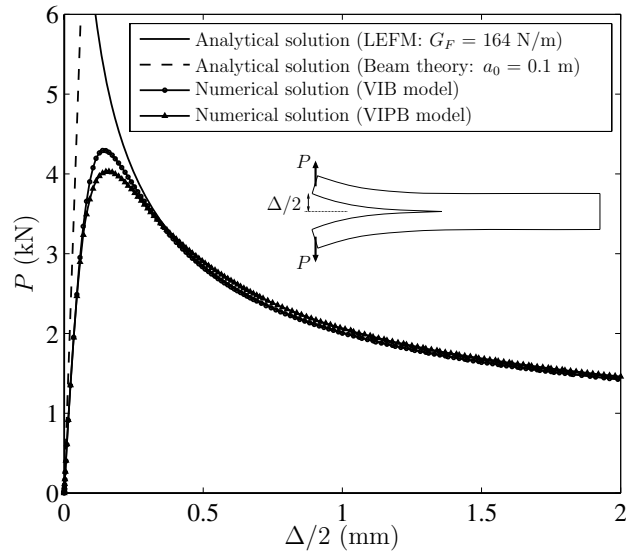


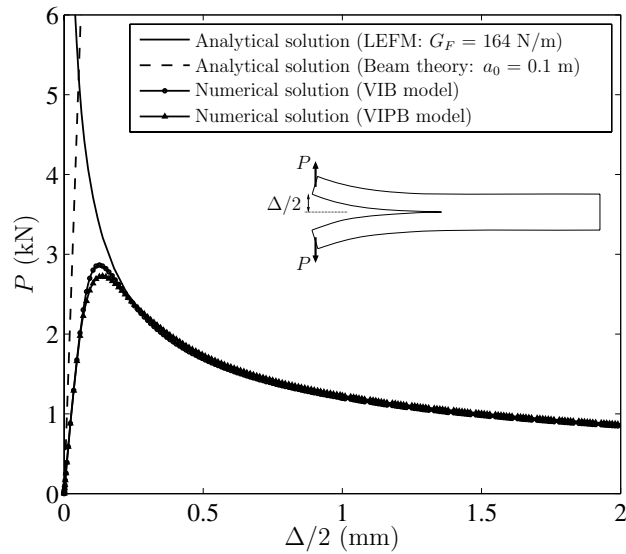
Figure 2.7: (a) The geometry of the DCB test; (b) mesh detail around initial notch with the element size varying from 0.5 mm (localization zone) to 2 mm (outer region); (c) normal stress, σ_{yy} , distribution under the deformed shape.

in order to relate the fracture energy to the localization zone size. Elements outside the localization zone are defined as linear elastic.

The numerical simulation of the DCB is implemented with two different VIB (or VIPB) element sizes ($h_L = 0.5$ mm, 0.25 mm), with the same original geometry and with the same constants in the bond density potential function. Figure 2.7(c)



(a)



(b)

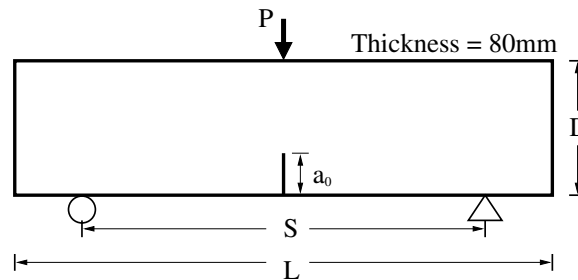
Figure 2.8: Numerical simulation results of the DCB test using the VIB and the VIPB models with the localization zone size of, (a) $h_L = 0.5$ mm and (b) $h_L = 0.25$ mm.

demonstrates the vertical stress (σ_{yy}) distribution under the deformed shape. The maximum stress corresponds to the cohesive strength (4.15 MPa), and the fracture behavior is localized with the large deformation where the VIB (or VIPB) element is defined.

Figure 2.8 illustrates the agreement of the numerical results and the analytical solution of linear elastic fracture mechanics (LEFM). For the size of 0.5 mm, the numerical results of the VIB model and the VIPB model are plotted in Figure 2.8(a) with the LEFM analytical solution whose fracture energy is 164 N/m. Similarly, the localization zone size is 0.25 mm for the numerical simulation (Figure 2.8(b)), and the fracture energy is 82 N/m for the analytical solution of LEFM. Additionally, the peak load of the VIPB model is lower than that of the VIB model because of the the different softening behavior as discussed previously (Figure 2.6).

2.6 Validation

In order to validate the VIPB model for quasi-brittle materials, numerical simulation results are compared with previous experimental results from three-point bending (TPB) tests of plain concrete (Roesler et al., 2007b) and FRC (Roesler et al., 2007a). For the plain concrete experiments, three sizes ($D = 63, 150, 250$ mm) of notched beam were designed with a constant thickness ($t = 80$ mm), notch to depth ratio ($a_0/D = 1/3$) and span to depth ratio ($S/D = 4$) (see Figure 2.9). For the FRC experiments, the beam depth was 150 mm with the thickness of 80 mm, notch to depth ratio of 1/3, and span to depth ratio of 4.



Size (D)	Length (L)	Span (S)	Notch (a_0)
63	250	350	21
150	600	700	50
250	1000	1100	83

Figure 2.9: Specimen geometry of a three-point bending (TPB) tests.

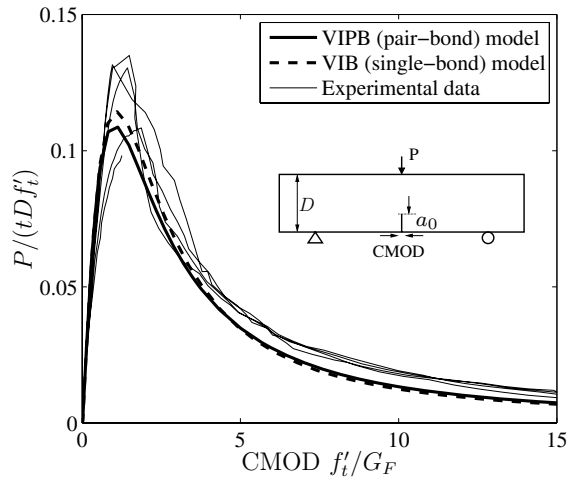
Table 2.2: Elastic and fracture parameters of concrete beam experiments by Roesler et al. (2007b).

Specimen size (mm)	Elastic modulus (GPa)	Tensile strength (MPa)	Initial fracture energy (N/m)	Strength ratio at the kink point (β_k)	Total fracture energy (N/m)
63	32	4.15	56.6	0.34	119
150	32	4.15	56.6	0.34	164
250	32	4.15	56.6	0.34	167

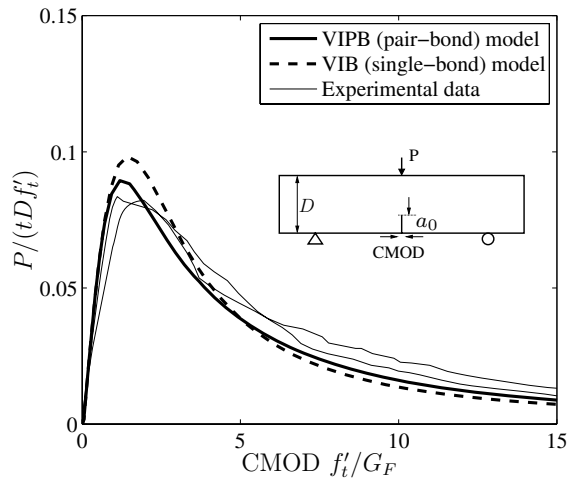
2.6.1 Three-Point Bending (TPB) Tests of Plain Concrete

Experimental elastic and fracture parameters of concrete are presented in Table 2.2. The tensile strength of 4.15 MPa was measured by the splitting test (Brazilian test). The total fracture energy was obtained by the work-of-fracture method (Hillerborg, 1985), and the initial fracture energy was estimated by the Two-Parameter Fracture Model (TPFM) (Jenq and Shah, 1985). Finally, the strength ratio ($\beta_k = 0.34$) in the pair-bond potential was calculated by using the critical crack tip opening displacement ($CTOD_c$) obtained from the TPFM (Park, 2005).

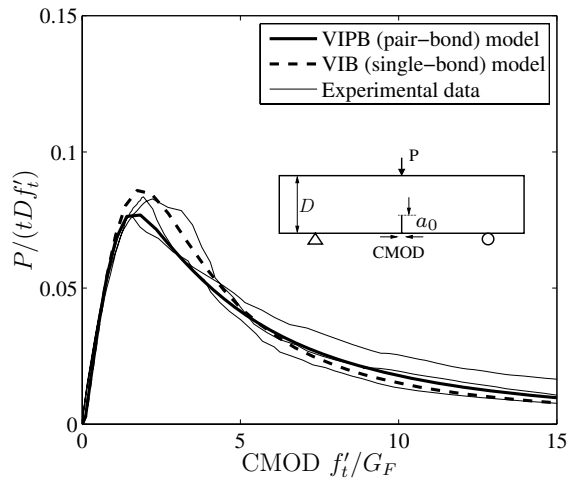
Based on the concrete properties in Table 2.2, the constants in the modified Morse potential are evaluated by expression (2.23) in conjunction with the numerical simulation of the pure tension test at a localization zone size of 0.5 mm. Table 2.3 illustrates the calculated constants in the bond density potential for the VIB (single-bond) model, and Table 2.4 provides those for the VIPB (pair-bond) model. The exponents in the bond density potential are calibrated by simulating the pure tension test so that the numerical fracture parameters corresponds to the material fracture parameters. In the VIPB model, the constants ($\alpha_1, m_1, \mathcal{D}_1$) in the steep short-range potential (Ψ_1) are the same for all specimen sizes, since the potential represents the size independent initial fracture energy (G_f). However, in the shallow long-range potential (Ψ_2), the constants ($\alpha_2, m_2, \mathcal{D}_2$) are different with respect to size, due to the size dependence of the total fracture energy (G_F), as shown in Table 2.4. The exponent m_2 of the long-range potential is not only greater than the exponent m_1 of the short-range potential, but the exponent m_2 also increases with size. The increased specimen size produces a larger total fracture energy for a fixed cohesive strength, resulting in a shallow long-range potential. This feature corresponds well to the characteristics of the Morse potential, the larger value of m , the longer the range, and the shallower the potential (Milstein, 1973).



(a)



(b)



(c)

Figure 2.10: Comparison of load-CMOD curves with experimental results: (a) specimen size $D = 63$ mm, (b) specimen size $D = 150$ mm and (c) specimen size $D = 250$ mm.

Table 2.3: Material properties and the constants in the bond density potential for each size of beam in the VIB (single-bond) model with the localization zone size of 0.5 mm.

Size D (mm)	E (GPa)	f_t' (MPa)	G_F (N/m)	α	m	\mathcal{D} (N-m/m ³)
63	32	4.15	119	34	315	41960
150	32	4.15	164	23	480	60170
250	32	4.15	167	22	510	61900

Table 2.4: The constants in each bond density potential for the VIPB (pair-bond) model with the localization zone size of 0.5 mm.

Size	$(1 - \beta_k)E, (1 - \beta_k)f_t', G_f$			$\beta_k E, \beta_k f_t', G_F - G_f$		
D (mm)	α_1	m_1	\mathcal{D}_1 (N-m/m ³)	α_2	m_2	\mathcal{D}_2 (N-m/m ³)
63	50	215	18760	19	630	25450
150	50	215	18760	9	1260	50900
250	50	215	18760	8	1480	54660

Figures 2.10(a),(b) and (c) illustrate the correspondence between the numerical predictions of the VIPB model and the experimental results for each specimen size with respect to the normalized load versus crack mouth opening displacement (CMOD) curves ($P/tDf_t' - \text{CMOD } f_t'/G_F$). The VIB model slightly overestimates the peak load, due to the VIB model consisting of a single-bond potential related to the total fracture energy, while the VIPB model employs two different potentials, i.e. the steep short-range and the shallow long-range potential, associated with the initial fracture energy and the total fracture energy.

2.6.2 On Size Effect

In general, the size effect due to the scaling of geometrically similar structures, can be characterized by the nominal strength of the structure, the maximum deflection and the maximum strain (Bazant, 1999). In this study, the size effect is examined by plotting the structural size (D) versus the nominal strength (σ_{Nu}) which is calculated as the peak load divided by the beam size (D) and thickness (t), as shown in Figure 2.11. The solid and dashed lines are calculated respectively by the size effect method (SEM) (Bazant and Planas, 1998) and the TPFM (Jenq and Shah, 1985) through

the size effect expression (Bazant and Kazemi, 1990),

$$\sigma_{Nu} = \frac{Bf_t'}{\sqrt{1 + D/D_0}}, \quad (2.27)$$

where the non-dimensional constant, B , and the length dimensional constant, D_0 , are determined by the three-point bending tests in Table 2.2. The numerical prediction of the VIPB model trends with the size effect expression (2.27), and is bounded by the SEM and the TPFM curves, as shown in Figure 2.11. The single potential (VIP) model, demonstrates overestimation of the strength with respect to the increase in structural size (D) for this specific example. Moreover, the strength differences between the VIB model and the VIPB model grow with respect to the increase of specimen size.

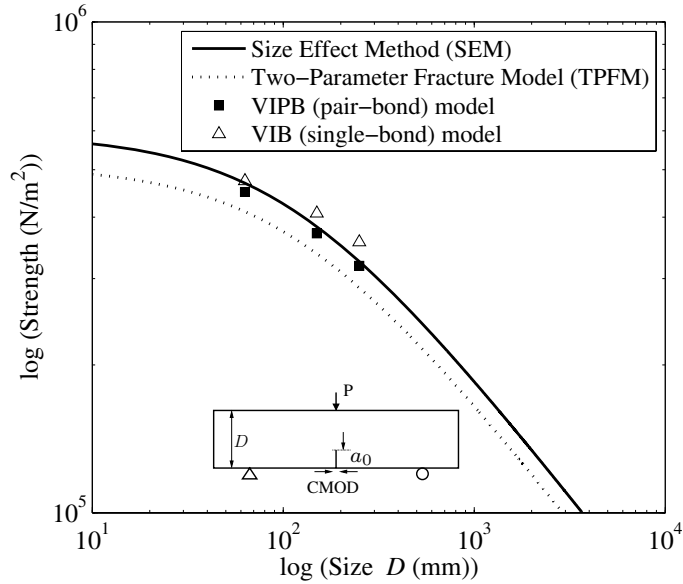


Figure 2.11: Size effect for three-point bending (TPB) fracture test configuration.

2.6.3 TPB Test of Fiber Reinforced Concrete (FRC)

FRC beams were cast with ordinary plain concrete and fiber volume fraction of 0.78%. Elastic and fracture parameters of the ordinary plain concrete are provided in Table 2.5. The total fracture energies of plain concrete and FRC are 120 N/m and 3531 N/m, respectively, which are obtained by the work-of-fracture method (Hillerborg, 1985). Based on these experimental elastic and fracture parameters, load versus CMOD curves of the FRC beams are predicted by simulating the VIPB model and

the VIB model. The simulation results are compared with the experimental data, as shown in Figure 2.12. The VIPB model demonstrates a similar load-CMOD curve to experimental data, while the VIB model overestimates the peak load and post-peak behavior in this example.

Table 2.5: Elastic and fracture parameters of plain concrete (Roesler et al., 2007a).

Elastic modulus (GPa)	Tensile strength (MPa)	Total fracture energy (N/m)	Strength ratio at the kink point (β_k)
26.9	3.4	120	0.28

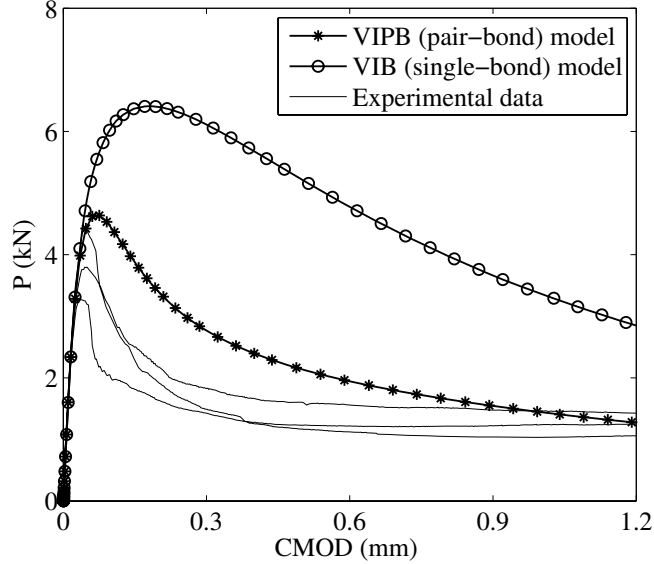


Figure 2.12: Prediction of load-CMOD curves of FRC beam tests compared with experimental data.

2.7 Conclusions

A virtual internal pair-bond (VIPB) model is proposed to consider two fracture energies, the initial fracture energy (G_f) and the total fracture energy (G_F), which are essential fracture parameters to represent the fracture behavior and size effect of quasi-brittle materials, such as concrete. The initial fracture energy is related to the steep short-range bond density potential, while the difference between the initial fracture energy and the total fracture energy is associated with the shallow long-range bond density potential. Furthermore, the VIPB model is extended to simulate

fracture behavior of fiber reinforced concrete (FRC) in conjunction with two fracture energies, the total fracture energy of plain concrete (G_F) and the total fracture energy of FRC (G_{FRC}).

A modified Morse function (atomistic potential) is proposed for the bond density potential in the VIPB model so that the potential function is independent of the discrete lattice parameter (ℓ_0). The elastic modulus, cohesive strength and fracture energy, which can be obtained by means of macroscopic experiments, determine the three constants in each modified Morse function ($m_i, \alpha_i, \mathcal{D}_i$).

The model parameters in the bond density potential are estimated from the experimental fracture parameters and a pure tension simulation. The DCB simulations are conducted simply to verify the relationship between the fracture energy (G_F) and the localization zone size (h_L). The VIPB model is validated by predicting the load-CMOD curves of three-point bending tests for both plain concrete and FRC. The later example involving FRC clearly demonstrates the advantage of the VIPB model over the usual VIB model (cf. Figure 2.12).

Furthermore, the present conceptual framework, i.e. the superposition of the two potential, can be extended to account for other physical behaviors. For instance, the VIPB model can be changed to a virtual internal multiple-bond potential model, which can represent other interactions between fractured surfaces, e.g., friction.

Chapter 3

PPR: Unified Potential-Based Cohesive Model of Mixed-Mode Fracture

A generalized potential-based constitutive model for mixed-mode cohesive fracture is proposed in conjunction with physical parameters such as fracture energy, cohesive strength and shape of cohesive interactions. It characterizes different fracture energies in each fracture mode, and can be applied to various material failure behavior (e.g. quasi-brittle). The unified potential leads to both intrinsic (with initial slope indicators to control elastic behavior) and extrinsic cohesive zone models. Path dependence of work-of-separation is investigated with respect to proportional and non-proportional paths – this investigation demonstrates consistency of the cohesive constitutive model. The potential-based model is verified by simulating a mixed-mode bending test. The actual potential is named PPR (Park–Paulino–Roesler). The chapter is organized as follows. Section 3.1 chronologically reviews the development of previous potential-based models. The unified potential-based model (PPR) for mixed-mode cohesive fracture is developed in Section 3.2. Section 3.3 discusses path dependence of the work-of-separation in the unified potential-based model for mixed-mode fracture. Section 3.4 verifies the proposed model. Finally, Section 3.5 concludes the present work.

3.1 Previous Potentials for Cohesive Fracture

There are several potential-based models, which describe different fracture modes for cohesive fracture, as summarized in Table 3.1 (including the proposed one). Needleman (1987) proposed a polynomial function-based potential to investigate void nucleation. Needleman (1990) also developed the exponential-periodic potential based on the universal atomistic potential by Rose et al. (1981). Later, Beltz and Rice (1991) obtained a generalized form of the exponential-periodic potential. Analogously to the exponential-periodic potential, Xu and Needleman (1993) proposed the exponential-exponential potential to improve the shear failure behavior. Such previ-

ous potential-based models listed in Table 3.1 are reviewed in detail including their limitations.

Table 3.1: Potentials for cohesive fracture.

Potential model	Normal interaction	Tangential interaction
Needleman (1987)	Polynomial	Linear
Needleman (1990)	Exponential	Periodic
Beltz and Rice (1991)	Exponential	Periodic
Xu and Needleman (1993)	Exponential	Exponential
Park et al. (2009a)	Polynomial	Polynomial

3.1.1 Needleman, 1987

A fracture energy potential, which defines the constitutive relationship along fracture interfaces, was proposed by Needleman (1987). The potential consists of a polynomial function expressed in terms of a normal separation (Δ_n) and a tangential separation (Δ_t) along the interface,

$$\begin{aligned} \Psi(\Delta_n, \Delta_t) = & \frac{27}{4} \sigma_{\max} \delta_n \left\{ \frac{1}{2} \left(\frac{\Delta_n}{\delta_n} \right)^2 \left[1 - \frac{4}{3} \left(\frac{\Delta_n}{\delta_n} \right) + \frac{1}{2} \left(\frac{\Delta_n}{\delta_n} \right)^2 \right] \right. \\ & \left. + \frac{1}{2} \alpha_s \left(\frac{\Delta_t}{\delta_n} \right)^2 \left[1 - 2 \left(\frac{\Delta_n}{\delta_n} \right) + \left(\frac{\Delta_n}{\delta_n} \right)^2 \right] \right\}, \end{aligned} \quad (3.1)$$

where σ_{\max} is the maximum traction carried by the interface under the mode I fracture, δ_n is a characteristic length, and α_s is a shear stiffness parameter. The first derivatives of the potential with respect to the normal and tangential separations provide the interfacial normal traction (T_n) and tangential traction (T_t) respectively, also called the cohesive interactions:

$$\begin{aligned} T_n = \frac{\partial \Psi}{\partial \Delta_n} &= \frac{27}{4} \sigma_{\max} \left\{ \left(\frac{\Delta_n}{\delta_n} \right) \left[1 - 2 \left(\frac{\Delta_n}{\delta_n} \right) + \left(\frac{\Delta_n}{\delta_n} \right)^2 \right] + \alpha_s \left(\frac{\Delta_t}{\delta_n} \right)^2 \left[\left(\frac{\Delta_n}{\delta_n} \right) - 1 \right] \right\}, \\ T_t = \frac{\partial \Psi}{\partial \Delta_t} &= \frac{27}{4} \sigma_{\max} \left\{ \alpha_s \left(\frac{\Delta_t}{\delta_n} \right) \left[1 - 2 \left(\frac{\Delta_n}{\delta_n} \right) + \left(\frac{\Delta_n}{\delta_n} \right)^2 \right] \right\}. \end{aligned} \quad (3.2)$$

The above potential describes only mode I fracture properties, i.e. fracture energy and cohesive strength, in conjunction with a characteristic length scale (δ_n). The interfacial normal traction reaches the cohesive strength when $\Delta_n = \delta_n/3$ and $\Delta_t = 0$.

The characteristic length is associated with the mode I fracture energy (ϕ_n) through the expression

$$\phi_n = 9\sigma_{\max}\delta_n/16, \quad (3.3)$$

the area under a traction-separation curve for mode I. Figure 3.1 illustrates the potential and its gradient with respect to the separations (Δ_n, Δ_t). The normal traction demonstrates elastic behavior from $\Delta_n = 0$ to $\Delta_n = \delta_n/3$, the maximum strength ($\sigma_{\max} = 30$ MPa) at $\Delta_n = \delta_n/3$, and softening behavior from $\Delta_n = \delta_n/3$ to $\Delta_n = \delta_n$. The tangential traction increases linearly with respect to the increase in tangential separation, although large shear separation should eventually result in the material weakening behavior. Therefore, the potential has the limitation for relatively large shear displacement jump (Needleman, 1990).

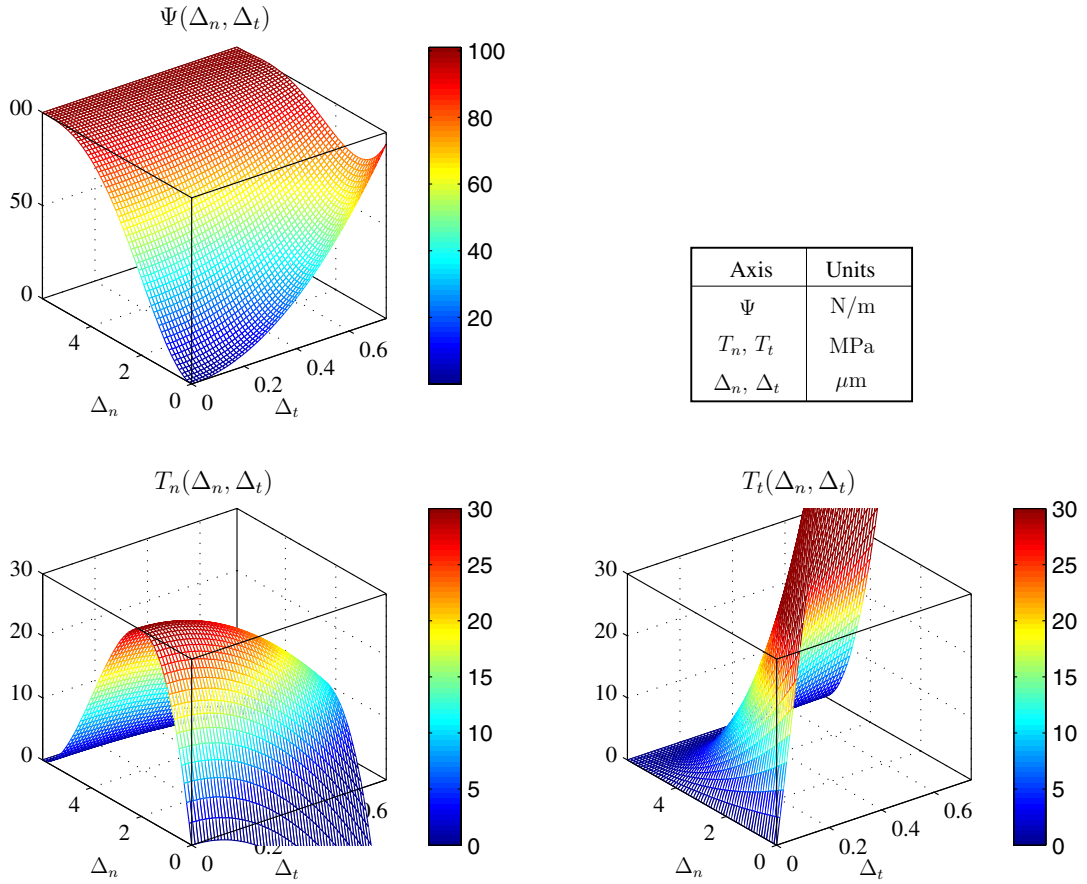


Figure 3.1: Needleman (1987) potential (Ψ) and its gradients (T_n, T_t) with respect to separations (Δ_n, Δ_t); $\phi_n = 100$ N/m, $\sigma_{\max} = 30$ MPa, and $\alpha_s = 10$.

3.1.2 Needleman, 1990

To accommodate large shear displacement, the exponential and periodic potential was proposed by Needleman (1990). An exponential expression was utilized for the normal traction-separation relationship, in order to represent the binding energy of metallic and bi-metallic interfaces (Rose et al., 1981). A periodic expression was employed for the tangential traction-separation relationship because of the periodic dependence of the underlying lattice. The exponential and periodic potential is expressed as

$$\Psi(\Delta_n, \Delta_t) = \frac{\sigma_{\max} e \delta_n}{z} \left\{ 1 - \left[1 + \frac{z \Delta_n}{\delta_n} - \beta_s z^2 \left[1 - \cos \left(\frac{2\pi \Delta_t}{\delta_t} \right) \right] \right] \exp \left(-\frac{z \Delta_n}{\delta_n} \right) \right\}, \quad (3.4)$$

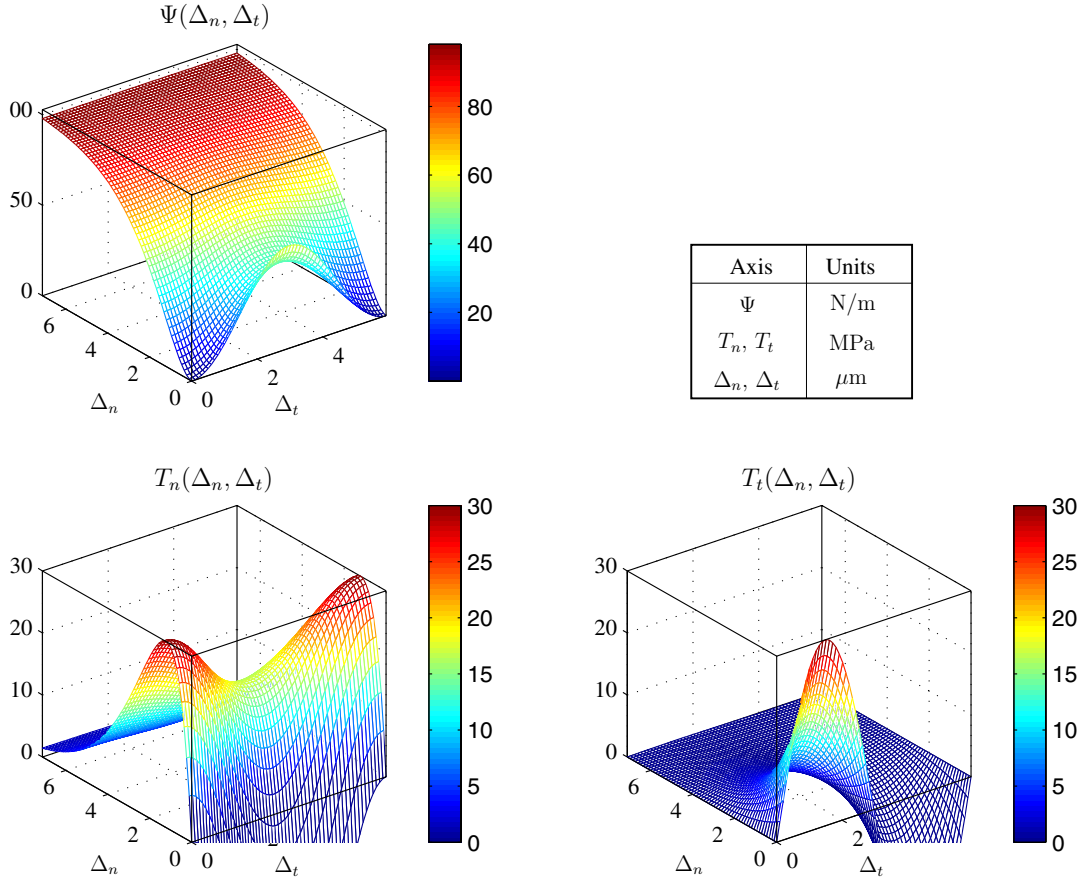


Figure 3.2: Needleman (1990) potential and its gradients; $\phi_n = 100$ N/m, and $\sigma_{\max} = 30$ MPa.

where $z = 16e/9$ and $e = \exp(1)$. The scalar parameters σ_{\max} , δ_n , δ_t and β_s characterize the interfacial cohesive responses, i.e.

$$\begin{aligned} T_n &= \sigma_{\max} e \left\{ \frac{z\Delta_n}{\delta_n} - \beta_s z^2 \left[1 - \cos \left(\frac{2\pi\Delta_t}{\delta_t} \right) \right] \right\} \exp \left(-\frac{z\Delta_n}{\delta_n} \right), \\ T_t &= \sigma_{\max} e \left\{ 2\pi\beta_s z \left(\frac{\delta_n}{\delta_t} \right) \sin \left(\frac{2\pi\Delta_t}{\delta_t} \right) \right\} \exp \left(-\frac{z\Delta_n}{\delta_n} \right). \end{aligned} \quad (3.5)$$

The cohesive strength, σ_{\max} , is attained when $\Delta_n = \delta_n/z$ and $\Delta_t = 0$. Additionally, the characteristic length, δ_n , is evaluated by its association with the mode I fracture energy,

$$\phi_n = \sigma_{\max} e \delta_n / z. \quad (3.6)$$

The other characteristic length, δ_t , is assumed to be the same as δ_n , and the nondimensional scalar parameter, β_s , is calibrated so that the maximum value of T_t with $\Delta_n = 0$ is the same as σ_{\max} .

The potential and the traction-separation relationships are plotted in Figure 3.2. The normal traction demonstrates exponential softening behavior, while the tangential traction illustrates the periodic function. However, the imposed fracture properties for the potential are based solely on the mode I fracture parameters, i.e., the energy (ϕ_n) and the cohesive strength (σ_{\max}), even though the potential considers mixed-mode cohesive fracture interaction. Therefore, this potential has limitation in appropriately characterizing macroscopic mixed-mode fracture behavior.

3.1.3 Beltz and Rice, 1991

Beltz and Rice generalized the exponential and periodic potential proposed by Needleman (1990) by considering mode II fracture parameters: the cohesive strength (τ_{\max}) and fracture energy (ϕ_t). Similarly to the potential proposed by Needleman (1990), the normal traction $T_n(\Delta_n, \Delta_t)$ is expressed as an exponential function,

$$T_n = [B(\Delta_t)\Delta_n - C(\Delta_t)] \exp(-\Delta_n/\delta_n), \quad (3.7)$$

while the tangential traction $T_t(\Delta_n, \Delta_t)$ is defined as a periodic function, based on the Peierls concept (Rice, 1992),

$$T_t = A(\Delta_n) \sin \left(\frac{2\pi\Delta_t}{\delta_t} \right), \quad (3.8)$$

where δ_n and δ_t are characteristic length scale parameters, and $A(\Delta_n)$, $B(\Delta_t)$ and $C(\Delta_t)$ are the functions to satisfy the following boundary conditions. First, a potential is an exact differential which satisfies the symmetry condition,

$$\frac{\partial T_n}{\partial \Delta_t} = \frac{\partial T_t}{\partial \Delta_n} . \quad (3.9)$$

Second, because the normal traction (3.7) is zero when normal and tangential displacements are zero (i.e. initial condition), $C(0)$ is equal to zero,

$$C(0) = 0 . \quad (3.10)$$

As the area under a cohesive interaction represents the fracture energy, the normal traction of a cleavage fracture is associated with the surface energy, γ_s ,

$$\int_0^\infty T_n(\Delta_n, 0) d\Delta_n = 2\gamma_s = \phi_n , \quad (3.11)$$

and the tangential traction of a dislocation nucleation procedure is related to the *unstable stacking energy*, γ_{us} ,

$$\int_0^{\delta_t/2} T_t(0, \Delta_t) d\Delta_t = \gamma_{us} = \phi_t \quad (3.12)$$

which is equivalent to the mode II fracture energy in the macroscopic fracture case. In addition, the tangential and the normal traction (T_n and T_t) satisfy the boundary condition at complete separation, i.e.

$$T_n(\infty, \Delta_t) = 0 , \quad T_t(\infty, \Delta_t) = 0 , \quad (3.13)$$

because fracture surfaces cannot transfer tractions when complete separation occurs along the normal direction ($\Delta_n = \infty$). However, the potential function does not introduce the boundary condition for the complete shear separation. In other words, although the tangential traction is set to be zero when $\Delta_t = \delta_t/2$, i.e. $T_t(\Delta_n, \delta_t/2) = 0$, the normal traction is not necessarily zero, i.e. $T_n(\Delta_n, \delta_t/2) \neq 0$. Because of this fact, Beltz and Rice (1991) introduced an additional length scale parameter, Δ_n^* , which satisfies $T_n(\Delta_n^*, \delta_t/2) = 0$.

From equations (3.9), (3.10), (3.11), (3.12) and (3.13), the general expression for $A(\Delta_n)$, $B(\Delta_t)$ and $C(\Delta_t)$ are

$$\begin{aligned} A(\Delta_n) &= \frac{\pi\gamma_{us}}{\delta_t} - \frac{2\pi\gamma_s}{\delta_t} \left\{ q \left[1 - \exp\left(-\frac{\Delta_n}{\delta_n}\right) \right] - \left(\frac{q-r}{1-r}\right) \frac{\Delta_n}{\delta_n} \exp\left(-\frac{\Delta_n}{\delta_n}\right) \right\} \\ B(\Delta_t) &= \frac{2\gamma_s}{\delta_n^2} \left\{ 1 - \left(\frac{q-r}{1-r}\right) \sin^2\left(\frac{2\pi\Delta_t}{\delta_t}\right) \right\} \\ C(\Delta_t) &= \frac{2\gamma_s}{\delta_n} \frac{r(1-q)}{1-r} \sin^2\left(\frac{2\pi\Delta_t}{\delta_t}\right) \end{aligned} \quad (3.14)$$

with

$$q = \gamma_{us}/(2\gamma_s) , \quad r = \Delta_n^*/\delta_n , \quad (3.15)$$

where δ_n , δ_t and Δ_n^* are length scale parameters. Substitution of (3.14) into (3.7) and (3.8), and integration of (3.7) and (3.8) lead to the generalized exponential and

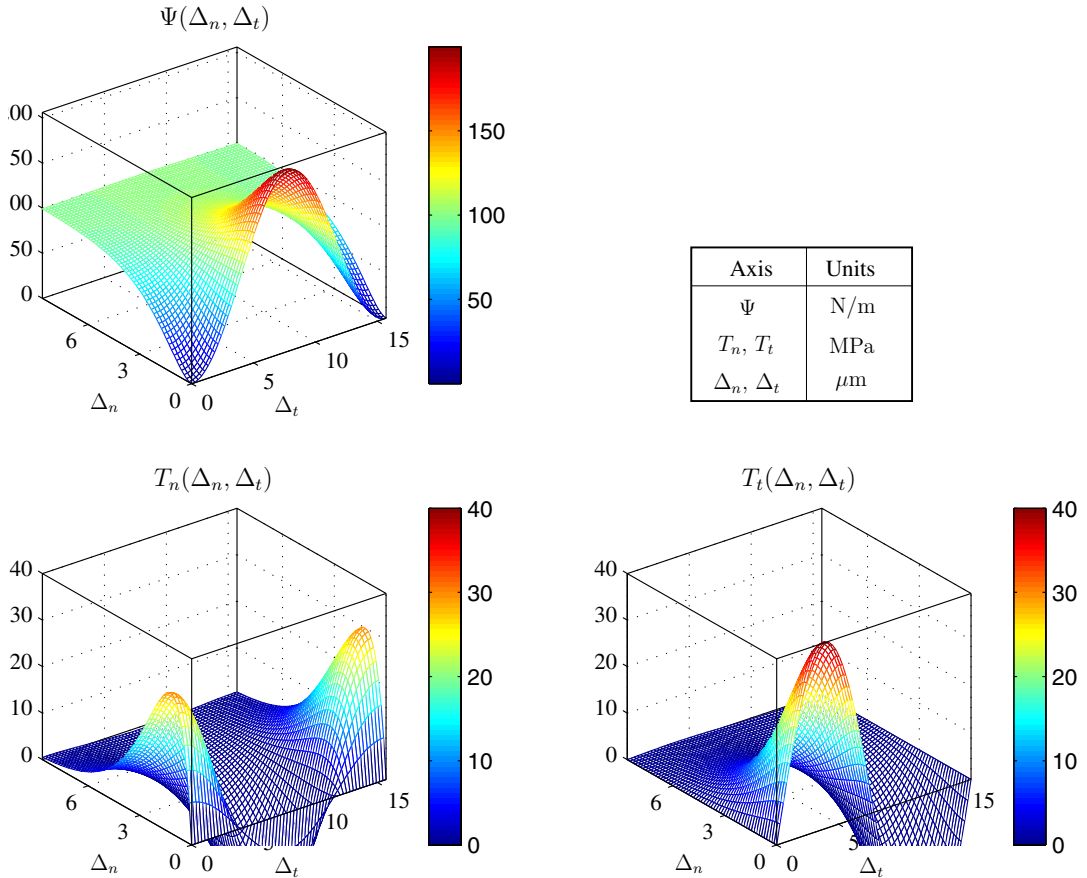


Figure 3.3: Beltz and Rice (1991) generalized exponential-periodic potential and its gradients; $\phi_n = 2\gamma_s = 100$ N/m, $\phi_t = \gamma_{us} = 200$ N/m, $\sigma_{\max} = 30$ MPa, $\tau_{\max} = 40$ MPa, and $r = 0$.

periodic potential of Beltz and Rice (1991):

$$\Psi = 2\gamma_s + 2\gamma_s \exp\left(-\frac{\Delta_n}{\delta_n}\right) \left\{ \left[q + \left(\frac{q-r}{1-r} \right) \frac{\Delta_n}{\delta_n} \right] \sin^2\left(\frac{2\pi\Delta_t}{\delta_t}\right) - \left[1 + \frac{\Delta_n}{\delta_n} \right] \right\}. \quad (3.16)$$

The characteristic length parameters (δ_n, δ_t) are determined through their association with the cohesive strengths ($\sigma_{\max}, \tau_{\max}$) and the fracture energies (ϕ_n, ϕ_t),

$$\delta_n = \phi_n / (\epsilon \sigma_{\max}), \quad \delta_t = \pi \phi_t / \tau_{\max}. \quad (3.17)$$

The other length scale parameter Δ_n^* is defined by Beltz and Rice (1991) as follows: “ Δ_n^* is the value of Δ_n after shearing to the state $\Delta_t = \delta_t/2$ under conditions of zero tension, $T_n = 0$, (i.e., relaxed shearing).”

Figure 3.3 demonstrates the potential function and the traction-separation relationships. The generalized exponential and periodic potential characterizes different fracture behaviors in mode I and mode II. However, the potential contains a length scale fracture parameter Δ_n^* , which is difficult to be evaluated. Furthermore, the potential cannot represent complete interfacial shear failure because of the periodic function employed along the tangential direction.

3.1.4 Xu and Needleman, 1993

In order to characterize complete interfacial shear failure, the exponential expression is employed for the tangential traction rather than the periodic function (Xu and Needleman, 1993). The exponential potential is expressed as

$$\begin{aligned} \Psi(\Delta_n, \Delta_t) = & \phi_n + \phi_n \exp\left(\frac{-\Delta_n}{\delta_n}\right) \\ & \left\{ \left[1 - r + \frac{\Delta_n}{\delta_n} \right] \frac{(1-q)}{(r-1)} - \left[q + \frac{(r-q)\Delta_n}{(r-1)\delta_n} \right] \exp\left(-\frac{\Delta_t^2}{\delta_t^2}\right) \right\}. \end{aligned} \quad (3.18)$$

The first derivative of the exponential potential results in the interfacial cohesive tractions,

$$\begin{aligned} T_n &= \frac{\phi_n}{\delta_n} \exp\left(\frac{-\Delta_n}{\delta_n}\right) \left\{ \frac{\Delta_n}{\delta_n} \exp\left(-\frac{\Delta_t^2}{\delta_t^2}\right) + \frac{(1-q)}{(r-1)} \left[1 - \exp\left(-\frac{\Delta_t^2}{\delta_t^2}\right) \right] \left[r - \frac{\Delta_n}{\delta_n} \right] \right\}, \\ T_t &= \frac{\phi_n}{\delta_n} \frac{2\delta_n}{\delta_t} \frac{\Delta_t}{\delta_t} \left[q + \frac{(r-q)\Delta_n}{(r-1)\delta_n} \right] \exp\left(\frac{-\Delta_n}{\delta_n}\right) \exp\left(-\frac{\Delta_t^2}{\delta_t^2}\right). \end{aligned} \quad (3.19)$$

where δ_n and δ_t are length scale parameters. Similarly to the generalized exponential and periodic potential (Beltz and Rice, 1991), the two length scale parameters are

evaluated by relating the fracture energies (ϕ_n, ϕ_t) to the cohesive strength $(\sigma_{\max}, \tau_{\max})$,

$$\phi_n = \sigma_{\max} \epsilon \delta_n, \quad \phi_t = \sqrt{e/2} \tau_{\max} \delta_t. \quad (3.20)$$

The nondimensional parameter q is the ratio of the mode II fracture energy (ϕ_t) to the mode I fracture energy (ϕ_n) . The nondimensional parameter r is also defined as

$$r = \Delta_n^* / \delta_n, \quad (3.21)$$

where Δ_n^* is the value of Δ_n after complete shear separation under the condition of zero normal tension, i.e. $T_n(\Delta_n^*, \infty) = 0$.

The exponential potential and its interfacial cohesive responses are plotted in Figure 3.4. The normal and tangential tractions not only demonstrate the exponentially decreasing softening but represent the different fracture parameters, i.e. fracture en-

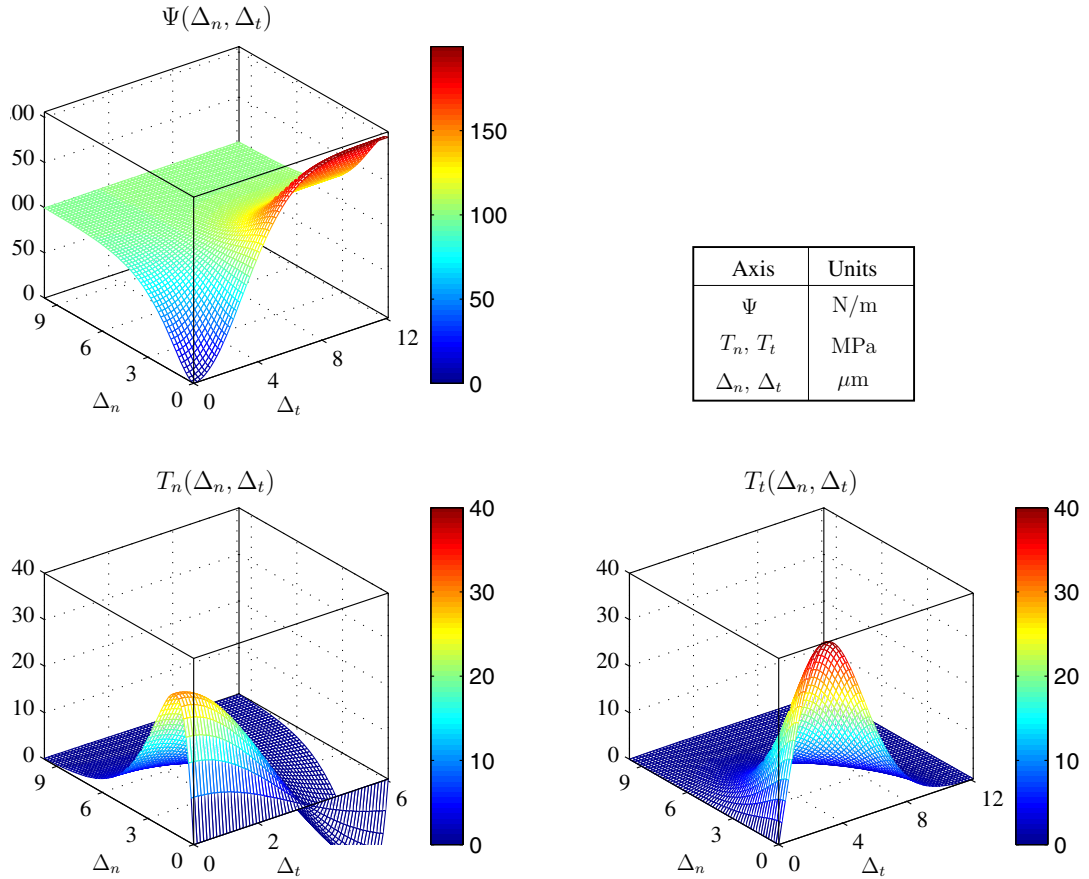


Figure 3.4: Xu and Needleman (1993) exponential potential and its gradients; $\phi_n = 100$ N/m, $\phi_t = 200$ N/m, $\sigma_{\max} = 30$ MPa, $\tau_{\max} = 40$ MPa, and $r = 0$.

ergy and cohesive strength, in mode I and mode II. The limitations of this potential are described next.

3.1.5 Limitations of the Exponential Potential

Although the exponential potential by Xu and Needleman (1993) has been extensively utilized, there are several limitations because of the fracture boundary conditions and the exponential expression. First, non-symmetric boundary conditions introduce the additional length scale parameter (Δ_n^*), and result in non-physical cohesive interactions for several cases (i.e. $r \neq 0$, $q \neq 0$). The exponential potential is derived by applying the same boundary conditions as the exponential-periodic potential derived by Beltz and Rice (1991). The boundary conditions for the cohesive zone model are summarized as follows:

- Mode I fracture energy: $\int_0^\infty T_n(\Delta_n, 0) d\Delta_n = \phi_n$
- Mode II fracture energy: $\int_0^\infty T_t(0, \Delta_t) d\Delta_t = \phi_t$
- Complete normal failure for the infinite normal separation: $T_n(\infty, \Delta_t) = 0$
- Complete tangential failure for the infinite normal separation: $T_t(\infty, \Delta_t) = 0$
- Complete tangential failure for the infinite shear separation: $T_t(\Delta_n, \infty) = 0$

The main difference between the exponential-periodic potential of Beltz and Rice (1991) and the exponential potential of Xu and Needleman (1993) is that $\Delta_t = \delta_t/2$ in the exponential-periodic potential is the necessary condition for complete failure along the normal direction, while the infinite tangential separation ($\Delta_t = \infty$) in the exponential potential is the sufficient condition for the complete failure along the normal and tangential directions. When shear separation reaches infinity ($\Delta_t = \infty$), therefore, the boundary condition for the complete normal failure, i.e. $T_n(\Delta_n, \infty) = 0$, should be introduced in the exponential potential, which results in the symmetric boundary conditions. Instead of the boundary condition, $T_n(\Delta_n, \infty) = 0$, the alternative boundary condition, $T_n(\Delta_n^*, \infty) = 0$, is utilized by introducing the additional length scale parameter Δ_n^* , as discussed previously. Both the length scale parameter Δ_n^* and the nondimensional parameter r are difficult to be evaluated on the basis of either physical experiments or explanations.

Because of the deficiency in the boundary condition of complete normal failure (the non-symmetric boundary condition), when the mode I fracture energy is greater

than mode II fracture energy, the cohesive interactions do not correspond to physical fracture behavior. Figure 3.5 illustrates that the potential provides unacceptably high normal traction around $(\Delta_n \approx 5\mu\text{m}, \Delta_t \gg 0)$ although almost complete tangential failure occurred around that region. The normal traction does not decrease with respect to increasing the tangential separation, $T_n(\Delta_n, \infty) \neq 0$, although the increase of the tangential separation physically weakens the material and results in the decrease of normal traction.

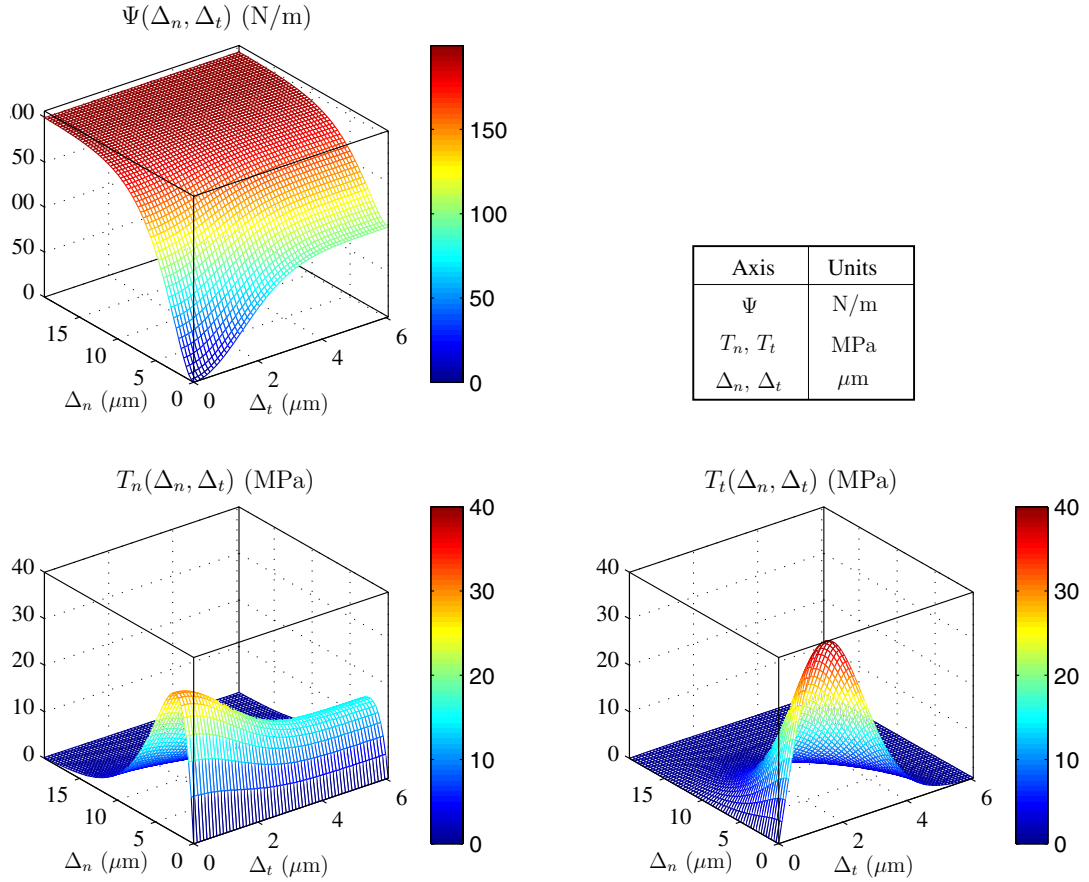


Figure 3.5: Xu and Needleman (1993) exponential potential and its gradients; $\phi_n = 200 \text{ N/m}$, $\phi_t = 100 \text{ N/m}$, $\sigma_{\max} = 30 \text{ MPa}$, $\tau_{\max} = 40 \text{ MPa}$, and $r = 0$.

Additionally, the exponential potential originates from an atomistic potential which includes elastic behavior. When cohesive surface elements are inserted in a large domain, numerical simulations of the cohesive zone models lead to large artificial compliance (Klein et al., 2001; Song et al., 2006). Ideally, the elastic behavior should be generally eliminated in numerical implementation of cohesive surface elements. Moreover, because of the exponential expression, the traction free condition

occurs when separation is infinite, although a final crack opening width is finite in macroscopic scale fracture.

The limitations of the exponential potential are summarized as follows:

- It contains an ill-defined fracture parameter, Δ_n^* , which is difficult to determine experimentally.
- It is not applicable when the mode I fracture energy is greater than the mode II fracture energy.
- It provides large artificial compliance for numerical simulation of cohesive surface elements because it does not allow any control of the elastic behavior.
- Due to the exponential function, the final crack opening width is infinite, which does not resemble macroscopic fracture behavior.

3.2 PPR: Unified Potential-Based Constitutive Model

In this section, the polynomial-based potential is proposed in conjunction with symmetric fracture boundary conditions and macroscopic fracture parameters. The proposed potential is defined in the cohesive interaction (softening) region where fractured surfaces transfer cohesive tractions. Both intrinsic and extrinsic cohesive zone constitutive models are derived from the unified potential.

3.2.1 Definition of the Unified Potential for Mixed-Mode Fracture

The unified PPR potential for cohesive fracture is proposed to describe physical macroscopic fracture, including explicit control of elastic behavior for intrinsic models. Physical macroscopic behavior is represented by the following fracture boundary conditions (Figure 3.6):

- Complete normal failure occurs ($T_n = 0$) when the normal or tangential separation reaches a certain length scale ($\delta_n, \bar{\delta}_t$), called the normal final crack opening width and the tangential conjugate final crack opening width, respectively,

$$T_n(\delta_n, \Delta_t) = 0, \quad T_n(\Delta_n, \bar{\delta}_t) = 0. \quad (3.22)$$

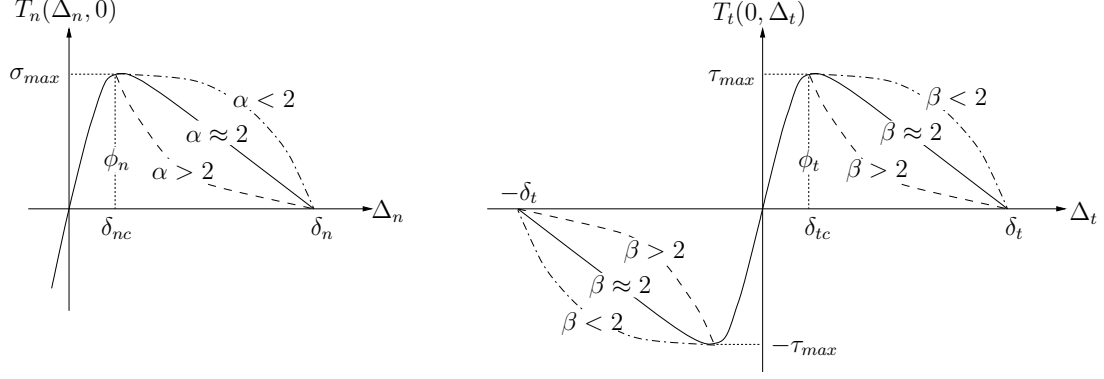


Figure 3.6: Fracture boundary conditions for the unified mixed-mode potential.

- Similarly, complete tangential failure occurs ($T_t = 0$) either when the normal separation reaches the normal conjugate final crack opening width ($\bar{\delta}_n$) or when the tangential separation reaches the tangential final crack opening width (δ_t),

$$T_t(\bar{\delta}_n, \Delta_t) = 0, \quad T_t(\Delta_n, \delta_t) = 0. \quad (3.23)$$

- The area under the cohesive interactions corresponds to the fracture energy. Therefore (ϕ_n, ϕ_t) are given by

$$\phi_n = \int_0^{\delta_n} T_n(\Delta_n, 0) d\Delta_n, \quad \phi_t = \int_0^{\delta_t} T_t(0, \Delta_t) d\Delta_t. \quad (3.24)$$

- The normal and tangential tractions are maximum when the separations reach the critical opening displacements $(\delta_{nc}, \delta_{tc})$,

$$\left. \frac{\partial T_n}{\partial \Delta_n} \right|_{\Delta_n = \delta_{nc}} = 0, \quad \left. \frac{\partial T_t}{\partial \Delta_t} \right|_{\Delta_t = \delta_{tc}} = 0. \quad (3.25)$$

- The maximum tractions correspond to the cohesive strengths $(\sigma_{\max}, \tau_{\max})$,

$$T_n(\delta_{nc}, 0) = \sigma_{\max}, \quad T_t(0, \delta_{tc}) = \tau_{\max}. \quad (3.26)$$

- The shape parameter indices (α, β) are introduced to characterize material softening responses, e.g. brittle, plateau and quasi-brittle.

Based on these physical macroscopic fracture parameters, the potential for mixed-

mode fracture, called the PPR potential, is expressed as

$$\Psi(\Delta_n, \Delta_t) = \min(\phi_n, \phi_t) + \left[\Gamma_n \left(1 - \frac{\Delta_n}{\delta_n}\right)^\alpha \left(\frac{m}{\alpha} + \frac{\Delta_n}{\delta_n}\right)^m + \langle \phi_n - \phi_t \rangle \right] \\ \left[\Gamma_t \left(1 - \frac{|\Delta_t|}{\delta_t}\right)^\beta \left(\frac{n}{\beta} + \frac{|\Delta_t|}{\delta_t}\right)^n + \langle \phi_t - \phi_n \rangle \right]. \quad (3.27)$$

The gradients of the PPR potential lead directly to the traction vector,

$$T_n(\Delta_n, \Delta_t) = \frac{\Gamma_n}{\delta_n} \left[m \left(1 - \frac{\Delta_n}{\delta_n}\right)^\alpha \left(\frac{m}{\alpha} + \frac{\Delta_n}{\delta_n}\right)^{m-1} - \alpha \left(1 - \frac{\Delta_n}{\delta_n}\right)^{\alpha-1} \left(\frac{m}{\alpha} + \frac{\Delta_n}{\delta_n}\right)^m \right] \\ \left[\Gamma_t \left(1 - \frac{|\Delta_t|}{\delta_t}\right)^\beta \left(\frac{n}{\beta} + \frac{|\Delta_t|}{\delta_t}\right)^n + \langle \phi_t - \phi_n \rangle \right], \\ T_t(\Delta_n, \Delta_t) = \frac{\Gamma_t}{\delta_t} \left[n \left(1 - \frac{|\Delta_t|}{\delta_t}\right)^\beta \left(\frac{n}{\beta} + \frac{|\Delta_t|}{\delta_t}\right)^{n-1} - \beta \left(1 - \frac{|\Delta_t|}{\delta_t}\right)^{\beta-1} \left(\frac{n}{\beta} + \frac{|\Delta_t|}{\delta_t}\right)^n \right] \\ \left[\Gamma_n \left(1 - \frac{\Delta_n}{\delta_n}\right)^\alpha \left(\frac{m}{\alpha} + \frac{\Delta_n}{\delta_n}\right)^m + \langle \phi_n - \phi_t \rangle \right] \frac{\Delta_t}{|\Delta_t|} \quad (3.28)$$

where $\langle \cdot \rangle$ is the *Macaulay bracket*, i.e.

$$\langle x \rangle = \begin{cases} 0, & (x < 0) \\ x, & (x \geq 0) \end{cases}. \quad (3.29)$$

The normal and tangential tractions satisfy basic symmetry and anti-symmetry requirements (with respect to Δ_t), i.e.

$$T_n(\Delta_n, \Delta_t) = T_n(\Delta_n, -\Delta_t), \quad T_t(\Delta_n, \Delta_t) = -T_t(\Delta_n, -\Delta_t), \quad (3.30)$$

respectively. Notice that the value of $T_t(\Delta_n, \Delta_t)$ at $\Delta_t = 0$ exists in the limit sense, i.e.

$$\lim_{\Delta_t \rightarrow 0^+} T_t(\Delta_n, \Delta_t) = 0, \quad \lim_{\Delta_t \rightarrow 0^-} T_t(\Delta_n, \Delta_t) = 0. \quad (3.31)$$

The eight characteristic parameters ($\Gamma_n, \Gamma_t; m, n; \delta_n, \delta_t; \alpha, \beta$) in the potential function are determined by satisfying the boundary conditions of macroscopic fracture. The energy constants, Γ_n and Γ_t , are related to the mode I and mode II fracture energies, which satisfy the boundary conditions of the fracture energies (3.24). When the mode I and mode II fracture energies are different, one obtains the energy constants

$$\Gamma_n = (-\phi_n)^{\frac{\langle \phi_n - \phi_t \rangle}{\phi_n - \phi_t}} \left(\frac{\alpha}{m}\right)^m, \quad \Gamma_t = (-\phi_t)^{\frac{\langle \phi_t - \phi_n \rangle}{\phi_t - \phi_n}} \left(\frac{\beta}{n}\right)^n \quad \text{for } (\phi_n \neq \phi_t). \quad (3.32)$$

If the mode I and mode II fracture energies are the same, the energy constants are simplified as

$$\Gamma_n = -\phi_n \left(\frac{\alpha}{m}\right)^m, \quad \Gamma_t = \left(\frac{\beta}{n}\right)^n \quad \text{for } (\phi_n = \phi_t). \quad (3.33)$$

The nondimensional exponents, m and n , are evaluated by the boundary conditions of the critical separations (3.25) and the initial slope indicators (λ_n, λ_t) ,

$$m = \frac{\alpha(\alpha - 1)\lambda_n^2}{(1 - \alpha\lambda_n^2)}, \quad n = \frac{\beta(\beta - 1)\lambda_t^2}{(1 - \beta\lambda_t^2)}. \quad (3.34)$$

The initial slope indicators are defined as the ratio of the critical crack opening width to final crack opening width, i.e.,

$$\lambda_n = \delta_{nc}/\delta_n, \quad \lambda_t = \delta_{tc}/\delta_t. \quad (3.35)$$

The initial slope indicators are introduced to control elastic behavior, which is eliminated in a constitutive model of the extrinsic cohesive zone model. Smaller values of λ_n, λ_t (or δ_{nc}, δ_{tc}) result in the higher initial slope, and decrease artificial elastic deformation. Therefore, λ_n and λ_t are generally selected to be “small” values within the range of numerical stability for the intrinsic cohesive zone model.

The length scale parameters (δ_n and δ_t) are the final normal and tangential crack opening widths whose boundary conditions (3.22, 3.23) are already satisfied by the potential function itself. The values of the final crack opening widths are determined by considering the boundary conditions of fracture energy (3.24) and of the cohesive strength (3.26),

$$\begin{aligned} \delta_n &= \frac{\phi_n}{\sigma_{\max}} \alpha \lambda_n (1 - \lambda_n)^{\alpha-1} \left(\frac{\alpha}{m} + 1\right) \left(\frac{\alpha}{m} \lambda_n + 1\right)^{m-1}, \\ \delta_t &= \frac{\phi_t}{\tau_{\max}} \beta \lambda_t (1 - \lambda_t)^{\beta-1} \left(\frac{\beta}{n} + 1\right) \left(\frac{\beta}{n} \lambda_t + 1\right)^{n-1}. \end{aligned} \quad (3.36)$$

The non-dimensional shape parameter indices (α, β) are introduced because the specific shape of the cohesive zone model can significantly affect results of the fracture analysis (see, for example, Volokh, 2004; Alfano, 2006; Song et al., 2008). If the shape parameter indices are equal to two, the order of the potential function is approximately two. Then, the resulting gradient of the potential represents almost a linearly decreasing cohesive relationship. When the shape parameters are less than

two, the gradient of the potential demonstrates a concave softening shape, which can represent a plateau-type function. If the shape parameter indices are chosen as larger values, the cohesive interaction has a convex shape.

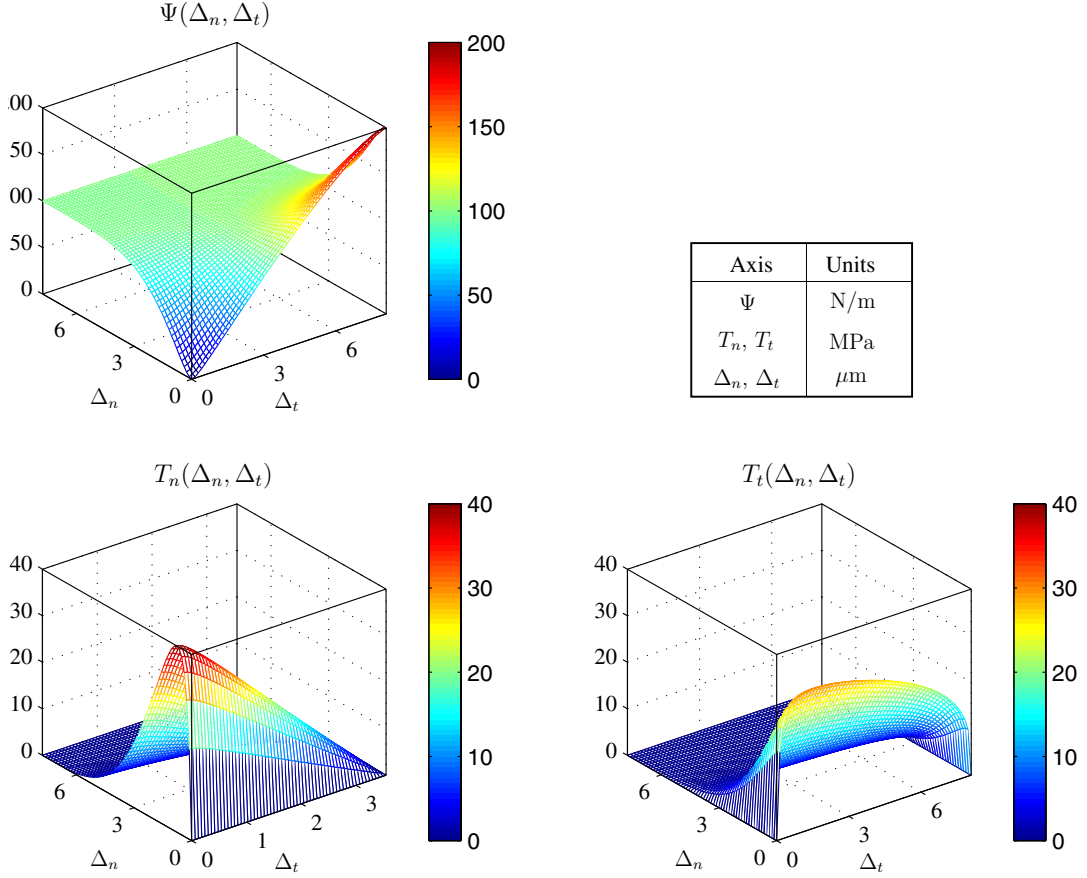


Figure 3.7: Unified mixed-mode potential (PPR) and its gradients for the intrinsic cohesive zone model with $\phi_n = 100$ N/m, $\phi_t = 200$ N/m, $\sigma_{\max} = 40$ MPa, $\tau_{\max} = 30$ MPa, $\alpha = 5$, $\beta = 1.3$, $\lambda_n = 0.1$, and $\lambda_t = 0.2$.

In summary, the potential function for mixed-mode cohesive fracture is developed by satisfying the boundary conditions of macroscopic fracture. The unified potential and its gradients are plotted in Figure 3.7. The plotted potential represents different fracture energies (e.g. $\phi_n = 100$ N/m, $\phi_t = 200$ N/m), cohesive strengths (e.g. $\sigma_{\max} = 40$ MPa, $\tau_{\max} = 30$ MPa), cohesive interactions (e.g. $\alpha = 5$, $\beta = 1.3$) and initial slope indicators (e.g. $\lambda_n = 0.1$, $\lambda_t = 0.2$). The mode I cohesive relationship illustrates fracture behavior of a typical quasi-brittle material, while the mode II cohesive relationship describes a plateau-type behavior. The potential is also applicable when the mode I fracture energy is greater than mode II fracture energy because the

potential is explicitly derived by using the symmetric boundary conditions for modes I and II.

3.2.2 Cohesive Interaction (Softening) Region

The proposed potential is a continuous polynomial function. Exponential potentials result in an infinite final crack opening width, while the polynomial-based potential provides a finite final crack opening width. Because of this fact, the polynomial potential is only valid in the defined softening region. For example, mathematically the unbounded polynomial potential provides non-zero traction even after a physical separation is greater than a final crack opening width. Therefore, one must define a region for each cohesive interaction (T_n , T_t) in terms of a set of material-derived final crack opening widths (e.g. δ_n , δ_t) and calculated conjugate final crack opening widths (e.g. $\bar{\delta}_n$, $\bar{\delta}_t$).

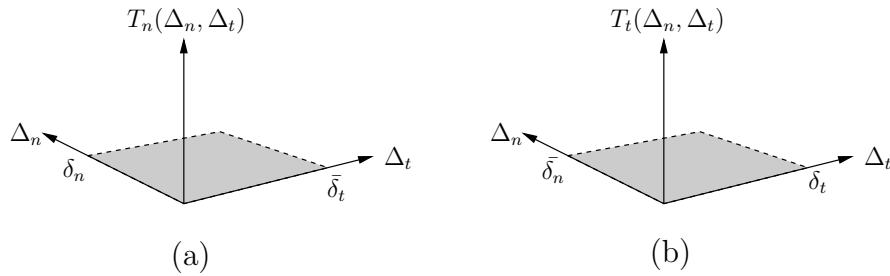


Figure 3.8: Description of each cohesive interaction (T_n , T_t) region defined by the final crack opening widths (δ_n , δ_t) and the conjugate final crack opening widths ($\bar{\delta}_n$, $\bar{\delta}_t$); (a) T_n versus $(\delta_n, \bar{\delta}_t)$ space; (b) T_t versus $(\bar{\delta}_n, \delta_t)$ space.

The cohesive interaction region is defined as a rectangular region for each cohesive interaction in conjunction with the final crack opening widths (δ_n , δ_t) and the conjugate final crack opening widths ($\bar{\delta}_n$, $\bar{\delta}_t$) as shown in Figure 3.8. For the normal cohesive interaction (T_n), one border of the softening region is the normal final crack opening width (δ_n). If the normal separation is greater than the normal final crack opening width ($\Delta_n > \delta_n$), the normal traction (T_n) is set to zero. The other border of the softening region is the tangential conjugate final crack opening width ($\bar{\delta}_t$). If the tangential separation is greater than the tangential conjugate final crack opening width ($\Delta_t > \bar{\delta}_t$), the normal traction is also set to be zero. The value of the tangential conjugate final crack opening width ($\bar{\delta}_t$) is obtained by satisfying the boundary condition of $T_n(\Delta_n, \bar{\delta}_t) = 0$. Since Δ_n is an arbitrary separation, the tangential conjugate

final crack opening width ($\Delta_t = \bar{\delta}_t$) is the solution of the nonlinear function

$$f_t(\Delta_t) = \Gamma_t \left(1 - \frac{|\Delta_t|}{\delta_t}\right)^\beta \left(\frac{n}{\beta} + \frac{|\Delta_t|}{\delta_t}\right)^n + \langle \phi_t - \phi_n \rangle = 0. \quad (3.37)$$

The uniqueness of the solution between 0 and δ_t is proved in the following way. When the mode II fracture energy (ϕ_t) is greater than the mode I fracture energy (ϕ_n), $f_t(0) = -\phi_n < 0$ and $f_t(\delta_t) = \phi_t - \phi_n > 0$. Because $f_t'(\Delta_t)$ is always positive within the range of $0 \leq \Delta_t \leq \delta_t$, the function $f_t(\Delta_t)$ has a single solution between 0 and δ_t . Additionally, when ϕ_t is not greater than ϕ_n , the solution of a function $f_t(\Delta_t)$ is the same as the tangential final crack opening width, i.e. $\bar{\delta}_t = \delta_t$.

Accordingly, the cohesive interaction region for the tangential traction is defined by the tangential final crack opening width (δ_t) and the normal conjugate final crack opening width ($\bar{\delta}_n$). The normal conjugate final crack opening width ($\Delta_n = \bar{\delta}_n$) is the solution of the nonlinear function

$$f_n(\Delta_n) = \Gamma_n \left(1 - \frac{\Delta_n}{\delta_n}\right)^\alpha \left(\frac{m}{\alpha} + \frac{\Delta_n}{\delta_n}\right)^m + \langle \phi_n - \phi_t \rangle = 0. \quad (3.38)$$

The derivative of $f_n(\Delta_n)$ is positive within the range of $0 \leq \Delta_n \leq \delta_n$ when ϕ_n is greater than ϕ_t . Then, because $f_n(0) < 0$ and $f_n(\delta_n) > 0$, the function $f_n(\Delta_n)$ has a single solution between 0 and δ_n . When ϕ_n is not greater than ϕ_t , the solution of a function $f_n(\Delta_n)$ is the normal final crack opening width, i.e. $\bar{\delta}_n = \delta_n$.

In summary, the normal cohesive interaction (T_n) is defined within the normal final crack opening with (δ_n) and the tangential conjugate final crack opening width ($\bar{\delta}_t$) space (Figure 3.8(a)). The tangential cohesive interaction (T_t) is defined within the tangential final crack opening width (δ_t) and the normal conjugate final crack opening with ($\bar{\delta}_n$) space (Figure 3.8(b)). The introduction of the conjugate final crack opening widths ($\bar{\delta}_n$, $\bar{\delta}_t$) guarantees that a non-zero traction will not occur when load bearing capacity is lost.

3.2.3 Extension to the Extrinsic Cohesive Zone Model

The PPR potential function is extended for the case of the extrinsic cohesive zone models. In this case, the potential function excludes the elastic behavior (or initial slope) in the cohesive interactions. The limit of initial slope indicators in the PPR potential function ($\lambda_n \rightarrow 0$ and $\lambda_t \rightarrow 0$) eliminates the initial slope indicators (λ_n , λ_t) and the exponents (m , n) from the resulting expression. Thus one obtains the

potential function for the extrinsic cohesive zone model expressed as

$$\Psi(\Delta_n, \Delta_t) = \min(\phi_n, \phi_t) + \left[\Gamma_n \left(1 - \frac{\Delta_n}{\delta_n} \right)^\alpha + \langle \phi_n - \phi_t \rangle \right] \left[\Gamma_t \left(1 - \frac{|\Delta_t|}{\delta_t} \right)^\beta + \langle \phi_t - \phi_n \rangle \right] . \quad (3.39)$$

The gradient of the potential leads to the normal and tangential tractions along the fracture surface,

$$\begin{aligned} T_n(\Delta_n, \Delta_t) &= -\alpha \frac{\Gamma_n}{\delta_n} \left(1 - \frac{\Delta_n}{\delta_n} \right)^{\alpha-1} \left[\Gamma_t \left(1 - \frac{|\Delta_t|}{\delta_t} \right)^\beta + \langle \phi_t - \phi_n \rangle \right] , \\ T_t(\Delta_n, \Delta_t) &= -\beta \frac{\Gamma_t}{\delta_t} \left(1 - \frac{|\Delta_t|}{\delta_t} \right)^{\beta-1} \left[\Gamma_n \left(1 - \frac{\Delta_n}{\delta_n} \right)^\alpha + \langle \phi_n - \phi_t \rangle \right] \frac{\Delta_t}{|\Delta_t|} . \end{aligned} \quad (3.40)$$

The normal and tangential tractions satisfy the symmetry and anti-symmetry requirements, respectively, according to Eq. (3.30). The tangential traction provides a finite value at the initiation point ($\Delta_t = 0$), and therefore introduces the discontinuity, i.e.

$$\begin{aligned} \lim_{\Delta_t \rightarrow 0^+} T_t(\Delta_n, \Delta_t) &= -\beta \frac{\Gamma_t}{\delta_t} \left[\Gamma_n \left(1 - \frac{\Delta_n}{\delta_n} \right)^\alpha + \langle \phi_n - \phi_t \rangle \right] , \\ \lim_{\Delta_t \rightarrow 0^-} T_t(\Delta_n, \Delta_t) &= \beta \frac{\Gamma_t}{\delta_t} \left[\Gamma_n \left(1 - \frac{\Delta_n}{\delta_n} \right)^\alpha + \langle \phi_n - \phi_t \rangle \right] , \end{aligned} \quad (3.41)$$

which corresponds to a feature of the extrinsic cohesive zone models.

The normal and tangential tractions are defined in a softening region associated with the final crack opening width (δ_n, δ_t) and the conjugate final crack opening width ($\bar{\delta}_n, \bar{\delta}_t$). The final crack opening widths are expressed as

$$\delta_n = \alpha \phi_n / \sigma_{\max} , \quad \delta_t = \beta \phi_t / \tau_{\max} , \quad (3.42)$$

which are associated with the fracture boundary conditions, such as the fracture energies and the cohesive strengths. The conjugate final crack opening widths ($\bar{\delta}_n, \bar{\delta}_t$) are given by

$$\bar{\delta}_n = \delta_n - \delta_n \left(\frac{\langle \phi_n - \phi_t \rangle}{\phi_n} \right)^{1/\alpha} , \quad \bar{\delta}_t = \delta_t - \delta_t \left(\frac{\langle \phi_t - \phi_n \rangle}{\phi_t} \right)^{1/\beta} , \quad (3.43)$$

which satisfy the conditions of $T_t(\bar{\delta}_n, \Delta_t) = 0$ and $T_n(\Delta_n, \bar{\delta}_t) = 0$, respectively. The

energy constants are expressed as

$$\Gamma_n = (-\phi_n) \frac{\langle \phi_n - \phi_t \rangle}{\phi_n - \phi_t}, \quad \Gamma_t = (-\phi_t) \frac{\langle \phi_t - \phi_n \rangle}{\phi_t - \phi_n} \quad (\phi_n \neq \phi_t), \quad (3.44)$$

for the different fracture energies. If the fracture energies are the same, one obtains the energy constants,

$$\Gamma_n = -\phi_n, \quad \Gamma_t = 1 \quad (\phi_n = \phi_t). \quad (3.45)$$

With the same fracture parameters as illustrated in Figure 3.7, the potential for the extrinsic cohesive zone model is plotted in Figure 3.9. The initial slope is excluded, and the traction discontinuity is introduced at zero separation. The shape of the potential is concave because the potential is only associated to behaviors which occur

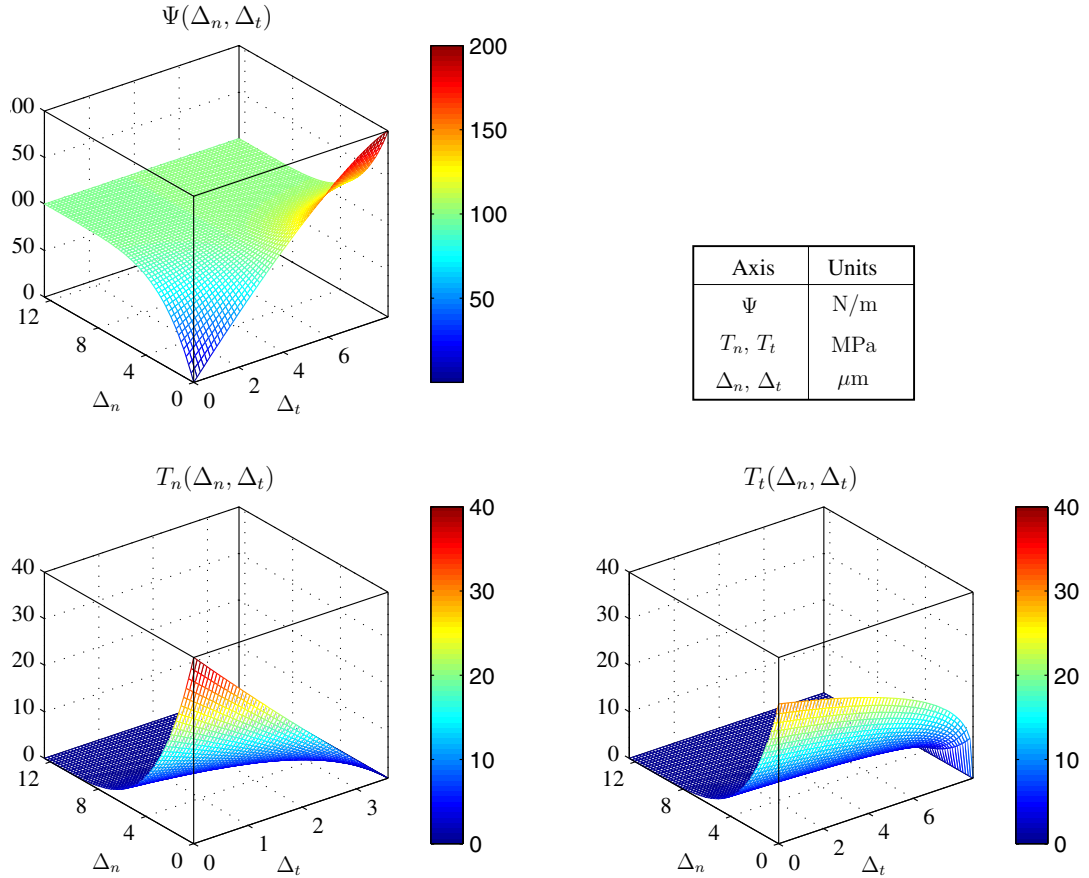


Figure 3.9: Proposed potential and its gradients for the extrinsic cohesive zone model with $\phi_n = 100$ N/m, $\phi_t = 200$ N/m, $\sigma_{\max} = 40$ MPa, $\tau_{\max} = 30$ MPa, $\alpha = 5$, and $\beta = 1.3$.

after the limit point (c.f. Figure 1.3). In summary, rather than providing infinite slope, the cohesive interactions for the extrinsic cohesive zone model are derived by taking the limit from the potential function. Thus, the discontinuities are naturally introduced at crack initiation.

3.2.4 Remarks

The PPR potential for mixed-mode cohesive fracture is associated with physical macroscopic fracture parameters, i.e., fracture energies (ϕ_n, ϕ_t) , cohesive strengths $(\sigma_{\max}, \tau_{\max})$, softening curves shape (α, β) and the initial slope indicators (λ_n, λ_t) . In addition, the potential-based model for the extrinsic cohesive zone model is within the same framework as for the intrinsic cohesive zone model. The characteristics of the proposed potential are summarized as follows:

- Differentiates fracture energies (ϕ_n, ϕ_t) and cohesive strengths $(\sigma_{\max}, \tau_{\max})$ in fracture modes I and II.
- Suitable for various material softening responses, e.g. “ductile” (plateau), brittle, and quasi-brittle, because of the shape parameters (α, β) .
- The normal and tangential tractions (T_n, T_t) are defined in a rectangular region associated with the final crack opening widths (δ_n, δ_t) and the conjugate final crack opening widths $(\bar{\delta}_n, \bar{\delta}_t)$.
- The initial slope indicators (λ_n, λ_t) control the artificial elastic behavior in the intrinsic cohesive zone model.
- The limit of the initial slope indicators results in the potential function for the extrinsic cohesive zone model.
- Obeys the symmetry condition, i.e. an exact differential $(\partial T_n / \partial \Delta_t = \partial T_t / \partial \Delta_n)$. The values of the differential at $\Delta_t = 0$ exists in the limit sense.
- The normal negative displacements are penalized to prevent material self penetration. Alternative approaches, involving contact mechanics, may also be used.
- Unloading and reloading are handled independently of the potential (see Chapter 4).

- Utilizes polynomial function to avoid the infinite final crack opening width of the exponential potential.

3.3 Path Dependence of Work-of-Separation

Energy dissipated due to the fracture depends on separation paths when the mode I fracture energy (ϕ_n) is different from the mode II fracture energy (ϕ_t). In order to evaluate the energy variation with respect to a path, the work-of-separation (W_{sep}) is defined as follows:

$$W_{sep} = \underbrace{\int_{\Gamma} T_n(\Delta_n, \Delta_t) d\Delta_n}_{W_n} + \underbrace{\int_{\Gamma} T_t(\Delta_n, \Delta_t) d\Delta_t}_{W_t}, \quad (3.46)$$

where Γ is a separation path. The first term in the work-of-separation expression is the work done by the normal traction (W_n), while the second term in the expression is the work done by the tangential traction (W_t). This study compares energy variations of the unified potential-based model (PPR) with those of the model by Xu and Needleman (1993) for proportional separation paths and non-proportional paths. Tables 3.2 and 3.3 illustrate the fracture parameters utilized in this investigation. The mode I fracture energy (ϕ_n) is arbitrarily selected as 100 N/m, and the mode II fracture energy (ϕ_t) as 200 N/m.

Table 3.2: Fracture parameters for the unified potential-based model (PPR).

ϕ_n	ϕ_t	σ_{\max}	τ_{\max}	α	β	λ_n	λ_t
100 N/m	200 N/m	3 MPa	12 MPa	3	3	0.01	0.01

Table 3.3: Fracture parameters for the model by Xu and Needleman (1993).

ϕ_n	ϕ_t	σ_{\max}	τ_{\max}	r
100 N/m	200 N/m	3 MPa	12 MPa	0.5

3.3.1 Proportional Separation

The proportional separation path is associated with the separation angle (θ), as shown in Figure 3.10. The work-of-separation for the unified potential-based model

is expressed in terms of Δ_r and θ ,

$$W_{sep} = \int_0^{\delta_r} T_n(\Delta_r \sin \theta, \Delta_r \cos \theta) \sin \theta d\Delta_r + \int_0^{\delta_r} T_t(\Delta_r \sin \theta, \Delta_r \cos \theta) \cos \theta d\Delta_r , \quad (3.47)$$

where $\delta_r = \sqrt{\delta_n^2 + \delta_t^2}$. When the separation angle is 90° , the material experiences mode I fracture for which the work-of-separation is equal to the mode I fracture energy. When $\theta = 0^\circ$, the material experiences mode II fracture for which the work-of-separation is the same as the mode II fracture energy. For the intermediate angles ($0^\circ < \theta < 90^\circ$), i.e. mixed-mode fracture, the work-of-separation is between the mode I and the mode II fracture energies.

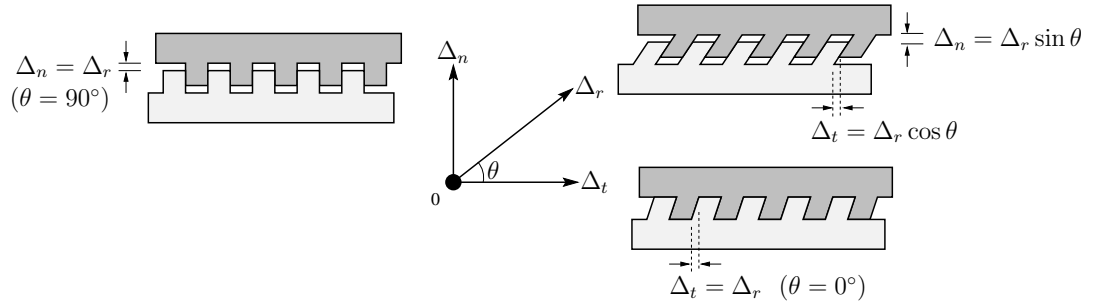


Figure 3.10: Proportional separation path (Δ_r) with the separation angle (θ).

Figures 3.11(a), (b) and (c) demonstrate the analytical variation of the work-of-separation (W_{sep}), the work done by the normal traction (W_n), and the work done by the tangential traction (W_t) with respect to the changes of the proportional angles, respectively. When the separation angle is 90° , i.e. mode I fracture, W_{sep} and W_n increase from 0 to the mode I fracture energy (100 N/m) with the increase of Δ_r , while W_t remains zero. When θ is equal to 0° , i.e. mode II fracture, W_{sep} and W_t change from 0 to the mode II fracture energy (200 N/m) with the increase of Δ_r , while W_n remains zero. For the intermediate angles ($0^\circ < \theta < 90^\circ$), i.e. mixed-mode fracture, W_{sep} , W_n and W_t vary monotonically including both the mode I and mode II fracture behavior.

Accordingly, for the cohesive fracture model by Xu and Needleman (1993), the work-of-separation expression is given as (cf. Eq. (3.47))

$$W_{sep} = \int_0^\infty T_n(\Delta_r \sin \theta, \Delta_r \cos \theta) \sin \theta d\Delta_r + \int_0^\infty T_t(\Delta_r \sin \theta, \Delta_r \cos \theta) \cos \theta d\Delta_r . \quad (3.48)$$

Figure 3.12 illustrates the variation of W_{sep} , W_n and W_t with respect to the separation angles. When the separation angle is 0° , W_{sep} and W_t reach the mode II fracture

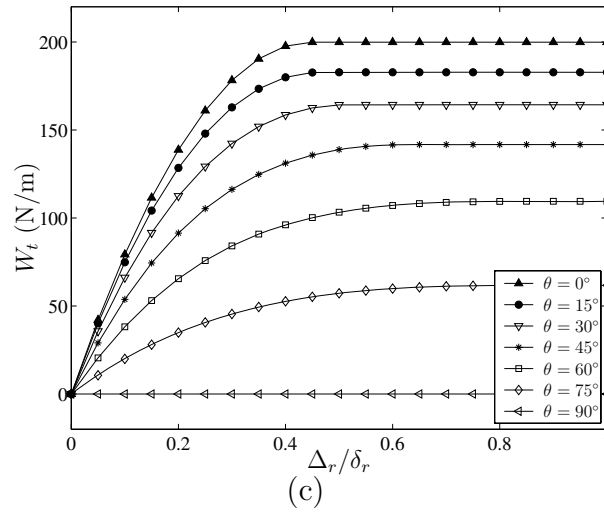
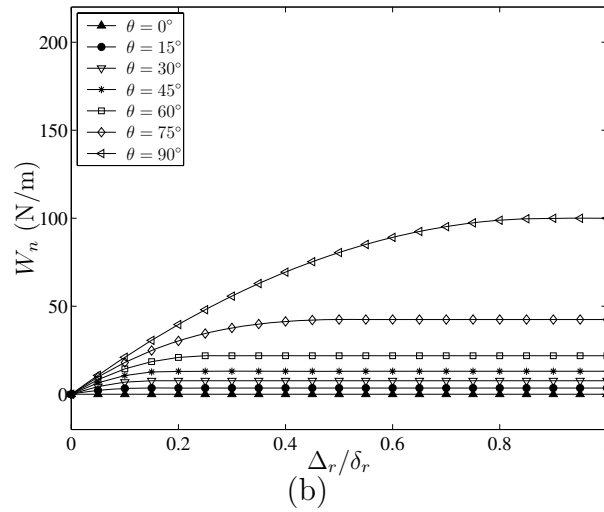
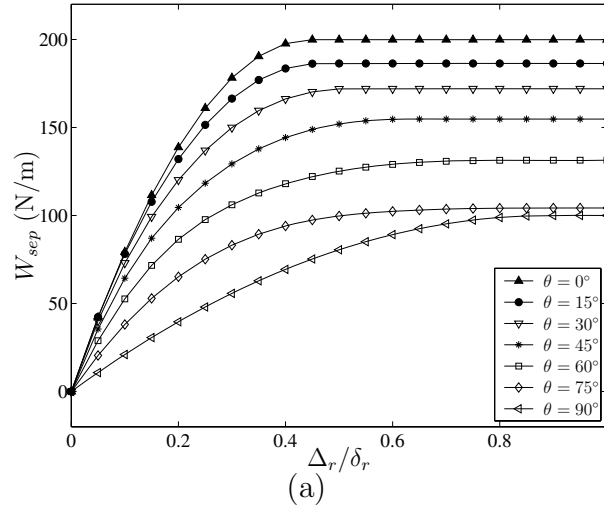


Figure 3.11: The PPR potential-based model: (a) work-of-separation, (b) work done by the normal traction, and (c) work done by the tangential traction with respect to the change of the proportional angle, θ .

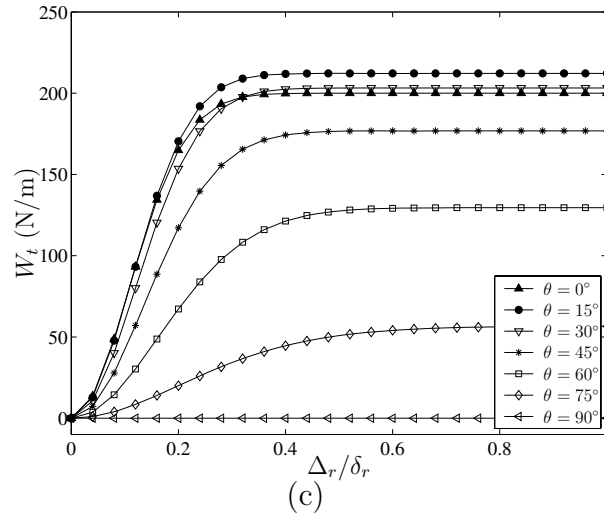
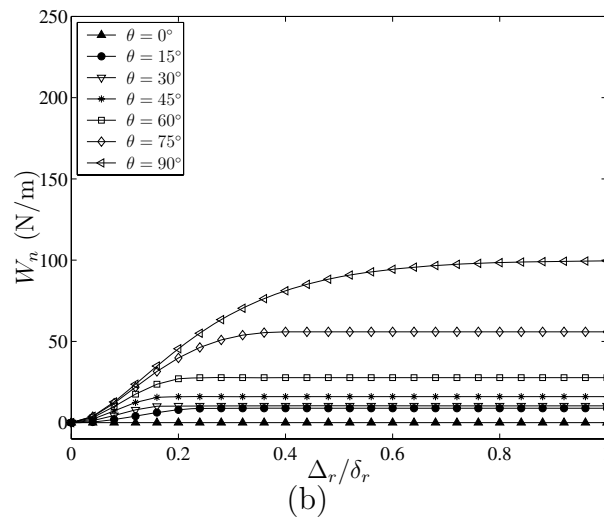
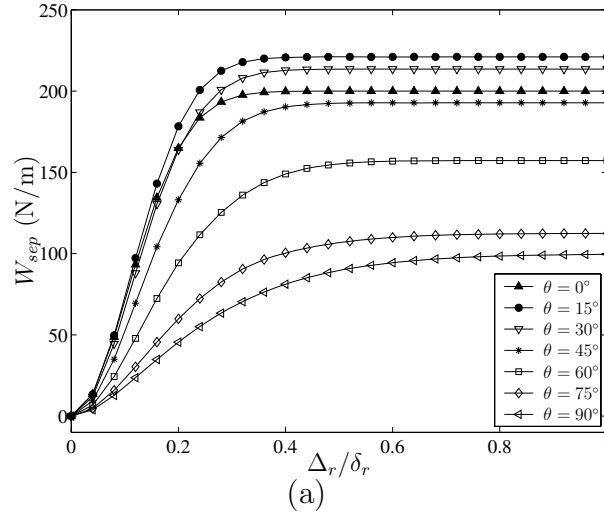


Figure 3.12: Xu and Needleman (1993) exponential potential: (a) work-of-separation, (b) work done by the normal traction, and (c) work done by the tangential traction with respect to the change of the proportional angle, θ .

energy (200 N/m), and W_n keeps zero. Increasing the separation angle results in the increase of the work done by the normal traction, and the decrease of W_{sep} and W_t . However, both W_{sep} and W_t increase monotonically with respect to the increase of the separation angle from 0° to 15° (see Figure 3.12(a) and (c)), but not with respect to 30° in this example. The work-of-separation does not change monotonically under mixed-mode fracture condition, and thus the exponential potential model does not guarantee the consistency of the cohesive constitutive model.

3.3.2 Non-Proportional Separation

For non-proportional separation paths, one could assume that material particles experience normal separation until $\Delta_n = \Delta_{n,max}$ and then the complete tangential separation occurs, i.e. **Path 1** in Figure 3.13(a). The other path is that material separates along the tangential direction first until $\Delta_t = \Delta_{t,max}$ and then the failure occurs along the normal direction, i.e. **Path 2** in Figure 3.13(b). For the first path, the work-of-separation of the PPR model is evaluated by the following expression:

$$W_{sep} = \int_0^{\Delta_{n,max}} T_n(\Delta_n, 0) d\Delta_n + \int_0^{\delta_t} T_t(\Delta_{n,max}, \Delta_t) d\Delta_t . \quad (3.49)$$

Accordingly, the work-of-separation for the second path is expressed as

$$W_{sep} = \int_0^{\Delta_{t,max}} T_t(0, \Delta_t) d\Delta_t + \int_0^{\delta_n} T_n(\Delta_n, \Delta_{t,max}) d\Delta_n . \quad (3.50)$$

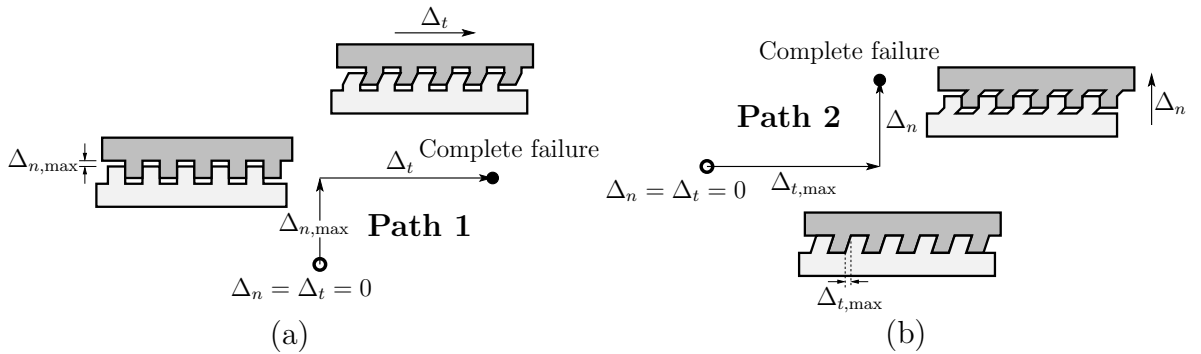


Figure 3.13: Two arbitrary separation paths for the material debonding process; (a) non-proportional **Path 1**; (b) non-proportional **Path 2**.

Figure 3.14 demonstrates the variation of the work-of-separation with respect to the two arbitrary separation paths. The mode I fracture energy is selected as 100 N/m and the mode II fracture energy as 200 N/m. The work done by the normal

separation is indicated as a thin solid line while the work done by the tangential separation is given as a dashed line. For the first non-proportional path (Figure 3.13(a)), $\Delta_{n,\max} = 0$ represents the mode II failure while $\Delta_{n,\max} = \delta_n$ describes the mode I failure. Then, the change of $\Delta_{n,\max}$ from 0 to δ_n demonstrates the gradual change of the mode mixity from the mode II fracture to the mode I fracture. The work done (W_t) by the tangential traction, therefore, monotonically decreases from ϕ_t to 0, while the work done (W_n) by the normal traction gradually increases from 0 to ϕ_n , as shown in Figure 3.14(a). The work-of-separation (W_{sep}) monotonically varies from the value of ϕ_t to the value of ϕ_n by increasing $\Delta_{n,\max}$ from 0 to δ_n . In the path 2 (Figure 3.13(b)), when $\Delta_{t,\max}$ is zero, the separation path illustrates the mode I failure while $\Delta_{t,\max} = \delta_t$ represents the mode II failure. The work-of-separation (W_{sep}) monotonically changes from the mode I fracture energy to the mode II fracture energy although there is a kink point as shown in Figure 3.14(b).

The separation at the kink point corresponds to the tangential conjugate final crack opening width ($\Delta_{t,\max} = \bar{\delta}_t$). When Δ_t is smaller than $\bar{\delta}_t$, the normal cohesive interaction is obtained by the derivative of the PPR potential with respect to the normal separation. When Δ_t is greater than $\bar{\delta}_t$, the normal cohesive interaction is set to zero. The normal cohesive interaction is then not smooth but piece-wise continuous at $\Delta_{t,\max} = \bar{\delta}_t$ in this example. The integration of the normal cohesive interaction is also piece-wise continuous at the same point. Therefore, the work done (W_n) by the normal separation changes from ϕ_n to zero between $\Delta_{t,\max} = 0$ (mode I) and $\Delta_{t,\max} = \bar{\delta}_t$ (mode II), and demonstrates piece-wise continuity at $\Delta_{t,\max} = \bar{\delta}_t$. As a

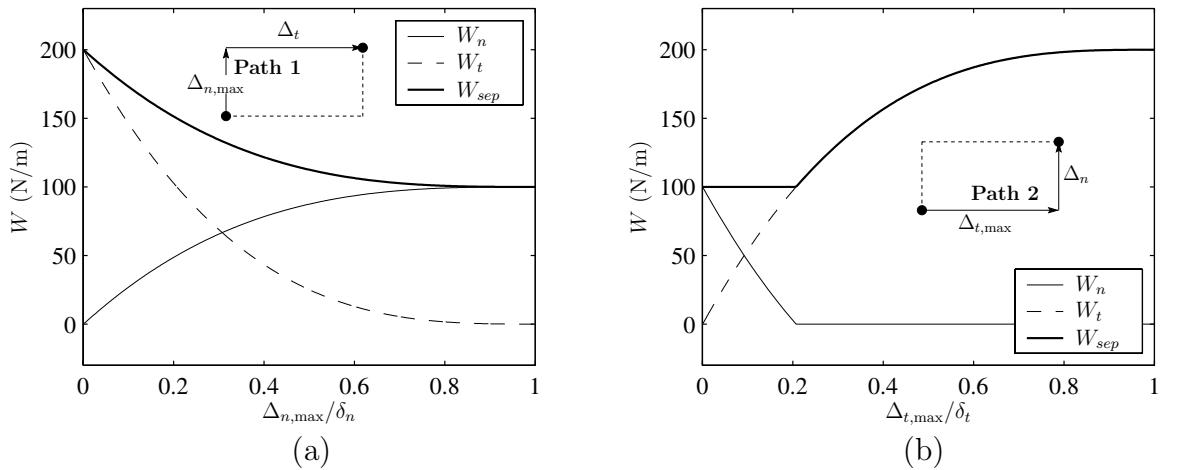


Figure 3.14: The PPR potential-based model: variation of the work-of-separation for the case of $\phi_n < \phi_t$ ($\phi_n = 100$ N/m, $\phi_t = 200$ N/m); (a) non-proportional **Path 1**; (b) non-proportional **Path 2**.

result, the work-of-separation ($W_{sep} = W_n + W_t$) also have the kink point at the same location.

Additionally, similar energy variation is expected when the mode I fracture energy is greater than the mode II fracture energy (e.g. $\phi_n = 200$ N/m, $\phi_t = 100$ N/m), as shown in Figure 3.15. This is because the potential function is based on the symmetric boundary conditions of fracture. The work-of-separation curve monotonically changes from one fracture mode to the other fracture mode. The kink point occurs in the first separation path because the tangential cohesive interaction (T_t) is piece-wise continuous at $\Delta_{n,max} = \bar{\delta}_n$.

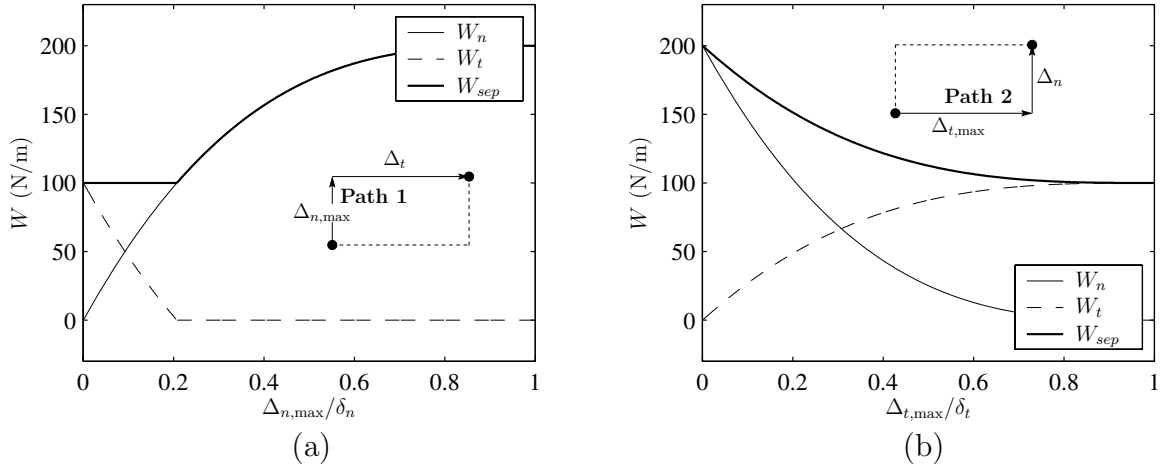


Figure 3.15: The PPR potential-based model: variation of the work-of-separation for the case of $\phi_n > \phi_t$ ($\phi_n = 200$ N/m, $\phi_t = 100$ N/m); (a) non-proportional **Path 1**; (b) non-proportional **Path 2**.

For the model by Xu and Needleman (1993), a similar investigation was implemented by van den Bosch et al. (2006). The work-of-separation for the first non-proportional path in Figure 3.13(a) is expressed as

$$W_{sep} = \int_0^{\Delta_{n,max}} T_n(\Delta_n, 0) d\Delta_n + \int_0^{\infty} T_t(\Delta_{n,max}, \Delta_t) d\Delta_t . \quad (3.51)$$

The work-of-separation for the second path (Figure 3.13(b)) is expressed as

$$W_{sep} = \int_0^{\Delta_{t,max}} T_t(0, \Delta_t) d\Delta_t + \int_0^{\infty} T_n(\Delta_n, \Delta_{t,max}) d\Delta_n . \quad (3.52)$$

The work-of-separations for the two arbitrary separation paths are plotted in Figures 3.16 and 3.17. Figure 3.16 is the case when the mode II fracture energy is greater than the mode I fracture energy (e.g. $\phi_n = 100$ N/m, $\phi_t = 200$ N/m), and Figure

3.17 is the case of $\phi_n > \phi_t$ (e.g. $\phi_n = 200$ N/m, $\phi_t = 100$ N/m). With respect to increasing the maximum normal separation ($\Delta_{n,max}$), the work-of-separation for the path 1 (Figure 3.16(a) and Figure 3.17(a)) does not monotonically vary from the mode I fracture energy to the mode II fracture energy. The second path in Figure 3.16(b) demonstrates the monotonic variation of the work-of-separation with the change in the maximum tangential separation ($\Delta_{t,max}$). The kink point in Figure 3.16(b) results from cutting off the negative normal traction region. In this example, when the tangential separation is greater than a certain value, the exponential potential leads to

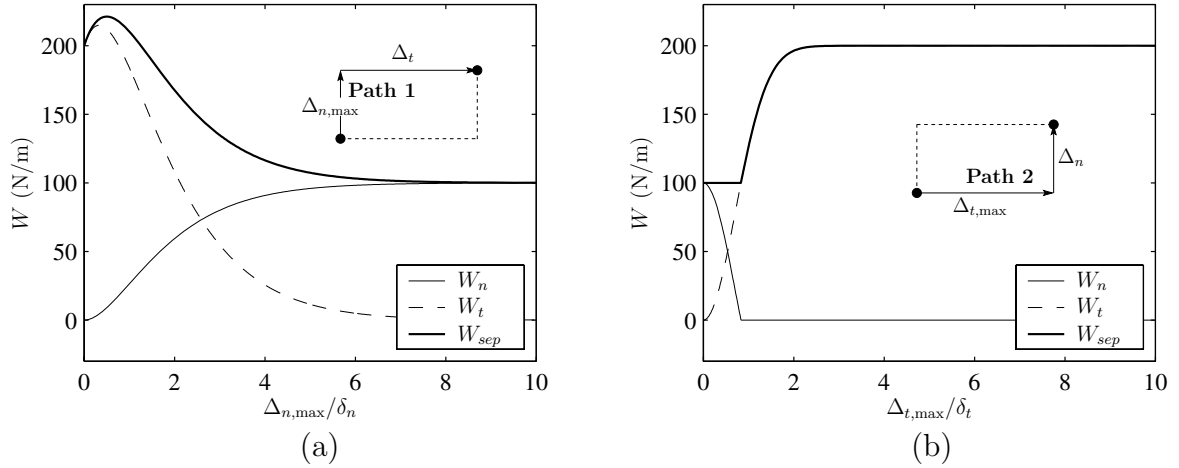


Figure 3.16: Xu and Needleman (1993) exponential potential: variation of the work-of-separation for the case of $\phi_n < \phi_t$ ($\phi_n = 100$ N/m, $\phi_t = 200$ N/m and $r = 0.5$); (a) non-proportional **Path 1**; (b) non-proportional **Path 2**.

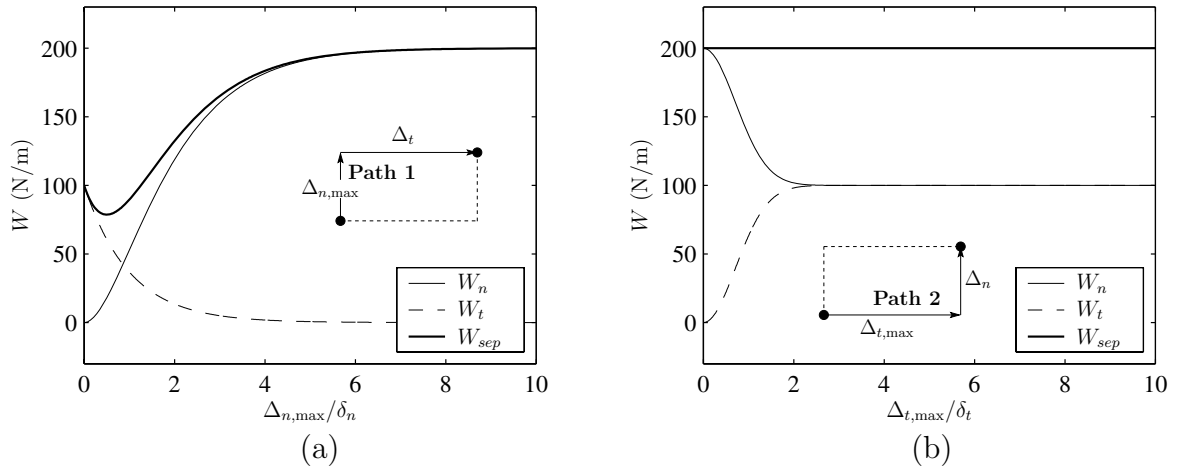


Figure 3.17: Xu and Needleman (1993) exponential potential: variation of the work-of-separation for the case of $\phi_n > \phi_t$ ($\phi_n = 200$ N/m, $\phi_t = 100$ N/m and $r = 0.5$); (a) non-proportional **Path 1**; (b) non-proportional **Path 2**.

negative normal traction. Since the work done should always be positive, one assumes that the normal cohesive interaction set to be zero within the negative traction range. Therefore, W_n and W_{sep} are not smooth but piece-wise continuous as shown in Figure 3.16(b). Additionally, for the path 2 in Figure 3.17(b), the work done by normal separation does not decrease to zero although material particles experience large shear separation.

3.4 Mixed-Mode Fracture Verification

The PPR potential-based model for cohesive fracture is verified by simulating a mixed-mode fracture problem, i.e. the mixed-mode bending (MMB) test. The MMB test was developed by Reeder and Crews Jr. (1990) in order to investigate the fracture toughness variation with respect to the mode mixity. The test has been standardized by ASTM (2006). The configuration of an MMB test is the combination of the double cantilever beam test (mode I loading) and the end-notch flexure test (mode II loading) as shown in Figure 3.18. Numerical simulations of the mixed-mode fracture are implemented by using the commercial software ABAQUS with a user-defined element (UEL) subroutine (see Chapter 4 and Appendix A). The formulation of cohesive surface elements is derived by the virtual work formulation with the updated Lagrangian finite element discretization.

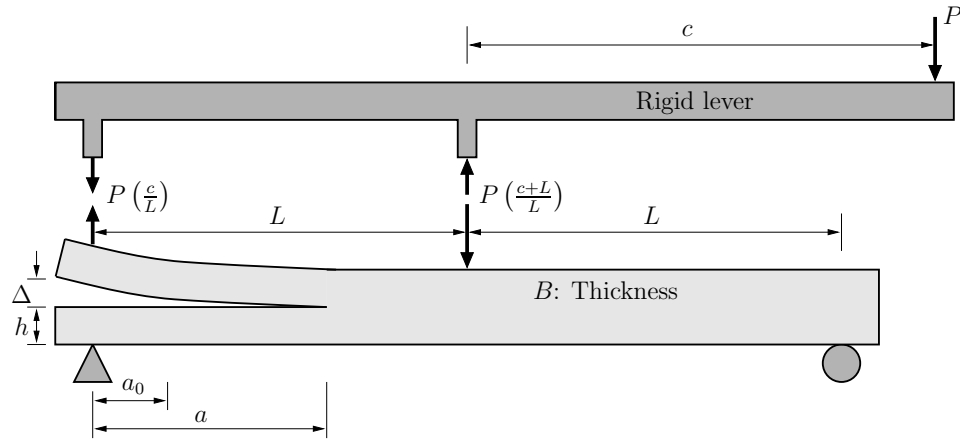


Figure 3.18: Mixed-mode bending test.

In this numerical verification, two hypothetical cases are simulated: one with the same fracture energy ($\phi_n = \phi_t = 1$ N/mm) and another with different fracture energies ($\phi_n = 1$ N/mm, $\phi_t = 2$ N/mm). The elastic modulus is 122 GPa, and Poisson's ratio is 0.25. The shape parameters are fixed to be equal to three ($\alpha = \beta =$

3), while the initial slope indicators are selected as a small value within numerical stability limits, e.g. $(\lambda_n, \lambda_t) \in [0.005, 0.025]$. The specimen size is provided in Table 3.4.

Table 3.4: Geometry of the MMB test specimen.

$L(\text{mm})$	$h(\text{mm})$	$a_0(\text{mm})$	$c(\text{mm})$	$B(\text{mm})$
51	1.56	33.7	60	25.4

The analytical solution for the MMB test consists of three parts based on the linear elastic beam theory (one part) and linear elastic fracture mechanics (two parts) (Mi et al., 1998). The beam theory provides the linear analytical solution,

$$\Delta = \frac{2}{3} \left(\frac{3c - L}{4L} \right) \frac{Pa_0^3}{EI}, \quad (3.53)$$

where I is the second moment of area and E is the elastic modulus. Next, the concept of the fracture energy based on linear elastic fracture mechanics (LEFM) provides the following load (P) versus displacement relationship (Δ),

$$\Delta = \frac{2P_I}{3EI} \left(\frac{8BEI}{8P_I^2/\phi_n + 3P_{II}^2/(8\phi_t)} \right)^{3/2} \quad (3.54)$$

where

$$P_I = (3c - L)P/(4L), \quad P_{II} = (c + L)P/L. \quad (3.55)$$

This expression is valid when a crack length (a) is smaller than the half length (L) of a beam ($a < L$). When a is greater than L , one obtains another expression:

$$\Delta = \frac{2}{3} \left(\frac{3c - L}{4L} \right) \frac{Pa^3}{EI}, \quad (3.56)$$

for the relationship between load (P) and displacement (Δ). For a given load and displacement, the a can be evaluated by solving following expression,

$$\left(\frac{8P_I^2}{\phi_n} + \frac{3P_{II}^2}{8\phi_t} - \frac{8P_IP_{II}}{\phi_t} \right) a^2 - \left(\frac{3P_{II}^2L}{2\phi_t} - \frac{8P_IP_{II}L}{\phi_t} \right) a + \frac{3P_{II}^2L^2}{2\phi_t} - 8BEI = 0. \quad (3.57)$$

Figure 3.19 compares the analytical solutions to the numerical results for the same fracture energy. The numerical simulation results converge to the analytical solutions with respect to the increase in the material cohesive strength. This is because the higher cohesive strength decreases the fracture process zone, and result in a more brittle failure.

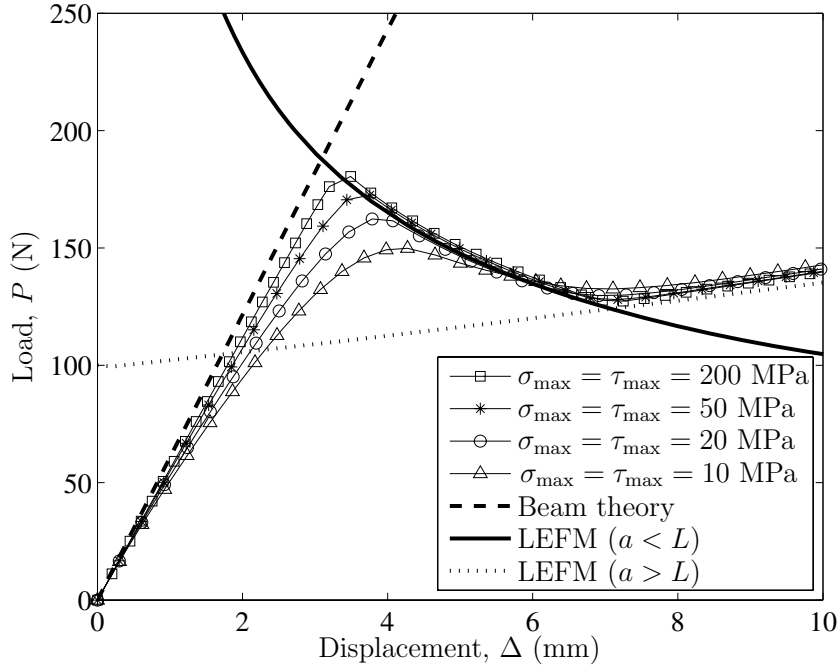
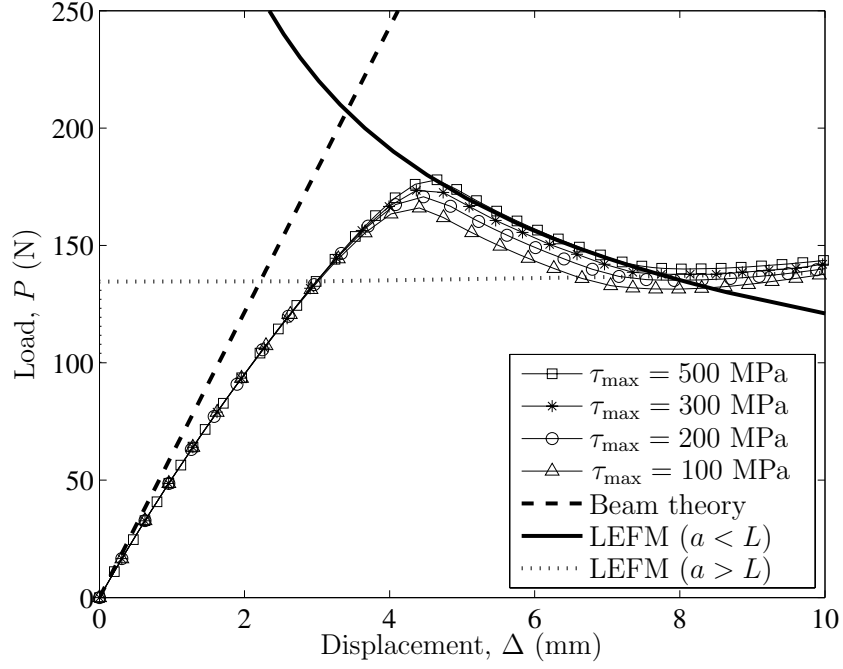
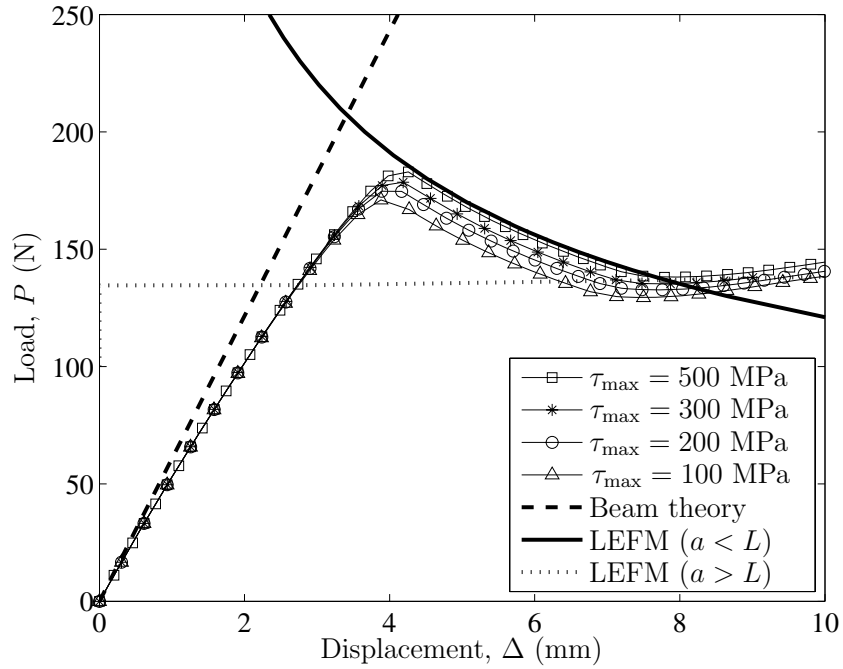


Figure 3.19: Comparison between the analytical solutions and the numerical simulation results considering the same fracture energy ($\phi_n = \phi_t = 1 \text{ N/mm}$).

Next, Figure 3.20 illustrates the agreement of the analytical solutions and the numerical simulation results for the different fracture energies in mode I and mode II. Mode I fracture energy is 1 N/mm and the mode II fracture energy increased to 2 N/mm . Due to the increase of the mode II fracture energy, the analytical solution of LEFM shifts upward (with respect to Figure 3.19) which represents a higher structural load capacity locally. In the simulations, the shear strength is increased from 100 MPa to 500 MPa with a fixed normal strength of 10 MPa (Figure 3.20(a)) and 20 MPa (Figure 3.20(b)). The increase of the normal and shear strength demonstrates the convergence to the analytical solutions of the beam theory and the LEFM.



(a)



(b)

Figure 3.20: Comparison between the analytical solutions and the numerical simulation results considering different fracture energies ($\phi_n = 1$ N/mm, $\phi_t = 2$ N/mm) (a) $\sigma_{\max} = 10$ MPa and (b) $\sigma_{\max} = 20$ MPa.

3.5 Concluding Remarks

The unified potential-based constitutive model (PPR) is proposed for cohesive fracture to characterize different fracture energies (ϕ_n, ϕ_t) and cohesive strengths ($\sigma_{\max}, \tau_{\max}$). The potential-based model is applicable to various material softening responses, i.e. plateau-type (e.g. ductile), brittle and quasi-brittle, due to controllable softening given by the shape parameters (α, β). The PPR model also includes initial slope indicators (λ_n, λ_t) to control elastic behavior, which can be selected as small values within numerical stability limits. The zero limit of the initial slope indicators leads to the potential function for extrinsic cohesive zone models. The cohesive interactions (T_n, T_t) are defined in a rectangular region associated with the final crack opening widths (δ_n, δ_t) and the conjugate final crack opening widths ($\bar{\delta}_n, \bar{\delta}_t$). The PPR potential-based model demonstrates that the work-of-separation depends on the separation paths, i.e. proportional and non-proportional paths, and monotonically changes from the mode I fracture energy to the mode II fracture energy with respect to the separation paths. The monotonic change of the work-of-separation demonstrates the consistency of the cohesive constitutive model. The numerical investigation of the mixed-mode bending test not only verifies the effect of different fracture energies (in modes I and II), but also demonstrates the convergence to the corresponding analytical solutions of beam theory and LEFM.

Chapter 4

Implementation of the PPR Potential-Based Cohesive Model

The PPR potential-based model is implemented within the framework of the Galerkin finite element method in conjunction with the intrinsic and extrinsic cohesive surface element approaches. For quasi-static fracture problems, the intrinsic cohesive zone model is employed through a user-defined element (UEL) subroutine of a commercial software, i.e. ABAQUS. For dynamic fracture problems, the extrinsic cohesive zone model is implemented by using a topological data structure TopS. The client-server approach of TopS is introduced in order to efficiently maintain consistent topology of a finite element mesh during adaptive mesh modification events. The central difference method (i.e. explicit) is utilized for time integration. The constitutive relationship of the PPR potential-based model is incorporated with unloading/reloading relations. Two unloading/reloading relationships are developed by introducing loading history indices. The chapter is organized as follows. Finite element formulation and time integration schemes are explained in Sections 4.1 and 4.2, respectively, for dynamic fracture simulation. Next, the client-server approach of TopS is presented in conjunction with application programming interface and callback functions in Section 4.3. Section 4.4 develops both coupled and uncoupled unloading/reloading relationships. Section 4.5 describes the systematic evaluation procedure of the cohesive traction vector and tangent matrix. Finally, simple mode I and II examples are provided for the verification of computational implementation.

4.1 Finite Element Formulation

Governing equations of fracture problems are solved by the Galerkin finite element method. A strong form is converted to a weak form through the principle of virtual work. The summation of the virtual strain energy and the virtual kinetic energy is equal to the sum of the virtual work done by external traction (\mathbf{T}^{ext}) and by cohesive

traction (\mathbf{T}^{coh}),

$$\int_{\Omega_0} (\delta \mathbf{E} : \mathbf{S} + \delta \mathbf{u} \cdot \rho_0 \ddot{\mathbf{u}}) d\Omega_0 = \int_{\Gamma_0} \delta \mathbf{u} \cdot \mathbf{T}^{ext} d\Gamma_0 + \int_{\Gamma_0} \delta \mathbf{\Delta} \cdot \mathbf{T}^{coh} d\Gamma_0, \quad (4.1)$$

where Ω_0 and Γ_0 are domain and boundary in the reference configuration, respectively. The 2nd Piola-Kirchhoff stress (\mathbf{S}) and the Green deformation strain (\mathbf{E}) are utilized. The superposed dots in $\ddot{\mathbf{u}}$ denotes the second time derivatives, \mathbf{u} is displacement vector, $\mathbf{\Delta}$ is displacement jump (or separation) across fracture surfaces, and ρ_0 is the material density. The weak form is discretized on the basis of the initial configuration, i.e. the total Lagrangian formulation.

4.2 Time Integration

The equation of motion without a damping term is expressed as

$$\mathbf{M}\ddot{\mathbf{u}} + \mathbf{K}\mathbf{u} = \mathbf{R}^{ext} \quad (4.2)$$

where \mathbf{M} and \mathbf{K} are the mass matrix and the stiffness matrix, respectively, and \mathbf{R}^{ext} is the external force vector. For cohesive fracture problems, \mathbf{K} consists of a continuum part (i.e. bulk element contribution) and a cohesive fracture part (i.e. cohesive surface element contribution). The stiffness matrix is decomposed as $\mathbf{K} = \mathbf{K}^b + \mathbf{K}^c$ where \mathbf{K}^b is the stiffness matrix of bulk elements and \mathbf{K}^c is the stiffness matrix of cohesive surface elements.

This equation of motion is solved by the Newmark algorithm (Newmark, 1959). The Newmark algorithm evaluates the displacement (\mathbf{u}_{n+1}) and velocity ($\dot{\mathbf{u}}_{n+1}$) at time $n+1$ on the basis of the displacement (\mathbf{u}_n), velocity ($\dot{\mathbf{u}}_n$) and acceleration ($\ddot{\mathbf{u}}_n$) at time n with the acceleration ($\ddot{\mathbf{u}}_{n+1}$) at time $n+1$, which are expressed as

$$\begin{aligned} \mathbf{u}_{n+1} &= \mathbf{u}_n + \Delta t \dot{\mathbf{u}}_n + \left(\frac{1}{2} - \beta\right) \Delta t^2 \ddot{\mathbf{u}}_n + \beta \Delta t^2 \ddot{\mathbf{u}}_{n+1} \\ \dot{\mathbf{u}}_{n+1} &= \dot{\mathbf{u}}_n + (1 - \gamma) \Delta t \ddot{\mathbf{u}}_n + \gamma \Delta t \ddot{\mathbf{u}}_{n+1} \end{aligned} \quad (4.3)$$

where parameters β and γ are associated with stability and accuracy of algorithm. The acceleration at time $n+1$ is obtained from the equation of motion

$$(\mathbf{M} + \beta \Delta t^2 \mathbf{K}) \ddot{\mathbf{u}}_{n+1} = \mathbf{R}_{n+1}^{ext} - \mathbf{K} \left(\mathbf{u}_n + \Delta t \dot{\mathbf{u}}_n + \left(\frac{1}{2} - \beta\right) \Delta t^2 \ddot{\mathbf{u}}_n \right). \quad (4.4)$$

In the Newmark algorithm, the kinetic energy (E_{kin}) and the strain energy (E_{int}) evolution between t_n and t_{n+1} is expressed (Krenk, 2006) as

$$\frac{1}{2} [\dot{\mathbf{u}}^T \mathbf{M} \dot{\mathbf{u}} + \mathbf{u}^T \mathbf{K}^b \mathbf{u}]_n^{n+1} = (\dot{\mathbf{u}}_{n+1} + \dot{\mathbf{u}}_n)^T \mathbf{M} (\dot{\mathbf{u}}_{n+1} - \dot{\mathbf{u}}_n) + (\mathbf{u}_{n+1} + \mathbf{u}_n)^T \mathbf{K}^b (\mathbf{u}_{n+1} - \mathbf{u}_n). \quad (4.5)$$

The substitution of Eq (4.3) into the energy evolution expression (4.5) leads to

$$\begin{aligned} \frac{1}{2} [\dot{\mathbf{u}}^T \mathbf{M} \dot{\mathbf{u}} + \mathbf{u}^T \mathbf{K}^b \mathbf{u}]_n^{n+1} &= (\dot{\mathbf{u}}_{n+1} + \dot{\mathbf{u}}_n)^T \mathbf{M} \left\{ \frac{\Delta t}{2} (\ddot{\mathbf{u}}_{n+1} + \ddot{\mathbf{u}}_n) + \left(\gamma - \frac{1}{2} \right) \Delta t (\ddot{\mathbf{u}}_{n+1} - \ddot{\mathbf{u}}_n) \right\} \\ &+ (\mathbf{u}_{n+1} + \mathbf{u}_n)^T \mathbf{K}^b \left\{ \frac{\Delta t}{2} (\dot{\mathbf{u}}_{n+1} + \dot{\mathbf{u}}_n) + \left(\beta - \frac{1}{2} \gamma \right) \Delta t^2 (\ddot{\mathbf{u}}_{n+1} - \ddot{\mathbf{u}}_n) \right\} \quad (4.6) \end{aligned}$$

Finally, one obtains the following energy variation expression

$$\begin{aligned} \frac{1}{2} [\dot{\mathbf{u}}^T \mathbf{M} \dot{\mathbf{u}} + \mathbf{u}^T \mathbf{K}^b \mathbf{u}]_n^{n+1} &= \frac{1}{2} (\mathbf{u}_{n+1} - \mathbf{u}_n)^T (\mathbf{R}_{n+1}^{\text{ext}} + \mathbf{R}_n^{\text{ext}}) - \frac{1}{2} (\mathbf{u}_{n+1} - \mathbf{u}_n)^T (\mathbf{K}^c \mathbf{u}_{n+1} + \mathbf{K}^c \mathbf{u}_n) \\ &+ \frac{\Delta t}{2} \left(\gamma - \frac{1}{2} \right) (\dot{\mathbf{u}}_{n+1} + \dot{\mathbf{u}}_n)^T \mathbf{M} (\ddot{\mathbf{u}}_{n+1} - \ddot{\mathbf{u}}_n) - \frac{\Delta t^2}{2} \left(\beta - \frac{1}{2} \gamma \right) (\ddot{\mathbf{u}}_{n+1} - \ddot{\mathbf{u}}_n)^T \mathbf{M} (\ddot{\mathbf{u}}_{n+1} + \ddot{\mathbf{u}}_n) \quad (4.7) \end{aligned}$$

by substituting the equation of motion (4.2) and the Eq (4.3) into the Eq (4.6). The first term on the right hand side is the external work (E_{ext}) between the time steps, and the second term is associated to the fracture energy (E_{fra}). The remaining two terms are zero for the case of $\gamma = 1/2$ and $\beta = 1/4$, which leads to the energy conservation in the time incrementation from n to $n + 1$. For the central difference method (i.e. $\gamma = 1/2$ and $\beta = 0$), the last term contributes to the total energy. However, this contribution is not significant if one selects smaller time step, which is discussed in Chapter 7.

In this study, the central difference method is employed for time integration of elasto-dynamic fracture problems, i.e. explicit method (Belytschko et al., 2000). The outline of the explicit time integration for the extrinsic cohesive zone model is described in Algorithm 4.1. First, the displacement (\mathbf{u}), velocity ($\dot{\mathbf{u}}$) and acceleration ($\ddot{\mathbf{u}}$) vectors are initialized, and the current displacement vector is obtained from the previous time step information. Then, one checks the insertion of cohesive elements based on an external criterion. For instance, Ortiz and Pandolfi (1999) inserted cohesive elements when an effective traction is greater than the cohesive strength, and Belytschko et al. (2003) employed the loss of hyperbolicity for an initiation criterion. In the current study, cohesive elements are adaptively inserted when the averaged normal traction is greater than the cohesive strength (σ_{max}).

After the insertion of cohesive elements, the external nodal force vector ($\mathbf{R}_{n+1}^{\text{ext}}$) and the internal nodal force vector ($\mathbf{R}_{n+1}^{\text{int}}$) are evaluated. The constitutive relationship

Algorithm 4.1 Explicit time integration for the extrinsic cohesive zone model.

Initialization: displacements (\mathbf{u}_0), velocity ($\dot{\mathbf{u}}_0$), acceleration ($\ddot{\mathbf{u}}_0$)
for $n = 0$ to n_{\max} **do**
 Update displacement: $\mathbf{u}_{n+1} = \mathbf{u}_n + \Delta t \dot{\mathbf{u}}_n + \Delta t^2 / 2 \ddot{\mathbf{u}}_n$
 Check the insertion of cohesive elements
 Update acceleration: $\ddot{\mathbf{u}}_{n+1} = \mathbf{M}^{-1}(\mathbf{R}_{n+1}^{ext} + \mathbf{R}_{n+1}^{coh} - \mathbf{R}_{n+1}^{int})$
 Update velocity: $\dot{\mathbf{u}}_{n+1} = \dot{\mathbf{u}}_n + \Delta t / 2 (\ddot{\mathbf{u}}_n + \ddot{\mathbf{u}}_{n+1})$
 Update boundary conditions
end for

of volumetric elements is assumed to be elastic. The cohesive force vector (\mathbf{R}_{n+1}^{coh}) is obtained by integrating the traction along cohesive surface elements. The traction is first set to be equivalent to the traction along the edge at the time of the cohesive element insertion. In the following time steps, the cohesive traction is evaluated on the basis of the PPR potential-based constitutive model. Alternatively, one can enforce \mathbf{R}_{n+1}^{coh} at the time of activation so that the acceleration of a duplicated node is equal to an original node (Papoulia et al., 2003). However, this approach can result in the violation of the conditions of $\text{sgn}(T_n) = \text{sgn}(\Delta_n)$ and $\text{sgn}(T_t) = \text{sgn}(\Delta_t)$, called traction locking (Papoulia et al., 2003). The lumped mass matrix (\mathbf{M}) is obtained by considering diagonal terms of the consistent mass matrix and scaling them to preserve the total mass (Hughes, 2000), which produces positive lumped masses. Finally, the nodal acceleration, velocity and boundary conditions are updated for the current time step.

4.3 Topological Data Structure

For an adaptive analysis environment, especially for the extrinsic cohesive zone model, classical finite element mesh representation, which consists of node table and element incidence, is not adequate because of the limited topological information available to handle adjacency relationship (Beall and Shephard, 1997; Celes et al., 2005a). In order to obtain efficient handling of adjacency relationship, this study utilizes a topology-based data structure, called TopS (Celes et al., 2005a,b). TopS is based on topological entities, i.e. node, element, vertex, edge and facet. Nodes and elements are *explicit* entities which are directly stored, while facets, edges and vertices are *implicit* entities which are derived on the basis of element templates. TopS is able to obtain adjacency information and to manage a consistent data structure in time proportional to the number of retrieved entities (Paulino et al., 2008). Furthermore,

in order to maintain a consistent data structure when modification events occur, the client-server approach is employed.

4.3.1 Client-Server Approach

TopS is a topological data structure for finite element mesh representation. It provides the geometric and topological support needed by numerical analysis applications, including adaptive simulations such as the insertion of a cohesive element, and edge-swap, edge-split and vertex-removal operators. One of the main advantages of using TopS to support an analysis application consists of decoupling a computational mechanics code from data representation and management codes. As a consequence, developers of analysis applications can focus uniquely on the mechanics, relying on an external library for mesh representation.

In this way, TopS is seen as a *service provider*: it provides all the functionality needed by the analysis application for mesh representation and management. The analysis application represents the *client* that uses the services provided by TopS. This scheme is illustrated in Figure 4.1. The client application invokes TopS using the TopS application programming interface (API). The TopS API consists of a large set of functions that the analysis code uses to set up the model, to attach the necessary attributes, and to query/update the stored information. TopS eventually needs to invoke functions, named *callbacks*, of the client side in order to notify the occurrence of events related to mesh modification.

In summary, TopS is responsible for managing the geometry and topology information. When the client application modifies the mesh, TopS ensures geometry and topology consistency. However, TopS has no knowledge regarding the properties attached to the model. The client application is responsible for maintaining the

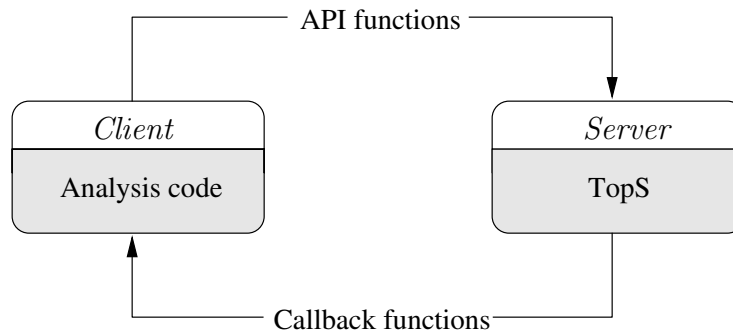


Figure 4.1: Client-server architecture.

consistency of property information. The properties are represented by attributes attached to the topological entities. Whenever the mesh is modified, the client application has to update the attributes accordingly.

4.3.2 API and Callback functions

The client application creates a model, and then modifies it by calling the functions provided by the TopS API. The TopS API is composed by a large set of functions that allow the client to create, destroy, or modify the model and its topological entities. Whenever creating, destroying or modifying a mesh, the client application has to consistently manage the attributes attached to the affected entities. The TopS API provides functions that directly modify the mesh. When using these functions, the client can update the attributes associated with the affected topological entities directly, just after invoking the function. For example, let us consider a function to insert a new node in the model. Let us also consider that a node attribute (e.g., `NodeAttrib` type) has to be associated with each node of the model. After inserting a new node, the client application is responsible for updating the node attribute accordingly. A typical excerpt of the client code in such a situation is (using the C API):

```
TopNode node;
NodeAttrib nAtt;
. . .
node = topModel_InsertNode (x, y, z);
nAtt = (NodeAttrib*) malloc (sizeof (NodeAttrib));
topNode_SetAttrib (model, node, nAtt);
. . .
```

In this case, managing the attributes is simple because the `topModel_InsertNode` function modifies a single entity in the mesh, the newly created node, and returns a reference to it. Thus, the client gets the returned reference and attaches the corresponding attribute.

However, in a few situations, the attribute managing cannot be done so straightforwardly because some API functions, when invoked, affect a variable number of topological entities. Let us consider the function that inserts a cohesive element in the mesh. The insertion of a cohesive element may require the duplication of nodes. Whether a node has to be duplicated or not depends on the topological classification of the fractured facet (Paulino et al., 2008). The client application cannot know in

advance how many and which nodes will be duplicated. In such cases, the callback mechanism is very handy, while executing the function that inserts a new cohesive element, whenever a node is duplicated, TopS calls back a function in the client application side. This client function, named callback function, is responsible for managing the attributes associated to the affected entities (in this case, the old and the new created nodes).

4.4 Unloading and Reloading Relationships

The unloading/reloading relationship is an important issue for mixed-mode fracture problems because a crack may close depending on a loading path. If one does not consider the unloading/reloading relationships, for example, the cohesive traction (T_n) would increase with respect to closing a crack opening width (Δ_n), as illustrated in Figure 4.2 (Path ①). Thus, there is no permanent dissipation if one does not consider the unloading/reloading relationships in the potential-based model. Because of such non-physical behavior, computational simulation may provide non-convergent results, or misleading simulation results. In this section, two unloading/reloading models (coupled and uncoupled) for the PPR potential-based model are developed in order to represent permanent dissipation, i.e. the non-conservative energy of fracture.

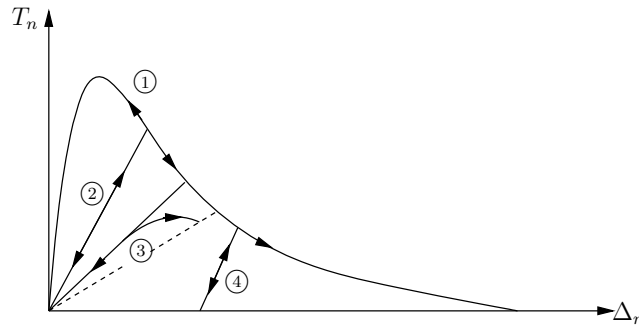


Figure 4.2: One-dimensional cohesive law and its unloading/reloading paths.

Previously, Camacho and Ortiz (1996) proposed a cohesive zone model with linear to origin unloading/reloading relationships (Path ② in Figure 4.2). An unloading/reloading function is defined by using an effective displacement. Ortiz and Pandolfi (1999) utilized the linear to origin unloading/reloading model for three-dimensional crack propagation analysis, and de Andres et al. (1999) extended the linear to origin model to the one-dimensional exponential cohesive zone model for fatigue crack growth analysis. The early work in Ortiz's group was revisited by Nguyen

et al. (2001) who presented a linear to origin unloading and a nonlinear reloading model (Path ③ in Figure 4.2). Deshpande et al. (2001, 2002) employed unloading/reloading paths, which were linear but not towards the origin (Path ④ in Figure 4.2), for mode I fatigue crack propagation. Roe and Siegmund (2003) extended the model to investigate mixed-mode crack growth behavior.

4.4.1 Coupled Unloading/Reloading Model

The coupled unloading/reloading model is developed by introducing a coupled loading history index,

$$\eta(\Delta_n, \Delta_t) = \sqrt{\Delta_n^2 + \Delta_t^2} . \quad (4.8)$$

Based on the loading history index (η), the unloading/reloading criterion is evaluated in conjunction with the maximum loading history index, defined as

$$\eta_{\max} = \sqrt{\Delta_{n_{\max}}^2 + |\Delta_{t_{\max}}|^2} , \quad (4.9)$$

where $\Delta_{n_{\max}}$ and $|\Delta_{t_{\max}}|$ are the maximum normal and tangential separations, respectively, in loading history. When the maximum loading history index (η_{\max}) is smaller than the (current) loading history index (i.e. $\eta > \eta_{\max}$), the current state of separations represents the loading condition, i.e. *softening* occurs. If η_{\max} is greater than η ($\eta < \eta_{\max}$), material locally experiences *unloading/reloading* condition. Since the unloading/reloading condition is governed by the loading history index, the unloading/reloading region is designated within a circle whose radius is η_{\max} ($\eta = \sqrt{\Delta_n^2 + \Delta_t^2} < \eta_{\max}$).

Within the unloading/reloading region, the traction-separation relationships are defined as

$$T_n^v(\Delta_n, \Delta_t) = T_n(\Delta_n^v, \Delta_t^v) \left(\frac{\eta}{\eta_{\max}} \right)^{\alpha_v} , \quad T_t^v(\Delta_n, \Delta_t) = T_t(\Delta_n^v, \Delta_t^v) \left(\frac{\eta}{\eta_{\max}} \right)^{\beta_v} \quad (4.10)$$

where

$$\Delta_n^v = \Delta_n \frac{\eta_{\max}}{\eta} , \quad \Delta_t^v = \Delta_t \frac{\eta_{\max}}{\eta} . \quad (4.11)$$

Notice that the variables Δ_n^v and Δ_t^v satisfy the condition of $\sqrt{\Delta_n^{v2} + \Delta_t^{v2}} = \eta_{\max}$, and thus Δ_n^v and Δ_t^v correspond to the separations on the boundary of the unloading/reloading region. The values of $T_n(\Delta_n^v, \Delta_t^v)$ and $T_t(\Delta_n^v, \Delta_t^v)$ (e.g. gray solids in Figure 4.3) represent the tractions on the boundary of the unloading/reloading region.

The normal and tangential unloading/reloading relations (Eq. 4.10) are obtained from the multiplication $(\eta/\eta_{\max})^{\alpha_v}$ and $(\eta/\eta_{\max})^{\beta_v}$ of $T_n(\Delta_n^v, \Delta_t^v)$ and $T_t(\Delta_n^v, \Delta_t^v)$, respectively, which interpolates between the unloading/reloading boundaries and the origin (e.g. black solids in Figure 4.3). Because of $0 \leq (\eta/\eta_{\max}) \leq 1$, the normal cohesive traction (T_n^v) is monotonic and bounded between 0 and $T_n(\Delta_n^v, \Delta_t^v)$, and the tangential cohesive traction (T_t^v) is also monotonic and bounded between 0 and $T_t(\Delta_n^v, \Delta_t^v)$. The cohesive tractions of the coupled unloading/reloading model (T_n^v , T_t^v) are the same as the traction obtained by the PPR model (T_n , T_t) when the loading history index equals the maximum loading history index ($\eta = \eta_{\max}$). This fact satisfies the continuity condition along the boundary of the unloading/reloading region, i.e. $T_n^v = T_n$ and $T_t^v = T_t$. In addition, the exponents α_v and β_v describe the shape of unloading/reloading surface along the radial direction. When an exponent value is equal to one, the unloading/reloading function is linear along the radial direction (e.g. Figure 4.3(a)). If an exponent is greater or smaller than one, the shape is convex or concave, respectively.

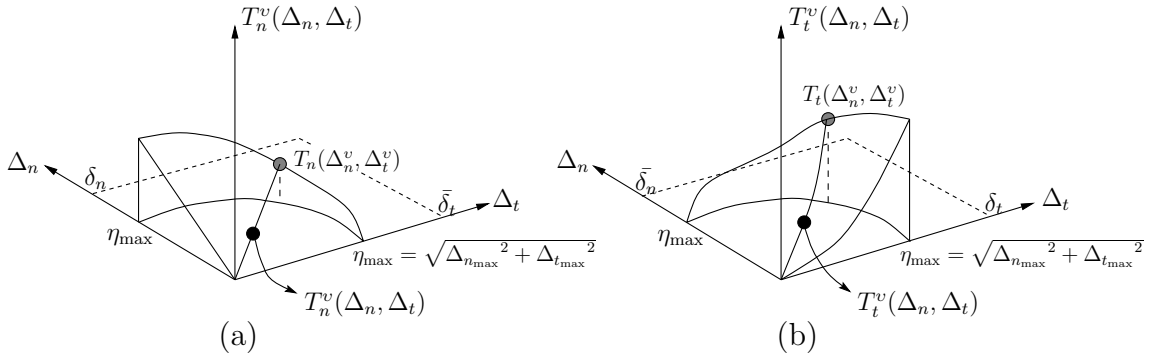


Figure 4.3: Schematics of the coupled unloading/reloading model: (a) normal interaction and (b) tangential interaction.

Figure 4.4 compares the cohesive interactions calculated from the intrinsic PPR potential with the cohesive interactions obtained from the coupled unloading/reloading model. The PPR potential-based model is plotted with $\phi_n = 100$ N/m, $\phi_t = 200$ N/m, $\sigma_{\max} = 40$ MPa, $\tau_{\max} = 30$ MPa, $\alpha = 5$, $\beta = 1.3$, $\lambda_n = 0.1$, and $\lambda_t = 0.15$. In the coupled unloading/reloading model, the maximum normal separation ($\Delta_{n_{\max}}$) and the maximum tangential separation ($|\Delta_t|_{\max}$) are arbitrarily selected as $0.3\delta_n$ and $0.2\delta_t$, respectively. The unloading/reloading shape parameters α_v and β_v are chosen as 0.4 and 4. The normal unloading/reloading interactions demonstrate the concave shape (e.g. $\alpha_v = 0.4$) while the unloading/reloading tangential relation illustrates the convex shape (e.g. $\beta_v = 4$). Both normal and tangential unload-

ing/reloading tractions are defined within the same unloading/reloading region (e.g. $\sqrt{\Delta_n^2 + \Delta_t^2} \leq \sqrt{0.3\delta_n^2 + 0.2\delta_t^2} = \eta_{\max}$).

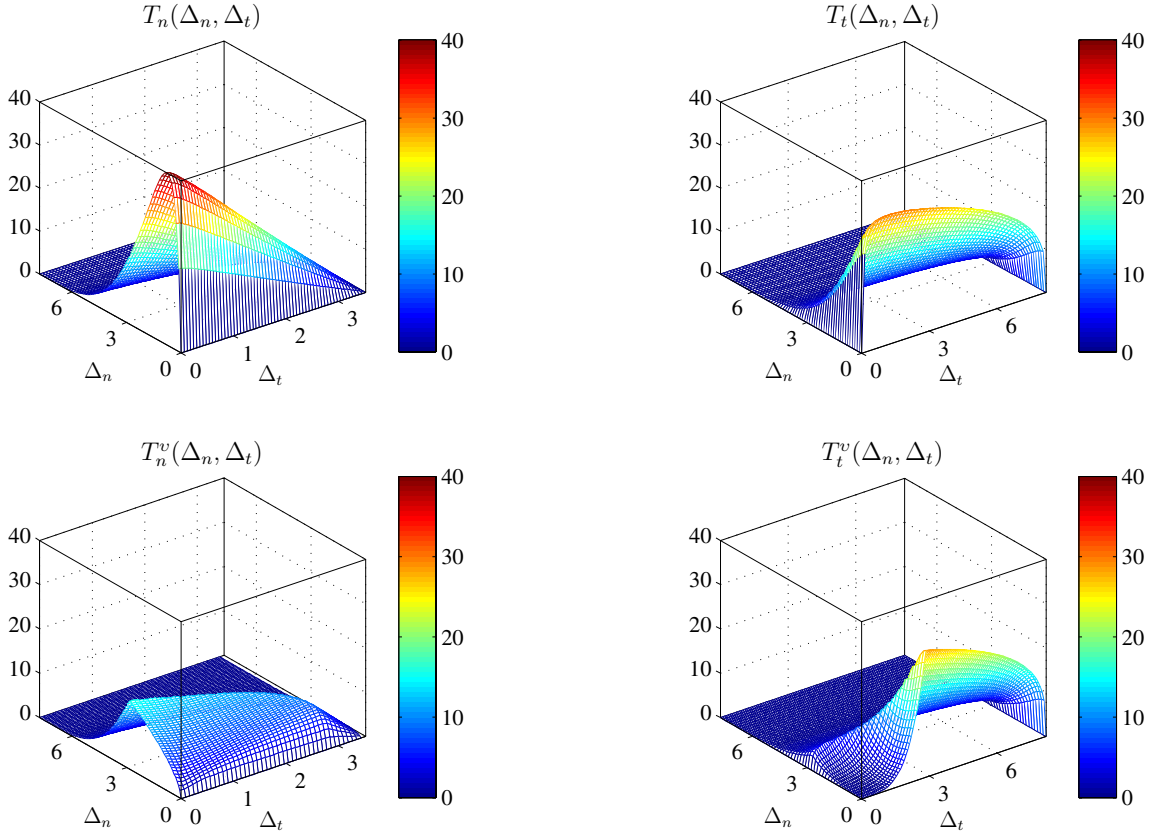


Figure 4.4: Comparison between the softening relationships obtained by the potential and the coupled unloading/reloading relationship with the maximum loading history index of $\eta_{\max} = \sqrt{0.3\delta_n^2 + 0.2\delta_t^2}$.

4.4.2 Uncoupled Unloading/Reloading Model

The uncoupled unloading/reloading model is based on two independent uncoupled loading history indices: one associated with the normal cohesive traction, and the other related to the tangential cohesive traction. For the normal cohesive interaction, a normal loading history index (η_n) is defined as the normal separation (Δ_n), and the normal maximum loading history index is given as $\eta_{n_{\max}} = \Delta_{n_{\max}}$. If the current normal loading history index is greater than the normal maximum loading history index ($\eta_n > \eta_{n_{\max}}$), the current separation state represents the softening condition. When $\eta_n < \eta_{n_{\max}}$, the normal cohesive interactions are evaluated by the uncoupled

unloading/reloading model. Therefore, the normal unloading/reloading model is defined within a rectangular domain ($0 \leq \Delta_n \leq \eta_{n_{\max}}$ and $|\Delta_t| \leq \bar{\delta}_t$), called the normal unloading/reloading region.

Similarly, the tangential unloading/reloading criterion is evaluated by introducing the tangential loading history index ($\eta_t = |\Delta_t|$) and the tangential maximum loading history index ($\eta_{t_{\max}} = |\Delta_t|_{\max}$). If the current separation is larger than the tangential maximum loading history index ($\eta_t > \eta_{t_{\max}}$), one expects the softening behavior. On the other hand, $\eta_t < \eta_{t_{\max}}$ represents the unloading/reloading condition. The tangential unloading/reloading model is defined within a rectangular region ($0 \leq \Delta_n \leq \bar{\delta}_n$ and $|\Delta_t| \leq \eta_{t_{\max}}$), called the tangential unloading/reloading region. As a result, the normal and tangential unloading/reloading criteria and regions are independently evaluated in the uncoupled unloading/reloading model.

The normal and tangential tractions of the uncoupled unloading/reloading model are defined as

$$T_n^v(\Delta_n, \Delta_t) = T_n(\eta_{n_{\max}}, \Delta_t) \left(\frac{\eta_n}{\eta_{n_{\max}}} \right)^{\alpha_v}, \quad T_t^v(\Delta_n, \Delta_t) = T_t(\Delta_n, \eta_{t_{\max}}) \left(\frac{\eta_t}{\eta_{t_{\max}}} \right)^{\beta_v}. \quad (4.12)$$

Notice that $T_n(\eta_{n_{\max}}, \Delta_t)$ and $T_t(\Delta_n, \eta_{t_{\max}})$ correspond to the normal and tangential tractions along the boundary of the unloading/reloading regions, respectively (e.g. gray solids in Figure 4.5). The cohesive interactions of the uncoupled unloading/reloading model (e.g. black solids in Figure 4.5) are obtained by multiplying $T_n(\eta_{n_{\max}}, \Delta_t)$ and $T_t(\Delta_n, \eta_{t_{\max}})$ by $(\eta_n/\eta_{n_{\max}})^{\alpha_v}$ and $(\eta_t/\eta_{t_{\max}})^{\beta_v}$, respectively. As a result, the normal and tangential cohesive interactions vary monotonically from zero to $T_n(\eta_{n_{\max}}, \Delta_t)$ and $T_t(\Delta_n, \eta_{t_{\max}})$, respectively, which satisfy the continuity condition.

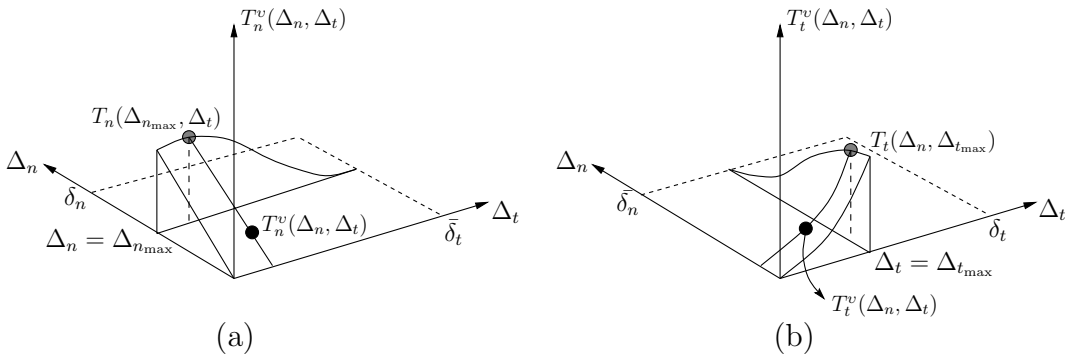


Figure 4.5: Schematics of the uncoupled unloading/reloading model: (a) normal interaction and (b) tangential interaction.

Figure 4.6 demonstrates the comparison between the softening behavior and the uncoupled unloading/reloading behavior. The fracture parameters are the same as the parameters in Figure 4.4. The normal unloading/reloading region is defined within $0 \leq \Delta_n \leq 0.3\delta_n$ and $0 \leq \Delta_t \leq \bar{\delta}_t$, and the tangential unloading/reloading region is assigned within $0 \leq \Delta_n \leq \bar{\delta}_n$ and $0 \leq \Delta_t \leq 0.2\delta_t$. Within the unloading/reloading regions, the normal unloading/reloading cohesive interaction illustrates concave shape while the tangential unloading/reloading cohesive interaction demonstrates convex shape.

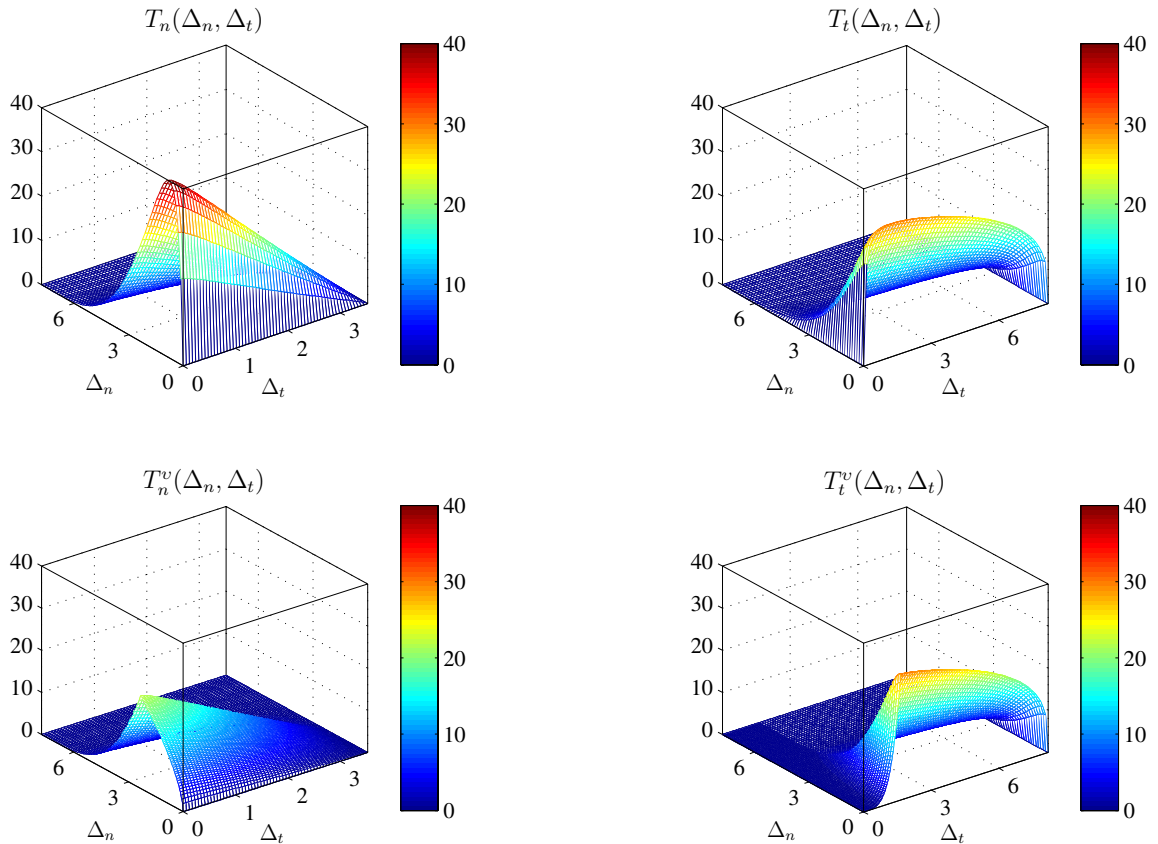


Figure 4.6: Comparison between the softening relationships obtained by the potential and the coupled unloading/reloading relationship with the maximum loading history indices of $\eta_{n_{\max}} = 0.3\delta_n$ and $\eta_{t_{\max}} = 0.2\delta_t$.

4.4.3 Remarks

The two unloading/reloading models (coupled and uncoupled) are proposed by introducing the loading history index and the maximum loading history index. Table 4.1

summarizes the two unloading/reloading models. The coupled loading history index is similar to the effective displacement (Eq. (1.2)) in the one-dimensional potential-based model (Tvergaard and Hutchinson, 1993). The uncoupled loading history indices are conceptually the same as the unloading/reloading model by Deshpande et al. (2001) and Roe and Siegmund (2003). Both coupled and uncoupled models provide the same unloading/reloading criteria. When the (current) loading history index is smaller than the maximum loading history index, the cohesive interaction follows the unloading/reloading model. The unloading/reloading constitutive relations are obtained by interpolating the normal and tangential cohesive tractions from the unloading/reloading boundary to the origin. The coupled unloading/reloading model provides the same unloading/reloading region for both normal and tangential tractions, while the uncoupled unloading/reloading model results in the different unloading/reloading regions for the normal and tangential tractions.

Table 4.1: Comparison between the coupled unloading/reloading and the uncoupled unloading/reloading.

	Coupled Unloading/Reloading	Uncoupled Unloading/Reloading
Loading history index	$\eta(\Delta_n, \Delta_t) = \sqrt{\Delta_n^2 + \Delta_t^2}$	$\eta_n = \Delta_n$ $\eta_t = \Delta_t $
Max. loading history index	$\eta_{\max} = \sqrt{\Delta_{n_{\max}}^2 + \Delta_{t_{\max}}^2}$	$\eta_{n_{\max}} = \Delta_{n_{\max}}$ $\eta_{t_{\max}} = \Delta_{t_{\max}} $
Criterion	$\eta < \eta_{\max}$	$\eta_n < \eta_{n_{\max}}$ $\eta_t < \eta_{t_{\max}}$
Constitutive relationship	$T_n^v(\Delta_n, \Delta_t) = T_n(\Delta_n^v, \Delta_t^v) \left(\frac{\eta}{\eta_{\max}} \right)^{\alpha_v}$ $T_t^v(\Delta_n, \Delta_t) = T_t(\Delta_n^v, \Delta_t^v) \left(\frac{\eta}{\eta_{\max}} \right)^{\beta_v}$	$T_n^v(\Delta_n, \Delta_t) = T_n(\eta_{n_{\max}}, \Delta_t) \left(\frac{\eta_n}{\eta_{n_{\max}}} \right)^{\alpha_v}$ $T_t^v(\Delta_n, \Delta_t) = T_t(\Delta_n, \eta_{t_{\max}}) \left(\frac{\eta_t}{\eta_{t_{\max}}} \right)^{\beta_v}$
Normal region		
Tangential region		

4.5 Constitutive Relationships

The constitutive relationship of the PPR potential-based model is evaluated by considering four conditions: softening, unloading/reloading, contact and complete failure. These conditions are determined on the basis of the softening region and the loading history index.

4.5.1 Determination of Cohesive Interaction Region

The cohesive interaction (softening) region is associated with the length scales: the final crack opening widths (δ_n, δ_t) and the conjugate final crack opening widths ($\bar{\delta}_n, \bar{\delta}_t$), as discussed in Chapter 3. The softening region of the normal cohesive traction is defined as $0 \leq \Delta_n \leq \delta_n$ and $-\bar{\delta}_t \leq \Delta_t \leq \bar{\delta}_t$ while the softening region of the tangential cohesive traction is defined as $0 \leq \Delta_n \leq \bar{\delta}_n$ and $-\delta_t \leq \Delta_t \leq \delta_t$. For the intrinsic cohesive zone model, the normal and tangential final crack opening widths are determined by the closed form (Eq. (3.36)), while the conjugate final crack opening widths are calculated by solving the nonlinear equations (Eqs. (3.37) and (3.38)).

The nonlinear equations can be solved by a root-finding algorithm, such as the Bisection method and the Newton-Raphson method. Alternatively, the softening region is defined without solving the nonlinear equation. The necessary and sufficient conditions of $(-\bar{\delta}_t \leq \Delta_t \leq \bar{\delta}_t)$, which is associated with the normal softening region, are $((-\delta_t \leq \Delta_t \leq \delta_t) \& (T_n(\Delta_n, \Delta_t) \geq 0))$. This is because the tangential conjugate final crack opening width is unique between zero and the tangential final crack opening width and because the normal cohesive traction is positive within the normal softening region. Similarly, one replaces $(0 \leq \Delta_n \leq \bar{\delta}_n)$ by $((0 \leq \Delta_n \leq \delta_n) \& (T_t(\Delta_n, |\Delta_t|) \geq 0))$ because $\bar{\delta}_n$ is unique between 0 and δ_n , and because the tangential traction is positive within the tangential softening region. Notice that, for the extrinsic cohesive zone model, both final crack opening widths (δ_n, δ_t) and conjugate final crack opening widths ($\bar{\delta}_n, \bar{\delta}_t$) are calculated by the closed forms, i.e. Eqs. (3.42) and (3.43), respectively.

4.5.2 Cohesive Traction Vector and Tangent Matrix

The cohesive traction vector and the material tangent stiffness matrix are evaluated by accounting for four cases: softening, unloading/reloading, contact and complete failure conditions. Algorithm 4.2 outlines the constitutive relationships with respect

to the four cases. Notice that the normal and tangential cohesive interactions are evaluated independently.

First, when separations are within the softening region and when the current loading history index is greater than the maximum loading history index, called the *softening condition*, the cohesive relationships are derived from the PPR potential. If both normal and tangential separations are in the softening condition, the cohesive tractions are evaluated by the expression (3.28) for the intrinsic cohesive zone model or by the expression (3.40) for the extrinsic cohesive zone model. The second derivative of the PPR potential leads to the material tangent stiffness matrix,

$$\mathbf{D}(\Delta_n, \Delta_t) = \begin{bmatrix} D_{nn} & D_{nt} \\ D_{tn} & D_{tt} \end{bmatrix} = \begin{bmatrix} \partial^2 \Psi / \partial \Delta_n^2 & \partial^2 \Psi / \partial \Delta_n \partial \Delta_t \\ \partial^2 \Psi / \partial \Delta_t \partial \Delta_n & \partial^2 \Psi / \partial \Delta_t^2 \end{bmatrix}, \quad (4.13)$$

Algorithm 4.2 Outline of the constitutive relationship for the four conditions: softening, unloading/reloading, contact and complete failure.

```

// Normal cohesive interaction:
if ( $\Delta_n \leq 0$ ) then // Contact
     $T_n = D_{nn} \Delta_n$ ,  $D_{nn} = \alpha_p$ ,  $D_{nt} = \alpha_p$ 
else if ( $(0 \leq \Delta_n \leq \delta_n) \ \& \ (|\Delta_t| \leq \bar{\delta}_t) \ \& \ (\eta \geq \eta_{\max})$ ) then // Softening
     $T_n = \frac{\partial \Psi(\Delta_n, \Delta_t)}{\partial \Delta_n}$ ,  $D_{nt} = \frac{\partial^2 \Psi(\Delta_n, \Delta_t)}{\partial \Delta_n^2}$ ,  $D_{nt} = \frac{\partial^2 \Psi(\Delta_n, \Delta_t)}{\partial \Delta_n \partial \Delta_t}$ 
else if ( $(0 \leq \Delta_n \leq \delta_n) \ \& \ (|\Delta_t| \leq \bar{\delta}_t) \ \& \ (\eta < \eta_{\max})$ ) then // Unloading/reloading
     $T_n = T_n^v(\Delta_n, \Delta_t)$ ,  $D_{nn} = \frac{\partial T_n^v(\Delta_n, \Delta_t)}{\partial \Delta_n}$ ,  $D_{nt} = \frac{\partial T_n^v(\Delta_n, \Delta_t)}{\partial \Delta_t}$ 
else if ( $(\Delta_n > \delta_n) \ | \ (|\Delta_t| > \bar{\delta}_t)$ ) then // Complete failure
     $T_n = 0$ ,  $D_{nn} = 0$ ,  $D_{nt} = 0$ 
end if

// Tangential cohesive interaction:
if ( $\Delta_n \leq 0$ ) then // Contact
     $\Delta_n = 0$ 
end if
if ( $(0 \leq \Delta_n \leq \bar{\delta}_n) \ \& \ (|\Delta_t| \leq \delta_t) \ \& \ (\eta \geq \eta_{\max})$ ) then // Softening
     $T_t = \frac{\partial \Psi(\Delta_n, \Delta_t)}{\partial \Delta_t}$ ,  $D_{tn} = \frac{\partial^2 \Psi(\Delta_n, \Delta_t)}{\partial \Delta_t \partial \Delta_n}$ ,  $D_{tt} = \frac{\partial^2 \Psi(\Delta_n, \Delta_t)}{\partial \Delta_t^2}$ 
else if ( $(0 \leq \Delta_n \leq \bar{\delta}_n) \ \& \ (|\Delta_t| \leq \delta_t) \ \& \ (\eta < \eta_{\max})$ ) then // Unloading/reloading
     $T_t = T_t^v(\Delta_n, \Delta_t)$ ,  $D_{tn} = \frac{\partial T_t^v(\Delta_n, \Delta_t)}{\partial \Delta_n}$ ,  $D_{tt} = \frac{\partial T_t^v(\Delta_n, \Delta_t)}{\partial \Delta_t}$ 
else if ( $(\Delta_n > \bar{\delta}_n) \ | \ (|\Delta_t| > \delta_t)$ ) then // Complete failure
     $T_t = 0$ ,  $D_{tn} = 0$ ,  $D_{tt} = 0$ 
end if

```

where the components of the matrix are given as

$$\begin{aligned}
D_{nn} &= \frac{\Gamma_n}{\delta_n^2} \left[(m^2 - m) \left(1 - \frac{\Delta_n}{\delta_n}\right)^\alpha \left(\frac{m}{\alpha} + \frac{\Delta_n}{\delta_n}\right)^{m-2} + (\alpha^2 - \alpha) \left(1 - \frac{\Delta_n}{\delta_n}\right)^{\alpha-2} \left(\frac{m}{\alpha} + \frac{\Delta_n}{\delta_n}\right)^m \right. \\
&\quad \left. - 2\alpha m \left(1 - \frac{\Delta_n}{\delta_n}\right)^{\alpha-1} \left(\frac{m}{\alpha} + \frac{\Delta_n}{\delta_n}\right)^{m-1} \right] \left[\Gamma_t \left(1 - \frac{\Delta_t}{\delta_t}\right)^\beta \left(\frac{n}{\beta} + \frac{\Delta_t}{\delta_t}\right)^n + \langle \phi_t - \phi_n \rangle \right], \\
D_{nt} &= \frac{\Gamma_n \Gamma_t}{\delta_n \delta_t} \left[m \left(1 - \frac{\Delta_n}{\delta_n}\right)^\alpha \left(\frac{m}{\alpha} + \frac{\Delta_n}{\delta_n}\right)^{m-1} - \alpha \left(1 - \frac{\Delta_n}{\delta_n}\right)^{\alpha-1} \left(\frac{m}{\alpha} + \frac{\Delta_n}{\delta_n}\right)^m \right] \\
&\quad \left[n \left(1 - \frac{\Delta_t}{\delta_t}\right)^\beta \left(\frac{n}{\beta} + \frac{\Delta_t}{\delta_t}\right)^{n-1} - \beta \left(1 - \frac{\Delta_t}{\delta_t}\right)^{\beta-1} \left(\frac{n}{\beta} + \frac{\Delta_t}{\delta_t}\right)^n \right], \\
D_{tn} &= D_{nt}, \\
D_{tt} &= \frac{\Gamma_t}{\delta_t^2} \left[(n^2 - n) \left(1 - \frac{\Delta_t}{\delta_t}\right)^\beta \left(\frac{n}{\beta} + \frac{\Delta_t}{\delta_t}\right)^{n-2} + (\beta^2 - \beta) \left(1 - \frac{\Delta_t}{\delta_t}\right)^{\beta-2} \left(\frac{n}{\beta} + \frac{\Delta_t}{\delta_t}\right)^n \right. \\
&\quad \left. - 2\beta n \left(1 - \frac{\Delta_t}{\delta_t}\right)^{\beta-1} \left(\frac{n}{\beta} + \frac{\Delta_t}{\delta_t}\right)^{n-1} \right] \left[\Gamma_n \left(1 - \frac{\Delta_n}{\delta_n}\right)^\alpha \left(\frac{m}{\alpha} + \frac{\Delta_n}{\delta_n}\right)^m + \langle \phi_n - \phi_t \rangle \right] \quad (4.14)
\end{aligned}$$

for the intrinsic cohesive zone model. In this case, one obtains the symmetric tangent stiffness matrix. Notice that the tangent stiffness matrix is not necessary for the explicit time integration scheme that is utilized for the extrinsic cohesive zone model in this study.

Next, when separations are within the softening region and when the current loading history index is smaller than the maximum loading history index, called the *unloading/reloading condition*, the cohesive relationships are obtained from the unloading/reloading models. One can utilize either the coupled unloading/reloading model or the uncoupled unloading/reloading model to evaluate the cohesive traction vector and the material tangent stiffness matrix. For the coupled unloading/reloading model, the Jacobian matrix entries are expressed as

$$\begin{aligned}
D_{nn}^v &= \left[D_{nn}(\Delta_n^v, \Delta_t^v) \left(1 - \frac{\Delta_n^2}{\eta^2}\right) - D_{nt}(\Delta_n^v, \Delta_t^v) \frac{\Delta_n \Delta_t}{\eta^2} + T_n(\Delta_n^v, \Delta_t^v) \frac{\alpha_v \Delta_n}{\eta_{\max} \eta} \right] \left(\frac{\eta}{\eta_{\max}}\right)^{\alpha_v - 1} \\
D_{nt}^v &= \left[D_{nt}(\Delta_n^v, \Delta_t^v) \left(1 - \frac{\Delta_t^2}{\eta^2}\right) - D_{nn}(\Delta_n^v, \Delta_t^v) \frac{\Delta_n \Delta_t}{\eta^2} + T_n(\Delta_n^v, \Delta_t^v) \frac{\alpha_v \Delta_t}{\eta_{\max} \eta} \right] \left(\frac{\eta}{\eta_{\max}}\right)^{\alpha_v - 1} \\
D_{tn}^v &= \left[D_{tn}(\Delta_n^v, \Delta_t^v) \left(1 - \frac{\Delta_n^2}{\eta^2}\right) - D_{tt}(\Delta_n^v, \Delta_t^v) \frac{\Delta_n \Delta_t}{\eta^2} + T_t(\Delta_n^v, \Delta_t^v) \frac{\beta_v \Delta_n}{\eta_{\max} \eta} \right] \left(\frac{\eta}{\eta_{\max}}\right)^{\beta_v - 1} \\
D_{tt}^v &= \left[D_{tt}(\Delta_n^v, \Delta_t^v) \left(1 - \frac{\Delta_t^2}{\eta^2}\right) - D_{tn}(\Delta_n^v, \Delta_t^v) \frac{\Delta_n \Delta_t}{\eta^2} + T_t(\Delta_n^v, \Delta_t^v) \frac{\beta_v \Delta_t}{\eta_{\max} \eta} \right] \left(\frac{\eta}{\eta_{\max}}\right)^{\beta_v - 1} \quad (4.15)
\end{aligned}$$

where

$$\mathbf{D}^v(\Delta_n, \Delta_t) = \begin{bmatrix} D_{nn}^v & D_{nt}^v \\ D_{tn}^v & D_{tt}^v \end{bmatrix} = \begin{bmatrix} \partial T_n^v / \partial \Delta_n & \partial T_n^v / \partial \Delta_t \\ \partial T_t^v / \partial \Delta_n & \partial T_t^v / \partial \Delta_t \end{bmatrix}. \quad (4.16)$$

For the uncoupled unloading/reloading model, the Jacobian matrix entries are given as

$$\begin{aligned}
D_{nn}^v &= T_n(\Delta_{n_{\max}}, \Delta_t) \frac{\alpha_v}{\Delta_{n_{\max}}} \left(\frac{\Delta_n}{\Delta_{n_{\max}}} \right)^{\alpha_v - 1} \\
D_{nt}^v &= D_{nt}(\Delta_{n_{\max}}, \Delta_t) \left(\frac{\Delta_n}{\Delta_{n_{\max}}} \right)^{\alpha_v} \\
D_{tn}^v &= D_{tn}(\Delta_n, \Delta_{t_{\max}}) \left(\frac{|\Delta_t|}{\Delta_{t_{\max}}} \right)^{\beta_v} \\
D_{tt}^v &= T_t(\Delta_n, \Delta_{t_{\max}}) \frac{\beta_v}{\Delta_{t_{\max}}} \left(\frac{|\Delta_t|}{\Delta_{t_{\max}}} \right)^{\beta_v - 1} \frac{\Delta_t}{|\Delta_t|}
\end{aligned} \tag{4.17}$$

In this case, the symmetric system is not guaranteed because the unloading/reloading model is not derived from a potential.

The *contact condition* occurs when the normal separation is negative. In this case, the normal negative separation can be penalized to prevent from material self-penetration. For example, the normal cohesive interaction is calibrated by using the penalty stiffness (α_p), i.e. $T_n = \alpha_p \Delta_n$. The tangential cohesive interaction is evaluated by penalizing $\Delta_n = 0$ (see Algorithm 4.2). Alternative approaches, involving contact mechanics, may also be possible.

Finally, material locally experiences *complete failure* when separations are outside of the softening region. The normal cohesive traction and normal stiffness matrix entries are set to be zero either when normal separation is greater than the normal final crack opening width ($\Delta_n > \delta_n$), or when absolute value of tangential separation is greater than the tangential conjugate final crack opening width ($|\Delta_t| > \bar{\delta}_t$). Notice that the normal cohesive interaction is continuous (i.e. no truncation) along the boundary of the normal softening region (i.e. $\Delta_n = \delta_n$ and $\Delta_t = \bar{\delta}_t$), because the normal cohesive interaction satisfies the boundary conditions of $(T_n(\delta_n, \Delta_t) = 0$ and $T_n(\Delta_n, \bar{\delta}_t) = 0)$. Similarly, the tangential cohesive interaction and tangential stiffness matrix entries are equal to zero when either $\Delta_n > \bar{\delta}_n$ or $|\Delta_t| > \delta_t$. The tangential cohesive interaction is continuous along the boundary of the tangential softening region (i.e. $\Delta_n = \bar{\delta}_n$ and $\Delta_t = \delta_t$), because the tangential cohesive interaction satisfies the boundary conditions of $(T_t(\bar{\delta}_n, \Delta_t) = 0$ and $T_t(\Delta_n, \delta_t) = 0)$.

Furthermore, the constitutive model is applicable for both two- and three-dimensional problems. In two-dimensional problems, the normal separation corresponds to the surface normal local coordinate (Δ_1) while the tangential separation agrees with the surface tangential local coordinate (Δ_2), shown in Figure 4.7(a). In three-dimensional

problems, the out-of-plane separation (Δ_1) matches the normal separation (Δ_n). The in-plane separations (Δ_2, Δ_3) are related to the tangential separation (Δ_t) by introducing an effective quantity, i.e. $\Delta_t = \sqrt{\Delta_2^2 + \Delta_3^2}$ (Figure 4.7(b)). The substitution of the effective quantity into the PPR potential expression, and the gradient of the potential lead to a cohesive traction vector

$$\mathbf{T} = \begin{Bmatrix} \partial\Psi/\partial\Delta_1 \\ \partial\Psi/\partial\Delta_2 \\ \partial\Psi/\partial\Delta_3 \end{Bmatrix} = \begin{Bmatrix} T_1 \\ T_2 \\ T_3 \end{Bmatrix} = \begin{Bmatrix} T_n \\ T_t\Delta_2/\Delta_t \\ T_t\Delta_3/\Delta_t \end{Bmatrix} \quad (4.18)$$

where T_1, T_2 and T_3 are cohesive tractions along the separation directions of Δ_1, Δ_2 and Δ_3 , respectively. The second derivatives of the PPR potential with respect to the separations in local coordinates result in the material tangent matrix,

$$\mathbf{D} = \begin{bmatrix} D_{nn} & D_{nt}\Delta_2/\Delta_t & D_{nt}\Delta_3/\Delta_t \\ D_{tn}\Delta_2/\Delta_t & D_{tt}\Delta_2^2/\Delta_t^2 + T_t\Delta_3^2/\Delta_t^3 & D_{tt}\Delta_2\Delta_3/\Delta_t^2 - T_t\Delta_2\Delta_3/\Delta_t^3 \\ D_{tn}\Delta_3/\Delta_t & D_{tt}\Delta_2\Delta_3/\Delta_t^2 - T_t\Delta_2\Delta_3/\Delta_t^3 & D_{tt}\Delta_3^2/\Delta_t^2 + T_t\Delta_2^2/\Delta_t^3 \end{bmatrix}. \quad (4.19)$$

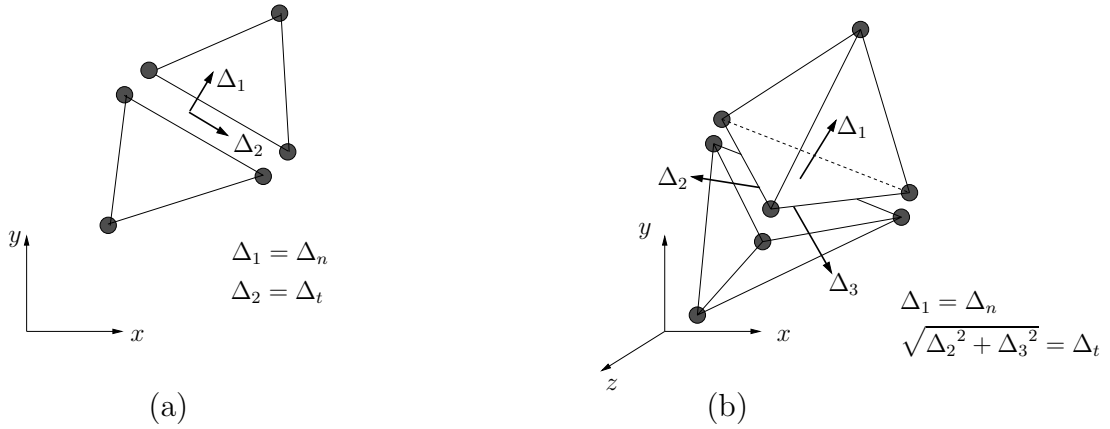


Figure 4.7: Cohesive fracture separations along the local coordinate system (a) two-dimensions (Δ_1, Δ_2) and (b) three-dimensions ($\Delta_1, \Delta_2, \Delta_3$).

4.6 Verification of Cohesive Elements

In order to verify computational implementation of the cohesive zone model, basic mode I and mode II problems are introduced. The geometry of mode I and II problems is described in Figure 4.8. The elastic modulus is 32 GPa, and the Poisson's ratio is 0.2. The fracture parameters of the PPR model are given as $\phi_n = 100$ N/m, $\phi_t = 200$

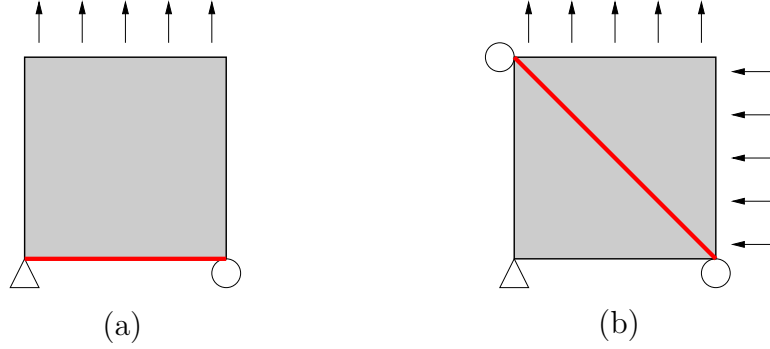


Figure 4.8: Geometry of (a) pure mode I, and (b) pure mode II simulation.

N/m, $\sigma_{\max} = 4$ MPa, $\tau_{\max} = 3$ MPa, $\alpha = 7$, $\beta = 2$, $\lambda_n = 0.005$, and $\lambda_t = 0.005$. The unloading/reloading shape parameters (α_v , β_v) are equal to one.

For mode I simulation, a square plate ($0.1 \text{ m} \times 0.1 \text{ m}$) is elongated at the top under the displacement control up to 0.05 mm . Next, the plate is compressed until the displacement at the top is -0.02 mm , and is elongated again to demonstrate complete failure condition. The plate is discretized by a bilinear quadrilateral element (Q4), and a cohesive element is inserted at the bottom of the plate. Stress versus displacement curve is plotted in Figures 4.9. While the plate is elongated, stress initially increases up to the cohesive strength (σ_{\max}), and then the plate demonstrates softening behavior. The softening curve is convex because the mode I shape parameter (α) is selected as 7. When the plate is unloaded, the constitutive relationship of the cohe-

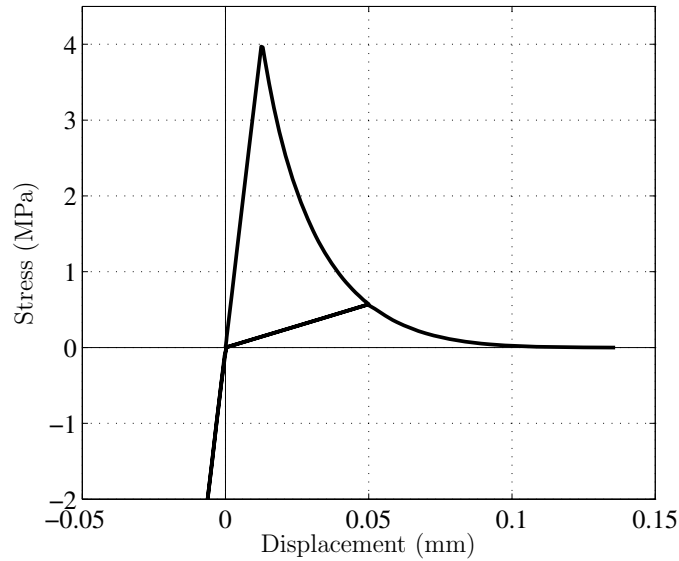


Figure 4.9: Computational result of the pure mode I test.

sive zone model evaluated on the basis of the unloading/reloading relationship. Since the unloading/reloading shape parameters equals to one, the unloading/reloading relationship is linear.

For a mode II problem, a 0.1 m by 0.1 m plate is elongated and compressed at the top and right hand sides, respectively, under the displacement control up to 0.04 mm. Next, the displacement directions are reversed until the complete failure. In this case, the principal stresses are along the horizontal and vertical directions. The maximum shear stress occurs along the 45°, and the magnitude of the maximum shear stress is equal to the magnitude of the principal stresses. The plate is discretized by two linear triangular elements (T3), and a cohesive element is inserted along the diagonal direction (see Figure 4.8(b)). Figure 4.10 illustrates that the maximum shear stress reaches the cohesive strength, and it decreases almost linearly because the mode II shape parameter (β) is two. Then, the plate is linearly unloaded and reloaded, while the applied displacement changes from 0.04 mm to -0.04 mm. The increase of the applied displacement leads to softening and complete failure conditions.

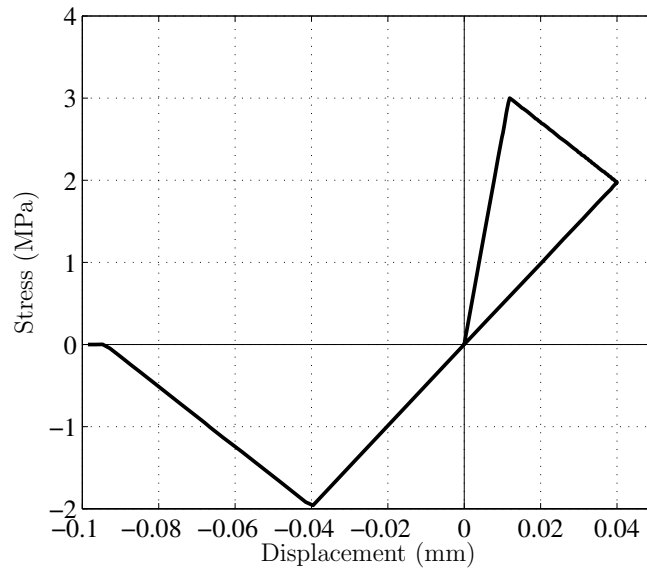


Figure 4.10: Computational result of the pure mode II test.

Chapter 5

Microstructural Particle/Matrix Debonding Process by the PPR Potential-Based Model

Macroscopic constitutive relationship is estimated by considering the microscopic particle/matrix interfacial debonding. For the interfacial debonding, the PPR potential-based cohesive model is utilized. The extended Mori-Tanaka model is employed for micromechanics, while a finite element-based cohesive zone model is used for the computational model. Both models (theoretical and computational) agree well with each other in representing the macroscopic constitutive relationship on the basis of the PPR model. The microscopic interfacial cohesive parameters of the PPR model are estimated from macroscopic composite material behavior. In addition, different microscopic debonding processes are observed with respect to different macroscopic constitutive relationships (e.g. hardening, softening, and snap-back).

5.1 Introduction

The development of the connections between different length scales, for example macroscopic behavior and microscopic behavior, is essential in understanding physical material behavior. Micromechanics models have been utilized to estimate the effective macroscopic elastic response of composite materials (Mura, 1987; Nemat-Nasser and Hori, 1999). For instance, the self-consistent method (Budiansky, 1965; Hill, 1965) approximates the effective elastic properties by embedding a particle in the infinite medium of unknown effective properties. The generalization of this method, called the generalized self-consistent method (Christensen and Lo, 1979), consists of introducing the matrix layer with the prescribed volume fraction between a particle and the effective infinite medium. The Mori-Tanaka method (Mori and Tanaka, 1973) is developed to calculate the average internal stress in the matrix of a material containing inclusions with transformation strain. The extension of the Mori-Tanaka model describes constitutive behavior of composites with interface debonding (Tan et al., 2007).

Several researchers have linked microscopic matrix/particle behavior with macroscopic continuum and fracture including either non-cohesive or cohesive behavior. Yin et al. (2004) developed micromechanics-based elastic constitutive model for functionally graded materials (FGMs) with particle interactions. The model was extended to represent effective thermo-elastic behavior of FGMs (Yin et al., 2007). Paulino et al. (2006) developed a micromechanical damage model for two-phase FGMs, considering the interfacial debonding of particles and pair-wise interactions between particles. Levy (1994) theoretically investigated separation of the matrix/particle interface under biaxial load. Siegmund and Brocks (1999) employed the modified Gurson relationship (Needleman and Tvergaard, 1984) to consider void nucleation and growth of materials, and to calibrate fracture parameters of the exponential traction-separation relationship. Allen and Searcy (2001) idealized the representative volume element (RVE) as fibrils that are surrounded by air, and obtained homogenized traction-separation relationships. Tan et al. (2005b) utilized digital image correlation technique to obtain macroscopic cohesive parameters. Based on these cohesive parameters, the extended Mori-Tanaka method was applied to obtain a microscale cohesive relationship for particle/matrix interface.

Micromechanical particle/matrix behaviors can be investigated by means of computational methods. Shen et al. (1994, 1995) studied the effect of particle shape and distribution on the effective elastic and plastic responses under perfect bonding between matrix and particle within the finite element analysis framework. In order to represent the matrix/particle debonding process, cohesive elements are incorporated with the finite element analysis (e.g. Xu and Needleman, 1993; Finot et al., 1994). Xu and Needleman (1993) investigated void nucleation along the interface in conjunction with an interfacial cohesive relationship, and Finot et al. (1994) demonstrated the influence of crack size, in addition to shape, spatial distribution, and volume fraction of the particles. Mogilevskaya and Crouch (2002) employed a Galerkin boundary integral method to study an infinite elastic plane containing randomly distributed circular elastic inclusions with homogeneously imperfect interfaces. Carpinteri et al. (2005) investigated snap-back instability in micro-structured composites under uniaxial displacement boundary conditions.

In this chapter, the constitutive relationship of materials with microstructures is investigated by using the PPR potential-based cohesive model for the interface relationship. This investigation is integrated with a theoretical micromechanics model and a finite element-based cohesive zone model. In addition, the fracture parameters of the PPR model are estimated in conjunction with a micromechanics model.

The chapter is organized as follows. Section 5.2 presents a theoretical micromechanics model that accounts for particle/matrix interface debonding. Next, the potential-based constitutive model for the interface between particle and matrix is explained in Section 5.3. Afterwards, Section 5.4 investigates the influence of cohesive fracture parameters, particle size and volume fraction on the constitutive relation under hydrostatic tension loading. Section 5.5 integrates the theoretical model with the computational model through investigation of particle/matrix debonding under equi-biaxial tension loading. The cohesive parameters of the PPR model are determined using macroscopic cohesive behavior in Section 5.6. Finally, the key findings of the chapter are summarized in Section 5.7.

5.2 Constitutive Behavior of Composites with Particle/Matrix Interface Debonding

This study considers a RVE with volume Ω of the composite material of N different particle sizes embedded in the matrix. The particles and matrix materials are assumed as linearly elastic. The matrix volume and particle volume of the k -th particle size are denoted by Ω^m and Ω_k^p , respectively ($k = 1, \dots, N$). The particle volume fraction f_k of the k -th particle size is given by Ω_k^p/Ω . The average stresses in the matrix ($\bar{\boldsymbol{\sigma}}^m$) and in the k -th particle ($\bar{\boldsymbol{\sigma}}_k^p$) are defined as

$$\bar{\boldsymbol{\sigma}}^m = \frac{1}{\Omega^m} \int_{\Omega^m} \boldsymbol{\sigma} dV, \quad \bar{\boldsymbol{\sigma}}_k^p = \frac{1}{\Omega_k^p} \int_{\Omega_k^p} \boldsymbol{\sigma} dV \quad (5.1)$$

respectively. The average stress in the RVE or macroscopic stress ($\bar{\boldsymbol{\sigma}}$) is given in terms of $\bar{\boldsymbol{\sigma}}^m$ and $\bar{\boldsymbol{\sigma}}_k^p$ (Taya and Chou, 1981; Benveniste, 1987; Weng, 1990) by

$$\bar{\boldsymbol{\sigma}} = (1 - f) \bar{\boldsymbol{\sigma}}^m + \sum_{k=1}^N f_k \bar{\boldsymbol{\sigma}}_k^p \quad (5.2)$$

where $f = \sum_{k=1}^N f_k$.

The average strains in the matrix ($\bar{\boldsymbol{\epsilon}}^m$) and in the particles ($\bar{\boldsymbol{\epsilon}}_k^p$) are defined as

$$\bar{\boldsymbol{\epsilon}}^m = \frac{1}{\Omega^m} \int_{\Omega^m} \boldsymbol{\epsilon} dV, \quad \bar{\boldsymbol{\epsilon}}_k^p = \frac{1}{\Omega_k^p} \int_{\Omega_k^p} \boldsymbol{\epsilon} dV \quad (5.3)$$

respectively. The average strain in the RVE or macroscopic strain $\bar{\boldsymbol{\epsilon}}$ is given in terms

of $\bar{\boldsymbol{\epsilon}}^m$ and $\bar{\boldsymbol{\epsilon}}_k^p$ (Tan et al., 2005a) by

$$\bar{\boldsymbol{\epsilon}} = (1 - f)\bar{\boldsymbol{\epsilon}}^m + \sum_{k=1}^N f_k (\bar{\boldsymbol{\epsilon}}_k^p + \bar{\boldsymbol{\epsilon}}_k^{\text{int}}) \quad (5.4)$$

where $\bar{\boldsymbol{\epsilon}}_k^{\text{int}}$ is the average strain which is contributed from the debonding interface S_k^{int} between particles of k -th size and matrix. In fact, $\bar{\boldsymbol{\epsilon}}_k^{\text{int}}$ is related to the displacement separation

$$\boldsymbol{\Delta}_k = [\mathbf{u}]_k = \mathbf{u}^m - \mathbf{u}_k^p \quad (5.5)$$

at the k -th particle/matrix interface by

$$\bar{\boldsymbol{\epsilon}}_k^{\text{int}} = \frac{1}{2\Omega_k^p} \int_{S_k^{\text{int}}} (\boldsymbol{\Delta}_k \otimes \mathbf{n} + \mathbf{n} \otimes \boldsymbol{\Delta}_k) dA \quad (5.6)$$

where \mathbf{u}^m and \mathbf{u}_k^p are the displacements on the interface of the matrix and the k -th particle, respectively, and \mathbf{n} is the unit normal vector on the interface pointing into the matrix (positive sign convention).

The average strains in the matrix and k -th particle are related to the correspondent average stresses by

$$\bar{\boldsymbol{\epsilon}}^m = \boldsymbol{\mathcal{M}}^m : \bar{\boldsymbol{\sigma}}^m, \quad \bar{\boldsymbol{\epsilon}}_k^p = \boldsymbol{\mathcal{M}}_k^p : \bar{\boldsymbol{\sigma}}_k^p \quad (5.7)$$

where $\boldsymbol{\mathcal{M}}^m$ and $\boldsymbol{\mathcal{M}}_k^p$ are the elastic compliance tensors of matrix and particle materials, respectively. Then, the averaged strain in the RVE (5.4) is rewritten as

$$\bar{\boldsymbol{\epsilon}} = \boldsymbol{\mathcal{M}}^m : \bar{\boldsymbol{\sigma}} + \sum_{k=1}^N f_k \{ (\boldsymbol{\mathcal{M}}_k^p - \boldsymbol{\mathcal{M}}^m) : \bar{\boldsymbol{\sigma}}_k^p + \bar{\boldsymbol{\epsilon}}_k^{\text{int}} \} \quad (5.8)$$

Expression (5.8) shows that, in order to obtain the constitutive relation of macroscopic strain and macroscopic stress, the average stresses in particles ($\bar{\boldsymbol{\sigma}}_k^p$) and the average strains from interface debonding ($\bar{\boldsymbol{\epsilon}}_k^{\text{int}}$) need to be determined in terms of macroscopic stress ($\bar{\boldsymbol{\sigma}}$) or macroscopic strain ($\bar{\boldsymbol{\epsilon}}$).

5.2.1 Hydrostatic Tension Stress State

In this section, for simplicity in evaluating $\bar{\boldsymbol{\sigma}}_k^p$ and $\bar{\boldsymbol{\epsilon}}_k^{\text{int}}$, a case of identical spherical particles embedded in an isotropic matrix subjected to hydrostatic tension stress state $\bar{\boldsymbol{\sigma}} = \bar{\sigma} \mathbf{I}$ (Tan et al., 2005a) is considered, where \mathbf{I} is the second-order identity tensor. All the particles are assumed to be isotropic and have the same elastic modulus and

radius a . From the tensorial equations of macroscopic stress and strain, one obtains

$$\bar{\sigma}_{ii} = (1 - f)\bar{\sigma}_{ii}^m + f\bar{\sigma}_{ii}^p \quad (5.9)$$

$$\bar{\epsilon}_{ii} = \frac{(1 - 2\nu^m)}{E^m}\bar{\sigma}_{ii} + f \left\{ \left(\frac{1 - 2\nu^p}{E^p} - \frac{1 - 2\nu^m}{E^m} \right) \bar{\sigma}_{ii}^p + \bar{\epsilon}_{ii}^{\text{int}} \right\} \quad (5.10)$$

where (E^m, ν^m) and (E^p, ν^p) are the elastic moduli and Poisson's ratios of the matrix and particles, respectively. The macroscopic stress ($\bar{\sigma}$), the average mean stresses in the matrix ($\bar{\sigma}^m$), and the average mean stress in the particles ($\bar{\sigma}^p$) are defined as

$$\bar{\sigma} = \bar{\sigma}_{ii}/3 \quad , \quad \bar{\sigma}^m = \bar{\sigma}_{ii}^m/3 \quad , \quad \bar{\sigma}^p = \bar{\sigma}_{ii}^p/3 \quad (5.11)$$

Hence, Eq. (5.9) is written as

$$\bar{\sigma} = (1 - f)\bar{\sigma}^m + f\bar{\sigma}^p \quad (5.12)$$

The average strain contribution from the interface debonding contribution $\bar{\epsilon}_{ii}^{\text{int}}$ is determined from Eq. (5.6) as

$$\bar{\epsilon}_{ii}^{\text{int}} = \frac{1}{\Omega^p} \int_{S^{\text{int}}} \Delta_n dA = \frac{3\Delta_n}{a} \quad (5.13)$$

where $\Delta_n = [u_n]$ is the average displacement discontinuity (separation) in the normal direction (or radial direction in this case) on the interfaces between particles and matrix. Therefore, from Eq. (5.10), the macroscopic strain $\bar{\epsilon}$ can be obtained as

$$\bar{\epsilon} = \frac{\bar{\epsilon}_{ii}}{3} = \frac{1 - 2\nu^m}{E^m}\bar{\sigma} + f \left\{ \left(\frac{1 - 2\nu^p}{E^p} - \frac{1 - 2\nu^m}{E^m} \right) \bar{\sigma}^p + \frac{\Delta_n}{a} \right\} \quad (5.14)$$

5.2.2 Extended Mori-Tanaka Method under Hydrostatic Tension

To determine the relation of $\bar{\sigma}^p$ and Δ_n in terms of macroscopic stress $\bar{\sigma}$, following the approach by Tan et al. (2005a), the Mori-Tanaka method (Mori and Tanaka, 1973) is extended, which is widely used for composite materials with high particle volume fraction. In the Mori-Tanaka method, the average stress in particles ($\bar{\sigma}^p$) is related to the average stress in the matrix ($\bar{\sigma}^m$) instead of the macroscopic stress ($\bar{\sigma}$). Therefore, a single spherical particle of radius a in an infinite matrix subject to

the remote hydrostatic tensile stress state $\bar{\sigma}^m \mathbf{I}$ is considered, shown in Figure 5.1(a). The average particle stress $\bar{\sigma}^p$ is uniform and equals the normal stress, σ^{int} , at the particle/matrix interface. Due to interface debonding, the normal displacement (or displacement in the radial direction) has a jump at the particle/matrix interface. At the outside boundary of the particle, the normal displacement is given as $\frac{a}{E^p}(1 - 2\nu^p)\sigma^{\text{int}}$, while at the inner boundary of the matrix, the normal displacement is given as $\frac{a}{2E^m} [3(1 - \nu^m)\bar{\sigma}^m - (1 + \nu^m)\sigma^{\text{int}}]$. The normal displacement separation, or the displacement separation in the radial direction, at the particle/matrix interface can be obtained as

$$\Delta_n = [u_n] = \left\{ \frac{3(1 - \nu^m)\bar{\sigma}^m - (1 + \nu^m)\sigma^{\text{int}}}{2E^m} - \frac{1 - 2\nu^p}{E^p}\sigma^{\text{int}} \right\} a \quad (5.15)$$

The average stress in the matrix $\bar{\sigma}^m$ can be expressed in terms of Δ_n and σ^{int} as

$$\bar{\sigma}^m = \frac{2E^m}{3(1 - \nu^m)} \left\{ \sigma^{\text{int}} \left(\frac{1 - 2\nu^p}{E^p} + \frac{1 + \nu^m}{2E^m} \right) + \frac{\Delta_n}{a} \right\} \quad (5.16)$$

Substituting Eq. (5.16) into the Eq. (5.12), one obtains the macroscopic stress $\bar{\sigma}$ in terms of Δ_n and σ^{int} as

$$\bar{\sigma} = (1 - f) \frac{2E^m}{3(1 - \nu^m)} \left\{ \sigma^{\text{int}} \left(\frac{1 - 2\nu^p}{E^p} + \frac{1 + \nu^m}{2E^m} \right) + \frac{\Delta_n}{a} \right\} + f\sigma^{\text{int}} \quad (5.17)$$

The macroscopic strain $\bar{\epsilon}$ in this case can be written as

$$\bar{\epsilon} = \frac{(1 - 2\nu^m)}{E^m} \bar{\sigma} + f \left\{ \left(\frac{1 - 2\nu^p}{E^p} - \frac{1 - 2\nu^m}{E^m} \right) \sigma^{\text{int}} + \frac{\Delta_n}{a} \right\} \quad (5.18)$$

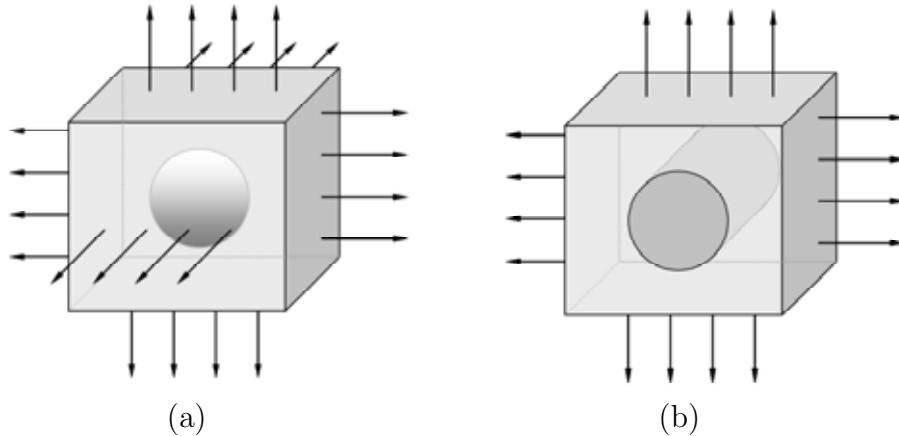


Figure 5.1: (a) Spherical particle under hydrostatic tension stress state, and (b) cylindrical particle under equi-biaxial tension stress state.

In order to obtain the constitutive relation between the macroscopic stress $\bar{\sigma}$ and macroscopic strain $\bar{\epsilon}$ from Eqs. (5.17) and (5.18), a relation of the normal stress σ^{int} and the normal displacement separation Δ_n at the particle/matrix interface is needed. The PPR potential-based cohesive model, presented in Chapter 3, for particle/matrix interface debonding is employed to establish the relation between the normal stress and the normal displacement separation at the interface.

5.2.3 Extended Mori-Tanaka Method under Equi-biaxial Tension

For equi-biaxial tension loading ($\bar{\sigma}$) under plane strain condition, this study considers the case that all the particles are isotropic, have the same elastic modulus and are cylindrical with radius a , as shown in Figure 5.1(b). Once again, the extended Mori-Tanaka method is employed, in which the macroscopic stress $\bar{\sigma}$ can be obtained from Eq. (5.12) and the macroscopic strain $\bar{\epsilon}$ can be obtained as

$$\bar{\epsilon} = \frac{(1 + \nu^m)(1 - 2\nu^m)}{E^m} \bar{\sigma} + f \left\{ \left(\frac{(1 + \nu^p)(1 - 2\nu^p)}{E^p} - \frac{(1 + \nu^m)(1 - 2\nu^m)}{E^m} \right) \bar{\sigma}^p + \frac{\Delta_n}{a} \right\} \quad (5.19)$$

where the average stress in the particle $\bar{\sigma}^p$ is uniform and equals the normal stress at the particle/matrix interface (σ^{int}), which is related to the normal displacement separation Δ_n by the cohesive relation of the PPR model. Accordingly, the average stress in the matrix $\bar{\sigma}^m$ is given by

$$\bar{\sigma}^m = \frac{E^m}{2(1 - \nu^m)(1 + \nu^m)} \left\{ \sigma^{\text{int}} \left(\frac{(1 - 2\nu^p)(1 + \nu^p)}{E^p} + \frac{1 + \nu^m}{E^m} \right) + \frac{\Delta_n}{a} \right\} \quad (5.20)$$

Notice that Eqs. (5.12), (5.19) and (5.20) provide the constitutive relation between macroscopic stress and macroscopic strain of composite materials accounting for interface debonding under equi-biaxial loading with plane strain conditions.

5.3 PPR: Potential-Based Cohesive Model for Interface Debonding

For tensile opening (mode I) fracture, McMeeking and Parks (1979) showed that in modified compact tension tests, the stress state ahead of the crack tip is nearly hydrostatic. Tan et al. (2005b) also showed that, in two-dimensional mode I fracture, the stress state is equi-biaxial within the cohesive zone ahead of the crack tip. For

those special cases of loadings, the tangential cohesive stress vanishes and the normal cohesive traction in Eq. (3.28) can be simplified by taking the tangential separation $\Delta_t = 0$. Thus, one obtains the following intrinsic cohesive zone model for normal cohesive stress σ^{int} in terms of normal separation Δ_n as

$$\sigma^{\text{int}} = \frac{\phi_n}{\delta_n} \left(\frac{\alpha}{m}\right)^m \left(1 - \frac{\Delta_n}{\delta_n}\right)^{\alpha-1} \left(\frac{m}{\alpha} + \frac{\Delta_n}{\delta_n}\right)^{m-1} (m + \alpha) \frac{\Delta_n}{\delta_n} \quad (5.21)$$

This relation between the normal cohesive stress and the normal separation provides the cohesive relationship of the interface debonding along the normal direction and is illustrated in Figure 5.2. For the sake of illustration, in this example, the tension cohesive strength (σ_{max}) is chosen to be 10 MPa and the fracture energy for mode I (ϕ_n) is 1 N/m. The shape parameter index (α) is set to 3, while the initial slope indicator (λ_n) is selected as 0.005.

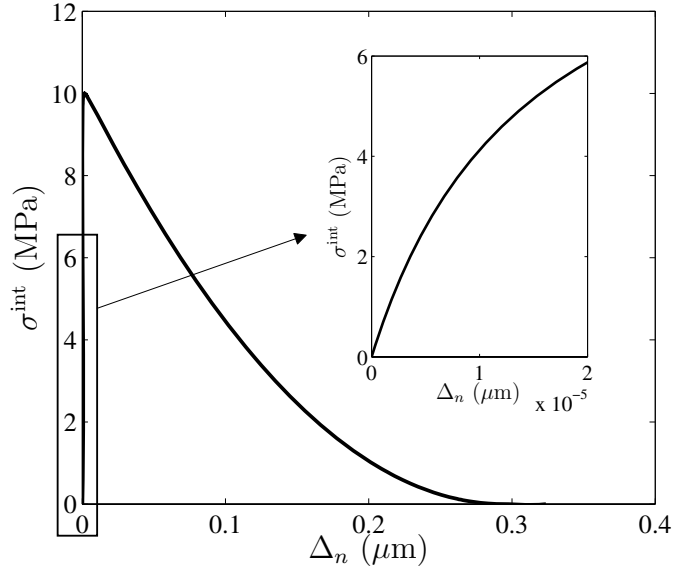


Figure 5.2: Illustrative intrinsic cohesive relation of normal interface debonding.

In the case of hydrostatic tension loading, the cohesive relation of σ^{int} in terms of Δ_n in Eq. (5.21), together with Eqs. (5.17) and (5.18), which represent the relation of macroscopic stress and strain in terms of σ^{int} and Δ_n , provide a system of parametric equations in terms of the normal displacement separation Δ_n . Based on these equations, the constitutive relation between the macroscopic stress and strain of the composite material can be determined.

5.4 Micromechanics Investigation of the PPR Model

The previous sections have shown that macroscopic constitutive behavior of composite materials accounting for particle/matrix debonding can be obtained by incorporating the PPR cohesive relation into the micromechanics model. This section investigates the effect of relevant PPR cohesive parameters, e.g. particle size and volume fraction, on the macroscopic constitutive behavior of the material. For simplicity, the micromechanics model in the hydrostatic tension loading case, presented in Section 5.2, is applied to the limit when the material is homogenous. Hence, both matrix and particle now have the same material properties. At this time, the particles have the role as microstructures in the material and the volume fraction (f) represents the amount of interface between the microstructure and the material. All the microstructures are assumed to be isotropic and have the same spherical shape with the radius a (see Figure 5.1(a)). Thus, the macroscopic stress and strain in Eqs. (5.17) and (5.18) are simplified to

$$\bar{\sigma} = (1 - f) \frac{2E}{3(1 - \nu)} \frac{\Delta_n}{a} + \sigma^{\text{int}} , \quad (5.22)$$

$$\bar{\epsilon} = \frac{1}{3K} \bar{\sigma} + f \frac{\Delta_n}{a} , \quad (5.23)$$

where K is the elastic bulk modulus of the material and σ^{int} is described in terms of normal separation Δ_n as shown in Eq. (5.21).

From the two parametric equations in terms of normal separation, i.e. Eqs. (5.22) and (5.23), the macroscopic constitutive relation of the material can be determined as illustrated in Figure 5.3 for particle size $a = 100 \mu\text{m}$. In Figure 5.3, the values of elastic modulus and Poisson's ratio for both matrix and particle are chosen as $E = 122 \text{ GPa}$ and $\nu = 0.25$, respectively. The PPR cohesive parameters are the same as the ones used in Figure 5.2, where cohesive strength $\sigma_{\text{max}} = 10 \text{ MPa}$, fracture energy $\phi_n = 1 \text{ N/m}$, shape parameter index $\alpha = 3$ and initial slope indicator $\lambda_n = 0.005$. Notice that the geometrical and material parameters, in this section and also in the next section, are illustrative quantities chosen to investigate the overall behavior of composites accounting for particle/matrix debonding with the PPR cohesive relation. The investigation of an actual material is provided later in this chapter (Section 5.6).

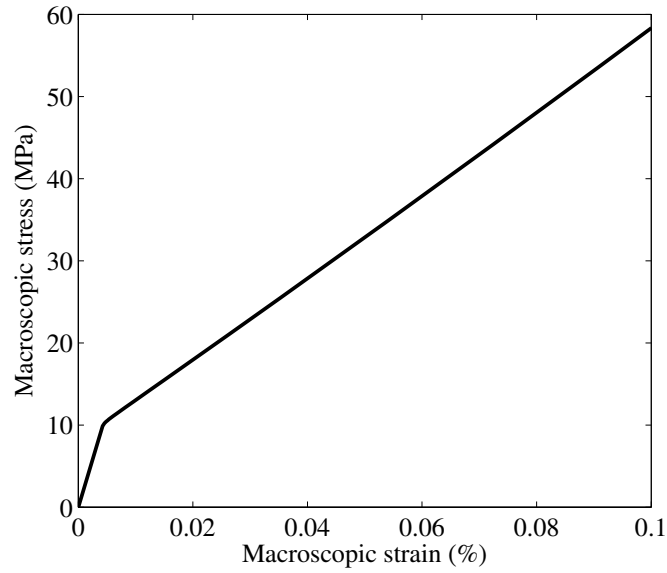


Figure 5.3: Stress versus strain curve of the material ($a = 100\mu m$).

5.4.1 Effect of Particle Size

The effect of particle size is investigated. Figure 5.4 illustrates the macroscopic stress-strain curves of the material for different particle sizes. Notice that all other parameters are fixed. The material tends to display hardening behavior when the size of the particles is small, while softening behavior appears in the case of large particles.

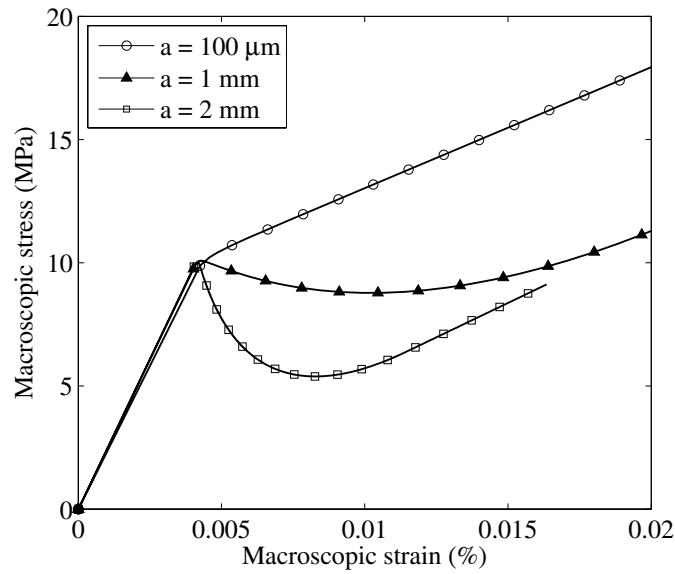


Figure 5.4: Effect of particle size (a) on the constitutive relation ($f = 0.6$).

5.4.2 Effect of Particle Volume Fraction

To examine the effect of particle volume fraction on the macroscopic constitutive relation, the value of the particle volume fraction changes, but all other parameters are fixed. In the case of fine particles ($a = 100 \mu\text{m}$), Figure 5.5 illustrates how the macroscopic stress-strain relation is influenced by the particle volume fraction. A higher volume fraction of particle gives a smaller slope of the stress-strain curve of the material in the hardening region. For the case of coarse particles ($a = 2 \text{ mm}$), Figure 5.6 shows that the softening effect increases when the volume fraction increases.

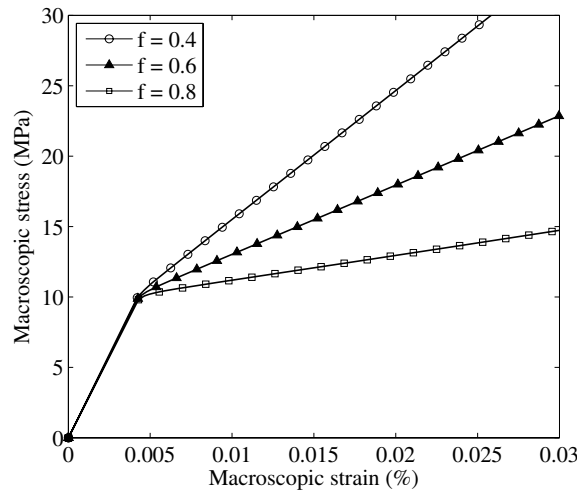


Figure 5.5: Effect of particle volume fraction (f) on the constitutive relation in the case of fine particles ($a = 100 \mu\text{m}$).

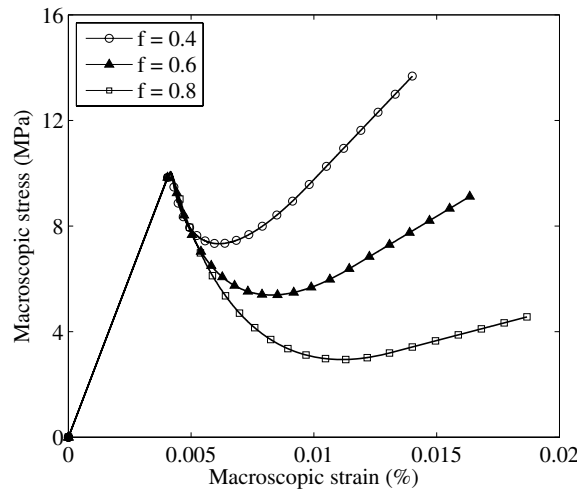
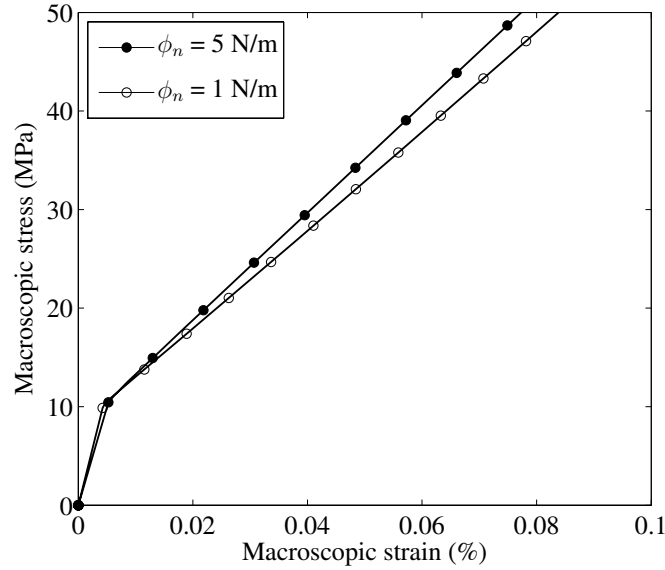


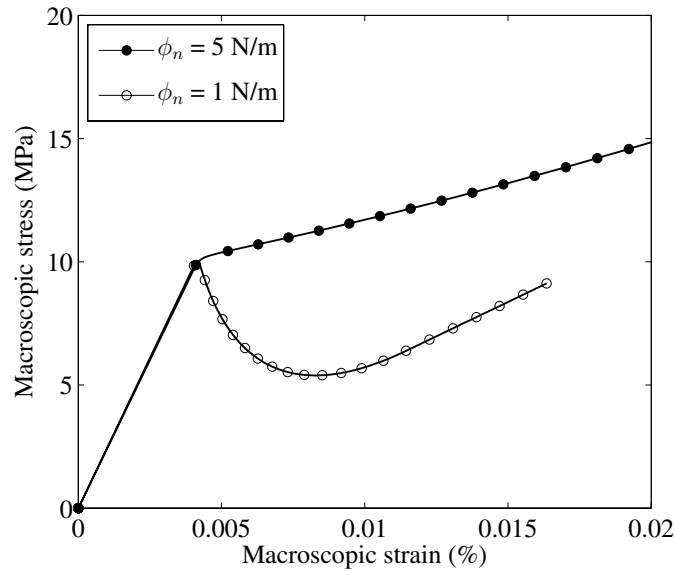
Figure 5.6: Effect of particle volume fraction (f) on the constitutive relation in the case of coarse particles ($a = 2 \text{ mm}$).

5.4.3 Effect of Cohesive Energy

The influence of cohesive energy on the macroscopic constitutive relation is examined and shown in Figure 5.7. When the cohesive energy increases, more energy is needed to separate the particle and the matrix; therefore, the stress-strain curve displays increased hardening effect.



(a)

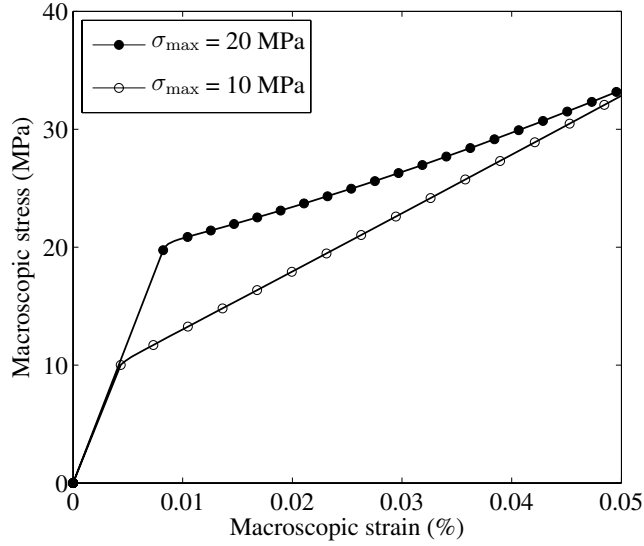


(b)

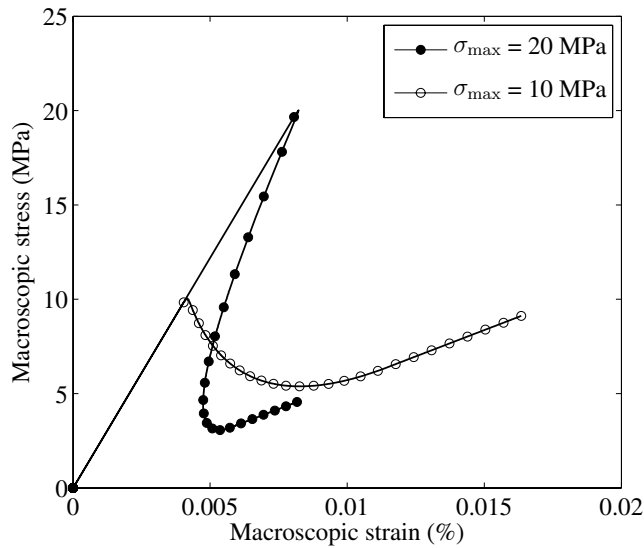
Figure 5.7: Effect of cohesive energy (ϕ_n) on the constitutive relation with volume fraction $f = 0.6$: (a) $a = 100 \mu\text{m}$, and (b) $a = 2 \text{ mm}$.

5.4.4 Effect of Cohesive Strength

The increase of the cohesive strength of the interface debonding relation provides higher stress before the macroscopic constitutive relation reaches the hardening-softening region. However, because the cohesive energy is fixed, the higher cohesive strength gives a smaller final normal separation. Hence, the complete debonding occurs earlier, which is shown clearly in the case of a large particle in Figure 5.8.



(a)



(b)

Figure 5.8: Effect of cohesive strength (σ_{\max}) on the constitutive relation with volume fraction $f = 0.6$: (a) $a = 100 \mu m$, and (b) $a = 2$ mm.

5.5 Theoretical and Computational Investigation of Materials with Microstructure Accounting for Particle/Matrix Interface Debonding

Particle/matrix debonding process and macroscopic constitutive relationships of composite material are investigated by utilizing both micromechanics and finite element method by means of an integrated approach. The geometry of the unit cell for computational investigation is illustrated in Figure 5.9(a) (cf. Figure 5.1(b)). As indicated before, the particle sizes (a) are $100\ \mu\text{m}$, $1\ \text{mm}$ and $2\ \text{mm}$, while the size of the RVE (b) is calculated on the basis of the particle volume fraction of the microstructures. The elastic modulus of both matrix and particle is $122\ \text{GPa}$, the Poisson's ratio is 0.25 , and the particle volume fraction of 0.6 are used in this study. In addition, in the computational model, the mode II fracture parameters ($\phi_t, \tau_{\max}, \beta, \lambda_t$) are assumed to be the same as the mode I fracture parameters ($\phi_n, \sigma_{\max}, \alpha, \lambda_n$) in the PPR model.

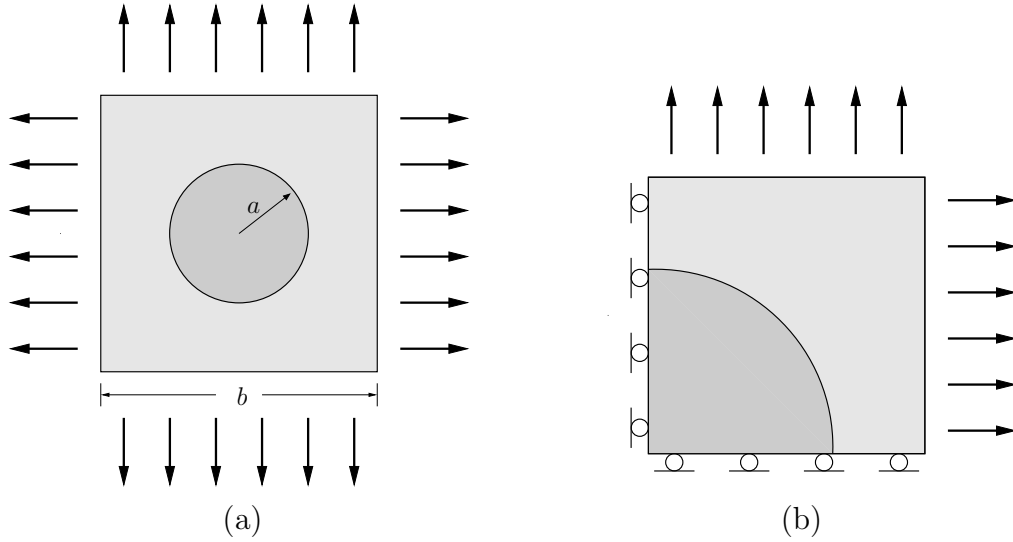
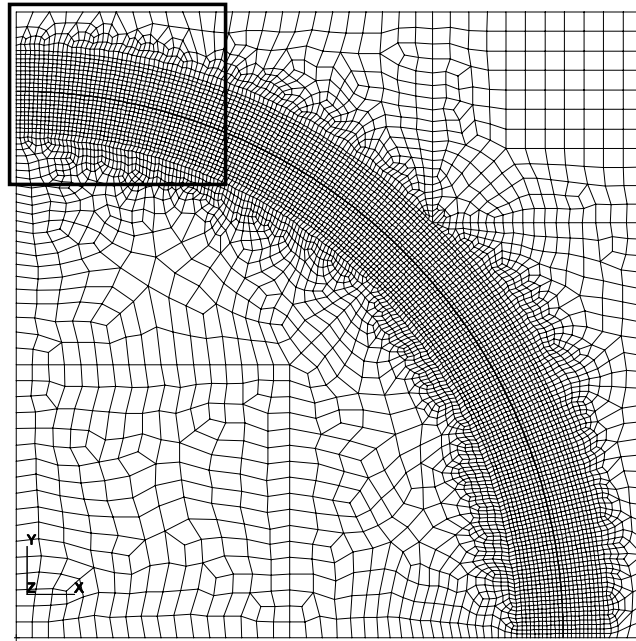


Figure 5.9: (a) Geometry of the square unit cell (size b) with particle of radius a , and (b) boundary conditions for the computational modeling.

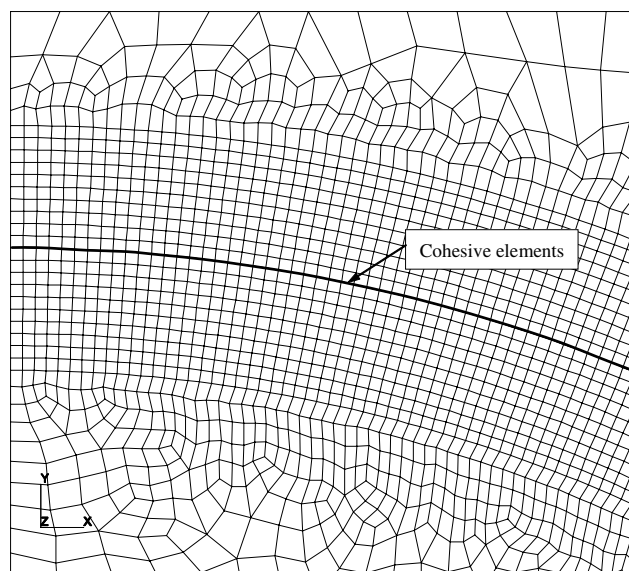
In the theoretical model, the extended Mori-Tanaka method under equi-biaxial loading with plane strain condition is employed. The expressions of the macroscopic strain (5.19), the average stress in the matrix (5.20), and the cohesive relationship of the PPR model (5.21) lead to the constitutive relationship between macroscopic stress and macroscopic strain, as discussed in Section 5.2.3.

In the computational simulation, a two-dimensional plane strain condition is employed, and a quarter of the unit cell is analyzed because of symmetry along the

horizontal and vertical directions (see Figure 5.9). Both the matrix and particle are represented by volumetric (or bulk) elements, while the interface debonding between particle and matrix is characterized by cohesive surface elements using the PPR model in conjunction with the coupled unloading/reloading relationship. The finite element



(a)



(b)

Figure 5.10: (a) Finite element mesh of the unit cell, and (b) zoom of the mesh along the interface between particle ($a = 2$ mm) and matrix.

mesh is illustrated in Figure 5.10(a), and cohesive surface elements are inserted *a priori* along the particle/matrix interface, as indicated by a thick solid line. The number of bulk elements is 6826 (Q4), the number of cohesive elements is 200, and the total number of nodes is 7128. The size of cohesive elements is $16\ \mu\text{m}$ for the particle size of 2 mm, which is small enough to capture the nonlinear particle/matrix debonding process. The computational results using the cohesive element size of $32\ \mu\text{m}$ are almost the same as the results using the size of $16\ \mu\text{m}$. A zoomed-in region of the mesh around the interface is shown in Figure 5.10(b), and the mesh in this region is uniform.

Displacement boundary conditions are applied to the unit cell. The left and bottom edges in the finite element mesh are fixed along the horizontal and vertical directions (Figure 5.9(b)), respectively, due to the symmetry of the unit cell. Along the right and top edges, uniform displacement is applied. In order to improve convergence of computational simulation in the matrix/particle debonding process, especially for a case of snap-back instability, slightly higher displacement (e.g. 1%) is applied along the horizontal direction. The averaged macroscopic strain is evaluated by dividing the corresponding displacement along the edge by half of the RVE size ($b/2$), while averaged macroscopic stress is calculated by dividing the summation of reaction forces along the edge by half of the RVE size ($b/2$).

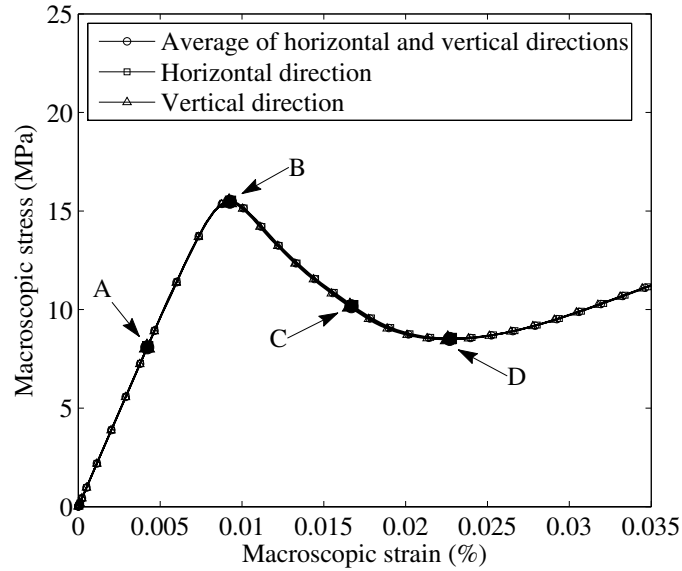
In the following subsection, the particle/matrix debonding process is observed for different types of macroscopic constitutive relationships. Next, the effect of microstructural size and material parameters on the macroscopic stress-strain relationship is theoretically and numerically investigated.

5.5.1 Particle/Matrix Debonding Process

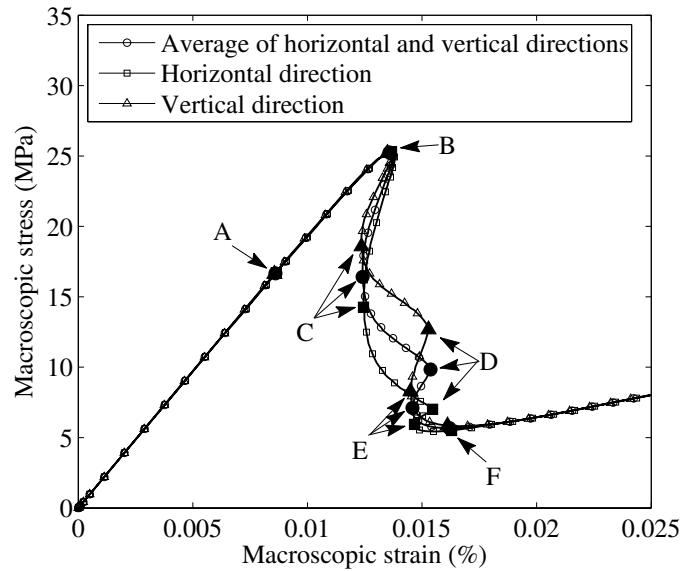
Different types of the particle/matrix debonding process are observed with respect to different types of the macroscopic constitutive relationships, which result from the change of microstructural size or material properties. In this study, for the configuration (Figure 5.9(b)) with the particle size $a = 2\ \text{mm}$, the fracture energy and the shape parameter are fixed as $\phi_n = 5\ \text{N/m}$ and $\alpha = 3$, respectively. The initial slope indicator is selected as a small value (e.g. $\lambda_n \in [0.002, 0.01]$) within numerical stability limits. With the cohesive strengths of $\sigma_{\max} = 15\ \text{MPa}$ and $25\ \text{MPa}$, averaged macroscopic stress-strain relationships along the horizontal and vertical directions are plotted in Figure 5.11. When the cohesive strength is $15\ \text{MPa}$, the macroscopic stress-strain relationship illustrates softening behavior (Figure 5.11(a)). On the other

hand, if the cohesive strength is 25 MPa, the macroscopic stress-strain relationship demonstrates snap-back instability behavior, as shown in Figure 5.11(b).

For the case of softening behavior (Figure 5.11(a)), the particle/matrix debonding process is observed at the four points: elastic range (point A), peak point (point B), softening range (point C), and complete separation (point D). Accordingly, Figure



(a)



(b)

Figure 5.11: Computational results displaying macroscopic strain versus strain along the horizontal and vertical directions with cohesive strength of (a) 15 MPa, and (b) 25 MPa.

5.12 illustrates the deformed shape and von Mises stress distribution at each point. Before reaching the peak point (Point B), the von Mises stress distribution is uniform, i.e. elastic stage (Figure 5.12(a)). After the peak point (Figure 5.12(b)), stress in the particle decreases while stress in matrix increases due to the particle/matrix debonding (Figure 5.12(c)). In this softening stage (e.g. point C), the separation along the particle/matrix interface is uniform. Finally, the stress in the particle reaches zero, and the complete debonding occurs, as shown in Figure 5.12(d). In this case, the debonding process is stable, and thus the separation is uniform along the interface.

When the macroscopic stress-strain relationship exhibits snap-back instability (Figure 5.11(b)), the particle/matrix debonding process is different from the pre-

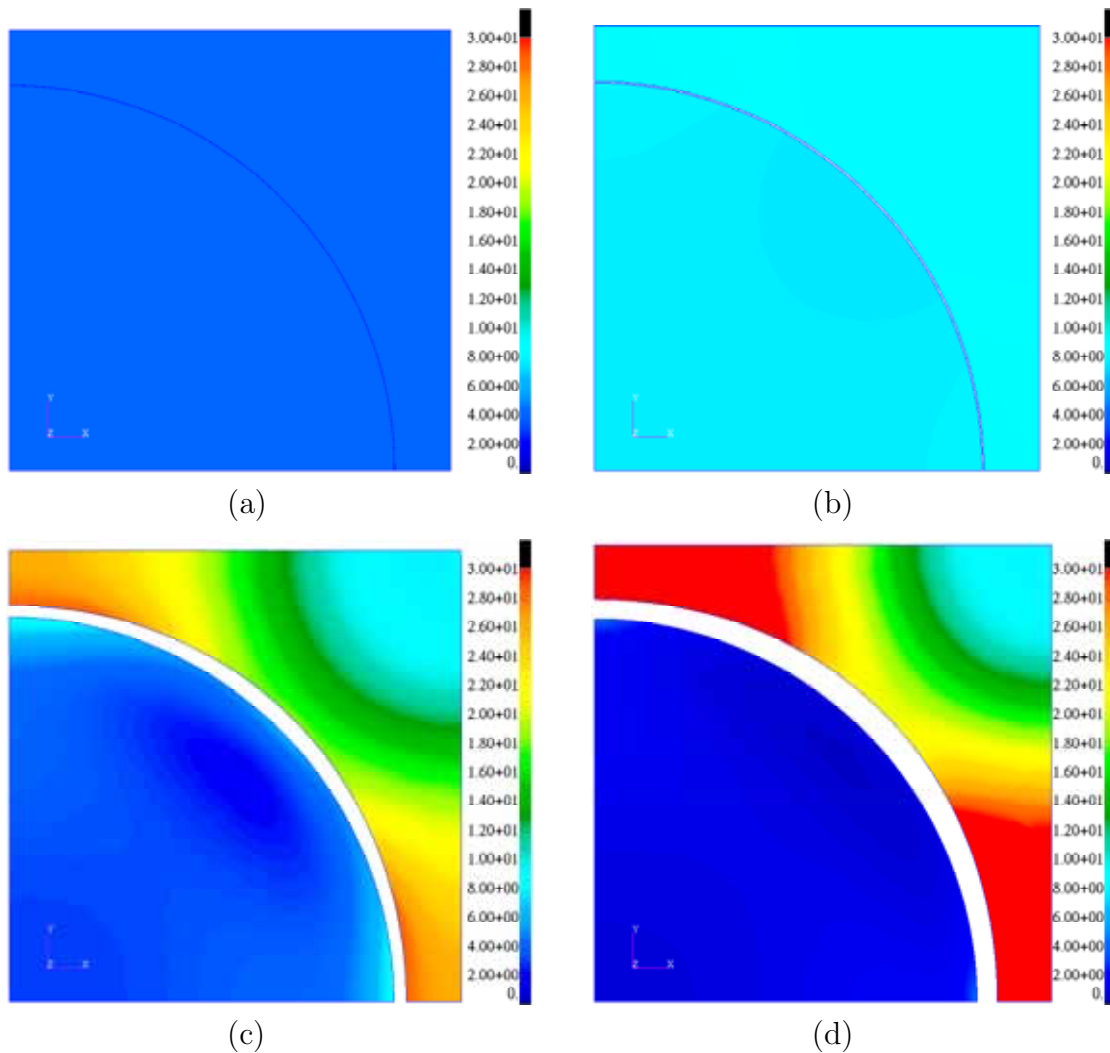


Figure 5.12: Particle/matrix debonding process for softening behavior (Figure 5.11(a)) at the stage of (a) point A, (b) point B, (c) point C, and (d) point D.

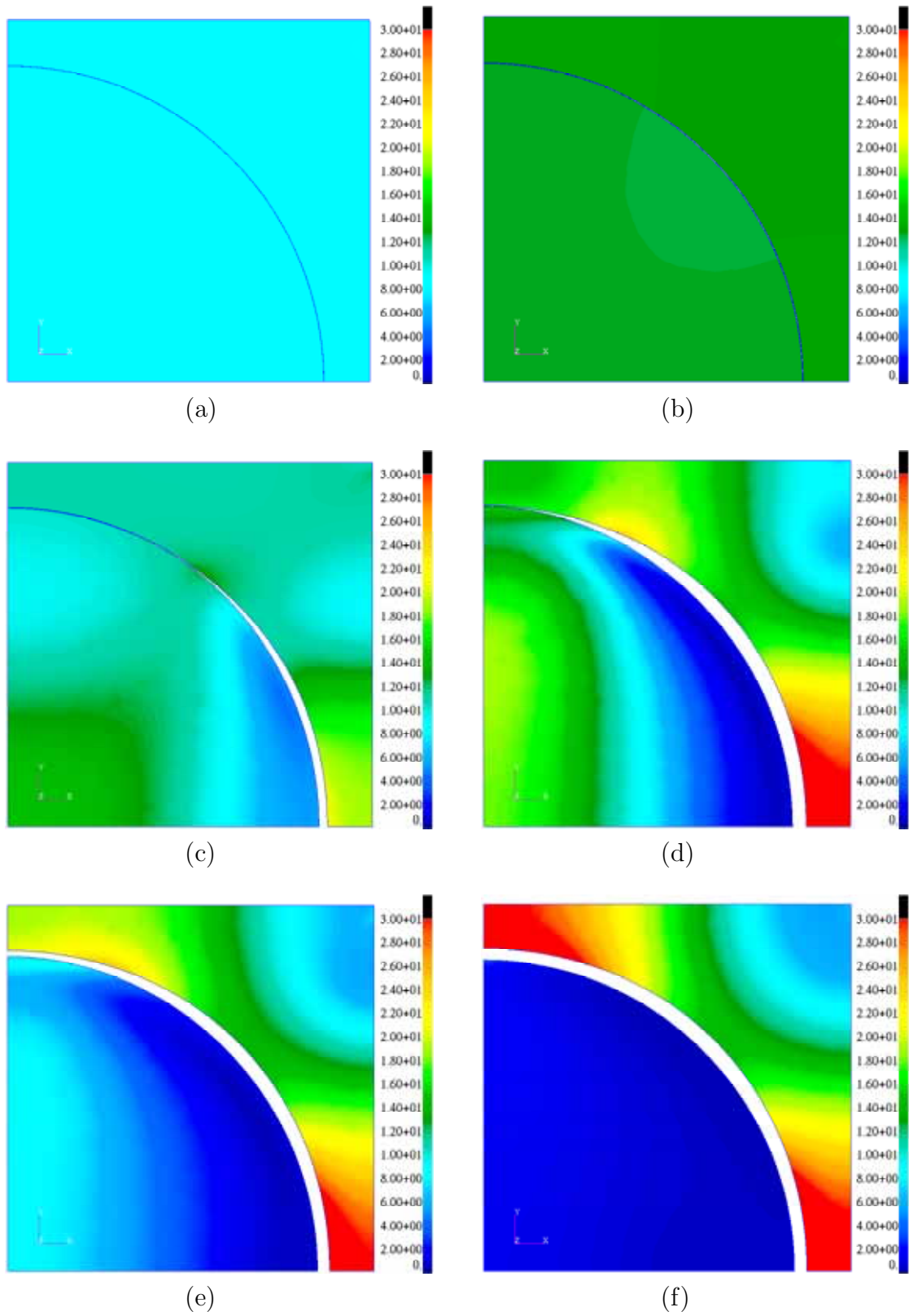


Figure 5.13: Particle/matrix debonding process for snap-back behavior (Figure 5.11(b)) at the stage of (a) point A, (b) point B, (c) point C, (d) point D, (e) point E, and (f) point F.

vious case. Until the microstructure reaches peak stress (Point B), the von Mises stress is generally uniform (Figure 5.13(a) and (b)), and almost no debonding occurs. At the onset of the snap-back instability, particle and matrix start to debond from each other. Because of the snap-back instability, unstable debonding process is expected. Thus the separation along the particle/matrix interface may not be uniform. In this numerical investigation, for example, the debonding occurs along the horizontal direction first, which corresponds to the stage from point B (Figure 5.13(b)) to point C (Figure 5.13(c)). The initiated crack propagates along the interface between matrix and particle, which corresponds to the stage from point C (Figure 5.13(d)) to point D (Figure 5.13(e)). The crack propagation in this stage is stable in the sense that the increase of separation along the interface leads to the decrease of the macroscopic stress, i.e. softening behavior. Next, a secondary snap-back instability is observed, which leads to the debonding along the vertical direction, i.e. the stage from point D to point E. In the end, the complete separation occurs at point F, as shown in Figure 5.13(e). The von Mises stress in the particle becomes zero, and stress concentration is observed in the matrix.

5.5.2 Effect of Microstructure Size

The macroscopic constitutive relationship varies with respect to the change of the microstructure size, elastic modulus, fracture energy and cohesive strength. First, the effect of microstructure size on macroscopic behavior is investigated. The particle sizes are 2 mm, 1 mm, and 100 μm ; with particle volume fraction $f = 0.6$. The

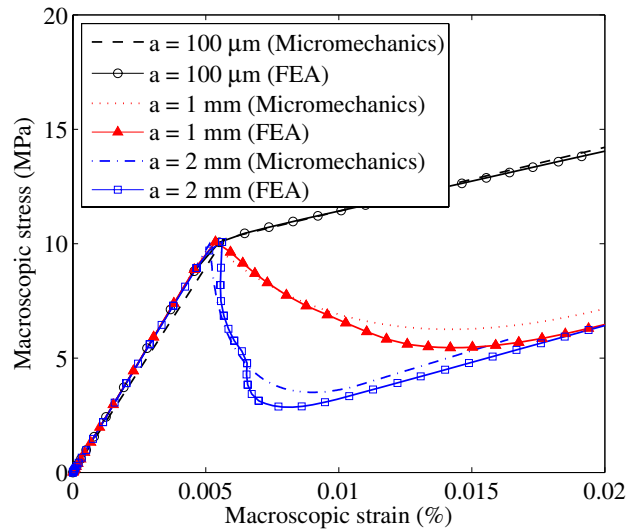


Figure 5.14: Effect of the particle size (a) on the constitutive relationship.

fracture energy is $\phi_n = 1 \text{ N/m}$, the cohesive strength is $\sigma_{\max} = 10 \text{ MPa}$, and the shape parameter is $\alpha = 3$. For the given fracture parameters, the constitutive relationships for each particle size demonstrate similar elastic behavior (i.e. almost linear) until the macroscopic stress reaches 10 MPa , which corresponds to the adopted cohesive strength. After the elastic limit is reached, the fine particle ($a = 100 \text{ }\mu\text{m}$) material demonstrates hardening behavior while the coarse particle ($a = 2 \text{ mm}$) material displays softening behavior, as shown in Figure 5.14.

5.5.3 Effect of Particle Elastic Modulus

Next, the effect of the particle elastic modulus is studied. The elastic modulus of the matrix is fixed ($E^m = 122 \text{ MPa}$), while the elastic modulus of particle (E^p) is selected as 61 MPa , 122 MPa , and 244 MPa , which leads to the ratio of the particle elastic modulus to the matrix elastic modulus of 0.5 , 1 , and 2 , respectively. The selected size of particle is 2 mm with the volume fraction $f = 0.6$. The fracture energy is $\phi_n = 5 \text{ N/m}$ with cohesive strength $\sigma_{\max} = 10 \text{ MPa}$, and shape parameter $\alpha = 3$. The higher elastic modulus of particles results in stiffer elastic behavior and shorter elastic range. The lower elastic modulus of particles leads to the slightly higher macroscopic stress of the elastic limit, as shown in Figure 5.15. At larger macroscopic strain, complete debonding occurs, and thus the elastic modulus of particle does not influence the macroscopic stress-strain relationship.

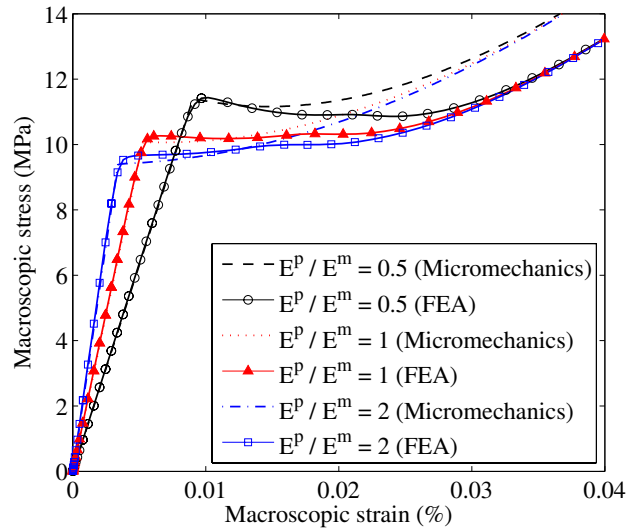
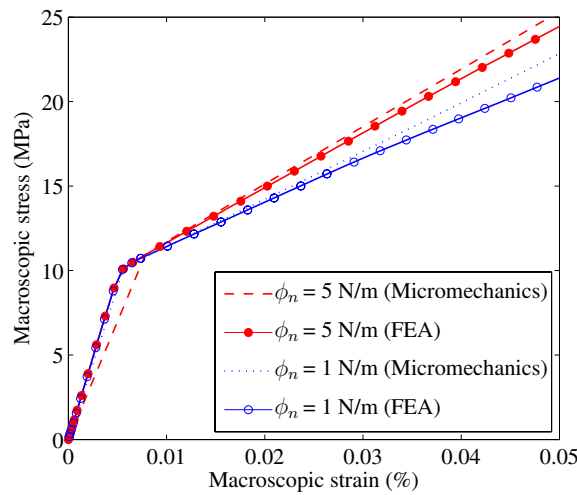


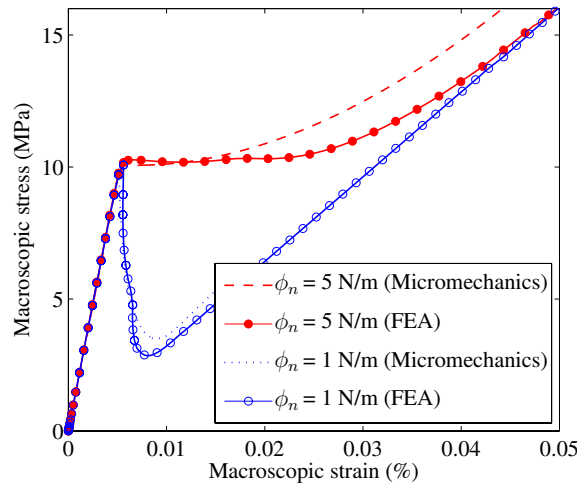
Figure 5.15: Effect of the ratio of elastic modulus on the constitutive relationship.

5.5.4 Effect of Fracture Energy and Particle Size

The change of cohesive fracture parameters also leads to different macroscopic constitutive relationships. Two particle sizes ($a = 2 \text{ mm}$ and $100 \mu\text{m}$) are investigated with respect to the fracture energies of $\phi_n = 1 \text{ N/m}$ and 5 N/m . The cohesive strength is $\sigma_{\max} = 10 \text{ MPa}$, and the shape parameter is $\alpha = 3$. For each particle size, elastic behavior is almost the same, as shown in Figure 5.16. After the averaged macroscopic stress reaches the elastic limit, which almost corresponds to the cohesive strength (10 MPa), the larger fracture energy provides higher load capacity for both coarse and fine



(a)



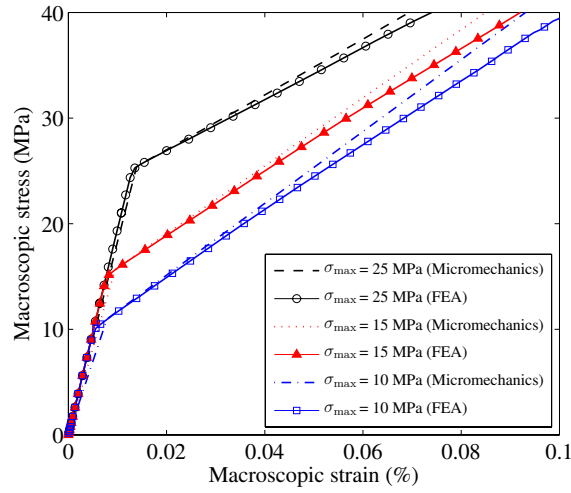
(b)

Figure 5.16: Effect of the fracture energy (ϕ_n) on the constitutive relationship with particle size of (a) $100 \mu\text{m}$, and (b) 2 mm .

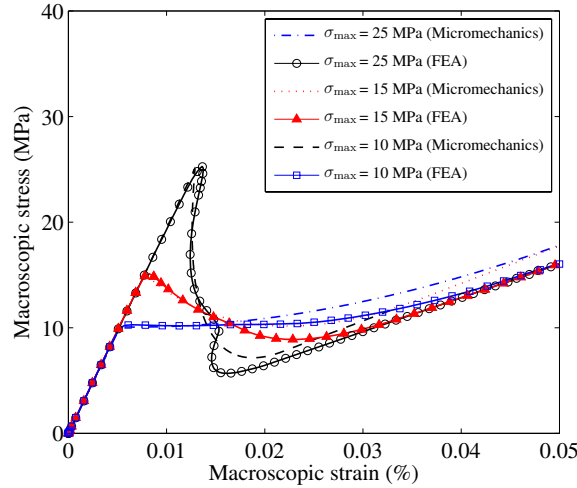
particle sizes. The increase of fracture energy changes the macroscopic stress-strain relationship from softening behavior to hardening behavior for the coarse particle ($a = 2\text{mm}$).

5.5.5 Effect of Cohesive Strength and Particle Size

The effect of the cohesive strength is also investigated. The particle sizes are $a = 2\text{ mm}$ and $100\ \mu\text{m}$; the cohesive strengths are $\sigma_{\max} = 10\text{ MPa}$, 15 MPa , and 25 MPa . The fracture energy and the shape parameters are fixed as $\phi_n = 5\text{ N/m}$ and $\alpha =$



(a)



(b)

Figure 5.17: Effect of the cohesive strength (σ_{\max}) on the constitutive relationship with particle size of (a) $100\ \mu\text{m}$, and (b) 2 mm .

3, respectively. In this simulation, the coarse particle configuration demonstrates hardening behavior, while the fine particle illustrates various post-peak behaviors such as hardening, softening and snap-back, with respect to the change of cohesive strength (Figure 5.17). The higher cohesive strength leads to higher macroscopic stress of the elastic limit. At the larger macroscopic strain, complete separation occurs along the interface between particle and matrix, and thus the macroscopic constitutive relationships become the same for the different cohesive strengths.

5.5.6 Remarks

The results from the finite element analysis (FEA) are described by a solid line with markers, and the results from the micromechanics model are illustrated by a dashed, dotted or dashed-dotted line. Both theoretical and computational results agree well each other (see Figures 5.14-5.17), especially when the strain is small. While the macroscopic strain increases, the finite element results with the cohesive zone model do not exactly match the micromechanics results. The difference may result from the fact that the finite element formulation considers geometrical nonlinearity with finite strains while the micromechanics model is based on small strain theory.

5.6 Case Study: Determination of the PPR Cohesive Relation

Macroscopic cohesive behavior of composite material might provide some important information to determine the PPR cohesive relation (Eq. (5.21)) for the particle/matrix interfaces. To illustrate the method that is used to estimate the key parameters in the PPR cohesive relation, the macroscopic cohesive behavior of PBX 9501 (Tan et al., 2005b) is used, as an example. The material PBX 9501 is a high explosive, which consists of polymeric binder matrix with elastic modulus $E^m = 1$ MPa, Poisson's ratio $\nu^m = 0.499$ and energetic HMX particles with bulk modulus $K^p = 12.5$ GPa. The size distribution of HMX particles can be considered as a bimodal distribution with the large particles having radii $a_1 = 125\mu\text{m}$, and the small particles having radii $a_2 = 4\mu\text{m}$, and their volume fractions of $f_1 = 69.5\%$ and $f_2 = 23.2\%$, respectively. The macroscopic cohesive relation of PBX 9501 between the macroscopic stress $\bar{\sigma}$ (normalized by the elastic modulus \bar{E} of PBX 9501, which is 1 GPa (Gray III et al., 1998)) and the opening displacement can be obtained from mode I fracture test of the modified compact tension specimen, as shown in Figure 5.18. In stage I,

the macroscopic cohesive stress ($\bar{\sigma}$) increases linearly from zero to the macroscopic cohesive strength with a very high slope. In stage II, the macroscopic cohesive stress reaches the macroscopic cohesive strength $\bar{\sigma}_{\max} = 1.66$ MPa. Next, stage III is the softening stage, where the cohesive stress decreases approximately linearly from $\bar{\sigma}_{\max}$ to zero when the separation reaches the final crack opening width. If separation is greater than the final crack opening width of 0.11 mm, the macroscopic cohesive relation is in stage IV, where the interface is completely debonded, and hence the macroscopic cohesive stress is always zero. The macroscopic cohesive fracture energy, or the total area below the cohesive stress-displacement curve in Figure 5.18, is measured as 89 N/m. The initial bulk modulus \bar{K} of PBX 9501 is reported as 1.11 GPa (Gray III et al., 1998).

The important data from the modified compact tension test of PBX 9501, such as the shape of macroscopic cohesive relation, the macroscopic fracture energy, the macroscopic cohesive strength and the initial bulk modulus, can be used to determine the four cohesive parameters: cohesive strength σ_{\max} , cohesive fracture energy ϕ_n , shape parameter α , and initial slope indicator λ_n in the PPR cohesive relation. It is important to note that the stress state ahead the crack tip in the mode I fracture test of the modified specimen can be approximated as a hydrostatic stress state because of large stress triaxiality (McMeeking and Parks, 1979). This approximation helps to apply micromechanics model in hydrostatic tension loading, as presented

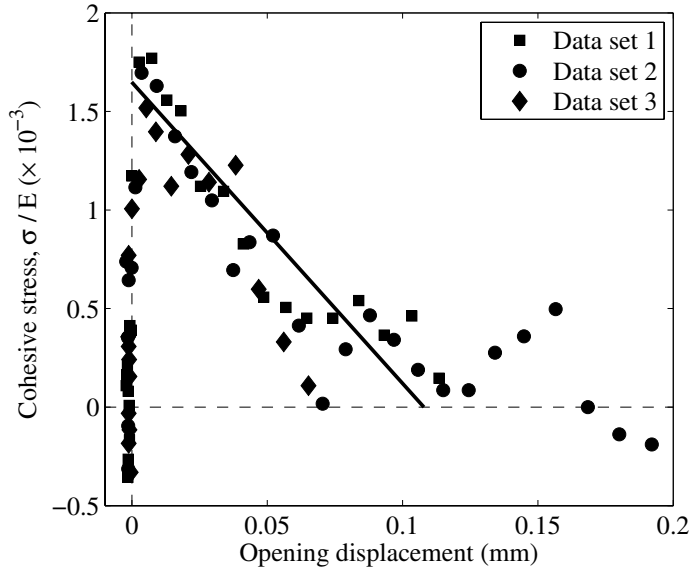


Figure 5.18: Case study: macroscopic cohesive relation of the high explosive material PBX 9501 (Tan et al., 2005b).

in the previous sections, to find the relation of these microscopic cohesive relation parameters to the properties of macroscopic behavior of the material, which are presented next.

Shape of macroscopic cohesive relation: In Figure 5.18, the macroscopic cohesive relation of PBX 9501 shows a linear softening stage after the peak stress. The microscopic cohesive relation is assumed to have a similar linear softening shape. Therefore, the shape parameter α could be estimated as 2.

Macroscopic fracture energy: To obtain the fracture energy of the microscopic cohesive relation, Tan et al. (2005b) proposed using energy balance along the “path of interface debonding” between the total macroscopic fracture energy release and the total microscopic energy release, which accounts for both microscopic fracture energy release from particle/matrix debonding and energy release due to tearing of the matrix. They estimated the fracture energy (ϕ_n) of particle/matrix interface in PBX 9501 as $\phi_n = 81$ N/m.

Initial bulk modulus: At the initial stage of loading the specimen, the normal displacement separation, Δ_n , of the particle/matrix interface is very small, hence the cohesive relation in Eq. (5.21) can be linearized in terms of Δ_n as

$$\sigma^{\text{int}} = k^{\text{int}} \Delta_n \quad (5.24)$$

where $k^{\text{int}} = \frac{\phi_n}{\delta_n^2} \left(\frac{\alpha}{m}\right)^m \left(\frac{m}{\alpha}\right)^{m-1} (m + \alpha)$ is a function of σ_{max} and λ_n . For the case of a linear relation between microscopic cohesive stress and the normal displacement separation under the hydrostatic tension loading, using Mori-Tanaka method, Tan et al. (2005a) derived a formula to determine initial bulk modulus \bar{K} for a composite with two different particle sizes that is given as

$$\bar{K} = \frac{1}{3} \frac{d\bar{\sigma}}{d\bar{\epsilon}} = \left[\frac{1}{K^m} + \frac{9(1-\nu^m)}{2E^m} \frac{f - \sum_{k=1}^2 f_k \alpha_k}{1 - f + \sum_{k=1}^2 f_k \alpha_k} \right]^{-1}, \quad (5.25)$$

where $\alpha_k = \frac{3(1-\nu^m)}{2E^m \left(\frac{1}{k^{\text{int}} a_k} + \frac{1+\nu^m}{2E^m} + \frac{1}{3K^p} \right)}$, and K^m and K^p are the elastic bulk moduli of the matrix and particle, respectively. With the value of initial bulk modulus $\bar{K} = 1.11$

GPa, Eq. (5.25) provides a nonlinear equation in terms of σ_{\max} and λ_n .

Macroscopic cohesive strength: Rae et al. (2002) observed that debonding between particle and matrix appears first for the large particles in PBX 9501. Therefore when the macroscopic cohesive stress $\bar{\sigma}$ reaches its peak (macroscopic cohesive strength), the microscopic cohesive stress of the large particle σ_1^{int} reaches the cohesive strength σ_{\max} , while the microscopic cohesive stress of the small particle σ_2^{int} is lower than the cohesive strength ($\sigma_2^{\text{int}} < \sigma_{\max}$). The relation between the macroscopic cohesive stress and the microscopic cohesive stresses for composite material with two particle sizes is given as

$$\bar{\sigma} = (1 - f)\bar{\sigma}^m + f_1\sigma_1^{\text{int}} + f_2\sigma_2^{\text{int}} . \quad (5.26)$$

The normal displacement separations for each particle size can be obtained by the Mori-Tanaka method as

$$(\Delta_n)_k = a_k \left\{ \frac{3(1 - \nu^m)}{2E^m} \bar{\sigma}^m - \left(\frac{1 + \nu^m}{2E^m} + \frac{1 - 2\nu^p}{E^p} \right) \sigma_k^{\text{int}} \right\} , \quad k = 1, 2 . \quad (5.27)$$

Cohesive relations for each particle size are given as

$$\sigma_k^{\text{int}} = \frac{\phi_n}{\delta_n} \left(\frac{\alpha}{m} \right)^m \left(1 - \frac{(\Delta_n)_k}{\delta_n} \right)^{\alpha-1} \left(\frac{m}{\alpha} + \frac{(\Delta_n)_k}{\delta_n} \right)^{m-1} (m + \alpha) \frac{(\Delta_n)_k}{\delta_n} , \quad k = 1, 2 . \quad (5.28)$$

By substituting Eqs. (5.26) and (5.27) into Eq. (5.28), when $\bar{\sigma}$ reaches $\bar{\sigma}_{\max} = 1.66$ MPa, one can obtain two nonlinear equations in terms of σ_{\max} , σ_2^{int} and λ_n as

$$\sigma_{\max} = h(\sigma_{\max}, \sigma_2^{\text{int}}, \lambda_n) , \quad (5.29)$$

$$\sigma_2^{\text{int}} = g(\sigma_{\max}, \sigma_2^{\text{int}}, \lambda_n) . \quad (5.30)$$

The cohesive strength σ_{\max} and the initial slope indicator λ_n of the PPR cohesive relation can be determined simultaneously from the initial bulk modulus of PBX 9501 and the maximum macroscopic stress. Thus Eqs. (5.29) and (5.30), together with Eq. (5.25) when $\bar{K} = 1.11$ GPa, provide a system of three nonlinear equations with three unknowns σ_{\max} , σ_2^{int} and λ_n . This system can be solved by using a nonlinear equations solver and the solutions for σ_{\max} , σ_2^{int} and λ_n are obtained as 1.6672 MPa, 1.6355 MPa and 0.006, respectively. The results are summarized in Table 5.1.

Table 5.1: Properties of high explosive material PBX9501.

Definition	Symbol	Value
PPR shape parameter	α	2
PPR cohesive fracture energy	ϕ_n	81 N/m
PPR initial slope indicator	λ_n	0.006
PPR cohesive strength	σ_{\max}	1.6672 MPa
Initial effective bulk modulus	\bar{K}	1.11 GPa
Polymeric binder matrix elastic modulus	E^m	1 MPa
Polymeric binder matrix Poisson's ratio	ν^m	0.499
HMX particle bulk modulus	K^p	12.5 GPa
Large particle radius	a_1	125 μm
Small particle radius	a_2	4 μm
Large particle volume fraction	f_1	69.5 %
Small particle volume fraction	f_2	23.2 %
Effective cohesive strength	$\bar{\sigma}_{\max}$	1.66 MPa
Microscopic cohesive stress of the large particle	σ_1^{int}	1.6672 MPa ($\approx \sigma_{\max}$)
Microscopic cohesive stress of the small particle	σ_2^{int}	1.6355 MPa

5.7 Concluding Remarks

Effective macroscopic behavior is investigated by means of an integrated approach involving micromechanics and a computational model. For the micromechanics investigation, the extended Mori-Tanaka model is incorporated with the PPR potential-based cohesive zone model. The computational analysis is performed by utilizing the finite element-based cohesive zone model in two-dimensions (plane strain). The effects of the PPR cohesive parameters, particle size and volume fraction on the constitutive relationship of material with microstructures are investigated for hydrostatic tensile stress state and equi-biaxial tension state. In general, the overall behavior observed considering hydrostatic tensile stress state (Figures 5.3 to 5.8) is qualitatively similar to the behavior observed considering equi-biaxial tension state (Figures 5.14 to 5.17). In addition, the microstructural debonding process is uniform when the macroscopic stress-strain relationship demonstrates hardening or softening behavior (cf. Figures 5.11(a) and 5.12). On the other hand, non-uniform microstructural debonding process is observed when the macroscopic stress-strain relationship provides snap-back instability (cf. Figures 5.11(b) and 5.13). The results of the micromechanics model demonstrate agreement with the results from the computational model. Finally, through multiscale arguments, the cohesive parameters of the PPR model are estimated using macroscopic cohesive behavior of composite material in conjunction with micromechanics theory.

Chapter 6

Adaptive Dynamic Cohesive Fracture Simulation Using Nodal Perturbation and Edge-Swap Operators

Dependence on mesh orientation impacts adversely the quality of computational solutions generated by cohesive zone models. For instance, when considering crack propagation along interfaces between finite elements of $4\mathbf{k}$ structured meshes, both extension of crack length and crack angle are biased according to the mesh configuration. To address mesh orientation dependence in $4\mathbf{k}$ structured meshes, and to avoid undesirable crack patterns, the use of nodal perturbation and edge-swap topological operation is proposed. From a fracture mechanics perspective, the PPR potential-based model is employed for the constitutive relationship of cohesive fracture. Three representative dynamic fracture examples using edge-swap and nodal perturbation operators are provided: crack propagation in the compact compression specimen, local branching instability, and fragmentation. These examples illustrate the features of the present computational framework in simulating a range of physical phenomena associated to cracking.

6.1 Introduction

In finite element analysis, $4\mathbf{k}$ structured meshes are widely utilized while possessing several features of interest. They are easily generated, even for irregular domains, and are convenient to perform mesh refinement with high quality discretization. As illustrated by Table 6.1, a regular $4\mathbf{k}$ mesh is structured both in the topology sense and in the geometry sense. In fact, being topologically structured is one of the major advantages of $4\mathbf{k}$ meshes. The mesh can be represented by a hierarchical topological subdivision, which is suitable for mesh refinement and coarsening (see Chapter 7). Simple, efficient and effective topological operators can be applied in order to locally adapt the mesh (Velho and Gomes, 2000; Celes et al., 2005b).

Table 6.1: Geometrical and topological considerations for cohesive zone model simulations.

Finite element mesh	Geometrically	Topologically
4k	structured	structured
Nodal perturbation	unstructured	structured
Edge swap	structured	unstructured
Nodal perturbation & edge swap	unstructured	unstructured

On the other hand, structured meshes may represent a drawback. For instance, the structured geometry may impose mesh bias in the case of crack propagation simulation, even for highly refined meshes. To address this problem, Papoulia et al. (2006) have proposed the use of pinwheel-based meshes for dynamic crack propagation problems. Because the pinwheel tiling possesses the “isoperimetric property”, any curve in the two-dimensional domain can be represented by edges of the pinwheel-based mesh, as the element size tends to zero (i.e. in the limit sense). However, elements used in numerical analysis are of finite size, generation of pinwheel mesh is non-standard, and the aspect ratio of the resulting mesh, although bounded, still needs improvements (Ganguly et al., 2006).

The discrepancy between the mathematical path of a crack and the path represented by a set of mesh edges can be measured by comparing the associated path lengths. Convergence of path length is meaningful because the energy needed to create a crack is related to its length (Papoulia et al., 2006).

However, besides length convergence, one should also analyze crack path deviation, especially for regular meshes. In quantitative terms, path deviation can be estimated by the Hausdorff distance. Given two arbitrary curves P and Q , with p and q denoting points on those curves, the Hausdorff distance is defined as (Huttenlocher et al., 1993):

$$H(P, Q) = \max(h(P, Q), h(Q, P)) \quad (6.1)$$

where

$$h(P, Q) = \max_{p \in P} \left[\min_{q \in Q} [dist(p, q)] \right] . \quad (6.2)$$

By considering P the discretized path, where p are the vertices along that path, and Q the mathematical path, represented by a line segment, and considering that the endpoints are coincident in both discretized and mathematical paths, the Hausdorff

distance to compute crack path deviation reduces to:

$$H(P, Q) = h(P, Q) \quad . \quad (6.3)$$

Figure 6.1 illustrates the importance of analysing both length convergence and crack path deviation. Figure 6.1(a), obtained from reference (Papoulia et al., 2006), illustrates the discrepancy between a mathematical path and a path represented by a **4k** structured mesh. With the same mesh discretization, the Hausdorff distance can be reduced even further by selecting another discretized shortest path, as shown in Figure 6.1(b). Moreover, Figure 6.1(c) demonstrates that the mesh refinement of the **4k** structured mesh leads to the reduction of the Hausdorff distance.

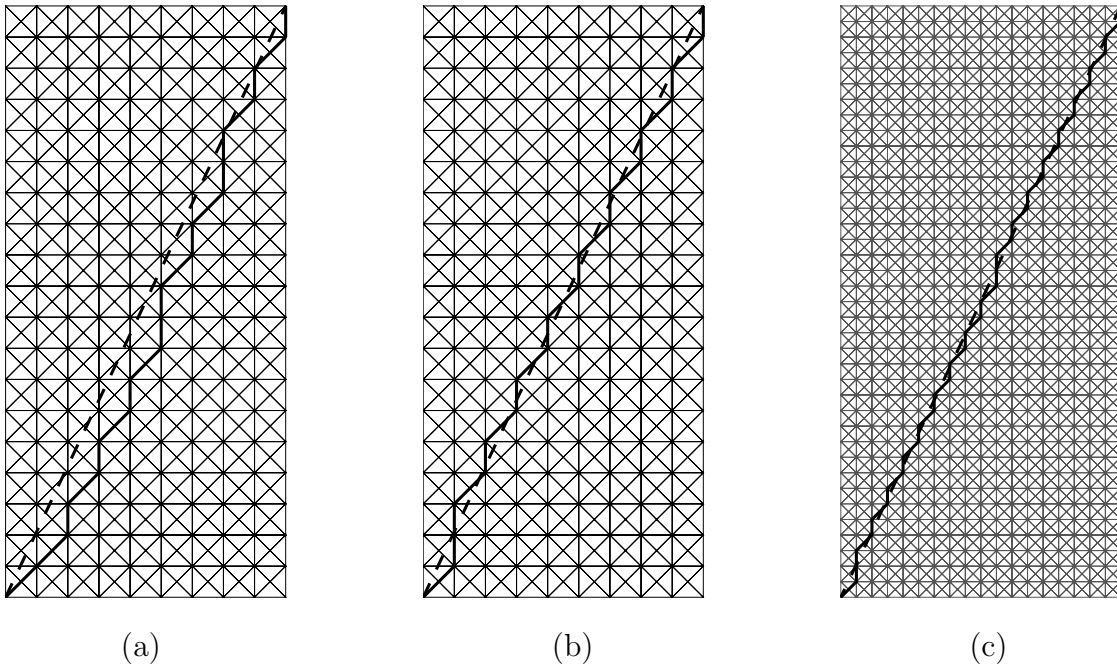


Figure 6.1: Discrepancy between a mathematical path (thick dashed line) and a discrete path (thick solid line). The aspect ratio of the rectangular domain is 1 : 2.11.

However, there is always a finite error between the mathematical length and the length represented by a **4k** structured mesh. For instance, Papoulia et al. (2006) stated that “*no matter how much the mesh is refined, the jagged path will always be approximately 8% longer than the mathematical path*” for standard **4k** structured meshes. To further illustrate, a simple geometric problem is constructed within the 1 by 1 square domain ($OABC$), shown in Figure 6.2(a). The point P is located between the upper left corner (point A) and the upper right corner (point B). The exact

distance (ℓ_{exact}) from the origin (point O) to the point P is $\sqrt{1+x^2}$, i.e. *mathematical length*, where x is a distance between the point A and the point P . Similarly, the path (\overline{OP}) can be also represented by a finite element mesh under the assumption that the path is only described by element boundaries (i.e. the path cannot go through the elements). If one utilizes **4k** structured meshes, the path (\overline{OP}) consists of piecewise linear lines with angles of 45° and 90° . Therefore, the length represented by a **4k** structured finite element mesh (ℓ_{FE}) is the summation of the length \overline{OD} ($\sqrt{2}x$) and the length \overline{DP} ($1-x$) (see Figure 6.2(a)), i.e. *discrete length*. Figure 6.2(b) demonstrates the relative error ($|\ell_{FE}-\ell_{exact}|/\ell_{exact}$) of the discrete length represented by the **4k** structured finite element mesh with respect to the location of the point P ($\overline{AP}(x)$). The **4k** structured mesh is able to represent the exact path when $x = 0$ or $x = 1$, while it provides error up to 8.24 % for the intermediate range. The maximum error occurs when the distance $\overline{AP}(x)$ is equal to $x = \sqrt{2} - 1$ and the angle ($\angle COP$) of 67.5° which is the mean value of 45° and 90° .

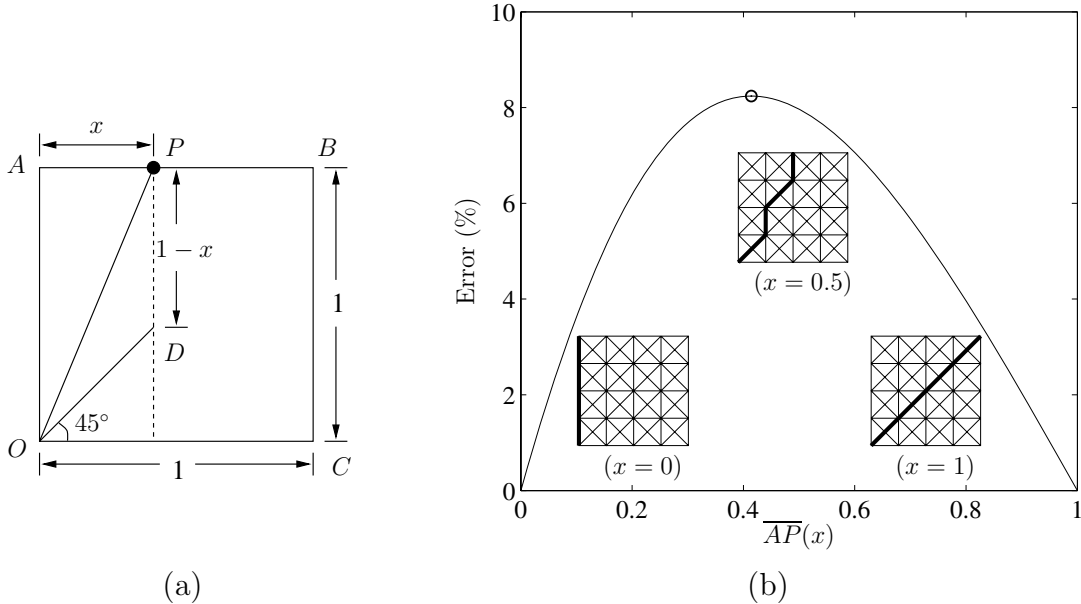


Figure 6.2: (a) Crack path test, and (b) error between the *mathematical length* (\overline{OP}) and the *discrete length* represented by the **4k** structured mesh. The maximum error occurs at $x = \sqrt{2} - 1$ (angle $\angle COP = 67.5^\circ$).

Another feature of **4k** structured meshes is that some internal nodes have eight adjacent edges while others have four adjacent edges, as shown in Figure 6.3(a). In other words, when cohesive crack propagation is considered, some nodes have eight potential directions at 45° increments, while others have four potential directions at 90° increments, as illustrated by Figure 6.3(a). A node that has eight potential di-

rections can have maximum error of 22.5° for the selection of a crack propagation direction, whereas a node that has four potential directions can have maximum error of 45° . Consequently, computational simulations using a $4\mathbf{k}$ structured mesh with cohesive elements may lead to undesirable (e.g. zigzag) crack patterns. For example, let us assume the potential crack path, as illustrated by the dashed line in Figure 6.3(b). Because the $4\mathbf{k}$ mesh is not able to represent the potential crack path, computational simulation may provide a zigzag crack pattern, as shown in Figure 6.3(c).

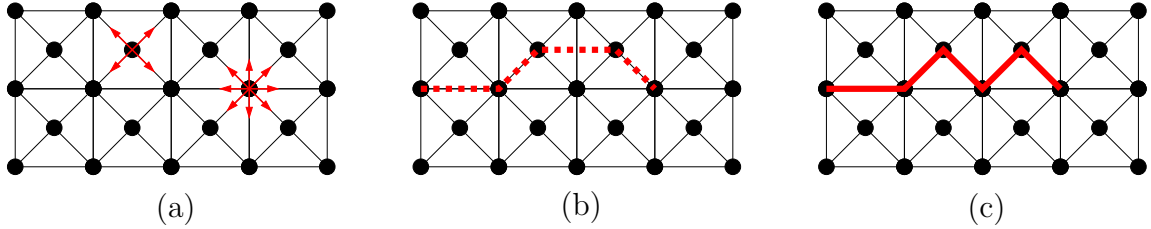


Figure 6.3: Schematic description of a potential zigzag pattern.

In order to reduce the error between the mathematical length and a length represented by edges of a $4\mathbf{k}$ mesh, and to alleviate zigzag crack patterns, this chapter proposes the use of nodal perturbation (NP) and/or edge-swap (ES) topological operator. The original $4\mathbf{k}$ meshes are geometrically and topologically structured. The nodal perturbation leads to geometrically unstructured meshes, while the edge swap provides locally unstructured meshes (topologically). Thus, both the nodal perturbation and the edge-swap operator result in geometrically and topologically unstructured meshes, as summarized in Table 6.1. As proof-of-concept, the effects of nodal perturbation factor and edge-swap operator on representation of crack length, angle, and path deviation are investigated in this work. *Computational experiments demonstrate that, for practical levels of mesh refinement, discrepancy between mathematical and discretized paths reduces more rapidly for modified $4\mathbf{k}$ meshes, as proposed in this chapter, than for pinwheel-based meshes.*

This chapter investigates dynamic mixed-mode crack propagation, microbranching, and fragmentation by means of $4\mathbf{k}$ meshes with nodal perturbation and/or edge-swap operator. The PPR potential-based model with the coupled unloading/reloading relation is used for the constitutive relationship of mixed-mode fracture. The topological data structure TopS (Celes et al., 2005a,b) is employed to maintain adjacency relationships under adaptive insertion of cohesive elements and edge-swap operation. This chapter is organized as follows. First, geometrical improvement of $4\mathbf{k}$ meshes is addressed by introducing nodal perturbation (Section 6.2), while topological improvement is achieved by employing edge-swap operator (Section 6.3). Path

convergence is quantified by comparing **4k** meshes with pinwheel-based meshes in Section 6.4. Section 6.5 explains algorithms of the nodal perturbation and the edge swap. Section 6.6 presents three numerical examples: compact compression specimen tests, microbranching experiments, and fragmentation. Some remarks on topology of **4k** meshes and pinwheel-based meshes are given in Section 6.7. Finally, Section 6.8 summarizes the key findings of this study.

6.2 Toward Unstructured Geometry – Nodal Perturbation (NP)

In order to reduce the maximum error of the discrete length that exists in the **4k** structured mesh, the internal nodes of a mesh are randomly perturbed (or shaken), with respect to a nodal perturbation (NP) factor and a given mesh quality metric. The algorithm for the nodal perturbation is explained in Section 6.5, and the effect

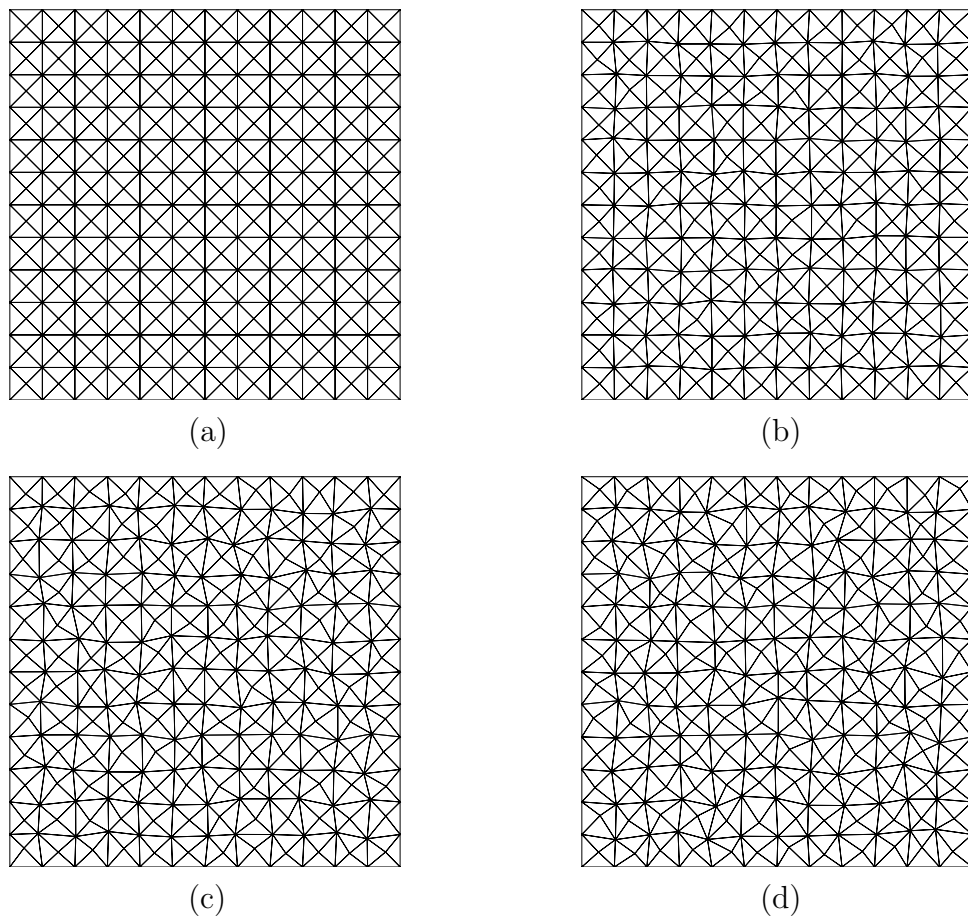


Figure 6.4: Effect of the nodal perturbation (NP) factor on a finite element mesh: (a) NP = 0.0 (unperturbed), (b) NP = 0.1, (c) NP = 0.2, and (d) NP = 0.3.

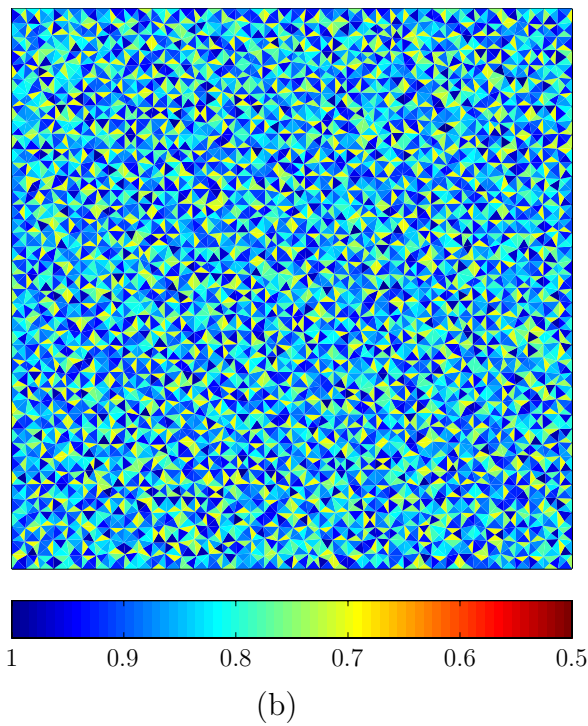
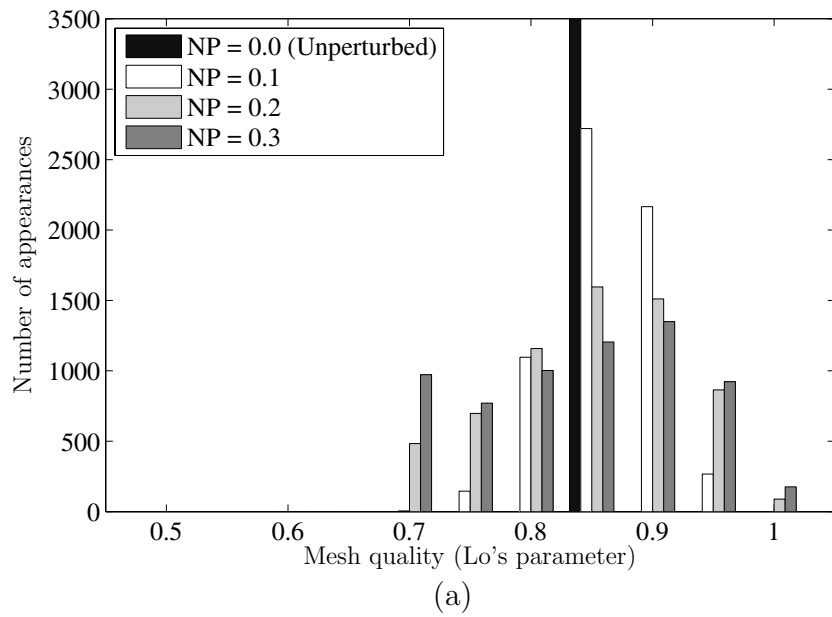


Figure 6.5: Mesh quality estimation: (a) histogram and (b) Lo's parameter for each element considering $NP = 0.3$. Notice that all 6400 elements in the unperturbed mesh ($NP = 0.0$) have Lo's parameter of 0.866.

of the nodal perturbation factors on a **4k** structured mesh is illustrated in Figure 6.4. The NP factors used in this study are 0.0 (unperturbed), 0.1, 0.2 and 0.3 with a fixed mesh quality parameter (e.g. Lo’s parameter (Lo, 1989)). The higher the nodal perturbation factor, the more randomness in the finite element mesh.

The mesh quality is estimated by the Lo’s parameter (Lo, 1989), which is defined as $4\sqrt{3}A/\sum_{i=1}^3 \ell_i^2$ where A is the area of a triangle and ℓ_i represents the length of edges. The parameter varies from 0 to 1. The Lo’s parameter is zero when the area of a triangle is equal to zero, and one for an equilateral triangle. Within a square domain of (1 : 1), a **4k** mesh grid of 40 by 40 is constructed, resulting in 6400 triangular elements, with the NP factors of 0.0 (unperturbed), 0.1, 0.2 and 0.3. The minimum mesh quality parameter is selected as 0.7, which is generally acceptable for finite element simulations. The histogram of the mesh quality with respect to the NP factors is illustrated in Figure 6.5(a). The Lo’s parameter of all elements is 0.866 for the zero nodal perturbation factor (NP = 0.0). The increase of the nodal perturbation factor leads to a broader distribution of the Lo’s parameter. Figure 6.5(b) demonstrates the spacial distribution of the Lo’s parameter for each element in the 40 by 40 **4k** mesh with NP = 0.3.

In the following subsections, the effects of the nodal perturbation factor are investigated by two examples: crack length convergence and crack angle convergence. The crack length convergence investigation compares a mathematical length to a length represented by edges of a finite element mesh, while the crack angle convergence investigation compares an arbitrarily given angle to a geometrically averaged angle.

6.2.1 Crack Length Convergence

For the crack length convergence investigation, the exact distance (ℓ_{exact}) between two points is compared to the shortest length along edges of finite element meshes (ℓ_{FE}). One can find the shortest geometrical crack length between two arbitrary points by using, for instance, the Dijkstra’s algorithm (Dijkstra, 1959). This study employs two cases: the worst and the best cases in a structured **4k** mesh for the representation of a crack geometry. The worst case uses a 1 by 2.4 rectangular domain so that a given problem provides approximately the maximum error of a crack length in the **4k** structured mesh. The exact crack length from the lower left corner $(x, y) = (0, 0)$ to the top right corner $(x, y) = (1, 2.4)$ is 2.6, and the angle of the path is $\tan^{-1}(2.4) = 67.38^\circ$ which is close to the mean value of 45° and 90° . The rectangular region is discretized into 5×12 , 10×24 , 20×48 and 40×96 finite element

meshes whose element sizes (i.e. the longest edge in an element) are 0.2, 0.1, 0.05 and 0.025, respectively. The internal nodes of each mesh are perturbed with NP = 0.0 (unperturbed) 0.1, 0.2 and 0.3.

The effect of the NP factors on the discrete crack length is investigated with the mesh grid of 10×24 (element size = 0.1). One hundred meshes are generated and

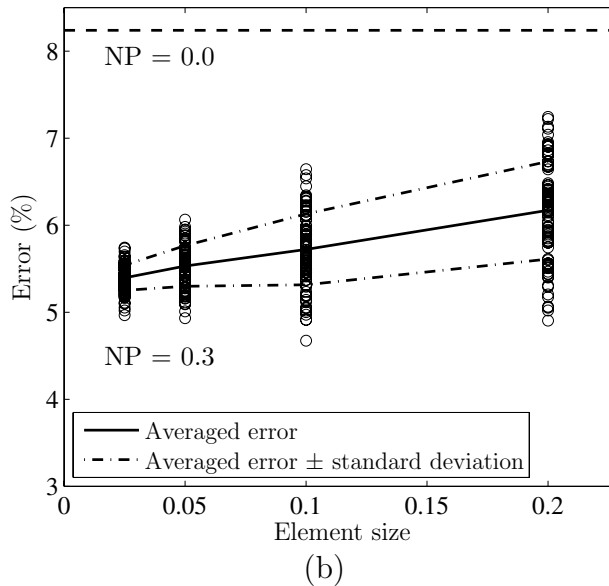
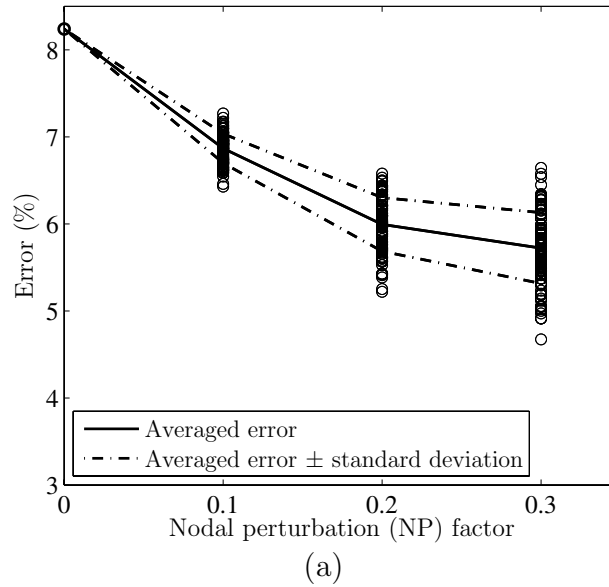


Figure 6.6: Error with respect to (a) nodal perturbation (NP) factor considering 10×24 mesh grid, and (b) element size considering the nodal perturbation factor of 0.3.

tested for each of the nodal perturbation factors, and all the results are plotted using white circles, as shown in Figure 6.6(a). The mean and standard deviation of error are plotted in solid line and dashed-dot lines, respectively. When the nodal perturbation factor is equal to zero ($NP = 0.0$), the shortest length in the finite element mesh is always 2.814 and its error is 8.24%. However, the increase of the NP factor results in a broader distribution of error level and lower averaged error. Next, with the same nodal perturbation factor of 0.3 ($NP = 0.3$), the influence of element sizes on the discrete crack length is investigated and the results are plotted in Figure 6.6(b). The larger the element size used, the wider is the range of error level. Moreover, notice that *the mesh refinement reduces both maximum and averaged error level*.

For the best case scenario, a **4k** structured mesh is able to represent the mathematical length along the 0° , 45° and 90° directions. Thus, a 2.4 by 2.4 square domain is discretized into a 24×24 **4k** mesh. The mathematical length between the lower left corner $(0, 0)$ and the upper right corner $(2.4, 2.4)$ is compared to the shortest length represented by edges of a **4k** mesh with the NP factors of 0.0 (unperturbed), 0.1, 0.2 and 0.3. Similarly, one hundred meshes are generated for each NP factor. All the results are plotted using white circles, and the averaged error and the standard deviation are described with solid line and dashed-dot lines, respectively, as shown in Figure 6.7. The increase of NP leads to the increase of the error in crack length because a **4k** structured mesh (i.e. no nodal perturbation) is able to precisely repre-

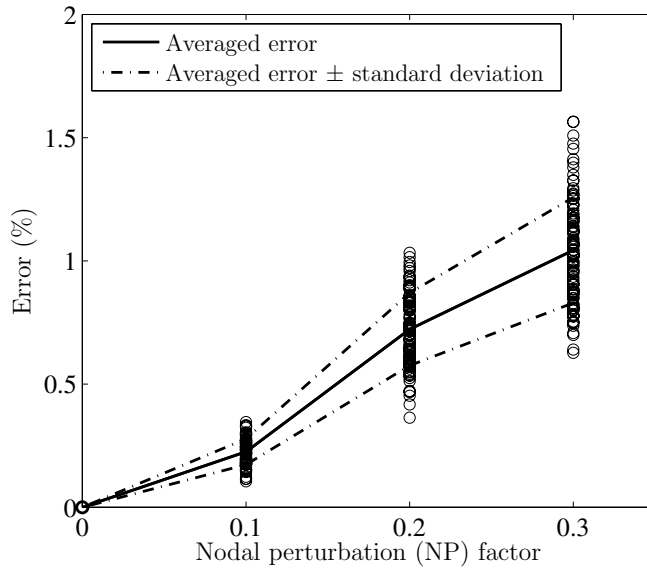


Figure 6.7: Error with respect to the nodal perturbation (NP) factor along the 45° direction.

sent a straight line along the 45° direction. However, the additional error along the 45° direction, introduced by the nodal perturbation, is less than the error reduction along the 67.38° direction due to the nodal perturbation (cf. Figure 6.6(a)).

6.2.2 Crack Angle Convergence

For the crack angle convergence study, an arbitrarily given angle (θ) is compared to a geometrically obtained angle (θ_{FE}). An averaged geometric angle (θ_{FE}) is obtained as follows. First, from a source point, one locally searches the closest edge direction with respect to a given angle (θ). Next, along the edge direction, one moves the source point to the adjacent point. One repeats the previous procedure until the source point reaches the domain boundary. Then, an averaged geometric angle is approximated by connecting the first source point to the last source point.

In this study, the arbitrarily angle (θ) is first selected as 67.38° within the 2.4 by 2.4 square domain (e.g. dashed line in Figure 6.8), which is the same as the angle in the previous length investigation. The domain is discretized into the 24 by 24 mesh grid, which leads to the element size of 0.1 . With the nodal perturbation factors of 0.0 (unperturbed), 0.1 , 0.2 and 0.3 , two hundred meshes are generated for each nodal perturbation factor. When the nodal perturbation factor is equal to zero, the geometrically obtained angle is always 45° , as shown in Figure 6.8(a). This is because 45° is always the closest direction for the target angle ($\theta = 67.38^\circ$). However, the nodal

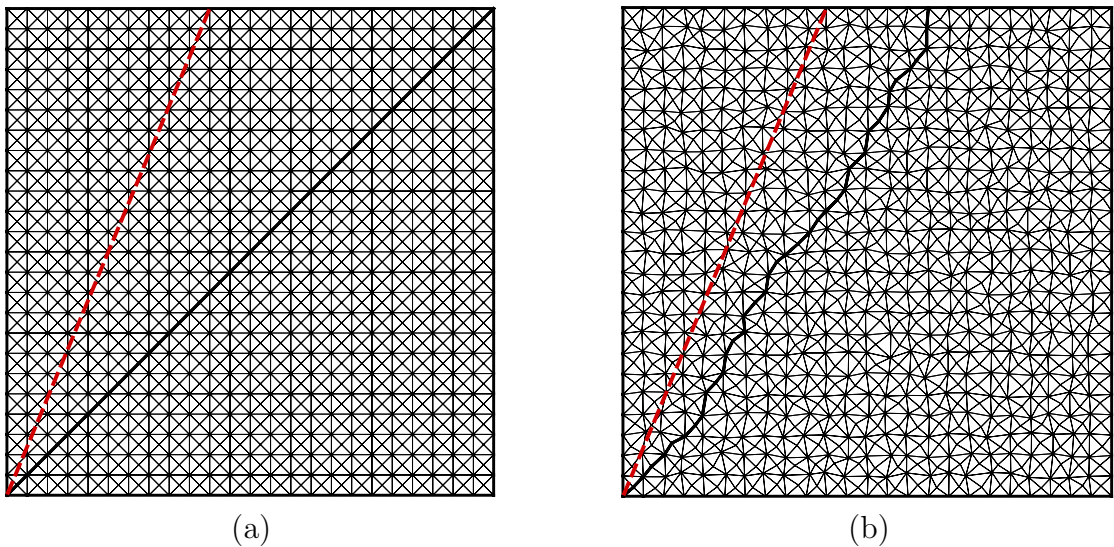


Figure 6.8: Representative results of crack angle convergence for (a) nodal perturbation factor of 0.0 ($NP = 0.0$), and (b) nodal perturbation factor of 0.3 ($NP = 0.3$).

perturbation factor improves the results of crack angle convergence. For example, Figure 6.8(b) shows the result of crack angle convergence using nodal perturbation factor of 0.3 ($NP = 0.3$), and the resulting averaged geometric angle of 59.7° . The histogram of the geometrically obtained angles (θ_{FE}) is plotted in Figure 6.9 with respect to the NP factors. The Gaussian curves are fitted to the histogram for each nodal perturbation factor. The nodal perturbation factor of 0.1 ($NP = 0.1$) results in the most number of appearance of θ_{FE} around 61.6° , and the nodal perturbation factors of 0.2 ($NP = 0.2$) and 0.3 ($NP = 0.3$) lead to the highest number of appearances around 59.7° . The distribution of the number of appearances demonstrates similar pattern (e.g. a bell-shape) across the nodal perturbation factors. Thus, the nodal perturbation factors ranging from 0.1, to 0.3 provide a similar degree of error level in this crack angle convergence example.

When the arbitrary angle (θ) is selected as 45° , the geometrically obtained angle (θ_{FE}) is always 45° for all NP factors (0.1, 0.2 and 0.3). Therefore, the nodal perturbation improves the results of crack angle convergence for the arbitrarily angle of 67.38° without introducing error in the geometrically obtained angle for the arbitrary angle of 45° .

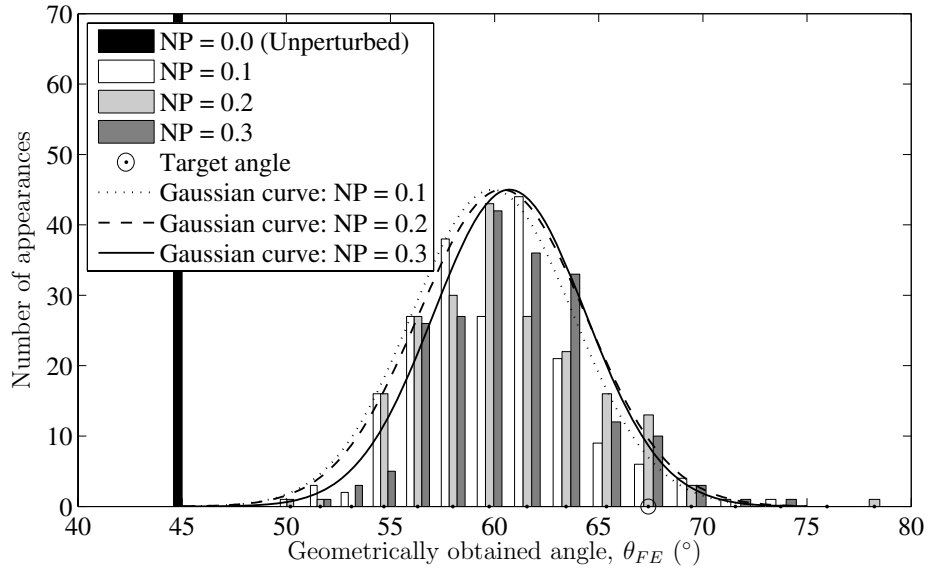


Figure 6.9: Number of appearances of geometrically obtained angles (θ_{FE}) for given nodal perturbation (NP) factors.

6.3 Toward Unstructured Topology – Edge Swap (ES)

In order to reduce undesirable crack patterns (e.g. zigzag) and to further improve the crack angle and length convergence, the edge-swap topological operator is introduced. This operator requires local change of connectivity information. However, it does not introduce additional nodes, and therefore, the original geometry, with respect to nodal location, remains the same.

Due to the edge-swap operator, all the internal nodes have the same number of potential directions. In $4k$ structured meshes with the edge-swap operator, the angle between two potential adjacent edges is initially 45° , and thus the maximum error of the crack direction is locally 22.5° . The edge-swap operator in $4k$ meshes, therefore, can lead to smoother crack patterns in computational simulations than without the edge-swap operator. For example, if physics dictates a crack growth along the horizontal direction (Figure 6.10(a)), one can activate the edge-swap topological operator (Figure 6.10(b)), and the crack patterns become smoother (e.g. Figure 6.10(c)). The edge-swap operator has also been utilized in a randomized incremental algorithm for the construction of planar Voronoi diagrams and Delaunay triangulations (Guibas et al., 1992).

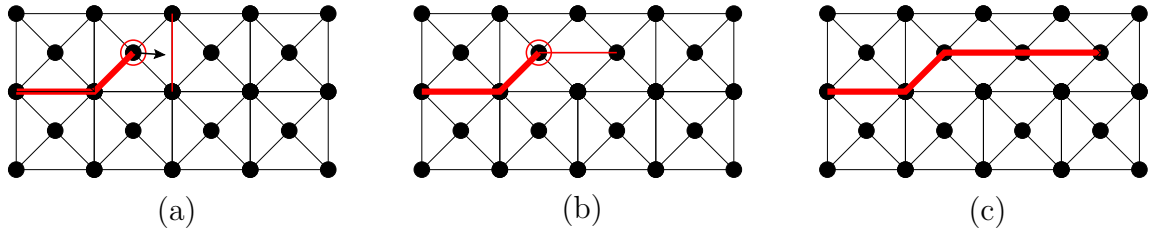


Figure 6.10: Three successive mesh instances showing a schematic description of the edge-swap (ES) operator.

In order to further investigate the influence of the edge-swap operator, the crack length convergence and the crack angle convergence examples are also utilized in this section. For comparison purposes, the two examples are the same as the ones in Section 6.2.

6.3.1 Crack Length Convergence

The 1 by 2.4 domain is discretized into a 10×24 grid. With the nodal perturbation factors of 0.0, 0.1, 0.2 and 0.3, one hundred meshes are generated for each nodal

perturbation factor. The shortest discrete length is obtained in conjunction with the edge-swap operator. The results are described by white circles and the averaged error is plotted with solid line (Figure 6.11(a)). For comparison purposes, the averaged error without the edge-swap operator (shown in Figure 6.6(a)) is plotted with dashed-dot line. According to Figure 6.11(a), the increase of the NP factor results in the decrease of the averaged error and a wider distribution of the shortest discrete length.

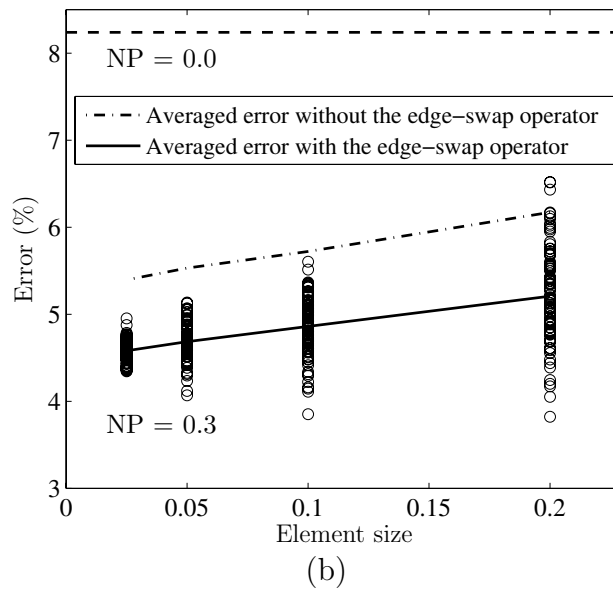
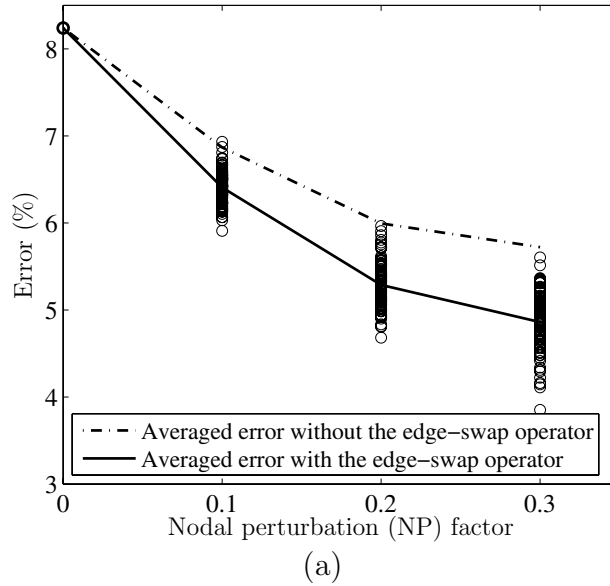


Figure 6.11: Error with respect to (a) the nodal perturbation factor and (b) element size in conjunction with the edge-swap operator.

The use of the edge-swap operator reduces the averaged error (Figure 6.11(a)) compared to without the edge-swap case (Figure 6.6(a)). Additionally, within the same domain, the effect of element size (0.2, 0.1, 0.05, 0.025) on a discrete crack length is observed in conjunction with the edge-swap operator and $NP = 0.3$. Figure 6.11(b) illustrates the error of discrete length with respect to element size. The mesh refinement leads to the decrease of the averaged error and a narrower distribution of the shortest discrete length. The edge-swap operator further reduces the error compared to the case without the edge swap (Figure 6.6(b)).

6.3.2 Crack Angle Convergence

The 2.4 by 2.4 domain is discretized into 24 by 24 finite element mesh grid, and nodal perturbation factors of 0, 0.1, 0.2 and 0.3 are applied to the finite element mesh. Similarly, for a given angle ($\theta = 67.38^\circ$), an averaged geometrical angle (θ_{FE}) is obtained by searching locally for a direction, which is the closest angle of an edge to the given angle. When a node has four original possible directions, four additional directions, which are associated with the edge swap, are also considered for potential search directions. Figure 6.12 illustrates the number of appearances of the geometrically obtained angles (θ_{FE}) from the finite element meshes, considering the edge-swap

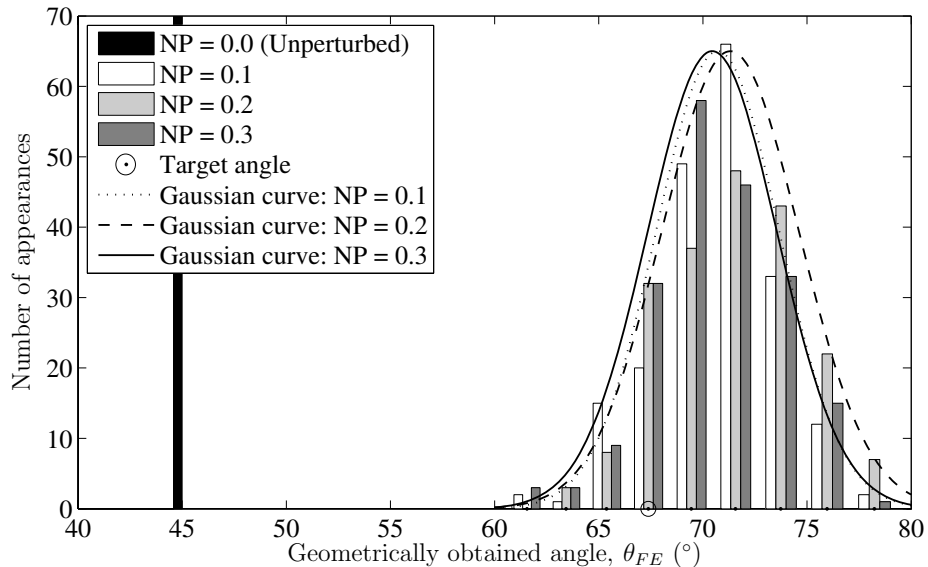


Figure 6.12: Number of appearances of geometrically obtained angles (θ_{FE}) with respect to the nodal perturbation (NP) factor in conjunction with the edge-swap (ES) operator.

operator. The Gaussian distribution is fitted to the histogram, as shown in Figure 6.12. The highest number of appearance occurs at the angle of 71.6° for the nodal perturbation factors of 0.1 and 0.2, while the highest number of appearance is at the angle of 69.4° for the nodal perturbation factor of 0.3. These angles (with the edge swap) are closer to the target angle than the previous investigation (without the edge swap, shown in Figure 6.9). Moreover, the distribution of the geometrically averaged angles with the edge-swap operator is narrower than the distribution without the edge-swap operator (compare Figures 6.12 and 6.9).

6.4 Computational Quantification of Isoperimetric Property

Path convergence of $4\mathbf{k}$ meshes with nodal perturbation and edge swap is quantified in conjunction with a computational experiment. First, the isoperimetric property is estimated by assessing length convergence of paths that connect pairs of vertices in the meshes to the corresponding straight lines. The results are compared with pinwheel-based meshes, which are known to possess the isoperimetric property in the limit sense (Radin and Sadun, 1996; Papoulia et al., 2006). Then, the Hausdorff distance of the shortest path in each mesh, with respect to a straight line, is computed and compared.

A sample rectangular domain (Ω) with dimensions 2 by 1 is discretized by four types of finite element mesh (Ω_{FE}). The first mesh type (Type I) is obtained from a pinwheel tiling by splitting triangles that have a hanging node (Ganguly et al., 2006) (e.g. Figure 6.13(a)). Pinwheel tiles are described by thick solid lines, while additional edges, which eliminate hanging nodes in pinwheel tiles, are illustrated by thin solid lines in Figure 6.13(a). The second type (Type II) is generated from a pinwheel tiling (thick solid line in Figure 6.13(b)) by applying a triangular subdivision (thin solid line in Figure 6.13(b)). Notice that Figures 6.13(a) and (b) have the same pinwheel tiling (i.e. same thick solid lines) but different ways to handle hanging nodes (i.e. different thin solid lines). Next, $4\mathbf{k}$ meshes are generated by using the nodal perturbation factor of 0.3 without the edge-swap operator (Type III), as shown in Figure 6.13(c). Finally, $4\mathbf{k}$ meshes with the nodal perturbation ($NP = 0.3$) and the edge-swap operator are employed (Type IV). Available edge-swap operations in a $4\mathbf{k}$ mesh, for example, are described by the thick dashed line used for crack path representation (Figure 6.13(d)).

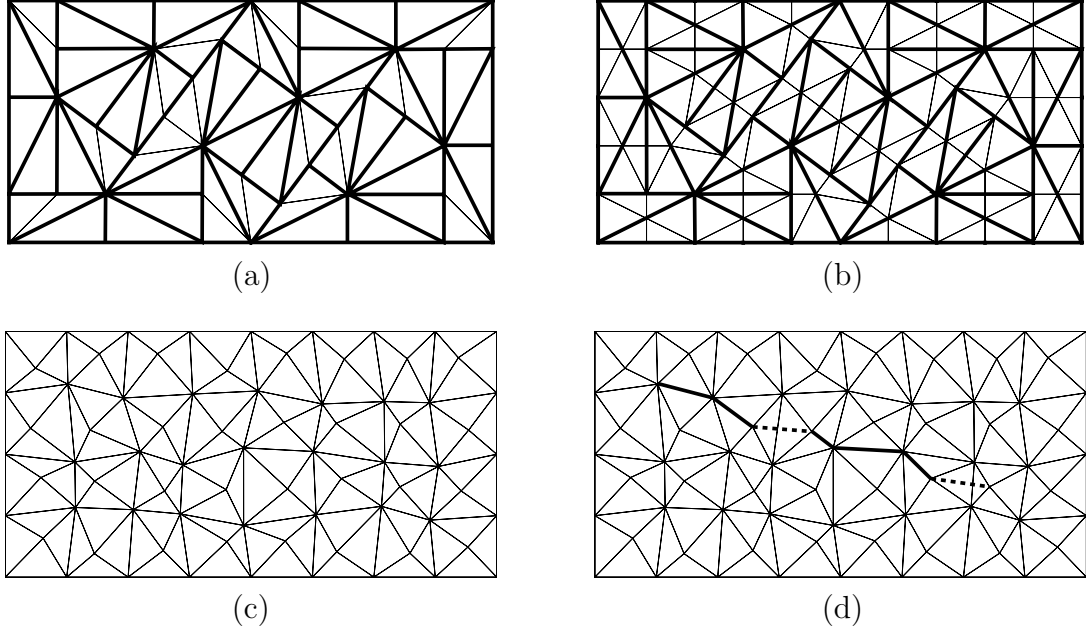


Figure 6.13: Examples of each mesh type: (a) Type I, (b) Type II, (c) Type III, and (d) Type IV.

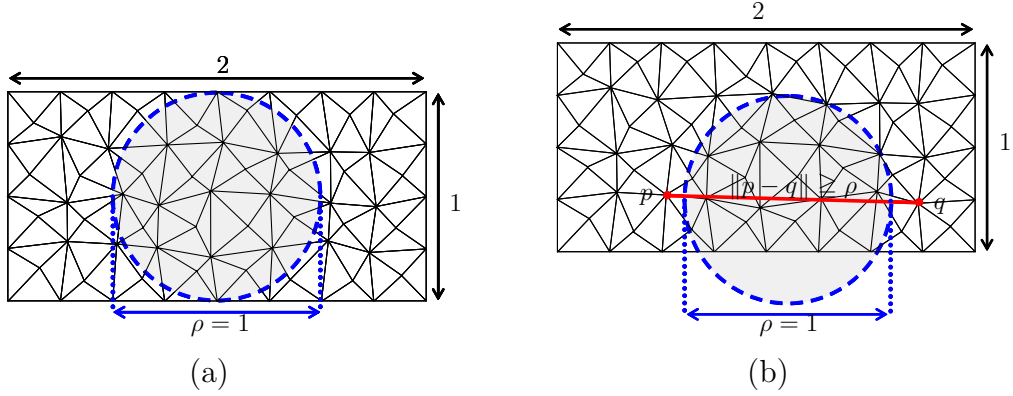


Figure 6.14: (a) Illustration of the parameter ρ in the rectangular domain, and (b) constraint for the set of vertices (p, q) related to the parameter ρ .

In order to quantify the isoperimetric property of these four mesh types, the ρ -path deviation ratio (Ganguly et al., 2006) is defined as

$$\text{dev}_\rho(\Omega_{FE}) = \max \left(\frac{\ell_{FE}(p, q)}{\|p - q\|} : p, q \in V(\Omega_{FE}) \text{ and } \|p - q\| \geq \rho \right) \quad (6.4)$$

where $V(\Omega_{FE})$ is the set of all vertices of a finite element mesh (Ω_{FE}) , and $\|p - q\|$ is the distance from p to q . In addition, $\ell_{FE}(p, q)$ is the shortest path represented by edges of a finite element mesh (see Sections 6.2 and 6.3). A positive parameter ρ is

selected as 1 so that the 2 by 1 domain contains a disk of diameter ρ , shown in Figure 6.14(a). The parameter ρ limits the range of the considered pairs of vertices (p, q) to the ones whose distance to each other is greater than or equal to ρ (Figure 6.14(b)). The ρ -path deviation ratio ($\text{dev}_\rho(\Omega_{FE})$) is the maximum relative error in representing a straight line by utilizing a finite element mesh (Ω_{FE}). Notice that Ganguly et al. (2006) performed the same computational experiment to quantify the isoperimetric property of a mesh based on a pinwheel-tiling.

For a **4k** mesh with the nodal perturbation factor of 0.3, twelve **4k** mesh grids are utilized. For each grid, five randomly perturbed meshes are tested, and the averaged deviation ratio ($\text{dev}_\rho(\Omega_{FE})$) among the five meshes is taken. Then, the ρ -path deviation ratio of the **4k** mesh with the nodal perturbation (Types III and IV) is compared with the other two mesh types which are based on a pinwheel tiling (Types

Table 6.2: ρ -path deviation ratio (dev_ρ) and Hausdorff distance ($H(p, q)$) with respect to the number of elements.

Mesh type I			Mesh type II		
# of elem	dev_ρ	$H(p, q)$	# of elem	dev_ρ	$H(p, q)$
16	1.3416	0.4	6	1.1441	0.3536
68	1.1948	0.3123	30	1.1749	0.2481
360	1.1843	0.0917	150	1.1755	0.12
1764	1.1264	0.0675	750	1.1156	0.1136
8880	1.0831	0.0552	3750	1.0827	0.0333
44292	1.0595	0.0414	18750	1.0606	0.0442
221640	1.0441	0.0291	93750	1.0456	0.0602
			468750	1.037	0.0309

		Mesh type III		Mesh type IV	
# of elem	mesh grid	dev_ρ	$H(p, q)$	dev_ρ	$H(p, q)$
8	2×1	1.1700	0.3986	1.0964	0.4158
32	4×2	1.2143	0.2511	1.1115	0.2123
128	8×4	1.1523	0.1926	1.0887	0.1672
648	18×9	1.1062	0.1386	1.0700	0.0996
1568	28×14	1.0904	0.1031	1.0650	0.0958
3528	42×21	1.0817	0.0858	1.0581	0.0880
8712	66×33	1.0739	0.0459	1.0537	0.0509
18432	96×48	1.0674	0.0519	1.0512	0.0501
43808	148×74	1.0619	0.0482	1.0476	0.0342
93312	216×108	1.0591	0.0427	1.0460	0.0323
220448	332×166	1.0557	0.0413	1.0438	0.0274
468512	484×242	1.0537	0.0242	1.0425	0.0276

I and II). The ρ -path deviation ratio versus the number of elements is provided in Table 6.2, and is plotted in Figure 6.15(a) on semi-logarithmic scale. The **4k** meshes with the nodal perturbation and the edge swap (Type IV) perform better than the pinwheel-based meshes in representing a straight line with approximately up to 0.1 million elements. In addition, in order to obtain the deviation ratio of 1.1, the required

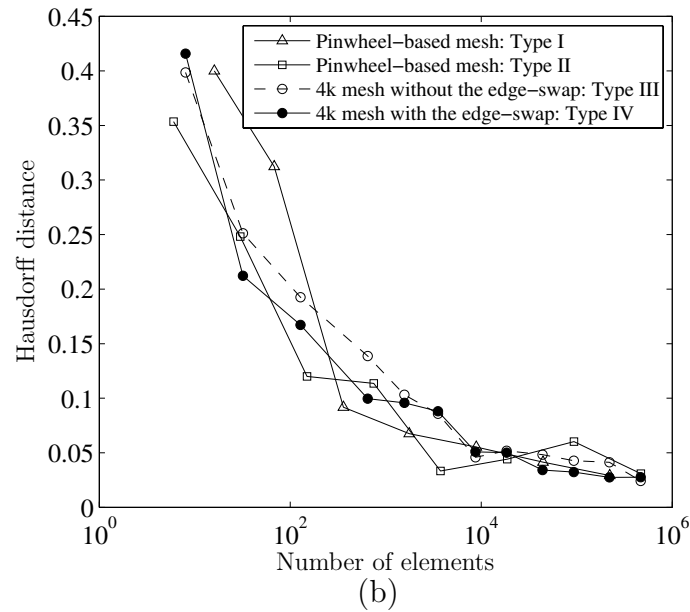
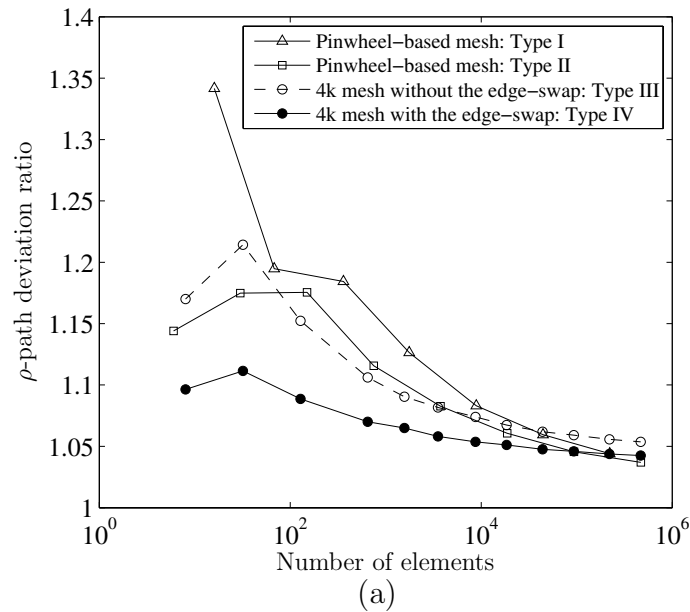


Figure 6.15: Quantification of the isoperimetric property in conjunction with (a) the ρ -path deviation ratio, and (b) the Hausdorff distance.

number of elements is approximately 100 for the **4k** meshes (Type IV), while it is 1000 for the pinwheel-based meshes (Types I and II), i.e. one order difference, in this example.

The Hausdorff distance between the shortest path in each mesh grid and the corresponding straight line is estimated based on the results above. For each **4k** mesh grid, the average Hausdorff distance of the shortest paths of the five perturbed meshes is taken. Then, it is compared with the Hausdorff distances of the shortest paths in the two other mesh types (Types I and II). The Hausdorff distance versus number of elements is presented in Table 6.2 and plotted in Figure 6.15(b). A general decreasing trend is observed for Hausdorff distance values as the number of elements increases for all the four mesh types.

The achieved results show that **4k** mesh with nodal perturbation and edge swap can perform either similarly or better than pinwheel-based mesh for some practical grid sizes. Although the pinwheel-based mesh has the isoperimetric property (in the limit sense), the exact path cannot be represented in numerical analysis (based on discretization). This is because the isoperimetric property assures spatial convergence only in the limit, and, in finite element analysis, the number of elements is finite.

6.5 Nodal Perturbation and Edge Swap Algorithm

The nodal perturbations and edge-swap operator are implemented within the framework of TopS. The nodal perturbation algorithm works as follows. First, the internal nodes of the mesh are traversed randomly. For each of them, one computes its minimum distance to the corresponding opposite edges in the incident elements. The node is then displaced by the computed distance multiplied by a fixed perturbation factor, along a randomly chosen direction. After applying the nodal perturbation, a simple Laplacian smoothing technique (Field, 1988) is utilized in order to improve the overall mesh quality. It is done by interactively averaging the coordinates of internal nodes. A mesh quality metric (e.g. Lo's parameter (Lo, 1989)) is used to check whether minimum quality parameters are achieved and thus determine the convergence of the algorithm. At each iteration step, all the elements of the mesh are visited. For each element that does not meet the required quality standards, the positions of its nodes are displaced by the average of the distance vectors to the corresponding neighbors on the incident edges. The displacement is computed with a simple arithmetic mean scaled by a fixed relaxation parameter set (ϕ) in the interval

[0, 1]. This is given by the following expression:

$$\mathbf{p}_0^{t+1} = \mathbf{p}_0^t + \frac{\phi}{n} \sum_{i=1}^n (\mathbf{p}_i^t - \mathbf{p}_0^t) \quad (6.5)$$

where \mathbf{p}_0^t is the position of the current node at step t , \mathbf{p}_i^t is the position of its corresponding i^{th} neighbor node, and n is the number of adjacent edges.

The edge-swap algorithm works by simply removing the two triangles adjacent to a given edge and inserting two new other triangles with the appropriate nodal incidence. The callback mechanism of TopS, explained in Section 4.3, is used to notify the application of the changed entities, such that the attached attributes can be correctly transferred.

In computational simulation, if the edge swap is applied to a $4\mathbf{k}$ structured mesh, a mid-node of the swapped edge remains at the same location for six-node triangular elements (Figure 6.16(a)). When the edge-swap operator is utilized in a perturbed mesh, the mid-node of the swapped edge is relocated so that the edge becomes a straight line (Figure 6.16(b)). Due to the modification of the nodal coordinates, nodal quantities of the relocated node are updated through the interpolation of nodal quantities. The original $4\mathbf{k}$ path (e.g. shaded quadrilateral) is mapped into a 2 by 2 square domain (e.g. $\xi - \eta$ coordinates) by using the nine Lagrange shape functions with the nine gray solid nodes, i.e. $\mathbf{x} = \sum_{i=1}^9 \mathbf{N}_i(\xi, \eta) \mathbf{x}_i$ (see Figure 6.16(b)). Then, the relocated nodal point in $\xi - \eta$ coordinates is calculated, and the nodal quantities, such as displacement, velocity and acceleration, are interpolated from the nine gray nodes by using the nine Lagrange shape functions.

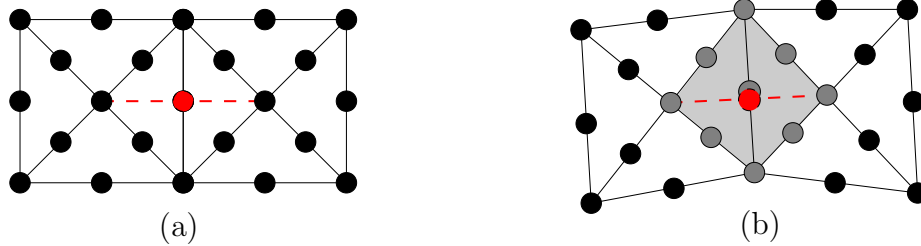


Figure 6.16: Location of the mid-point in the edge-swap operator: (a) $4\mathbf{k}$ structured mesh, and (b) $4\mathbf{k}$ perturbed mesh.

6.6 Numerical Examples

The nodal perturbation and the edge-swap operators are employed for dynamic fracture simulations. The nodal perturbation is applied to a finite element mesh before computational simulation, while the edge-swap operator is adaptively requested during computation. The computational implementation such as time integration, the topology based data structure TopS, and the unloading/reloading relationship, are presented in Chapter 4. This section provides three examples: compact compression specimen tests, microbranching experiments and fragmentation simulations.

6.6.1 Compact Compression Specimen (CCS) Test

The compact compression specimen (CCS) test was developed by Rittel and Maigre (1996) to investigate mixed-mode dynamic crack initiation in PMMA. The CCS is fractured by applying the impact with a Hopkinson bar. The geometry and the boundary conditions of the CCS is shown in Figure 6.17. The incident pulse is applied on the left side of the specimen by an incident bar whose diameter is 16.5 mm. The magnitude of the pulse is approximately 2.2 kN, and the pulse lasts about 350 μs . They observed that a crack initiated by forming angle at a kink of about 45°, and the dynamic stress intensity factor reached an experimental value of the fracture toughness at time $t = 96 \sim 126$ (μs). Previously, Papoulia et al. (2006) utilized cohesive surface elements with reduced dimension to investigate convergence of a crack initiation angle. Menouillard et al. (2008) simulated the CCS test with the

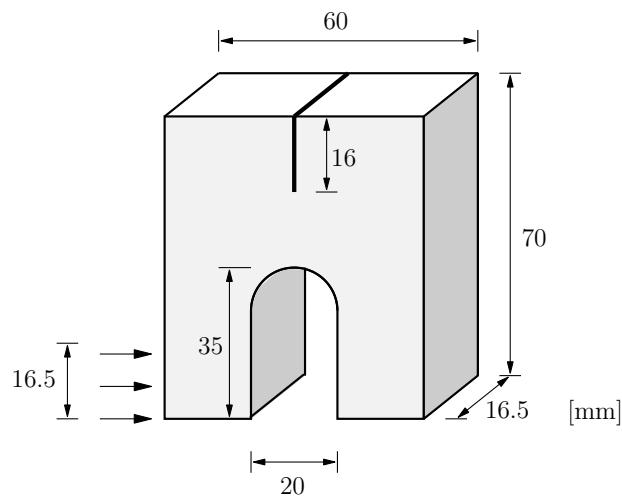
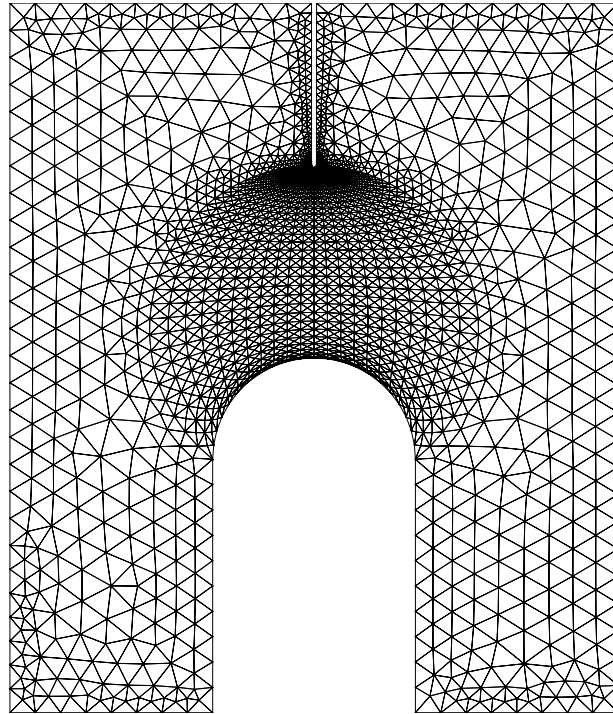


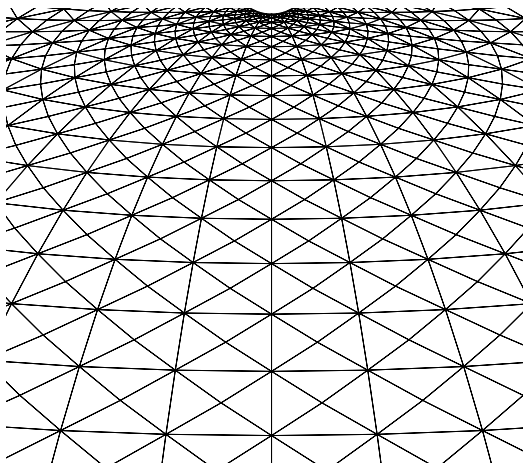
Figure 6.17: Geometry of compact compression specimen tests and its boundary condition.

Heaviside enrichment in conjunction with linear elastic fracture mechanics (LEFM) approach.

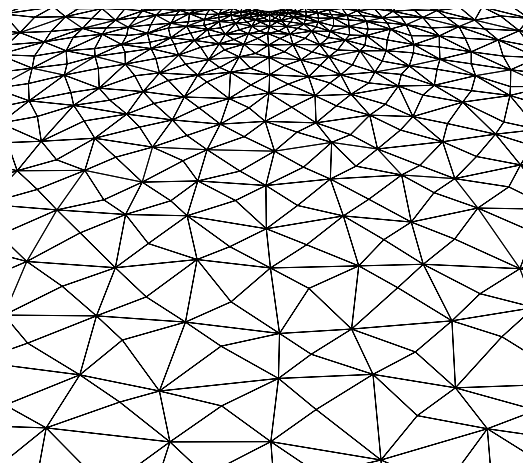
In this computational simulation, the plane strain condition is employed, and the impact pulse is applied as an acceleration on the traction boundary along the lower left segment 16.5 mm long. The elastic modulus of PMMA is 5.76 GPa, and the Pois-



(a)



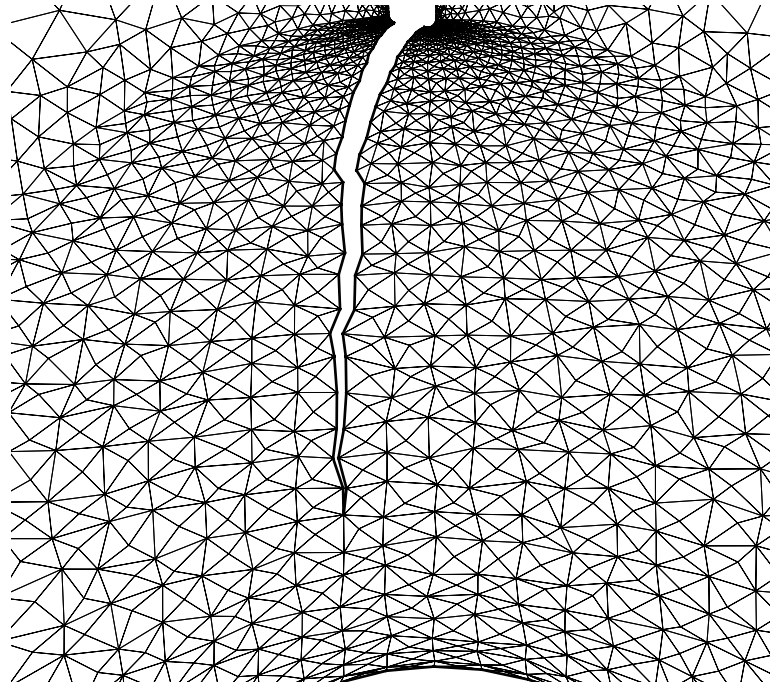
(b)



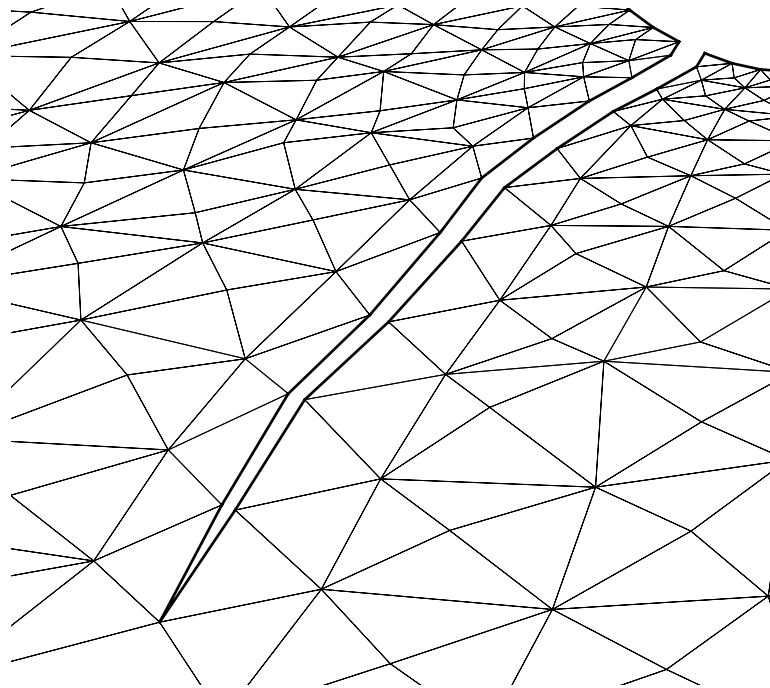
(c)

Figure 6.18: Finite element mesh of the compact compression specimen.

son's ratio is 0.42 (Rittel and Maigre, 1996). The mode I fracture energy (ϕ_n) and the normal cohesive strength (σ_{\max}) are 352.3 N/m and 129.6 MPa, respectively. The



(a)



(b)

Figure 6.19: Crack path of CCS simulation results.

mode II fracture parameters are assumed to be the same as the mode I parameters. The shape parameters (α , β) are two so that the softening model provides a linear softening relationship. Figure 6.18(a) illustrates the finite element mesh of the specimen. The mesh around a crack tip is generated by utilizing the curvilinear coordinate transformation and the conformal mapping (Papoulia et al., 2006) so that the mesh provides many crack initiation directions. Figure 6.18(b) shows the zoom of the mesh around a crack tip, and Figure 6.18(c) demonstrates the perturbed mesh with the nodal perturbation factor of 0.3. The number of nodes is 10908 and the number of elements is 5345 at the initial discretization. A cohesive element is inserted at $80 \mu s$, and the cohesive element experiences complete failure at $90 \mu s$. The crack path of the computational simulation is illustrated in Figure 6.19. During simulation, nineteen edge-swap operations are requested, and the crack path is generally smooth because of the use of the edge-swap operator. Additionally, the crack initiation angle is close to 45° , which corresponds to the experimental observation. After the initiation, the crack propagation direction changes along the vertical direction, which is similar to the previous computation by Menouillard et al. (2008).

6.6.2 Microbranching Experiments

Microbranching experiments were performed by Sharon et al. (1995), and Sharon and Fineberg (1996) to investigate microbranching instability. Specimens are PMMA sheets having a thickness of either 0.8 mm or 3 mm, a width of $50 \sim 200$ mm and a length of $200 \sim 400$ mm. The initial stress of $\sigma_0 = 10 \sim 18$ MPa is applied by clamping the top and the bottom of a PMMA sheet. When a sharp crack is created by a razor blade, a crack initiates and propagates. The higher energy input results in the higher crack velocity (v) and the more microbranching along the major crack, shown in Figure 6.20. The fracture surfaces are smooth when a crack velocity is lower than a critical velocity (v_c). When a crack velocity is greater than a critical value ($v > v_c$), one can observe that fracture surfaces are rough and more microbranching occurs. These physical phenomena are quantitatively investigated by Miller et al. (1999) and Zhang et al. (2007) in conjunction with cohesive surface elements. In addition, Ganguly (2006) observed that unstructured mesh probably performs even better than the pinwheel mesh in replicating the branching pattern for high initial strain.

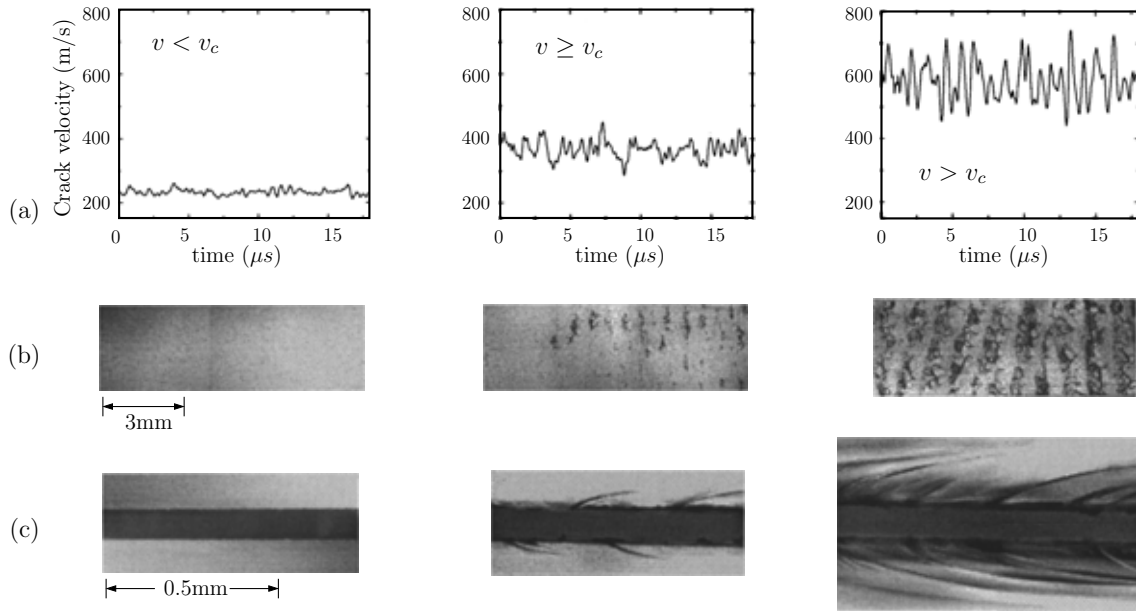


Figure 6.20: Observation of microbranching experiment: (a) crack velocity (v), (b) fractured surface, and (c) crack patterns with respect to different crack speeds ($v \sim 300\text{m/s} < v_c$, $v \sim 400\text{m/s} \sim v_c$, $v \sim 600\text{m/s} > v_c$). Figure is reproduced from Figure 4 of Sharon and Fineberg (1996).

The geometry and boundary conditions for computational simulations are described in Figure 6.21. The domain size is reduced as 16 mm by 4 mm, and the plane stress condition is employed with the unit thickness. The two-dimensional domain is initially discretized by the $4k$ mesh grid of 192 by 48, and then the nodal perturbation factor of 0.3 is applied. The edge-swap operator is activated when it is necessary during computational simulation. The number of nodes is 74257 and the number of elements is 36864 at the initial discretization. The time step (Δt) is 0.002 (μs),

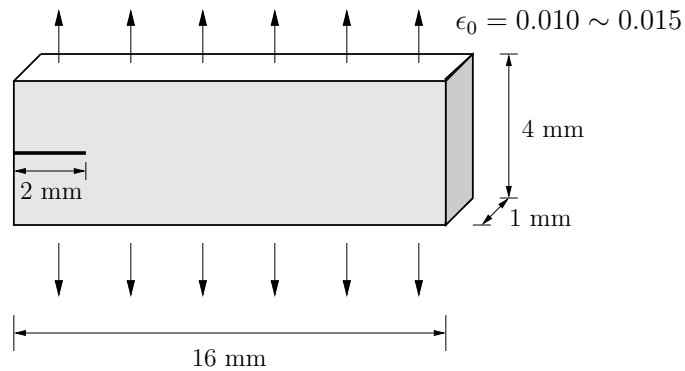


Figure 6.21: Schematics of geometry and boundary conditions for the microbranching experiments.

which is approximately one order lower than the characteristic time step (Pandolfi et al., 1999; Zhang et al., 2007). The initial strain ($\epsilon_0 = 0.010 \sim 0.015$) is applied by imposing an initial displacement boundary condition within the domain. The material properties of PMMA are based on the properties listed in the reference (Xu and Needleman, 1994). The elastic modulus of PMMA was 3.24 GPa, the Poisson's ratio was 0.35, and the density was 1190 kg/m³. The fracture parameters of PMMA were selected as the same as those in the CCS simulation.

Figure 6.22 compares microbranching patterns with respect to different initial strains ($\epsilon_0 = 0.01, 0.012$ and 0.015). The higher initial strain represents the more energy input, and thus one can expect the more microbranching, which is captured in the experimental results. The simulation results also demonstrate that the overall length of microbranching increases with respect to the increase of the initial strain. The major crack propagates along the horizontal direction, although it demonstrates a little deviation from the center line for the initial strain of 0.012 (Figure 6.22(b)).

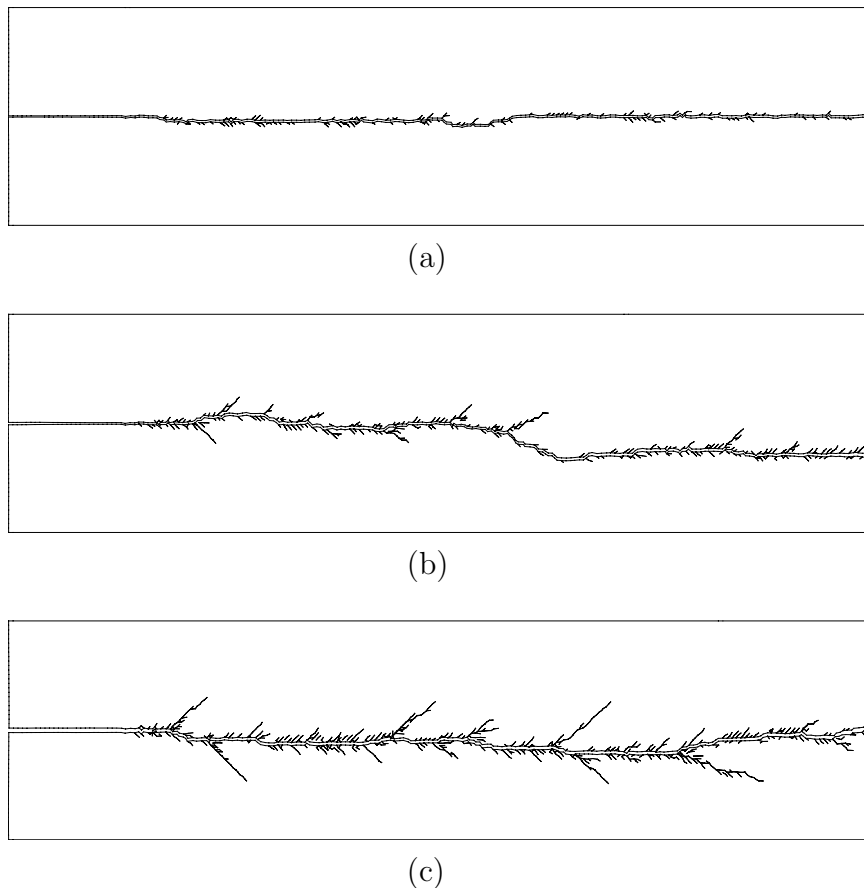
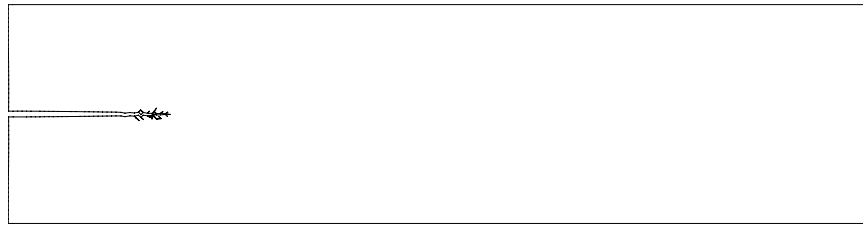
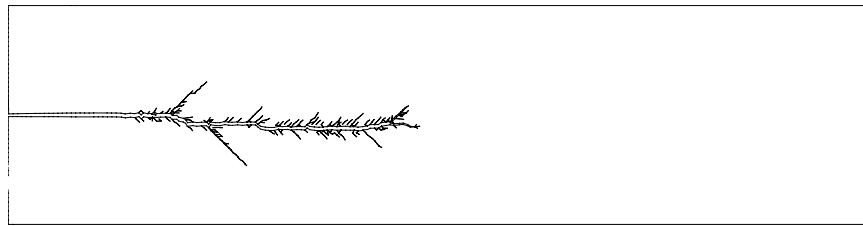


Figure 6.22: Branching patterns with respect to different initial strains: (a) $\epsilon_0 = 0.01$, (b) $\epsilon_0 = 0.012$, and (c) $\epsilon_0 = 0.015$ for the **4k** mesh grid of 192×48 .

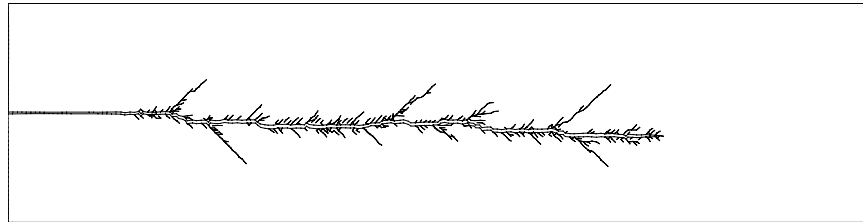
The microbranching evolution with respect to time for the initial strain of 0.015 is illustrated in Figure 6.23. In addition, the crack velocity is estimated through the linear regression of time and crack tip position. Crack tip position is defined when the constitutive relationship of a cohesive element provides complete separation at all integration points. Figure 6.24 illustrates the crack velocity versus time with respect to the different initial strains. The higher initial strain leads to the higher averaged crack velocity and more fluctuation in the velocity, which qualitatively corresponds



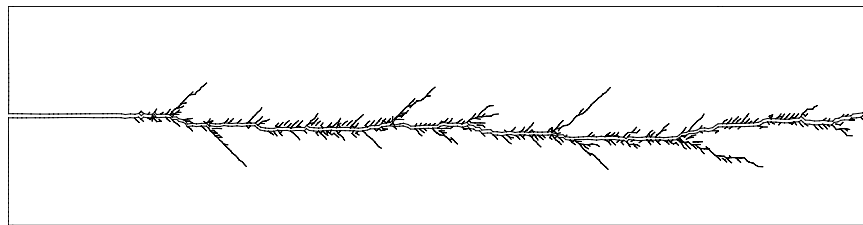
(a)



(b)



(c)



(d)

Figure 6.23: Microbranching evolution with respect to time: (a) $2\mu s$, (b) $8\mu s$, (c) $14\mu s$, and (d) $20\mu s$.

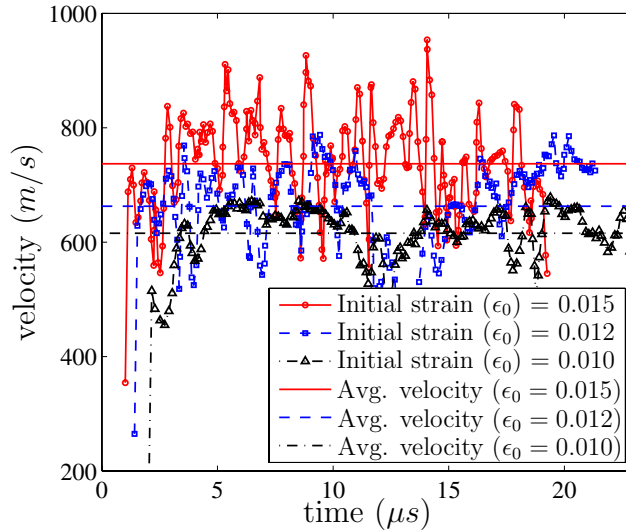


Figure 6.24: Crack velocity versus time and averaged velocity for initial strains (ϵ_0) of 0.01, 0.012 and 0.015 with the **4k** mesh grid of 192×48 .

to experimental results.

Mesh refinement is performed with the **4k** mesh grid of 256×64 , which leads to 131777 nodes and 65536 elements at the initial discretization. Figure 6.25 illustrates branching patterns with respect to different initial strains (a) $\epsilon_0 = 0.01$, (b) $\epsilon_0 = 0.012$ and (c) $\epsilon_0 = 0.015$. These microbranching patterns well correspond to the results with the **4k** mesh grid of 192×48 . The crack velocities versus time and the averaged velocities are plotted in Figure 6.26 for each initial strain. The averaged velocities obtained from the 256×64 mesh grid are similar to the velocities obtain from the 192×48 mesh grid. Thus, the computational results are consistent under mesh refinement regarding crack patterns and velocities.

In order to investigate the effect of randomness and the edge-swap operator on computational results, three finite element meshes are consecutively generated with the nodal perturbation factor of 0.3, and all the nodal locations are stored. For each finite element mesh, the microbranching problem with the initial strain of 0.015 is simulated with the edge-swap operator (Figure 6.27) and without the edge-swap operator (Figure 6.28). Although the detailed microbranching patterns are different from each other because of the different discretizations, the overall crack patterns are all similar to each other. In addition, Figures 6.27 and 6.28 illustrate that one can obtain more consistent results with the edge-swap operator than without the edge-swap operator because the edge-swap operator provides more number of potential crack propagation directions. Notice that 66, 70 and 70 edge-swap operations are adaptively employed in Figures 6.27(a), (b) and (c), respectively. Moreover, the

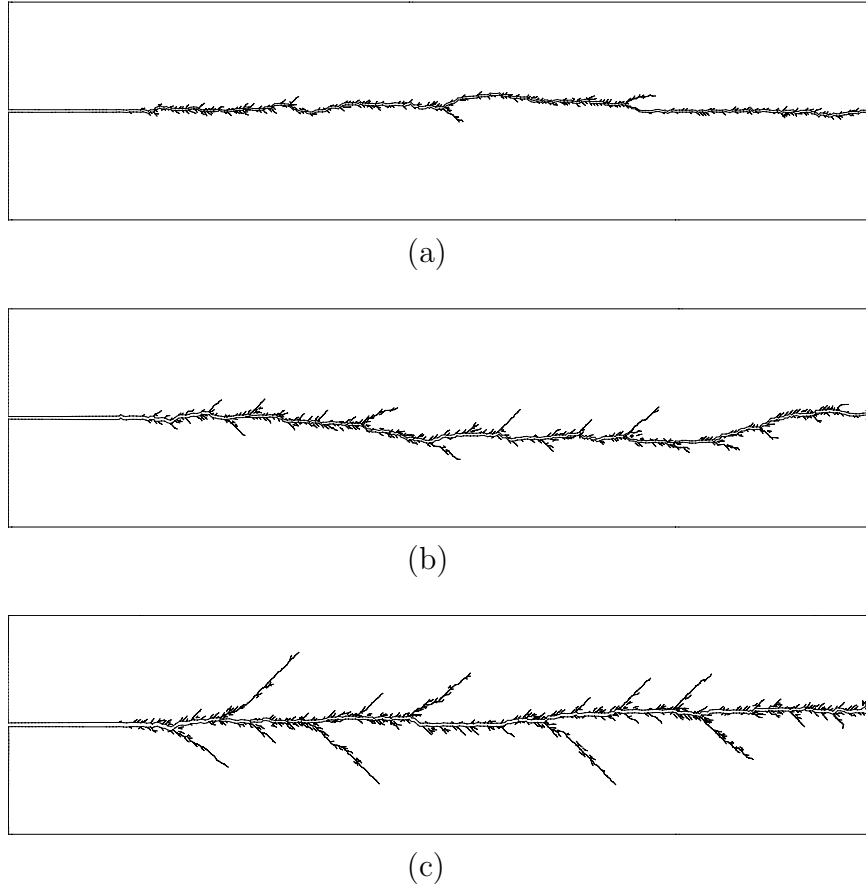


Figure 6.25: Branching patterns with respect to different initial strains: (a) $\epsilon_0 = 0.01$, (b) $\epsilon_0 = 0.012$, and (c) $\epsilon_0 = 0.015$ for the **4k** mesh grid of 256×64 .

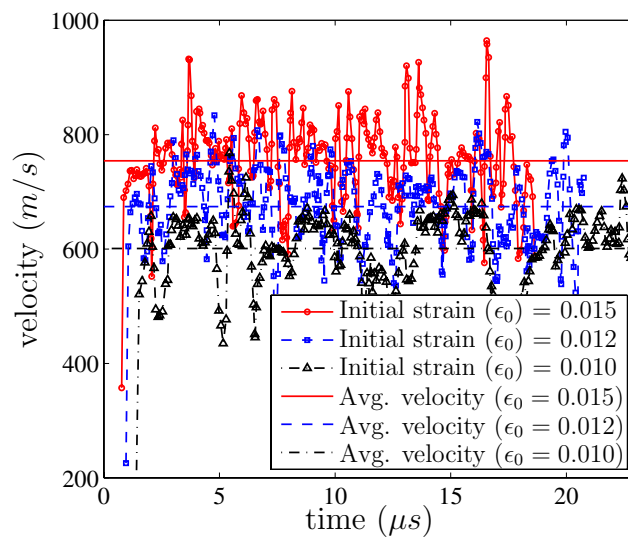
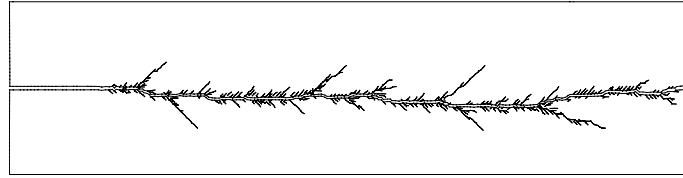
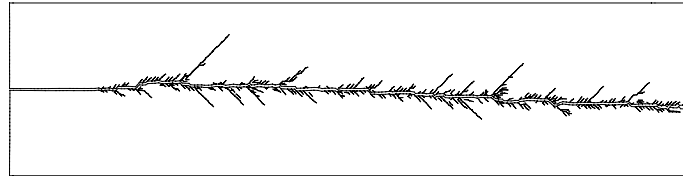


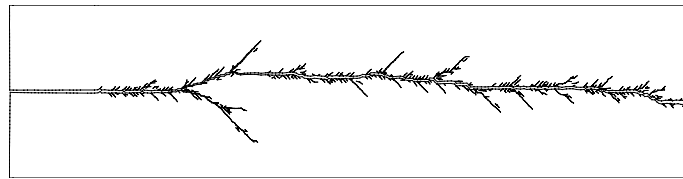
Figure 6.26: Crack velocity versus time and averaged velocity for initial strains (ϵ_0) of 0.010, 0.012 and 0.015 with the **4k** mesh grid of 256×64 .



(a)

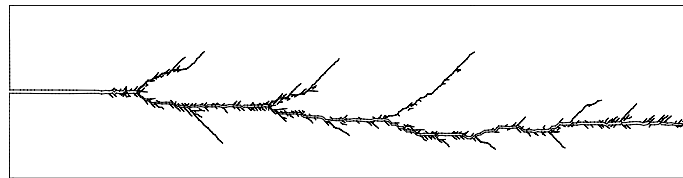


(b)

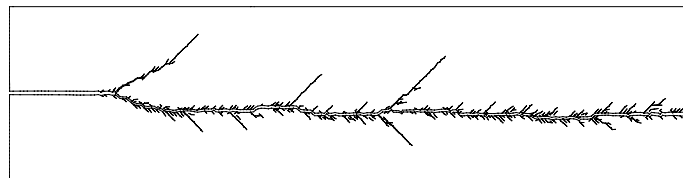


(c)

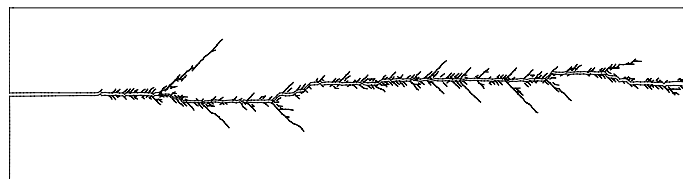
Figure 6.27: Three consecutive simulations for the initial strain of 0.015 with the edge-swap operator.



(a)



(b)



(c)

Figure 6.28: Three consecutive simulations for the initial strain of 0.015 without the edge-swap operator.

maximum deviation of the major crack from the straight center line is approximately 0.4 mm for the three results with the edge-swap (Figure 6.27), while the maximum deviations are 0.4 mm, 0.6 mm and 1.1 mm for the results without the edge-swap (Figure 6.28).

The energy balance is a necessary condition to ensure the numerical stability (Belytschko et al., 2000). Figure 6.29 illustrates the energy conservation with respect to time for the initial strain of 0.015. The total energy (E_{tot}) consists of the external work (E_{ext}), strain energy (E_{int}), kinetic energy (E_{kin}) and work done by fracture (E_{fra}). In this simulation, the total energy is a constant, which corresponds to the initial strain energy, i.e. no external work ($E_{\text{ext}} = 0$). After a crack initiates and propagates, the strain energy decreases while the kinetic energy and the fracture energy increase. The computational result of energy evolution demonstrates the total energy conservation, as shown in Figure 6.29.

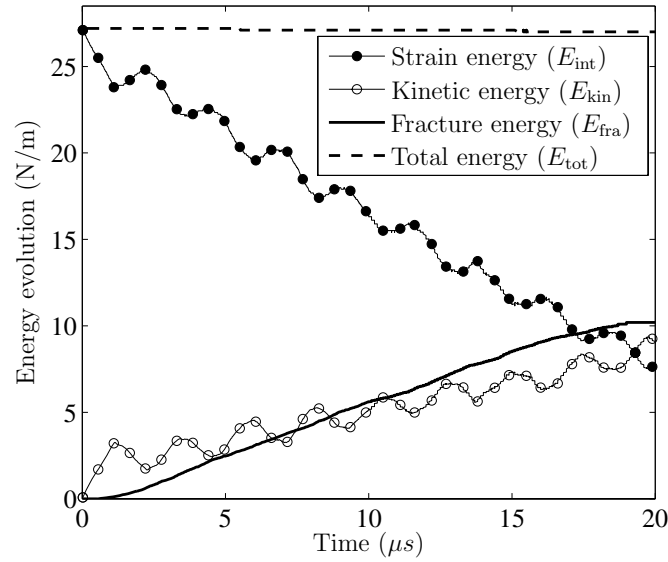


Figure 6.29: Energy evolution with respect to the time for $\epsilon_0 = 0.015$.

6.6.3 Fragmentation Simulations

Fragmentation of a thick cylinder due to an impact load is investigated. The geometry of the cylinder is shown in Figure 6.30(a). The inner radius is 80 mm, while the outer radius is 150 mm. Impact pressure is applied along the inner rim, and the impact pressure with respect to time is shown in Figure 6.30(b). The elastic modulus is 210 GPa, and the Poisson's ratio is 0.3 with a density of 7850 kg/m³.

The fracture energy is 2000 N/m and the cohesive strength is 850 MPa. Previously, Rabczuk and Belytschko (2004) investigated the fragmentation problem by using a mesh-free method with cracking particles. Zhou and Molinari (2004) addressed mesh dependency in fragmentation problems, and Song and Belytschko (2009) solved this problem by using the cracking node method.

The cylindrical domain is discretized into a **4k** mesh grid of 20×160 with a transformation. The number of nodes is 25920 and the number of element is 12800 at the initial discretization. Three finite element meshes are generated with the nodal perturbation factors of 0.3, and the edge-swap operators are adaptively employed during computation. A crack nucleation in the middle of the domain is prevented. Fragmentation patterns of three consecutive computational results are demonstrated in Figure 6.31. The numbers of the edge-swap operations used in Figures 6.31(a), (b) and (c) are 116, 139 and 149, respectively. The numbers of major fragments for each result are 24, 20 and 23, which correspond to the results by Song and Belytschko (2009). Figure 6.32 illustrates the fragmentation process with strain energy density at different time. Stress and strain are concentrated along the inner rim (Figure 6.32(a)) due to the internal pressure. Multiple cracks are initiated from the inner rim, and propagate along the radial direction (Figures 6.32(b) and (c)). Some of cracks are arrested during the fragmentation process while others propagate up to outer rim with the formation of crack branching (Figures 6.32(d) and (e)). The number of major fragments is 24, as shown in Figure 6.32(f).

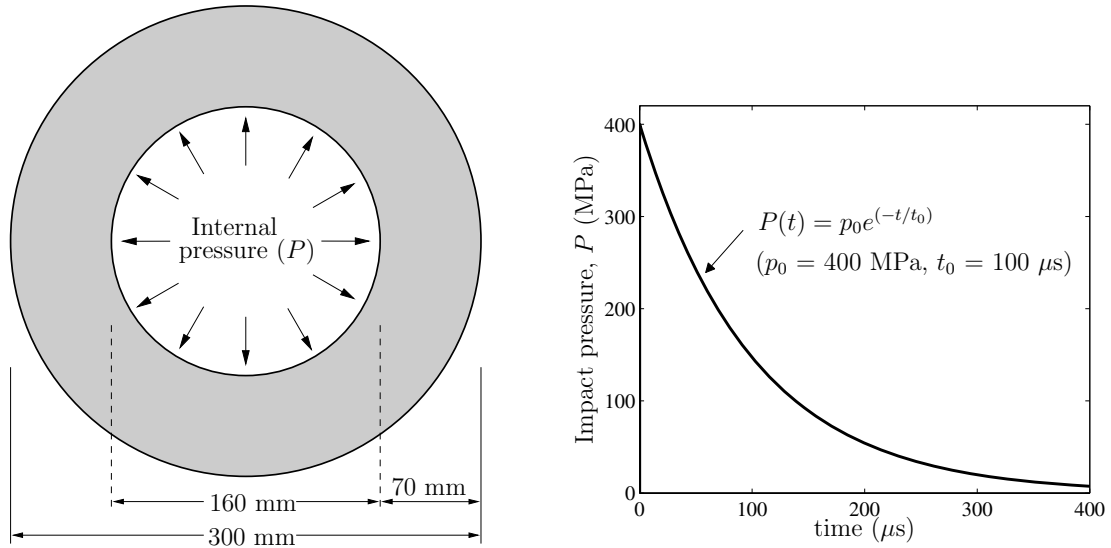
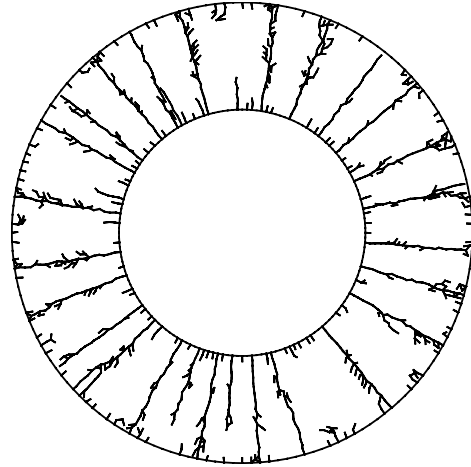
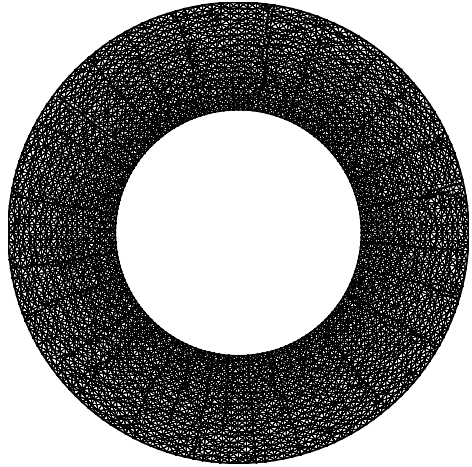
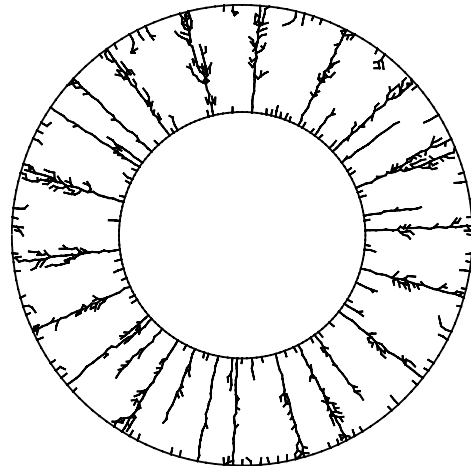
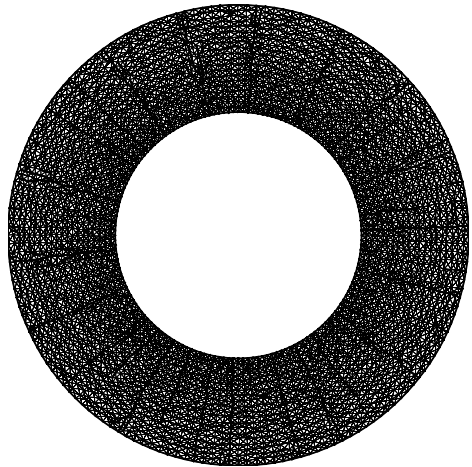


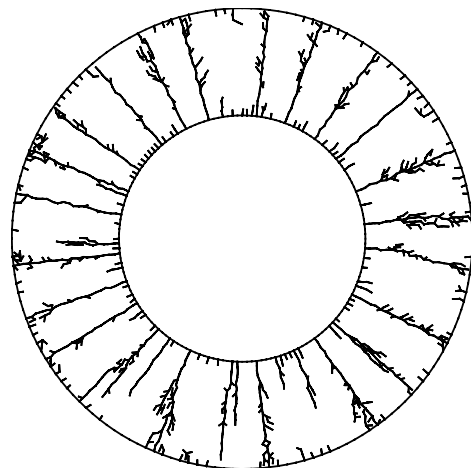
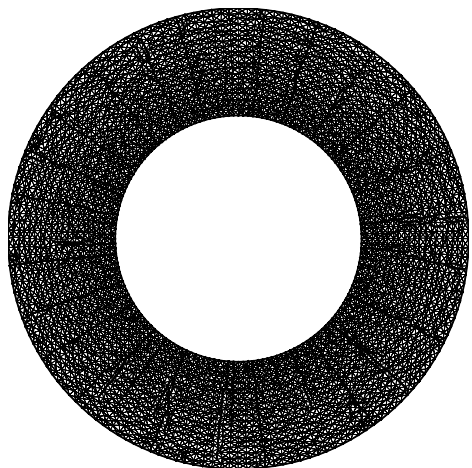
Figure 6.30: (a) Geometry of a thick cylinder, and (b) applied impact pressure with respect to time.



(a)



(b)



(c)

Figure 6.31: Fragmentation patterns of three consecutive computational results with the nodal perturbation factor of 0.3.

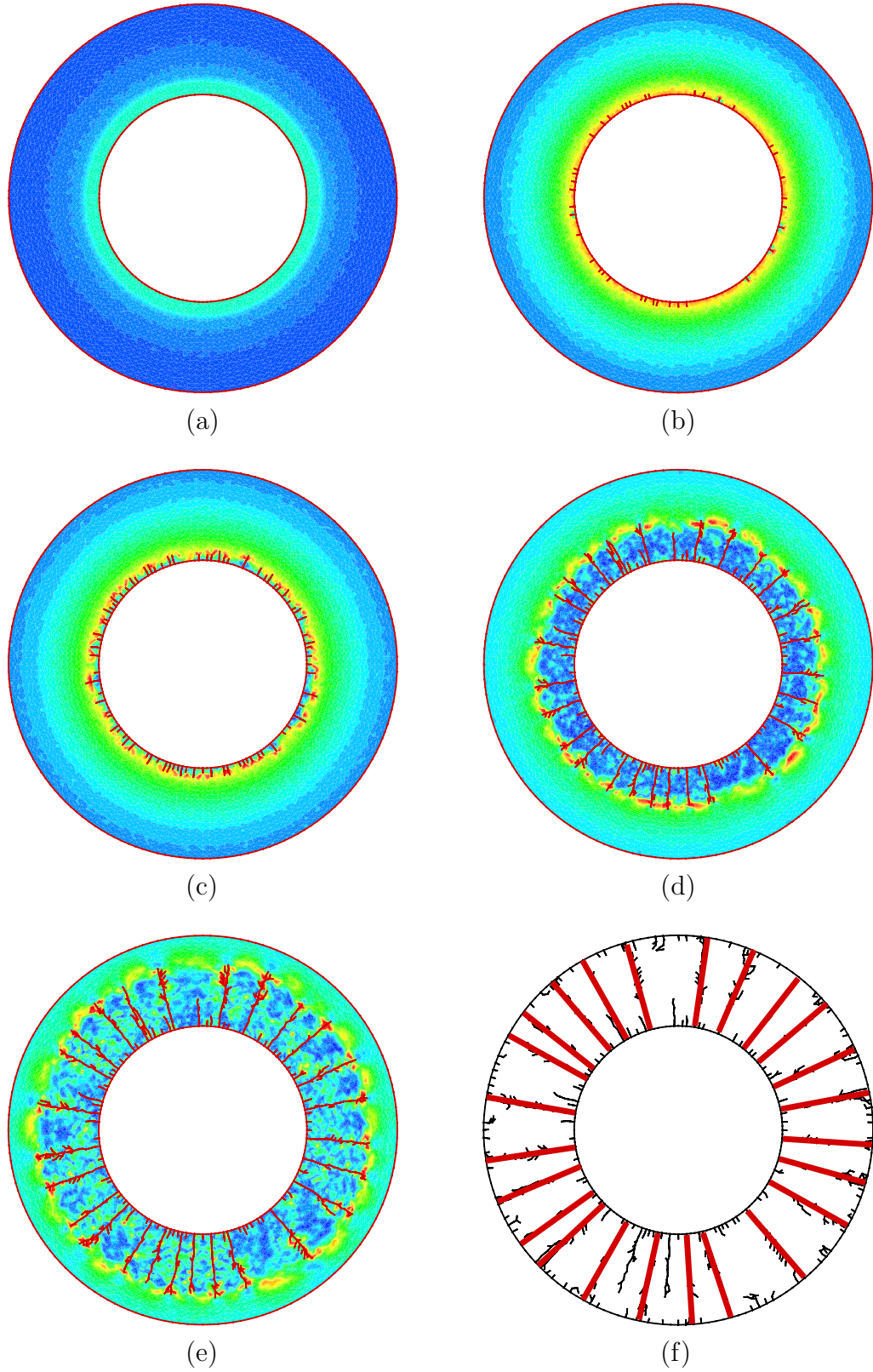


Figure 6.32: Fragmentation procedure with respect to time: (a) 26 μs , (b) 37 μs , (c) 39 μs , (d) 47 μs , (e) 54 μs , and (f) 64 μs .

6.7 Some Remarks on $4k$ and Pinwheel Meshes

A $4k$ structured mesh is compared with a pinwheel-based mesh (i.e. 1 level). The pinwheel-based mesh consists of the pinwheel tiling and triangles of the subdivision shown in Figure 6.33(a). The solid line in the pinwheel-based mesh is the original pinwheel tiling, while the dashed line provides additional sub-triangles to eliminate hanging nodes in the pinwheel tiling. Then, both the solid and the dashed lines are mapped into the $4k$ structured mesh (Figure 6.33(b)). The edges of an individual pinwheel tiling and its subdivision can be represented by a subset of the edges of a $4k$ mesh, although a $4k$ structured mesh has a different aspect ratio of triangles compared to a pinwheel-based mesh. However, notice that a set of pinwheel tiles (e.g. 2 level) is not equivalent to a $4k$ mesh, as illustrated in Figure 6.34. The topology between the pinwheel tiles and the $4k$ mesh are different along the line that has solid circles.

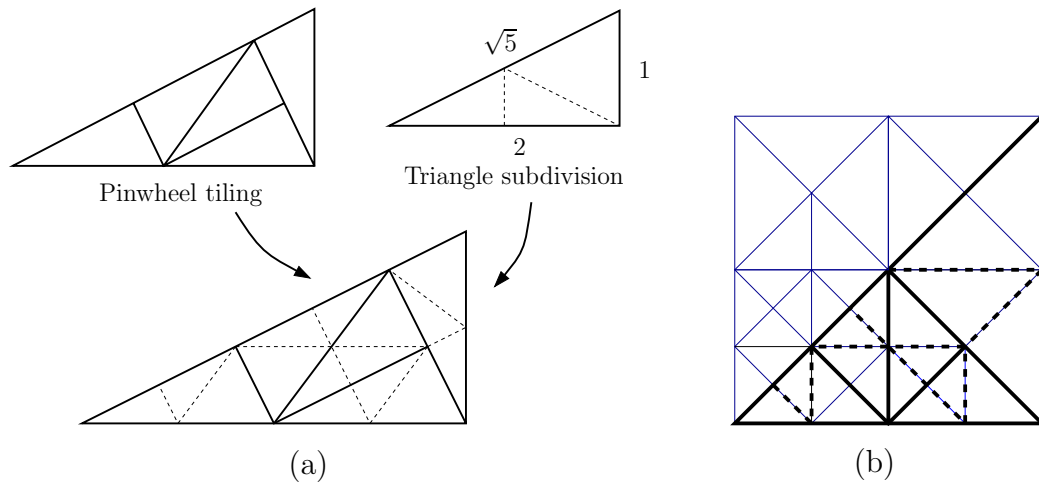


Figure 6.33: Comparison by mapping edges of pinwheel-based mesh into edges of $4k$ structured mesh.

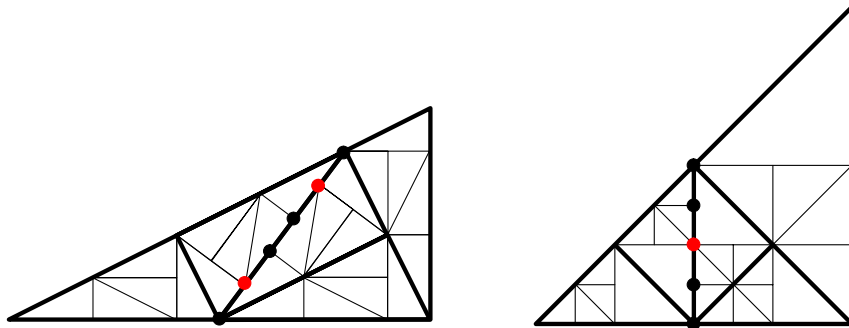


Figure 6.34: Comparison between a set of pinwheel tiles and a $4k$ mesh.

Reversely, edges of a **4k** mesh (Figure 6.35(a)) are mapped into edges of a pinwheel-based mesh (Figure 6.35(b)). In this case, one has to create additional edges (dashed-red lines) in a pinwheel-based mesh because a **4k** mesh has more edges (or directions) at a node than a pinwheel-based mesh, which implies that **4k** meshes have rich topology. Notice that a finite element mesh whose internal nodes have more adjacent edges is always preferable for crack propagation simulation with cohesive surface elements. As discussed previously, **4k** meshes with the edge-swap operator provide 8 potential directions for all internal nodes. On the other hand, some internal nodes of pinwheel-based meshes have 4, 5 or 6 directions, as shown in Figure 6.13(b). Therefore, **4k** meshes with the edge-swap provide more (or the same) number of potential directions than pinwheel-based meshes for any internal nodes.

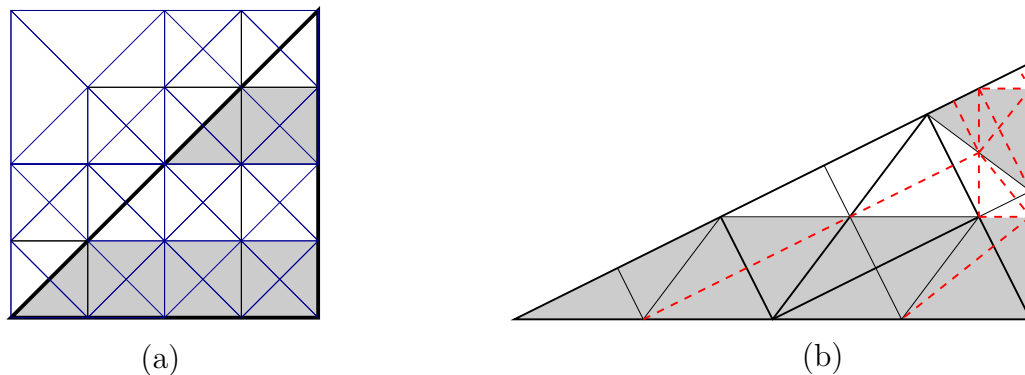


Figure 6.35: Comparison by mapping edges of **4k** structured mesh into edges of pinwheel-based mesh with additional dashed-red edges.

6.8 Concluding Remarks

The use of the nodal perturbation and the edge-swap operator are proposed in cohesive fracture simulations. The nodal perturbation leads to the geometrically unstructured **4k** mesh while the edge-swap operator provides the topologically unstructured **4k** mesh. These two operators reduce mesh bias, which exists in finite element analysis of fracture problems. Geometrical representation of a crack length and angle is addressed in conjunction with mathematical and probabilistic arguments. Moreover, both the nodal perturbation and the edge-swap operator reduce discrepancy between mathematical and discretized paths more rapidly than pinwheel-based meshes, for practical levels of mesh refinement.

The potential-based PPR cohesive zone modeling with TopS leads to an effective computational framework to simulate physical phenomena associated with dynamic

fracture, branching and fragmentation. Compact compression specimen (CCS) tests, microbranching experiments and fragmentation problems are investigated by using the nodal perturbation and the edge-swap operator. Simulation of the CCS tests illustrates a smoother crack pattern with the edge-swap operator. In the microbranching experiments, computational simulation provides consistent results in terms of microbranching patterns and crack velocity. The use of the edge-swap operator reduces the maximum deviation of the major crack from a straight center line. In addition, the total energy is conserved during adaptive insertion of cohesive elements and the edge-swap operators. Finally, fragmentation of a thick cylinder is investigated. The fragmentation patterns and the number of fragments obtained from this study illustrate agreement with previous computational results.

Chapter 7

Adaptive Mesh Refinement and Coarsening for Cohesive Dynamic Fracture

Adaptive mesh refinement and coarsening schemes are developed for the simulation of dynamic fracture and branching problems while reducing computational cost significantly. The adaptive mesh refinement consists of a sequence of edge-split operators while the adaptive mesh coarsening is based on a sequence of vertex-removal (or edge-collapse) operators. Nodal perturbation and edge-swap operators are also employed around a crack tip region, and cohesive surface elements are adaptively inserted whenever and wherever they are needed, i.e. the extrinsic cohesive zone model. Such adaptive mesh modification events are maintained in conjunction with the topological data structure TopS. The PPR potential-based cohesive model is utilized for the constitutive relationship of the cohesive zone model. Mode I fracture, mixed-mode fracture and branching problems are investigated. The computational results with the adaptive mesh refinement and coarsening are consistent to the results with the uniform mesh refinements.

7.1 Introduction

Adaptive mesh refinement schemes were utilized to control and minimize error in the finite element analysis (Babuska and Rheinboldt, 1978; Zienkiewicz and Zhu, 1987; Ainsworth and Oden, 1997; Paulino et al., 1999). Since then, researchers have applied mesh adaptation schemes to several engineering problems while reducing computational cost. For linear elastic problems, mesh around a crack tip region is regenerated by a recursive spatial decomposition algorithm (Swenson and Ingraffea, 1988; Wawrzynek and Ingraffea, 1991; Kim and Paulino, 2004), while the crack propagates. Belytschko and Tabbara (1993) adaptively refined finite element meshes, i.e. an h -adaptive technique, through subdividing a rectangular element into four, and introduced the L_2 projection of strains for error estimation in solving elasto-dynamic problems. Molinari and Ortiz (2002) performed adaptive mesh refinement and coars-

ening for dynamic-plastic problems. The mesh refinement scheme is implemented by using Rivara's longest-edge propagation path bisection algorithm (Rivara, 1997) while the coarsening scheme is based on the elimination of elements by edge-collapse.

Furthermore, adaptive mesh refinement techniques can be a good candidate for multiscale numerical methods. For example, Bryan (1999) utilized the adaptive mesh refinement technique in cosmology in order to represent the evolution of a cluster of galaxies in high-resolution. Trangenstein (2002) investigated multi-component flow in porous media in conjunction with adaptive mesh refinement. Other multiscale numerical methods have been developed in conjunction with various techniques, for instance, variational multiscale method (Hughes, 1995), multi-scale enrichment method (Fish and Yuan, 2005), and multi-scale finite element method (Hou and Wu, 1997). Notice that Hou and Wu (1997) emphasized the importance of boundary conditions for the accuracy of numerical methods. The adaptive mesh refinement techniques do not suffer from the accuracy of boundary conditions between coarse and fine scales because the finite element mesh can be fully compatible between coarse and fine meshes. However, the major challenge in adaptive finite element analysis is to transfer field variables between two discretizations, and to maintain a data structure to retrieve adjacency relationships efficiently.

In this chapter, for dynamic cohesive fracture problems, a fine mesh is utilized to capture micro-cracks and nonlinear crack tip behavior, while a coarse mesh is employed in a far field from a crack tip region in conjunction with adaptive mesh refinement and coarsening schemes. The mesh refinement and coarsening are performed systematically by keeping the topology of a $4\mathbf{k}$ mesh with edge-split and vertex-removal operators. The mesh adaptation is incorporated with TopS (Celes et al., 2005a,b), which provides compact and efficient topological representation. The nonlinear cohesive zone is represented by extrinsic cohesive surface elements, and the PPR potential-based model is utilized for the constitutive model of the cohesive zone. In addition, the nodal perturbation and edge-swap operators are utilized to reduce a mesh bias and to improve crack patterns in a $4\mathbf{k}$ mesh, as discussed in Chapter 6. The computational framework is verified and validated by solving a predefined crack path, mixed-mode crack propagation, and branching problems.

The chapter is organized as follows. Section 7.2 presents the adaptive mesh refinement schemes and the interpolation of new nodes, while Section 7.3 explains the adaptive mesh coarsening schemes and coarsening criterion. Computational results of mode I fracture, mixed-mode fracture and branching problems are provided in Section 7.4. Finally, Section 7.5 summarizes the key findings of this study.

7.2 Adaptive Mesh Refinement

Adaptive mesh refinement requires an efficient and robust data structure in order to retrieve adjacency relationships. In this study, the topological data structure TopS (Celes et al., 2005a,b) is used for representing $4k$ meshes. This data structure provides efficient element-to-element adjacency and representation of vertices and edges, which are convenient for the implementation of refinement and coarsening operations. A sample initial non-deformed mesh and the convention used for the local incidences of elements are shown in Figure 7.1. The mesh is composed of a uniform set of right isosceles triangles and internal vertices with valence 4 or 8. Element incidence is defined such that the third local vertex ($v3$) of each triangle is associated to the right angle and corresponds to a global vertex of valence 4. The first local edge ($e1$) is opposite to the third vertex ($v3$).

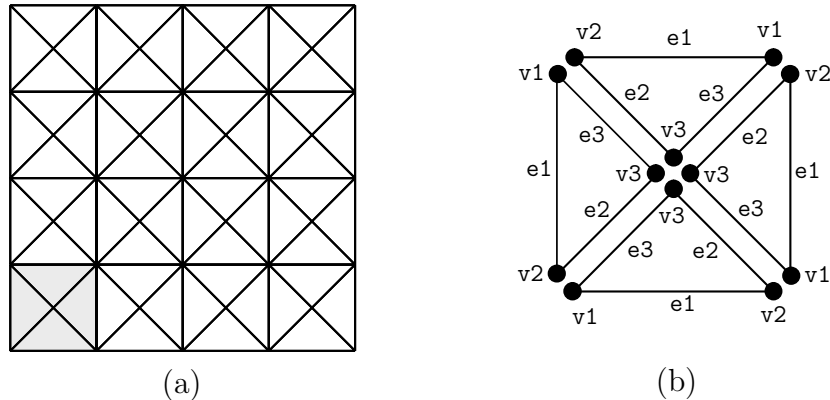


Figure 7.1: (a) Sample initial non-deformed mesh, and (b) local nodal incidences of triangles of a region of the mesh.

In the following subsection, mesh refinement schemes of $4k$ meshes are explained in conjunction with edge-split operators. Next, adaptive mesh refinement criterion and the interpolation schemes of new nodal quantities are presented.

7.2.1 Mesh Refinement Schemes

Mesh refinement is implemented by using an edge-split operator. The operator subdivides an edge into two new other edges. In order to maintain the $4k$ structure, internal edge splits are defined on specific clusters of two triangles, as in the literature (Velho and Gomes, 2000), and boundary edges. Figure 7.2 illustrates the two possible cases of the edge split. An interior edge split replaces the two adjacent triangles with four triangles (Figure 7.2(a)) while a boundary edge split replaces a triangle

with two triangles (Figure 7.2(b)).

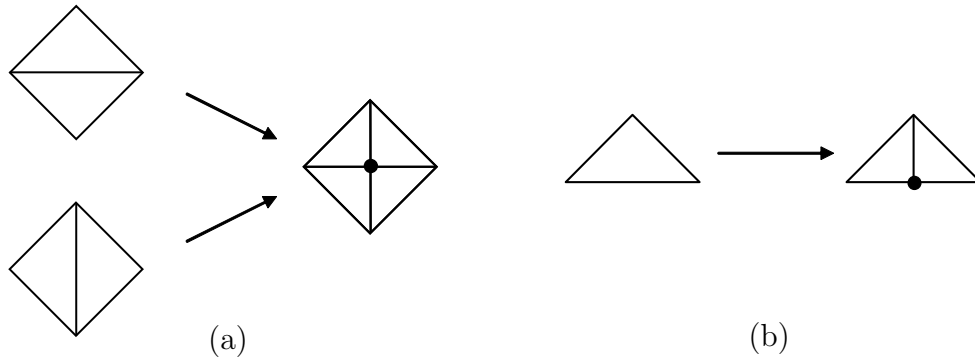


Figure 7.2: Local mesh patterns for which edge splits are allowed: (a) mesh around an interior edge (b) boundary edge.

In a $4k$ mesh, the split-edge is the first local edge (e_1), described in Figure 7.1(b), of the adjacent triangles. When the edge-split operator is applied to other edges (e_2 or e_3), a recursive procedure is introduced in order to transform the local sub-mesh into one of the patterns in Figure 7.2. The procedure works by splitting edges of neighboring triangles until an allowable pattern is achieved, i.e. recursive edge-split procedure, as illustrated in Figure 7.3. When the dashed edge in Figure 7.3(a) is to be split, the edge does not fit in any of the patterns in Figure 7.2. Then, other edges are split (Figure 7.3(b)) in order to create an allowable pattern for the edge's split (Figure 7.3(c)). Therefore, one can select any edge in a $4k$ mesh for the edge-split operator.

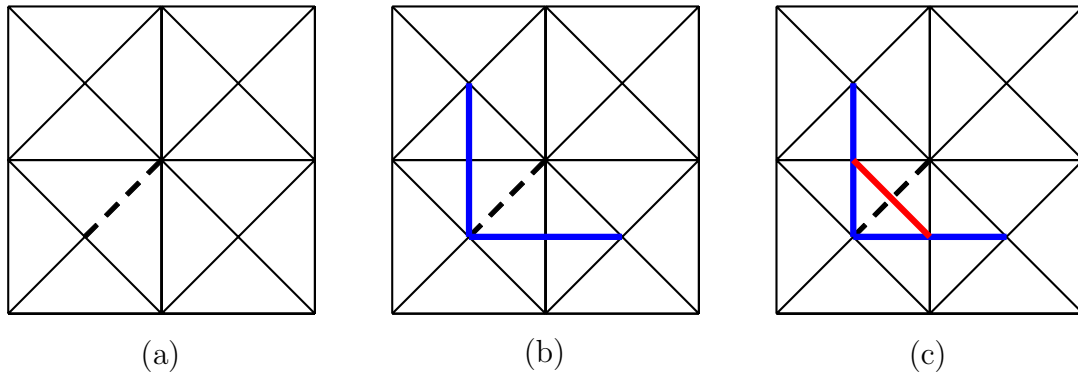


Figure 7.3: Recursive edge split procedure; (a) request for an edge-split along the edge with a dashed line, (b) split edges to create an allowable pattern, and (c) split edge along the dashed edge.

In addition, edge splits are allowed when a cohesive element exists between the two triangles of the patterns of Figure 7.2(a). When one of the edges of cohesive elements is split, the other edge is also split by the edge-split operator in order to keep mesh topology consistent. As a consequence, the cohesive element is divided into two new elements (Figure 7.4(b)). However, the edge-split operator on cohesive elements is not employed in computational simulation, because a finite element mesh is refined before inserting cohesive elements.

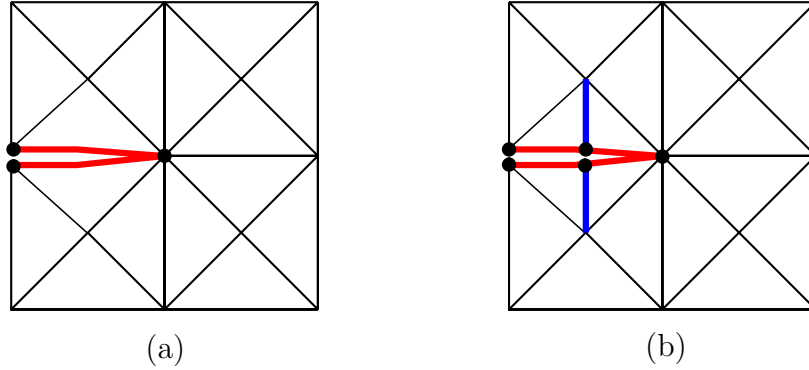


Figure 7.4: Edge split along a cohesive surface element.

During the edge-split operations, edge depths are computed. The initial depth of all the edges of an unmodified mesh is zero. The value assigned to the newly created edges is equal to the maximum depth of all the edges of the triangles adjacent to the split edge, plus one ($\text{MaxDepth}(\text{edges}) + 1$). For example, when the horizontal dashed edge on the left is split, the two vertical edges are created, as shown in Figure 7.5. The depth value assigned to the vertical edges is ③, which is equal to the maximum depth of the edges (②) of the adjacent triangles plus one. The depth of the two new horizontal edges (①) is the same as the original edge. In addition, Figure 7.6 shows a sequence of edge splits executed on a sample mesh. At each step, the dashed edges are split, and depth values are assigned to the newly created ones, shown in Figures 7.6(a), (b) and (c). The depth values are illustrated by the numbered labels

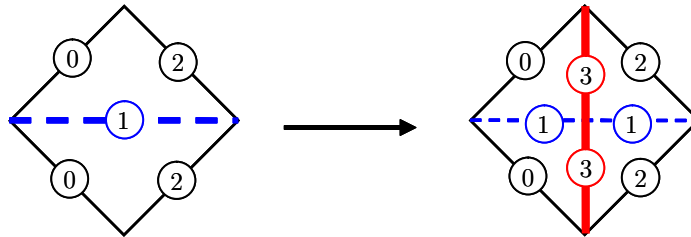
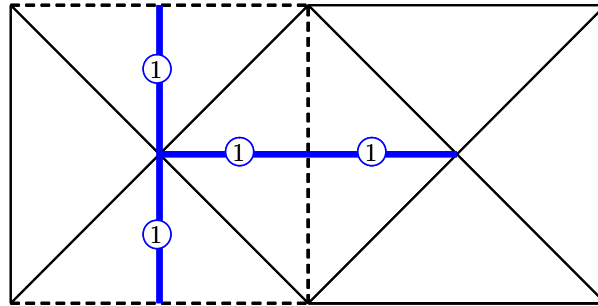
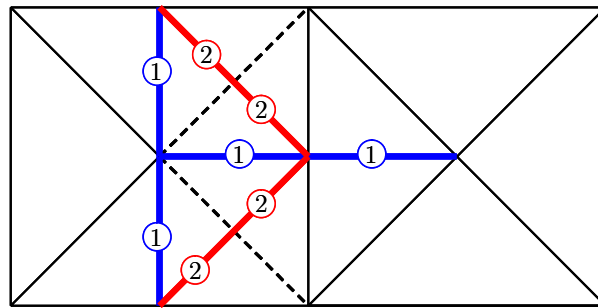


Figure 7.5: Example of the edge-split operation and computed edge depth.

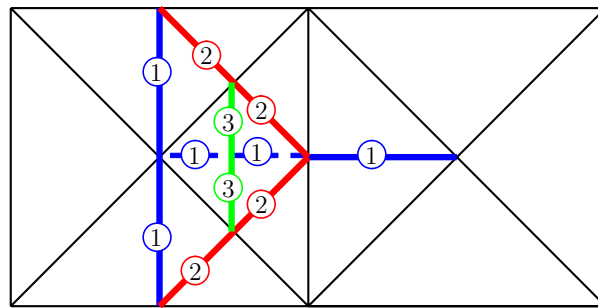
on them. Notice that labels of edges with zero-depth value (initial value) are omitted. The depth value is associated with a relative local ordering for edge splits, which is utilized for the adaptive mesh coarsening schemes, discussed in Section 7.3.



(a)



(b)



(c)

Figure 7.6: Sequence of edge-split operations along the dashed edges.

7.2.2 Refinement Criterion and Interpolation of New Nodes

In computational simulation of cohesive fracture problems, the adaptive mesh refinement is performed by employing *a priori* knowledge that a fine mesh is usually utilized around a crack tip region in order to capture high stress and strain gradients.

In order to have a uniformly refined mesh around crack tip regions, the edge-split operator is used non-recursively. The mesh refinement procedure is to split all the allowable edges located within a circular region around the crack tip. This is done in several steps until a maximum level of refinement is reached. Figure 7.7 illustrates the refinement procedure on a sample mesh for three levels of refinement. However, the edge-split operator along a cohesive element is not allowed in computational simulation, as mentioned previously.

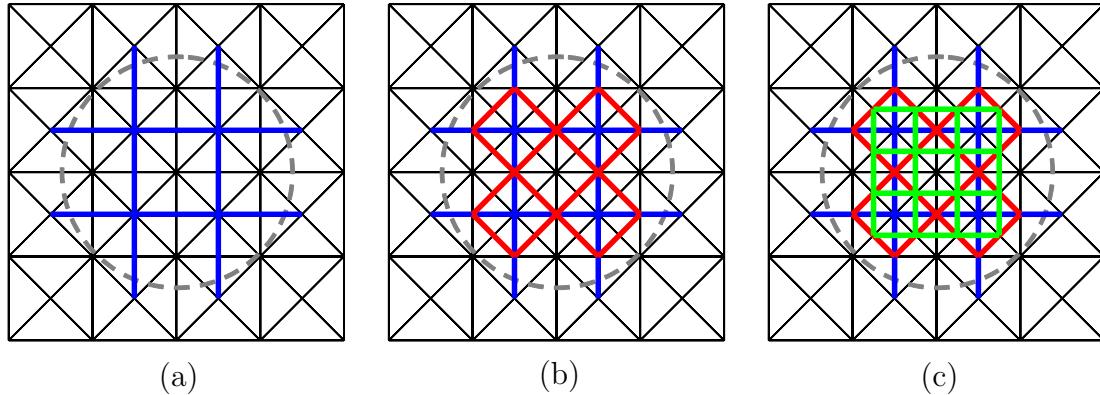


Figure 7.7: Three refinement steps executed inside a circular region: (a) level 1, (b) level 2, and (c) level 3.

The adaptive mesh refinement with the edge-split operations leads to new nodes whose quantities should be interpolated from adjacent nodes in the nonlinear finite element analysis. For example, in the $4k$ mesh with quadratic triangular elements of 6 nodes each (Figure 7.8(a)), two red-dashed edges are split: one edge is on the boundary and the other is on the interior. The boundary edge-split operation provides three new nodes, while the interior edge-split operation leads to four new nodes, as shown in Figure 7.8(b). One can further split the blue-dashed interior edge (Figure

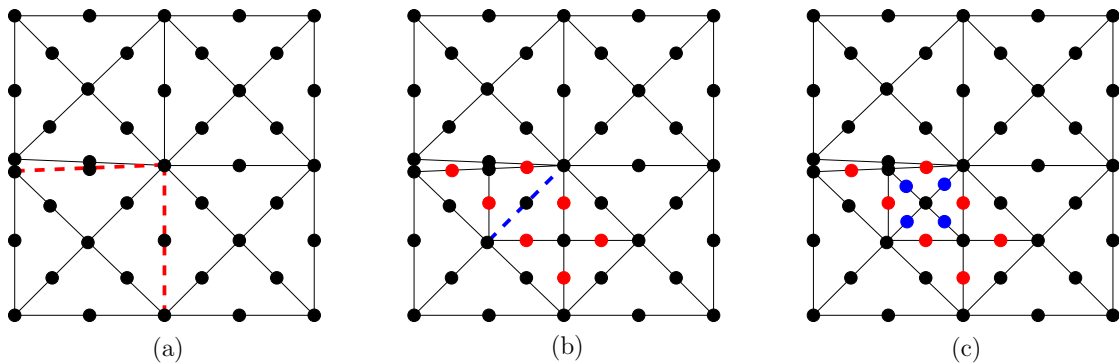


Figure 7.8: Example of the edge-split operations.

7.8(b)), and this operation provides four additional blue nodes, as shown in Figure 7.8(c). Notice that these new nodes can be locally relocated (or perturbed) at the time of the insertion of new nodes, if one utilize the nodal perturbation. In addition, nodal quantities (e.g. displacement, velocity and acceleration) of new nodes should be interpolated from neighboring nodes for the explicit time integration in elastodynamic problems.

For the interpolation of new nodes, the choices of sampling nodes and interpolation functions are essential. First, sampling nodes are selected in a recursive procedure. For example, the three new red nodes, which are resulted from the boundary edge-split operation, are interpolated from six nodes, which correspond to the members of a triangular element that shares the boundary edge (see Figure 7.9(a)). Next, the four new red nodes, which are resulted from the interior edge-split operation, are interpolated from nine nodes, which are the members of the adjacent elements that share the interior edge (see Figure 7.9(a)). Similarly, the four blue nodes are interpolated from nine nodes, which are the members of the adjacent elements that share the interior edge, as shown in Figure 7.9(b). Because the blue nodes are interpolated from four black nodes and four red nodes, the red nodes are interpolated before the blue nodes are interpolated. In other words, new nodes, which are inserted first, should be interpolated first. Therefore, the sequence of the interpolations is the same as the sequence of the edge-split operations.

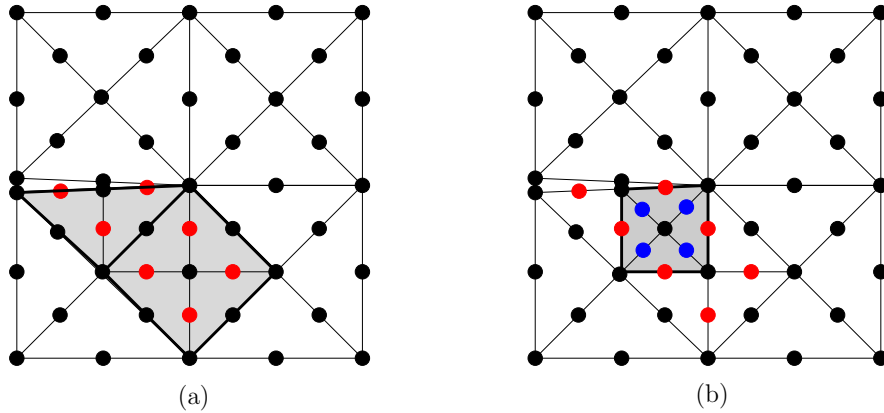


Figure 7.9: Interpolation scheme for new nodes.

For interpolation functions, the quadratic Lagrange basis functions (i.e. shape functions) are utilized. The nine node quadratic interpolation functions are used for the interior edge-split, while the six node quadratic interpolation functions are utilized for the boundary edge-split. The approximated nodal quantities of a new

node (e.g. displacement, \tilde{u}_i) are obtained by

$$\tilde{u}_i = \sum_{j=1}^n N_j(\xi_i, \eta_i) u_j \quad (7.1)$$

where n is the number of interpolation functions, N_j are the Lagrange basis functions, and ξ_i and η_i are nodal locations in the mapped coordinate system (e.g. Figure 7.10(b)).

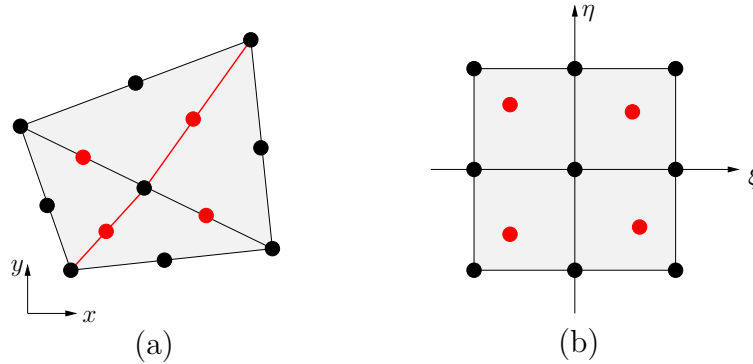


Figure 7.10: (a) Physical coordinate system, and (b) mapped coordinate system.

The nodal locations of new nodes are mapped from the physical coordinate $(x - y)$ system to the mapped coordinate $(\xi - \eta)$ systems. For example, the transformation of a quadrilateral from the mapped coordinate system (Figure 7.10(b)) to the physical coordinate system (Figure 7.10(a)) is given as $T : (\xi, \eta) \longrightarrow (x, y)$ where $x = \sum_{i=1}^n N_i(\xi, \eta) x_i$ and $y = \sum_{i=1}^n N_i(\xi, \eta) y_i$. Then, the inverse mapping ($T^{-1} : (x, y) \longrightarrow (\xi, \eta)$) is performed by utilizing Newton's algorithm to evaluate the nodal locations of new nodes in the mapped coordinate system. Notice that the size of nonlinear system for the inverse mapping in two-dimensions is two, and thus the computational cost of this inverse mapping is not significant.

7.3 Adaptive Mesh Coarsening

The coarsening procedure reverses a sequence of edge-splits by utilizing a vertex-removal (or edge-collapse) operator. This operator works by removing a vertex and merging adjacent elements in order to restore a previous level of refinement. In this section, mesh coarsening schemes and coarsening criterion are presented.

7.3.1 Mesh Coarsening Schemes

Mesh coarsening consists of a sequence of vertex-removal operators. Mesh structure is maintained by constraining internal vertex removals to vertices of valence 4 (Velho and Gomes, 2000; Velho, 2001), and boundary vertex removals to vertices of valence 2. This corresponds to the four-face and two-face triangle clusters presented respectively in Figures 7.11(a) and (b). Because the local sub-mesh in Figure 7.11(a) can be originated from two distinct cases (see Figure 7.2), the refinement procedure must record historical data so that ambiguities can be consistently handled. The pattern in Figure 7.11(b) occurs on mesh boundaries, and does not require handling of ambiguous cases.

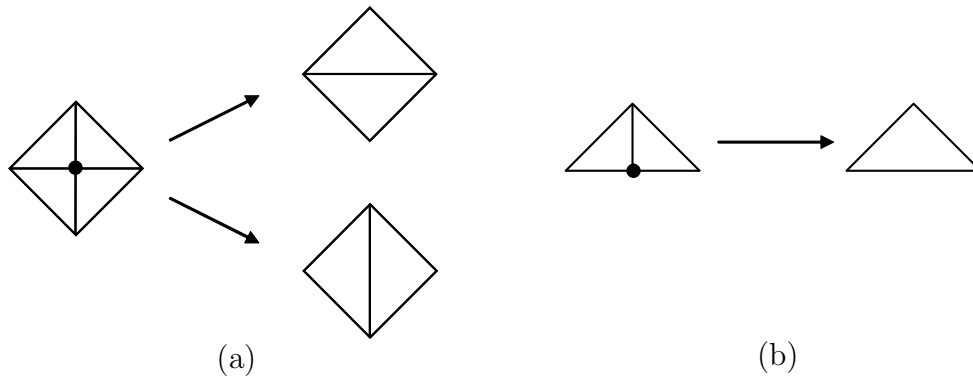


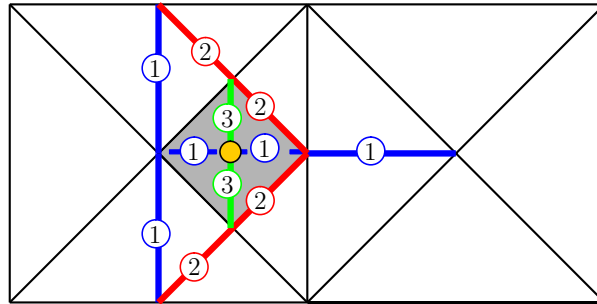
Figure 7.11: Vertex-removal operator for mesh coarsening: (a) interior vertex-removal and (b) boundary vertex-removal.

In order to reverse a sequence of mesh refinements in a consistent way, the vertex-removal operator needs to determine from which pattern the current local sub-mesh originated. To accomplish this, we record the history of edge-split operations executed so far. However, instead of keeping a direct acyclic graph (DAG) of edge splits explicitly, a single integer value is assigned to each edge in order to identify its corresponding *depth* in the graph. Edge depth values are stored during the edge-split operations, as discussed in the previous section. This is sufficient for the purpose of the adaptive procedures used in this work and allows the reduction of the memory required by them.

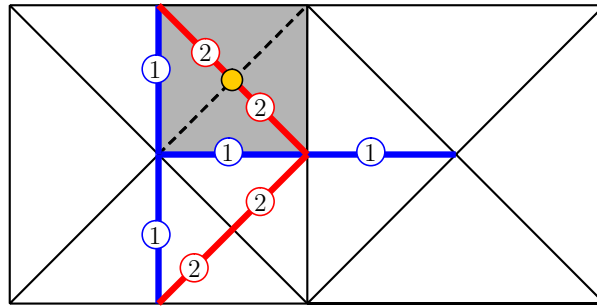
The execution of the vertex-removal operator is illustrated in Figure 7.12. For each removed vertex, the incident edges with the greatest depth are deleted, and the corresponding adjacent elements merged. For example, the vertex-removal operator is applied in a shaded $4\mathbf{k}$ patch. The maximum edge depths in the $4\mathbf{k}$ patches in Figures 7.12(a) and (b) are ③ and ② along the green and red lines, respectively.

Then, the two edges, which possess higher edge depth, are deleted, and the other two edges are merged from the each mesh.

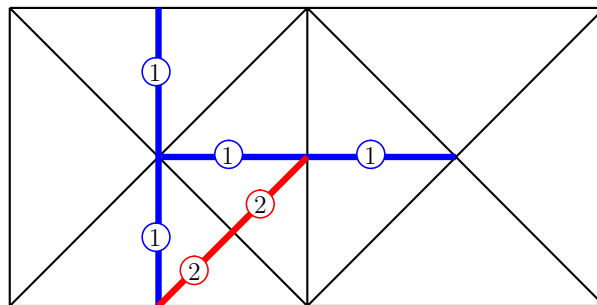
In order to preserve attributes and geometry of crack paths and mesh boundary, we impose some additional constraints to the coarsening procedure. The vertex-removal operator is neither applied to vertices of cohesive elements nor on mesh boundary. Edge-swaps can occur as cracks propagate (see Chapter 6), and undoing edge swaps is not necessary because vertices of cohesive elements are not removed.



(a)



(b)



(c)

Figure 7.12: Sequence of vertex-removal operations in shaded $4k$ patches.

7.3.2 Coarsening Criterion and Local Update

The adaptive mesh coarsening is performed on the basis of a *a posteriori* coarsening criterion, i.e. the root mean square of strain error, which is convenient to use because it is non-dimensional. The strain error indicator for volume of i th element (Ω_i) is expressed as

$$e_i = \left[\frac{\int_{\Omega_i} (\boldsymbol{\epsilon}_{\text{exact}} - \bar{\boldsymbol{\epsilon}})^T (\boldsymbol{\epsilon}_{\text{exact}} - \bar{\boldsymbol{\epsilon}}) d\Omega}{\Omega_i} \right]^{1/2} \quad (7.2)$$

where $\boldsymbol{\epsilon}_{\text{exact}}$ is exact strain, and $\bar{\boldsymbol{\epsilon}}$ is the finite element solution for the strain. In this study, because an original $4\mathbf{k}$ patch (Figure 7.13(a)) generally provides better approximation in displacement field than a coarsened $4\mathbf{k}$ patch (Figure 7.13(b)), the strain of the original $4\mathbf{k}$ patch ($\bar{\boldsymbol{\epsilon}}_f$) is used for $\boldsymbol{\epsilon}_{\text{exact}}$ while the strain of the coarsened $4\mathbf{k}$ patch ($\bar{\boldsymbol{\epsilon}}_c$) is utilized for $\bar{\boldsymbol{\epsilon}}$. Then, the strain error indicator for the $4\mathbf{k}$ patch is expressed as

$$e_{4k} = \left[\sum_{i=1}^4 \frac{\int_{\Omega_i} (\bar{\boldsymbol{\epsilon}}_f - \bar{\boldsymbol{\epsilon}}_c)^T (\bar{\boldsymbol{\epsilon}}_f - \bar{\boldsymbol{\epsilon}}_c) d\Omega}{\Omega_i} \right]^{1/2} \quad (7.3)$$

where the integration is performed numerically in four elements (Ω_i) of the original $4\mathbf{k}$ patch. When the approximated error is smaller than a specified value (e.g. 2%), an original $4\mathbf{k}$ patch is coarsened. In addition, mesh coarsening is not performed around a crack tip region in order to avoid consecutive mesh coarsening and refinement. Notice that Belytschko and Tabbara (1993) introduced a strain-projection criterion by replacing $\boldsymbol{\epsilon}_{\text{exact}}$ with the strain obtained from the L_2 projection of the finite element strain. In addition, the root mean square of strain error, the L_2 norm of strain, and the energy norm in terms of strain have a similar structure, and thus these can be similarly approximated (Zienkiewicz et al., 2005).

Adaptive mesh coarsening leads to removing shape functions while adaptive mesh refinement results in adding shape functions. The reduction of a solution space (i.e.

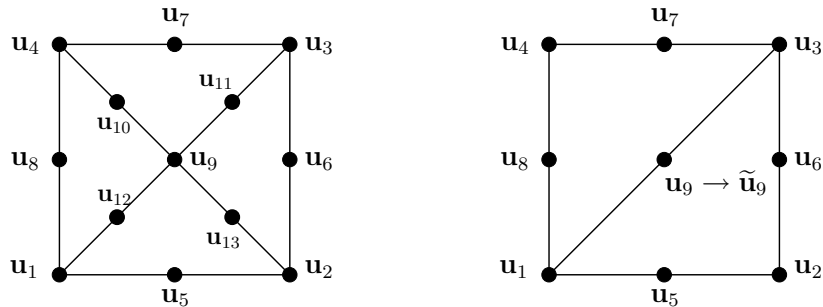


Figure 7.13: (a) Original $4\mathbf{k}$ patch, and (b) coarsened $4\mathbf{k}$ patch.

mesh coarsening) does not guarantee the conservation of the strain energy between the original $4\mathbf{k}$ patch (Figure 7.13(a)) and the coarsened $4\mathbf{k}$ patch (Figure 7.13(b)). In order to minimize the difference of the strain energies, the nodal displacement of a center node (\mathbf{u}_9) is locally modified by matching the strain energy between two different discretizations. Notice that this modification does not influence the adjacent elements of the $4\mathbf{k}$ patch. The updated displacement ($\tilde{\mathbf{u}}_9$) is utilized to evaluate the velocity and acceleration in a coarsened $4\mathbf{k}$ patch.

The nodal displacement of the center node can be updated by two approaches. First, one can optimize the displacement through minimizing the difference between the original displacement (\mathbf{u}_9) and the updated displacement ($\tilde{\mathbf{u}}_9$),

$$\min \|\mathbf{u}_9 - \tilde{\mathbf{u}}_9\|^2 \quad (7.4)$$

under the condition such that

$$g(\tilde{\mathbf{u}}_9) = E_{\text{int}} - \tilde{E}_{\text{int}}(\tilde{\mathbf{u}}_9) = 0 \quad (7.5)$$

where E_{int} is the strain energy in the original $4\mathbf{k}$ patch, and \tilde{E}_{int} is the strain energy in the coarsened $4\mathbf{k}$ patch, which is a function of the updated displacement ($\tilde{\mathbf{u}}_9$). The constraint function can be expressed in a closed form, and the optimization problem is solved by introducing the Lagrange multiplier. The computational cost in solving this optimization problem is not expensive because the number of unknown is two and because the objective function and the constraint function is quadratic which leads to a constant Hessian matrix of the objective function.

The second approach is that the nodal displacement (\mathbf{u}_9) is updated by equating the strain energy of the original $4\mathbf{k}$ patch to the strain energy in the coarsened $4\mathbf{k}$ patch along horizontal and vertical directions. For two-dimensional problems, the strain energy of the original $4\mathbf{k}$ path is decomposed into the strain energy associated with the horizontal direction ($E_{\text{int}(x)}$) and the energy related to the vertical direction ($E_{\text{int}(y)}$), i.e. $E_{\text{int}} = E_{\text{int}(x)} + E_{\text{int}(y)}$. Similarly, the strain energy of the coarsened $4\mathbf{k}$ patch is also divided into the two component, i.e. $\tilde{E}_{\text{int}}(\tilde{\mathbf{u}}_9) = \tilde{E}_{\text{int}(x)}(\tilde{\mathbf{u}}_9) + \tilde{E}_{\text{int}(y)}(\tilde{\mathbf{u}}_9)$. Each directional strain energy is set to be the same, which provides two equations for two unknowns. Then, these nonlinear equations are solved by using the Newton's algorithm.

7.4 Numerical Examples

The adaptive mesh refinement and coarsening schemes are employed for computational simulation of dynamic crack propagation. A finite element mesh is adaptively refined after inserting cohesive elements and updating displacement, velocity, acceleration and boundary conditions in time step. The new nodes resulted from the adaptive mesh refinement are relocated (or perturbed) on the basis of a given nodal perturbation factor (e.g. 0.2). After the perturbation of the new nodes, new nodal quantities are interpolated in the recursive order. The adaptive mesh coarsening is performed on the basis of the coarsening criterion, for example, in every 200 time steps before evaluating acceleration and velocity. When a $4\mathbf{k}$ patch is coarsened, the displacement of the center node is updated, and the updated displacement is utilized for the calculation of the internal force vector, acceleration and velocity. Notice that the nodal perturbation and the edge-swap operators are adaptively employed for mixed-mode fracture and branching problems in order to obtain realistic crack patterns, as discussed in Chapter 6. In this section, mode I predefined crack path, mixed-mode crack propagation and branching problems are investigated.

7.4.1 Predefined Crack Path Problem: Mode I Fracture

The geometry of a single end notched specimen is described in Figure 7.14, and the initial strain (ϵ_0) of 0.036 is applied on a specimen. A potential crack path is predefined along the horizontal direction, which provides mode I fracture, in this study. The elastic modulus is 3.24 GPa, the Poisson's ratio is 0.35, and the density is 1190 kg/m³. For the cohesive fracture parameters, the mode I fracture energy (G_I), the cohesive strength (σ_{max}), the shape parameters (α) are 352 N/m, 324 MPa, and 2, respectively. The mode II fracture parameters are assumed to be the same as the

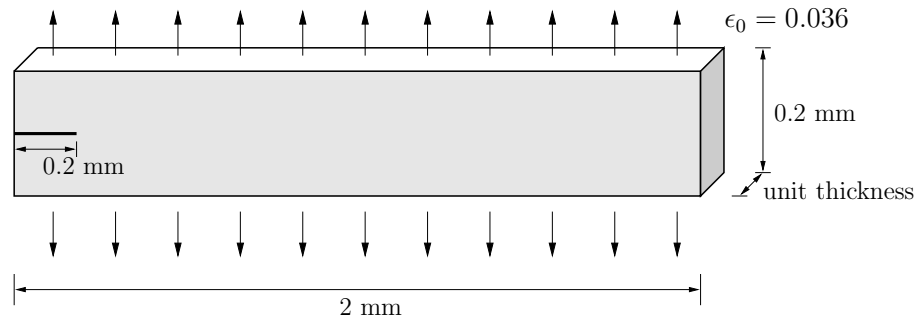


Figure 7.14: Schematics of geometry and boundary condition.

mode I fracture parameters.

The extrinsic cohesive zone model is employed with a predefined crack path, and finite element meshes are generated by a $4k$ structured mesh, shown in Figure 7.15(a). Notice that Zhang and Paulino (2005) investigated the predefined crack path problem with the intrinsic cohesive zone model (Figure 7.15(b)). Because of the discontinuous nature of the extrinsic cohesive zone model, convergence analysis are firstly performed for uniformly refined meshes. Then, the computational results with the adaptive mesh refinement & coarsening are compared to the results with a uniformly refined mesh.

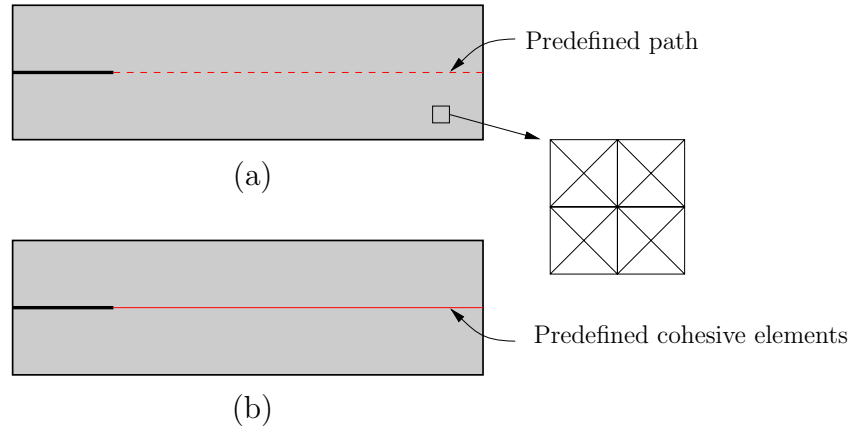


Figure 7.15: Mode I fracture problem: (a) Extrinsic cohesive zone model with predefined path, and (b) intrinsic cohesive zone model with predefined cohesive surface elements.

Convergence Analysis

Convergence of computational results with respect to the time increments and element sizes is investigated. For convergence analysis of time increments (Δt), two finite element meshes are generated within the domain. One mesh has the 100×10 mesh grid with element size of $20 \mu m$, and the other has the 200×20 mesh grid with element size of $10 \mu m$. Four time increments ($\Delta t = 1 \times 10^{-3} \mu s$, $0.4 \times 10^{-3} \mu s$, $0.2 \times 10^{-3} \mu s$ and $0.1 \times 10^{-3} \mu s$) are tested for each mesh. The normalized crack tip location versus time is plotted for the element size of $20 \mu m$ (Figure 7.16(a)) and the element size of $10 \mu m$ (Figure 7.16(b)). The decrease of the time increment results in the decrease of the slope of the crack tip location versus time curve, i.e. velocity. The computational result with $\Delta t = 0.2 \times 10^{-3} \mu s$ is almost the same as the result with $\Delta t = 0.1 \times 10^{-3} \mu s$ for both finite element meshes. This fact demonstrates that the smaller time step leads to converged results in this problem. Additionally, the element size of $20 \mu m$

provides more sensitive results than the element size of $10\ \mu\text{m}$ with respect to the change of the time increments.

In addition, the contribution of the last term in the energy variation expression (4.7), i.e. $\frac{\Delta t^2}{2} (\beta - \frac{1}{2}\gamma) (\ddot{\mathbf{u}}_{n+1} - \ddot{\mathbf{u}}_n)^T \mathbf{M} (\ddot{\mathbf{u}}_{n+1} + \ddot{\mathbf{u}}_n)$, is estimated with respect to different time increments. Five time increments ($\Delta t = 1 \times 10^{-3}\ \mu\text{s}$, $0.8 \times 10^{-3}\ \mu\text{s}$, $0.4 \times 10^{-3}\ \mu\text{s}$, $0.2 \times 10^{-3}\ \mu\text{s}$ and $0.1 \times 10^{-3}\ \mu\text{s}$) are tested with the 200×20 **4k** mesh

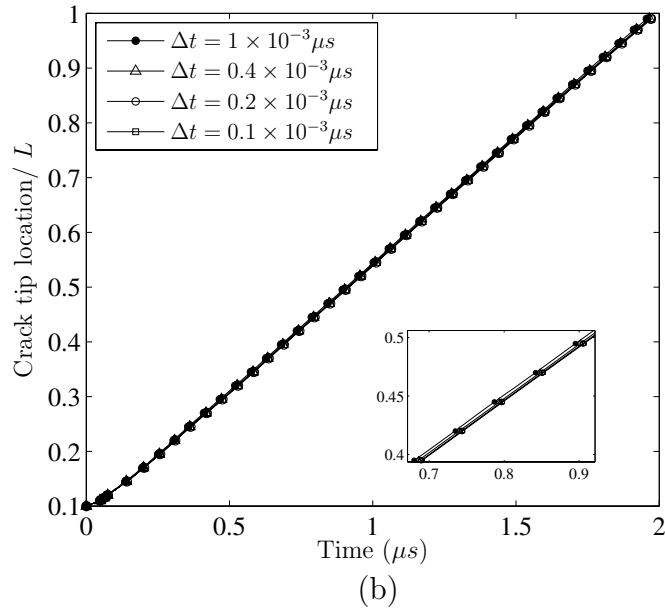
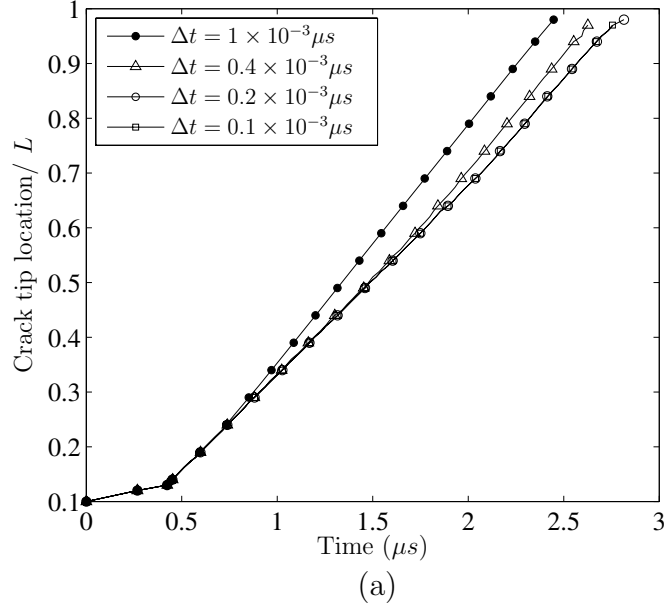


Figure 7.16: Convergence of crack tip location with respect to the time increment: (a) element size of $20\ \mu\text{m}$, and (b) element size of $10\ \mu\text{m}$.

grid. Figure 7.17 illustrates that the contribution is not significant when one selects small time step in the time integration.

For convergence analysis of element sizes, five **4k** structured meshes are generated with the mesh grid of 80×8 , 100×10 , 140×14 , 200×20 and 400×40 whose element sizes (h_{el}) are $25\mu m$, $20\mu m$, $14\mu m$, $10\mu m$ and $5\mu m$, respectively. Time increment

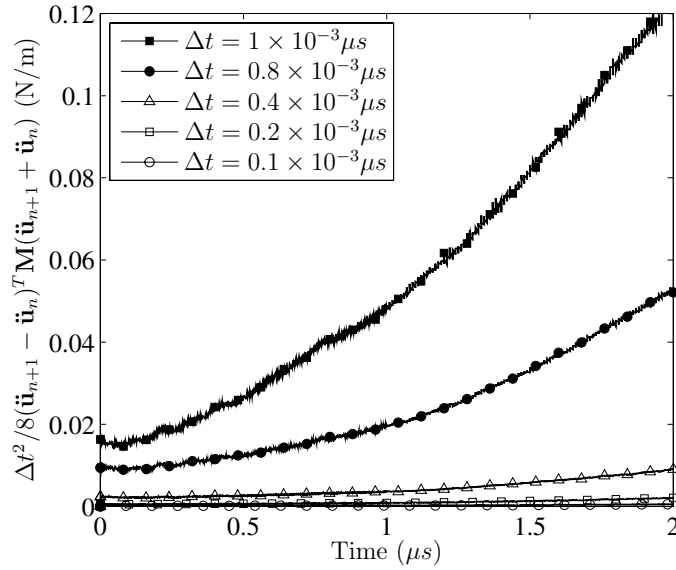


Figure 7.17: The contribution of $\Delta t^2/8(\ddot{\mathbf{u}}_{n+1} - \ddot{\mathbf{u}}_n)^T \mathbf{M}(\ddot{\mathbf{u}}_{n+1} + \ddot{\mathbf{u}}_n)$ with respect to the time increments.

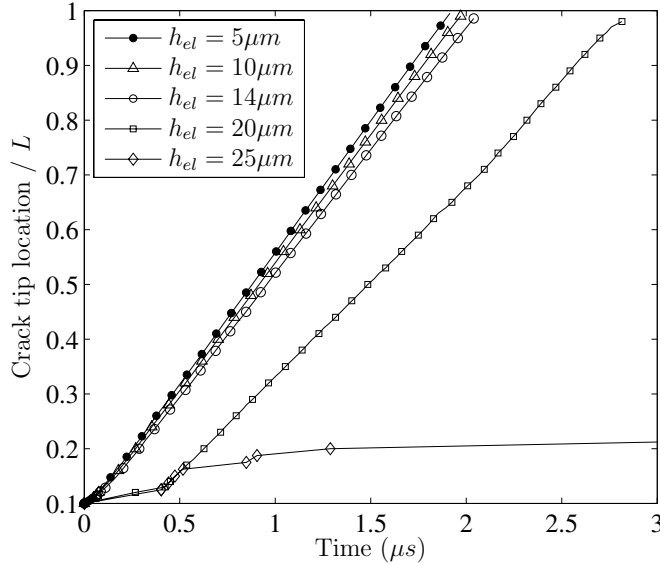


Figure 7.18: Convergence of crack tip location with respect to the element size.

(Δt) is $0.2 \times 10^{-3} \mu s$ for all five meshes, which is small enough to obtain converged results. The crack tip location versus time is plotted in Figure 7.18 for each element size. The decrease of element sizes leads to the increase of the velocity (or slope). When element size is smaller than $14 \mu m$, the change of crack tip velocity is less significant. Notice that this study focuses on the convergence of crack path and crack velocity with respect to mesh refinement.

The cohesive element size should be selected with great care. Previous researchers suggested that size of cohesive elements be at least two to three times smaller than size of the cohesive process zone so that cohesive elements represents nonlinear traction-separation relationships (Klein et al., 2001; Zhang, 2007). The size of the process zone is theoretically estimated (Rice, 1968a), which is proportional to $E\phi_n/\sigma_{\max}^2$ for quasi-static problems. Yang and Ravi-Chandar (1996) demonstrated that the process zone size also depends on loading rate for mode III dynamic fracture problems. Zhang (2007) investigated the effect of material properties and loading rate on the process zone size in conjunction with a rate-dependent constitutive model for mode I dynamic fracture problems. Figure 7.19 illustrates the convergence of the process zone size under mesh refinement for the predefined crack path problem with the initial strain of 0.025. Alternatively, cohesive element size can be determined on the basis of *a posteriori* error estimation. One can, for example, compare the traction obtained from a displacement jump (i.e. constitutive model) with the traction resulted from

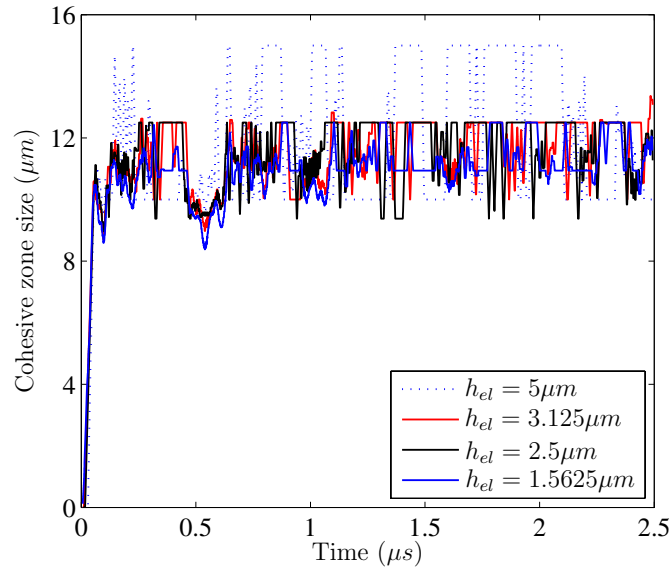


Figure 7.19: Cohesive process zone size versus time with respect to mesh refinement.

bulk elements (i.e. computational results), and determine whether to refine a finite element mesh around a crack tip or not (Haber, 2009).

Adaptive Mesh Refinement (AMR)

In order to demonstrate the accuracy of the adaptive mesh refinement (AMR) in the extrinsic cohesive zone model, the computational results with adaptive mesh refinement are compared with the results with a uniformly refined mesh. A finite element mesh with uniform element size of $5\mu\text{m}$ is generated by the 400×40 mesh grid, which provides 64000 elements and 128881 nodes. The zoom of the uniform mesh around the crack tip is shown in Figure 7.20(a). Finite element mesh for adaptive mesh refinement simulation is initially generated by the 100×10 mesh grid with the refined element in a crack tip region. The coarse mesh grid has element size of $20\mu\text{m}$, while element size at the crack tip region is $5\mu\text{m}$, which corresponds to the element size of a uniform mesh. The zoom of the mesh around the crack tip is illustrated in Figure 7.20(b). The number of elements is 4448, and the number of nodes 9147 is at the initial discretization. Since the adaptive local mesh refinement significantly

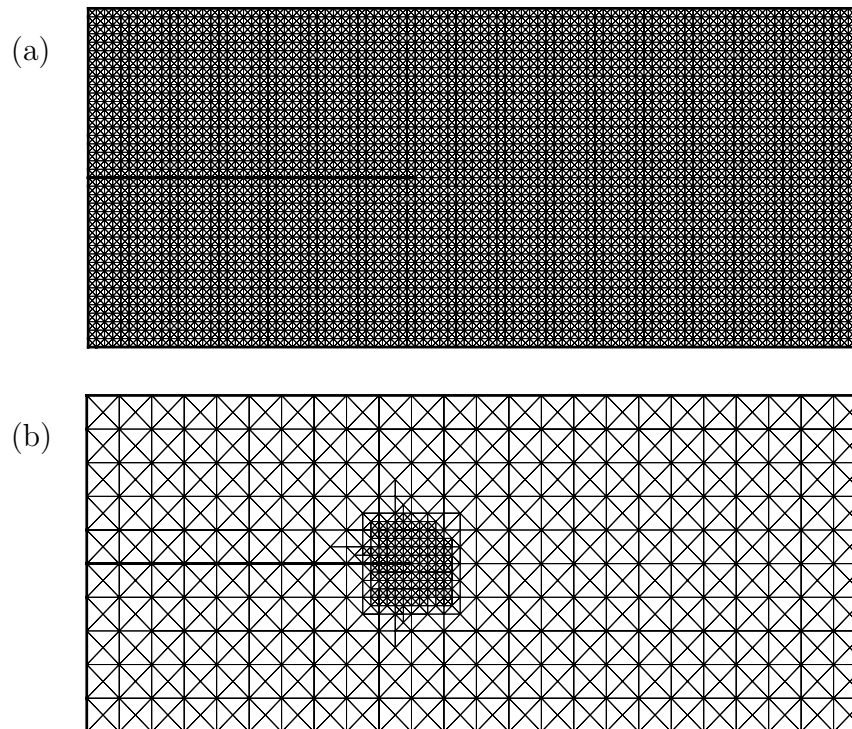


Figure 7.20: (a) Finite element mesh with uniform element size of $5\mu\text{m}$, and (b) finite element mesh with local refinement around crack tip and the size of $5\mu\text{m}$.

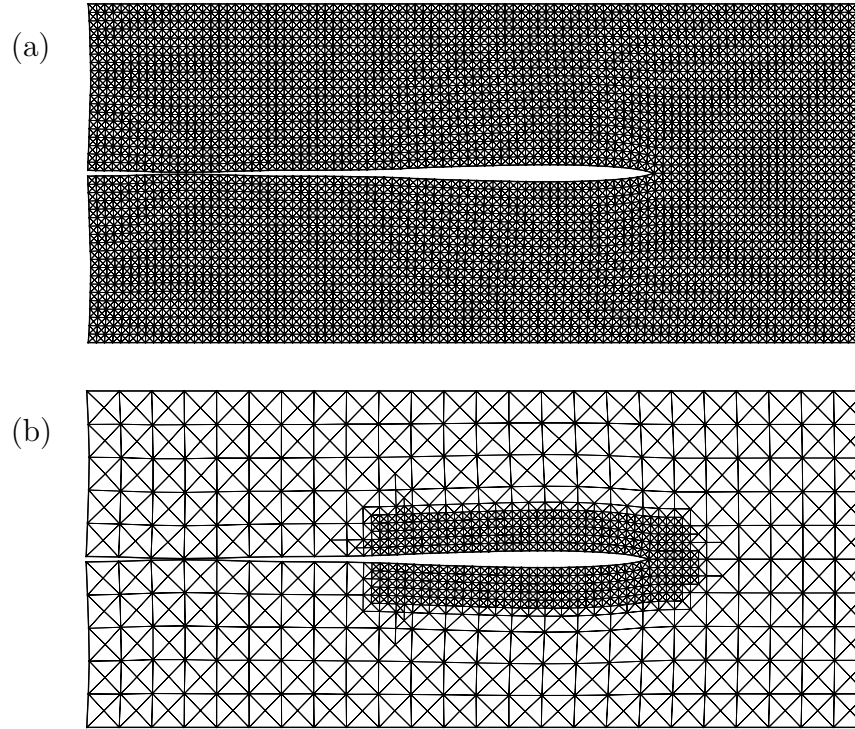


Figure 7.21: Deformed shape with finite element mesh at $t = 0.2\mu s$ (a) uniform 400×40 mesh grid, and (b) 100×10 mesh grid with adaptive local mesh refinement.

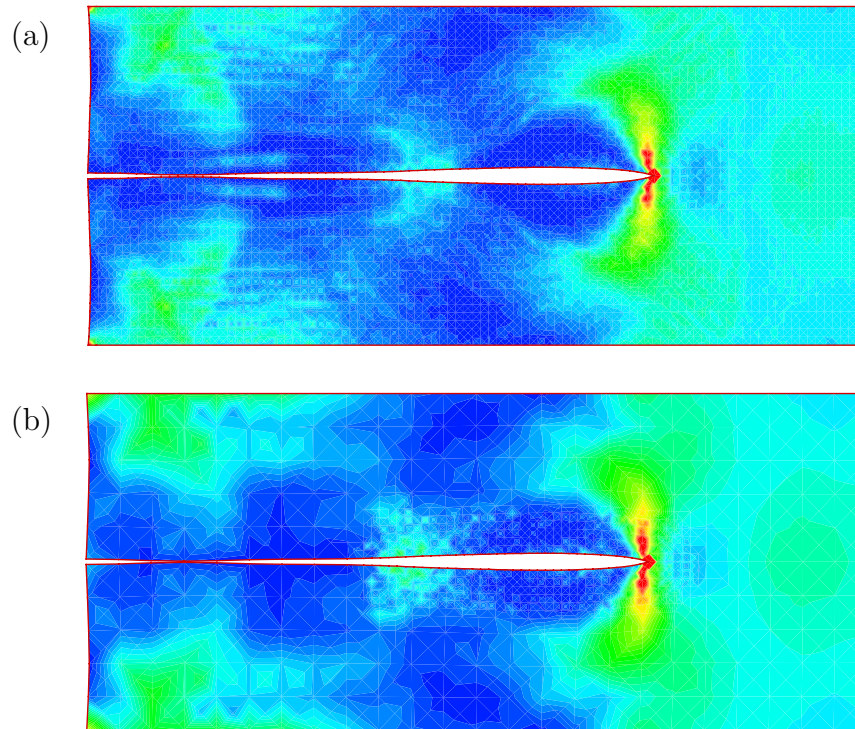


Figure 7.22: Strain energy at $t = 0.2\mu s$ (a) 400×40 mesh grid, and (b) 100×10 mesh grid with the AMR.

reduce the number of nodes and the number of elements, the computational cost with the AMR technique is considerably cheaper than standard computational simulations with a uniformly refined mesh.

While a crack propagates, the crack tip position is updated, and finite element mesh around a crack tip is adaptively refined, as shown in Figure 7.21(b). Deformed shapes for both finite element meshes at the time (t) $0.2 \mu s$ are illustrated in Figure 7.21. The crack tip position and shape obtained from the AMR technique are almost identical to those resulted from a uniformly refined mesh. Figure 7.22 (a) and (b) illustrate the strain energy at $0.2 \mu s$ for the uniform 400×40 mesh grid and the 100×10 mesh grid with the AMR, respectively. Both meshes demonstrate the high strain energy around the crack tip, and globally similar strain energy variation. However, the 400×40 mesh grid provides more detailed description of the strain energy, like the expanding wave from the crack tip, than the 100×10 mesh grid with the AMR, as expected.

The energy balance is a necessary condition to ensure the numerical stability (Belytschko et al., 2000). The total energy (E_{tot}) consists of the external work (E_{ext}), strain energy (E_{int}), kinetic energy (E_{kin}) and work done by fracture (E_{fra}). In this simulation, the total energy is a constant, which corresponds to the initial strain

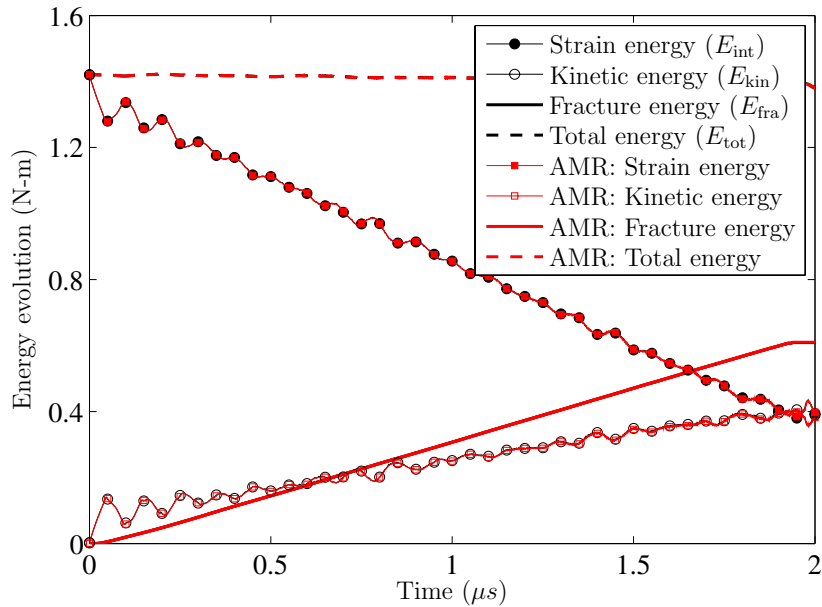


Figure 7.23: Energy evolution with respect to the time for the uniform mesh refinement (black lines) and the AMR (red lines).

energy, i.e. no external work ($E_{\text{ext}} = 0$). After a crack initiates and propagates, the strain energy decreases while the kinetic energy and the fracture energy increase. Figure 7.23 illustrates the energy conservation with respect to time for both the uniform mesh refinement (black dashed line) and the adaptive mesh refinement (red dashed line). The energy evolutions of strain energy, kinetic energy and fracture energy for the uniform mesh refinement (black lines) are almost the same as the evolutions for the adaptive mesh refinement (red lines). Therefore, the AMR technique in the extrinsic cohesive zone model provides equivalently accurate computational results compared to the results with the uniformly refined mesh in this example.

Adaptive Mesh Coarsening

Adaptive mesh coarsening reduces a solution space, and thus leads to numerical error in finite element analysis. The error due to the adaptive coarsening is investigated on the basis of the energy evolution. Element size is $20\mu\text{m}$ and $5\mu\text{m}$ for the coarse and fine mesh grids, respectively. While a crack propagates, the crack tip region is adaptively refined, and the outside of the crack tip region is coarsened on the basis of the coarsening criterion, as discussed previously. Two sets of finite element analysis are performed with the initial strain of 0.036 and 0.028. Four error levels (0.01, 0.02, 0.05, 0.1) are used for the coarsening criterion.

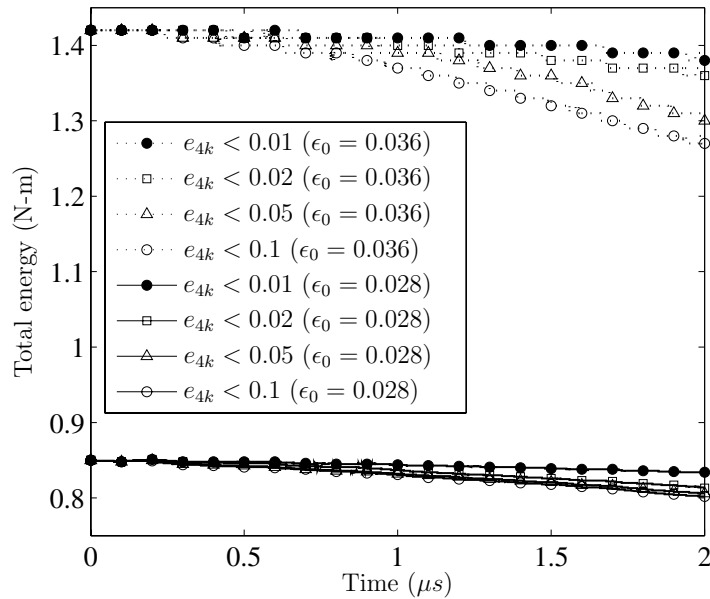


Figure 7.24: Total energy variation with respect to time for different coarsening error level of e_{4k} .

Table 7.1: Numbers of nodes and elements, and relative error of the total energy with respect to the coarsening error levels (e_{4k}).

	$\epsilon_0 = 0.036$			$\epsilon_0 = 0.028$		
	# of nodes	# of elem	$\Delta E_{\text{tot}}/E_{\text{tot}}$	# of nodes	# of elem	$\Delta E_{\text{tot}}/E_{\text{tot}}$
$e_{4k} < 0.01$	37530	18274	0.0282	33974	16496	0.0188
$e_{4k} < 0.02$	28250	13634	0.0423	19098	9058	0.0424
$e_{4k} < 0.05$	19622	9320	0.0845	17546	8282	0.0518
$e_{4k} < 0.1$	18904	8556	0.1056	17542	8280	0.0565

0.05 and 0.1) are tested for the coarsening criterion. Figure 7.24 illustrates the total energy evolution with respect to time for different coarsening error levels of e_{4k} . The lower value of the coarsening criterion, which corresponds to more tighter criterion for the coarsening, results in less deviation for the constant total energy. Table 7.1 demonstrates the numbers of elements and nodes, and the relative error of the total energy ($\Delta E_{\text{tot}}/E_{\text{tot}}$) at the final discretization with respect to different coarsening error levels. A loose mesh coarsening criterion yields fewer nodes and elements (i.e. coarser mesh), which results in a higher relative error at the final discretization.

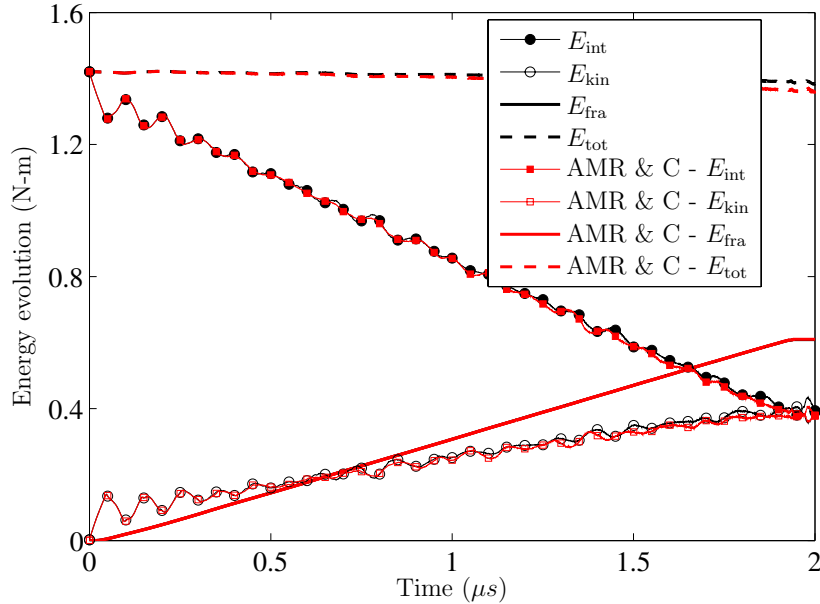


Figure 7.25: Energy evolution with respect to the time for the uniform mesh refinement (black lines) and the adaptive mesh refinement & coarsening (AMRC) (red lines).

In addition, the energy evolution with the adaptive mesh refinement and coarsening is compared to the energy evolution with the uniform mesh refinement. The initial strain is 0.036, and $4\mathbf{k}$ patches are coarsened when the root mean square of strain error (e_{4k}) is less than 0.02. Figure 7.25 illustrates the well agreement of the energy evolution between the uniform mesh refinement (black lines) and the adaptive mesh refinement and coarsening (red lines). Although the total energy slightly decreases for the case of the adaptive mesh refinement and coarsening, the fracture energy (E_{fra}) evolutions are almost identical to each other.

7.4.2 Mixed-Mode Crack Propagation

For a mixed-mode fracture problem, a doubly notched specimen under impact load is investigated. The geometry of the specimen is shown in Figure 7.26(a), and the impact loading is applied by a projectile. Kalthoff and Winkler (1987) tested the specimen to investigate failure mode transition with respect to the loading rates. They observed that relatively lower loading rate resulted in brittle failure with a crack propagation angle of about 70° while higher loading rate generated a shear band ahead of the initial notch with a negative angle of about -10° . This study mainly focuses on brittle fracture behavior.

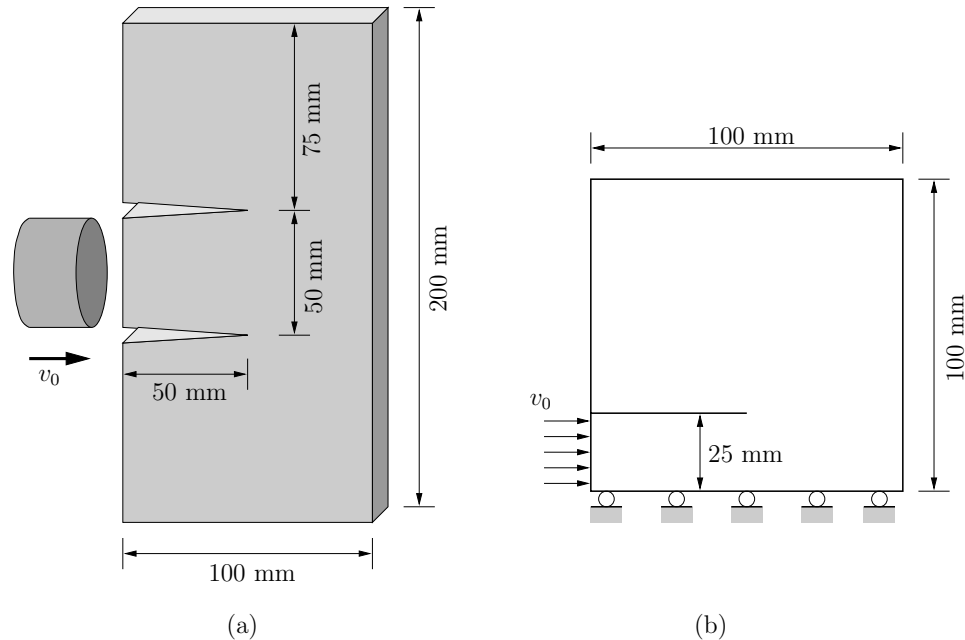


Figure 7.26: (a) Geometry and boundary condition of a doubly notched specimen, and (b) its symmetry domain for finite element analysis.

In the computational simulation, the symmetry condition is utilized, and thus fixed displacement along the vertical direction is imposed at the bottom of the specimen, shown in Figure 7.26(b). The projectile is assumed to have the same elastic impedance as the doubly notched specimen, and thus one-half of the projectile speed is applied as the impact velocity (Lee and Freund, 1990). The impact velocity (v_0) of 16.54 m/s is applied at the lower left region. Maraging steel 18Ni(300) is used as a representative material property of the doubly notched specimen (Belytschko et al., 2003; Zhang and Paulino, 2005). The elastic modulus is 190 GPa, the Poisson's ratio is 0.3, and the density is 8000 kg/m³, which lead to the Rayleigh wave speed of 2800 m/s. For mode I fracture parameters, fracture energy and cohesive strength are 22.2 kJ/m² and 1.733 GPa, respectively. The shape parameter is selected as two, which leads to an almost linear softening behavior. The mode II fracture parameters are assumed to be the same as the mode I fracture parameters.

In the analysis of the adaptive mesh refinement and coarsening, the finite element mesh is initially discretized as shown in Figure 7.27(a). The mesh has 20×20 coarse mesh grid with element size of 5mm, and is refined around a crack tip with element size of 1.25mm. The numbers of elements and nodes are 4191 and 5351, respectively. A cohesive surface element is first inserted at time 25.4 μ s, and the complete separation of the cohesive element occurs at time 26.5 μ s. The finite element mesh discretization at time 55 μ s and 77.5 μ s are illustrated in Figures 7.27(b) and (c), respectively. The crack tip region is adaptively refined, and the far field from the crack tip is coarsened. During this dynamic crack propagation, the nodal perturbation (NP = 0.2) is adaptively employed around crack tip region, and 28 edge-swap operations are performed when and where they are needed. More **4k** patches on the left hand side of the main crack are coarsened than **4k** patches on the right hand side because the right hand side of the crack provides more complicated displacement field. The strain energy density at time 77.5 μ s is shown in Figure 7.27(d), and it clearly illustrates that the right hand side has higher strain energy than the left hand side. The initiation angle is approximately 62°, which is obtained by the linear regression. These computational results well agree with the previous computational results by Belytschko et al. (2003); Zhang and Paulino (2005); Song and Belytschko (2009). Belytschko et al. (2003) simulated the brittle fracture behavior based on loss of hyperbolicity criterion in conjunction with a discontinuous enrichment functions (i.e. X-FEM). Zhang and Paulino (2005) utilized an intrinsic cohesive zone model for dynamic crack propagation, and further investigated the effect of material gradation. Song and Belytschko (2009) introduced a cracking node method for this problem.

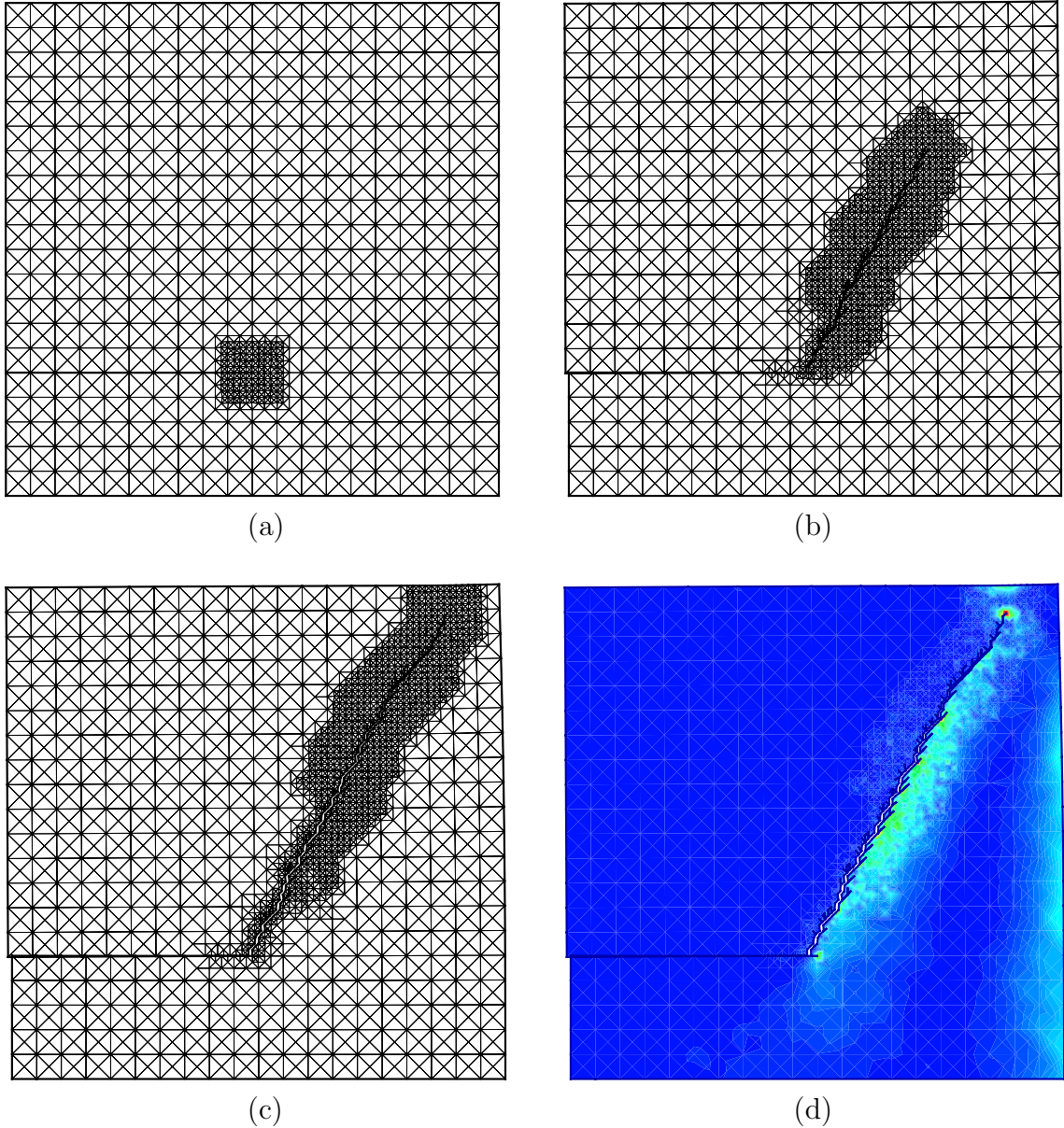


Figure 7.27: Finite element discretization for the adaptive mesh refinement and coarsening (a) at the initial time step, (b) at time $t = 55\mu s$ and (c) at time $t = 77.5\mu s$, and (d) strain energy density at time $t = 77.5\mu s$.

In addition, the entire doubly notched specimen is analyzed without employing the symmetric boundary condition for the comparison purpose. The problem is not fully symmetric after a crack propagates because of the nodal perturbation around two crack tip regions. Since the interaction between two crack tip regions is not significant, the computational results with the symmetric boundary condition is consistent with the results without the symmetric boundary condition, as illustrated in Figure 7.28.

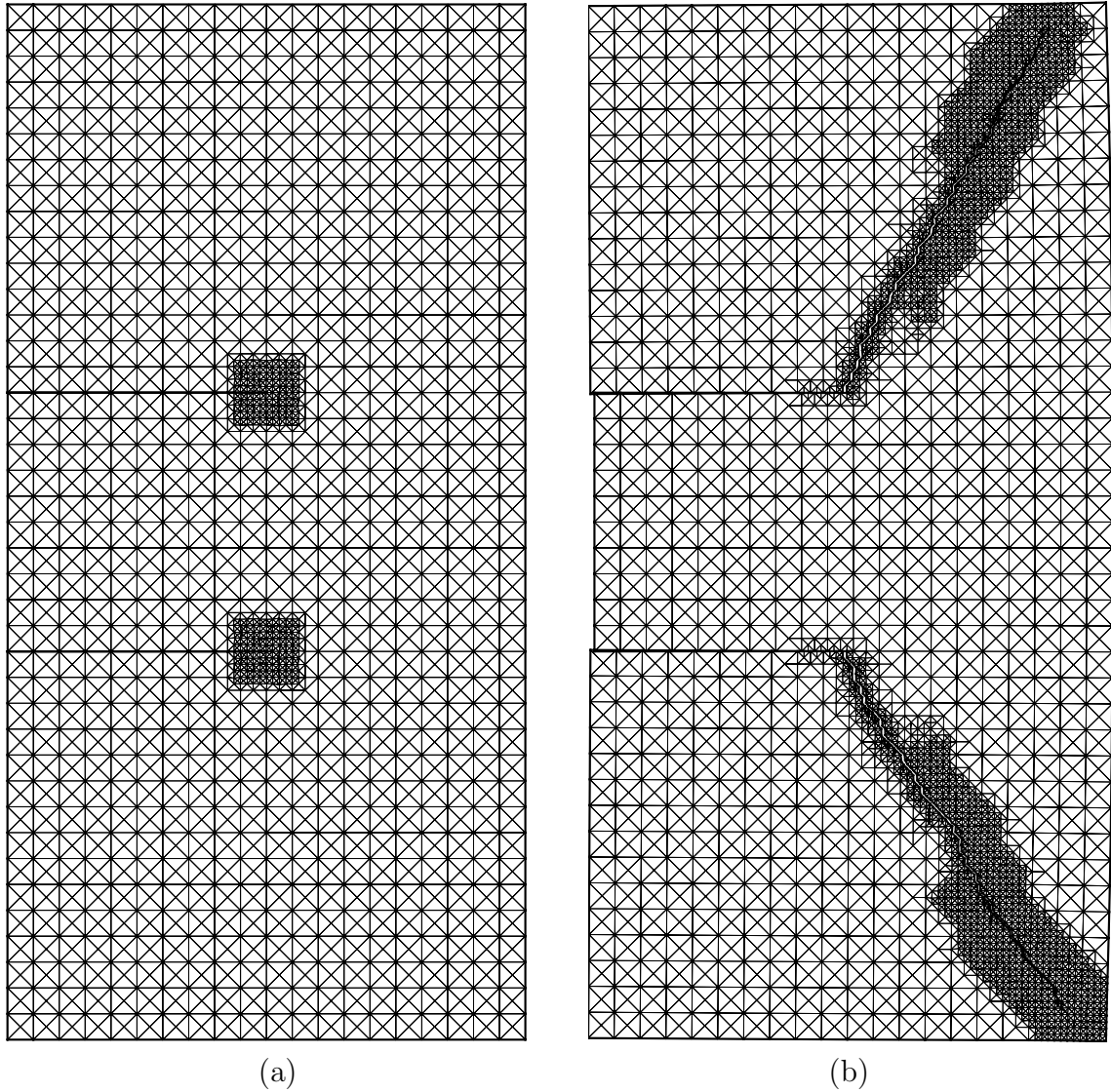


Figure 7.28: Finite element discretization without employing the symmetry boundary conditions (a) at the initial time step, and (b) at time $t = 77.5\mu s$.

The finite element analysis of the adaptive mesh refinement & coarsening (AMR & C) is compared to the analysis with the uniform mesh refinement and the adaptive mesh refinement (AMR). Finite element meshes for the uniform mesh refinement and the adaptive mesh refinement at time $t = 77.5\mu s$ are shown in Figure 7.29 (a) and (b), respectively. The uniform $4k$ mesh has 80×80 mesh grid, and element size is 1.25 mm. The numbers of elements and nodes are initially 51601 and 25600, respectively, which are almost ten times higher than the numbers for the adaptive mesh refinement and coarsening. The analysis of the adaptive mesh refinement has the same initial discretization as the analysis of the adaptive mesh refinement & coarsening. The

Table 7.2: Computational cost comparison for the mixed-mode crack propagation.

	Uniform mesh	AMR	AMR & C
Computational time	256 min	36 min	25 min

computational time is listed in Table 7.2. Computation with the adaptive mesh refinement and coarsening is approximately ten times faster than computation with the uniform mesh, while computation with the adaptive mesh refinement is almost seven times faster than computation with the uniform mesh. The crack path for each analysis is described in Figure 7.30(a), and the overall crack path corresponds well with each other. The crack velocity is estimated by the linear fitting of three adjacent crack tip points with respect to time. The crack velocities for the uniform mesh refinement, the adaptive mesh refinement, and the adaptive mesh refinement & coarsening illustrate similar trends, as shown in Figure 7.30(b). The crack velocity steeply increases at the crack initiation, and gradually decreases around time $t = 50\mu s$. The average crack velocity is about 2000 m/s, which is 71% of the Rayleigh wave speed.

Two different element sizes are compared in the analysis of the adaptive mesh refinement & coarsening. One finite element mesh has 20×20 coarse mesh grid with element size of $5mm$, and is locally refined around the crack tip with element size of

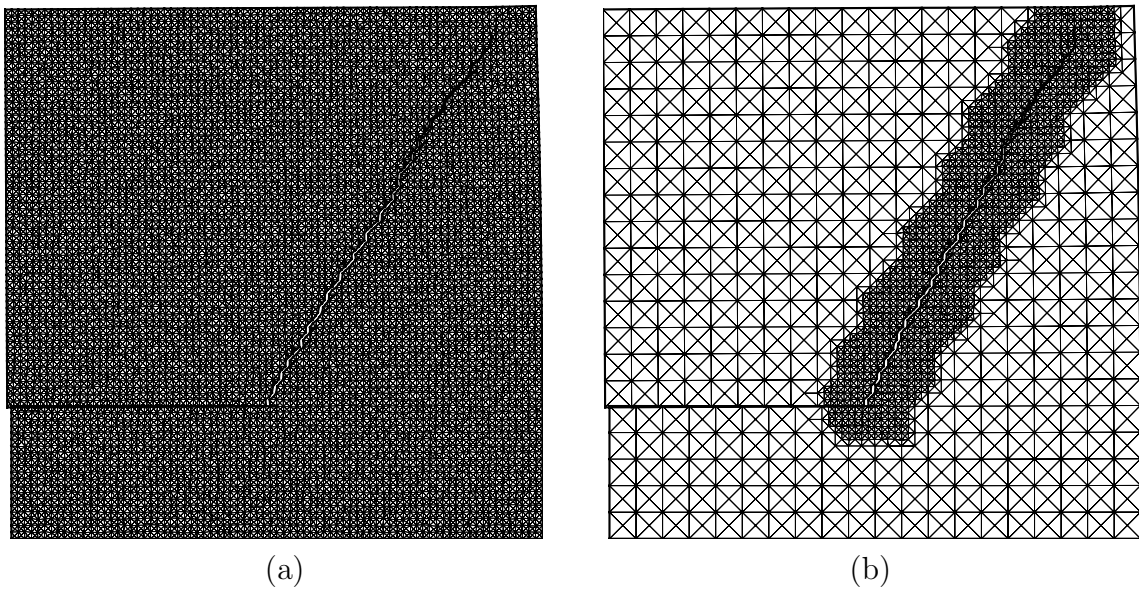
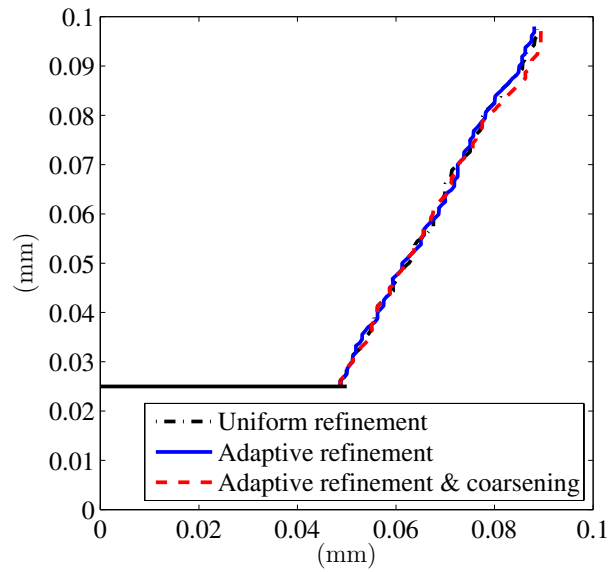
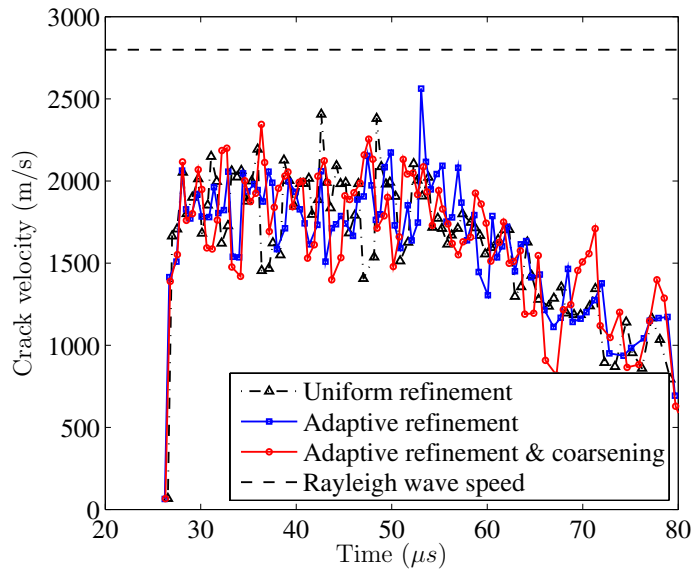


Figure 7.29: Finite element discretization at time $t = 77.5\mu s$ for (a) the uniform mesh refinement, and (b) the adaptive mesh refinement.

1.25mm. The other has 40×40 coarse mesh grid with element size of 2.5mm, and is locally refined around the crack tip with element size of 0.625mm. Figure 7.31 demonstrates the agreement of the crack path and velocity for the two sizes of the coarse mesh grid. In the evaluation of the crack velocity, three adjacent points are used for the 20×20 coarse mesh grid while six adjacent points are utilized for the



(a)

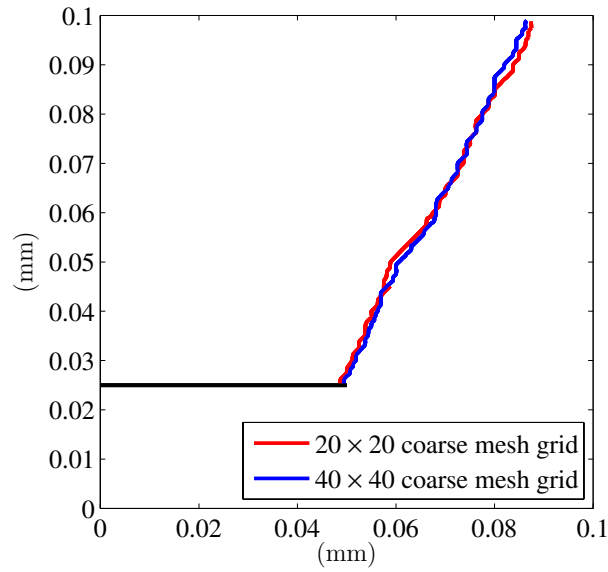


(b)

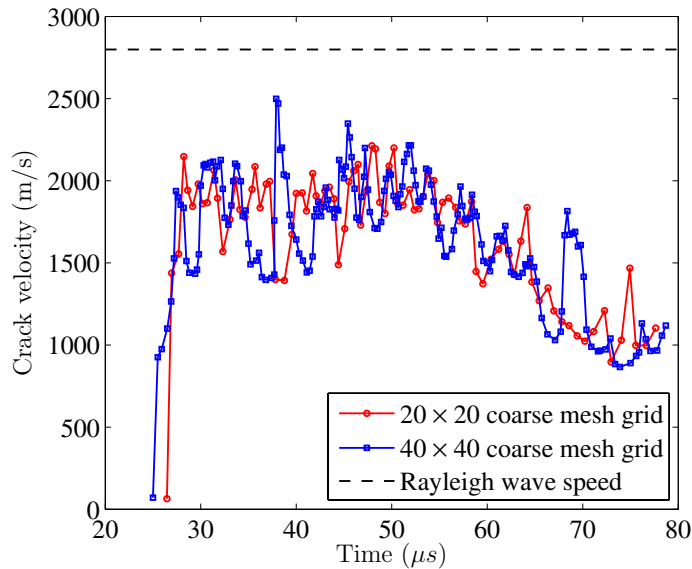
Figure 7.30: (a) Crack path, and (b) crack velocity for the uniform mesh refinement, the adaptive mesh refinement, and the adaptive mesh refinement & coarsening.

40×40 coarse mesh grid.

The energy evolutions are estimated for adaptive mesh refinement and adaptive mesh refinement & coarsening during computational simulation, as shown in Figures 7.32(a) and (b), respectively. The external energy (E_{ext}) is resulted from the impact velocity, and is converted into the strain energy (E_{int}), the kinetic energy (E_{kin}) and



(a)



(b)

Figure 7.31: (a) Crack path, and (b) crack velocity for different sizes of the coarse mesh grid.

the fracture energy (E_{fra}). The strain energy initially increases because of the impact, and slightly decreases while a crack propagates. Both kinetic and fracture energies increase with respect to time. The summation of E_{int} , E_{kin} and E_{fra} is almost the same as the external energy for the case of adaptive mesh refinement (Figure 7.32(a)), i.e. energy conservation. On the other hand, the adaptive mesh coarsening leads to a little

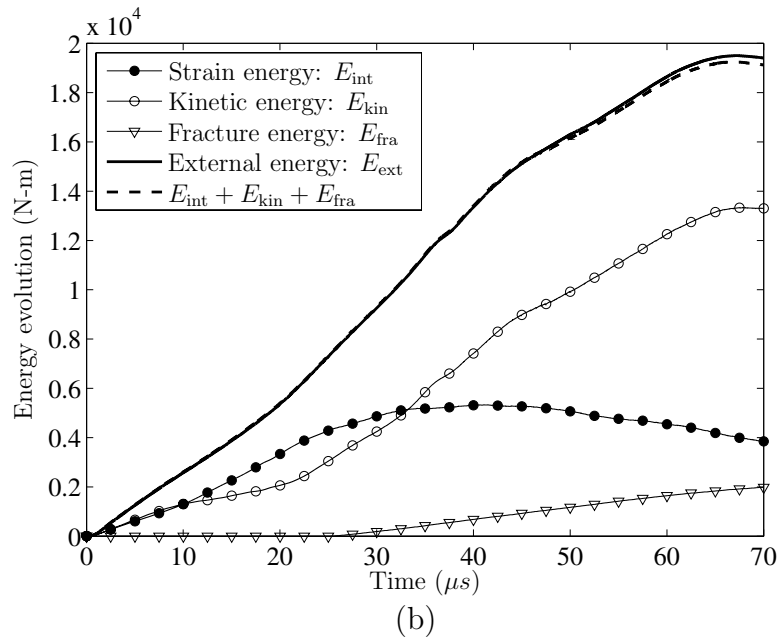
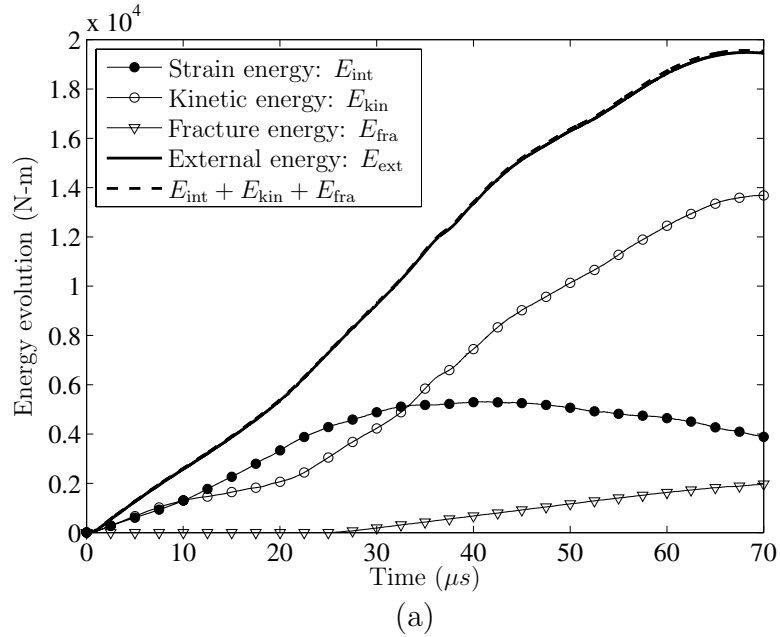


Figure 7.32: Energy evolution with respect to time for (a) adaptive mesh refinement, and (b) adaptive mesh refinement and coarsening.

energy dissipation, as shown in Figure 7.32(b). Notice that such energy dissipation is also observed in the previous mode I problem (see Figure 7.25).

7.4.3 Crack Branching Problem

For a crack branching problem, the geometry of a specimen is illustrated in Figure 7.33, and the uniform traction of 1.5 MPa is applied at the top and bottom edges of the specimen. For elastic properties, the elastic modulus and the Poisson's ratio are 32 GPa and 0.2, respectively, and the density is 2450 kg/m³, which provide the Rayleigh wave speed of 2125 m/s. For mode I fracture parameters, the fracture energy (ϕ_n) is 3 N/m, the cohesive strength (σ_{\max}) is 12 MPa, and the shape parameter (α) is selected as two. The mode II parameters are assumed to be the same as the mode I parameters. Notice that Belytschko et al. (2003) studied this problem in conjunction with a discontinuous shape function (X-FEM), while Song and Belytschko (2009) simulated this problem by using the cracking node method.

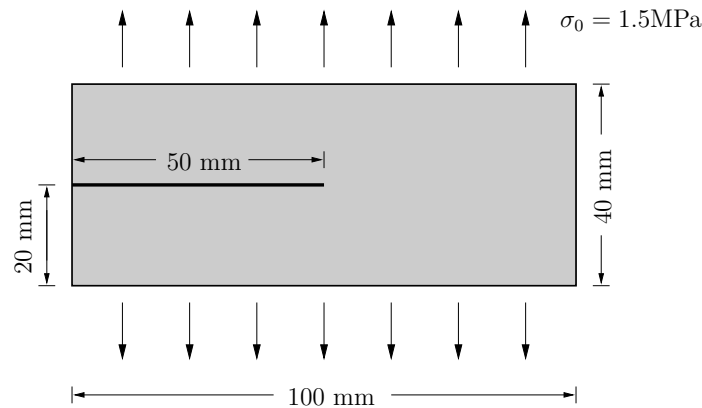


Figure 7.33: Geometry of a branching problem.

The branching problem is computed by utilizing three different approaches: uniform mesh refinement, adaptive mesh refinement, and adaptive mesh refinement & coarsening. For the uniform mesh refinement, the domain is discretized with the 160×64 mesh grid which leads to element size of 0.625 mm. The number of nodes is 82529, and the number of elements is 40960 at the initial discretization. For the adaptive mesh refinement, the domain is discretized with a coarse mesh grid of 40×16 with element size of 2.5 mm. The crack tip region is refined with element size of 0.625 mm, which is the same size as the uniformly refined mesh. For the adaptive mesh coarsening, **4k** patches are coarsened when the root mean square of strain error is less than 0.02 for the outside of crack tip regions.

Table 7.3: Computational cost comparison for the crack branching problem.

	Uniform mesh	AMR	AMR & C
Computational time	397 min	62 min	55 min

For the three different approaches, the crack patterns at the time $60\mu s$ are illustrated in Figure 7.34, and the overall crack patterns are similar to each other. The crack initiation time is $11\mu s$ for all cases. After a crack propagates about $15\sim 18$ mm, the major branching occurs at the corresponding time of $27\sim 30\mu s$. In addition, the numbers of nodes in Figures 7.34(a), (b) and (c) are 83191, 24559 and 16867, and the numbers of volumetric elements are 40960, 11845 and 7988, respectively. The computational time for each simulation is provided in Table 7.3. Computation with the adaptive mesh refinement & coarsening is approximately seven times faster than

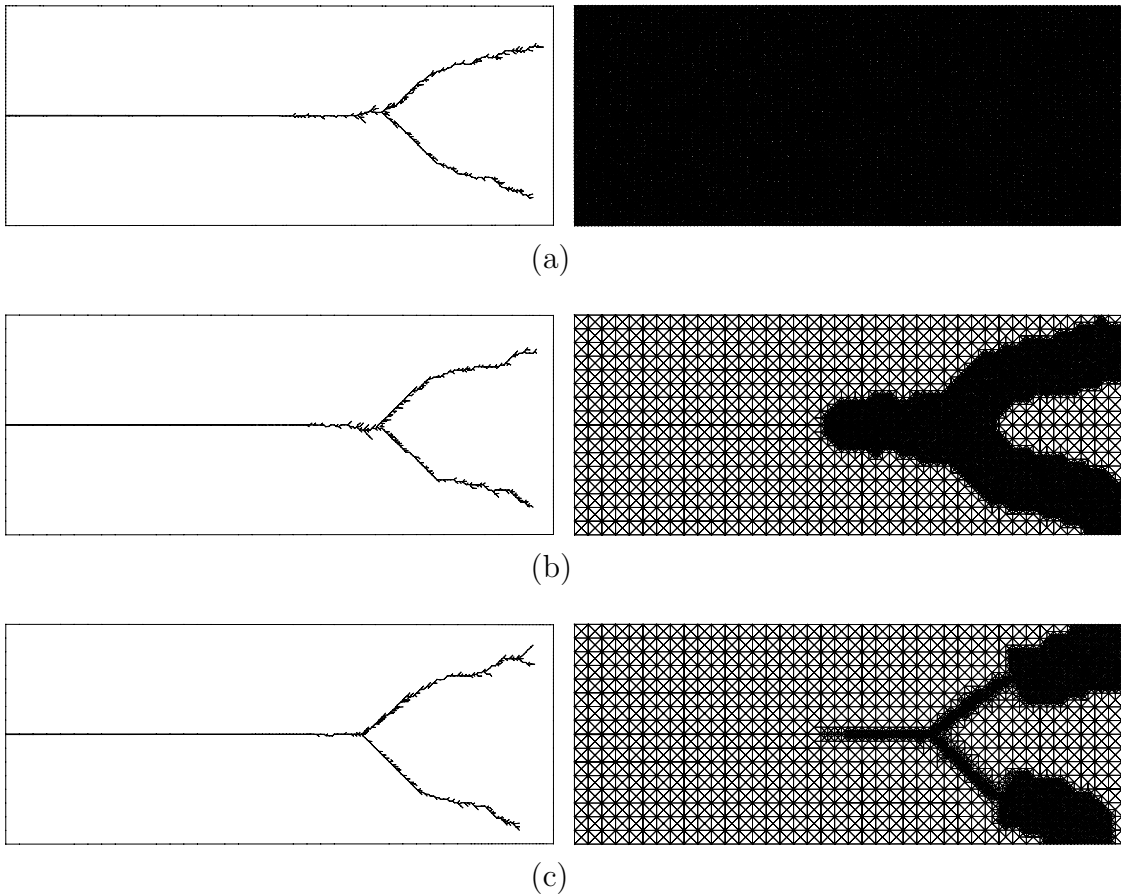


Figure 7.34: Comparison of crack patterns and finite element meshes (a) uniformly refined mesh, (b) adaptive mesh refinement, and (c) adaptive mesh refinement and coarsening.

computation with the uniform mesh. Therefore, the adaptive mesh refinement & coarsening technique is able to significantly reduce the number of degrees of freedom and the computational cost, while providing almost equivalent computational results to the use of the uniformly refined mesh.

In addition, Figure 7.35 plots the crack velocity for the three approaches, and all three results agree with each other. The crack velocity initially increases up to 1500 m/s (60% of the Rayleigh wave speed) until 15 μ s. Then, the velocity decreases from 1500 m/s to 500 m/s, and increases to 1600 m/s (65% of the Rayleigh wave speed) until 27 μ s, which corresponds to the time of the major branching initiation. Such velocity change is correlated with vertical stress wave propagation. Vertical stress with respect to time is illustrated in Figure 7.36 for the computation with the adaptive mesh refinement & coarsening. Because of the applied traction (σ_0), the tension wave propagates along the vertical direction, and stress is concentrated at the crack tip before the crack initiation (Figure 7.36(a)). While a crack propagates, vertical stress is released from the top and bottom edges of the specimen (Figure 7.36(b)). Then, vertical stress ahead of the crack tip region decreases, as shown in Figures 7.36(c) and (d), which correspond to the time when the crack velocity decreases. Vertical stress ahead of the crack tip region increases (Figures 7.36(e), (f) and (g)) with respect to the increase of the crack velocity, and the major branching occurs, as shown in Figure 7.36(h).

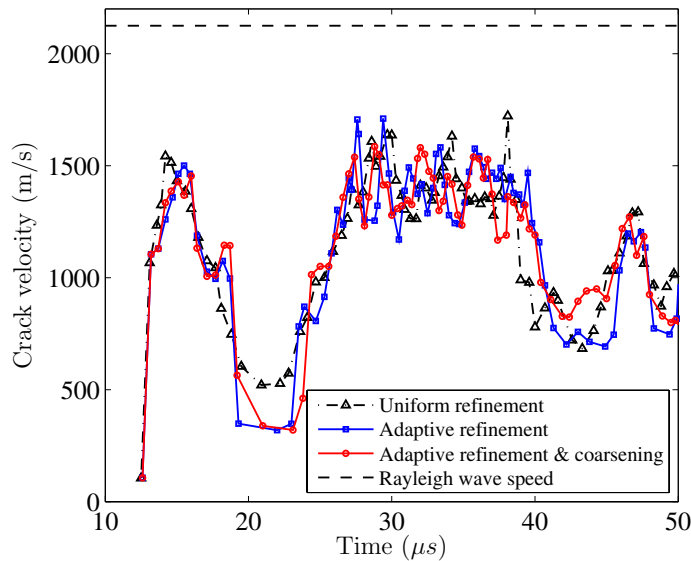


Figure 7.35: Crack velocity for the uniform mesh refinement, the adaptive mesh refinement, and the adaptive mesh refinement & coarsening.

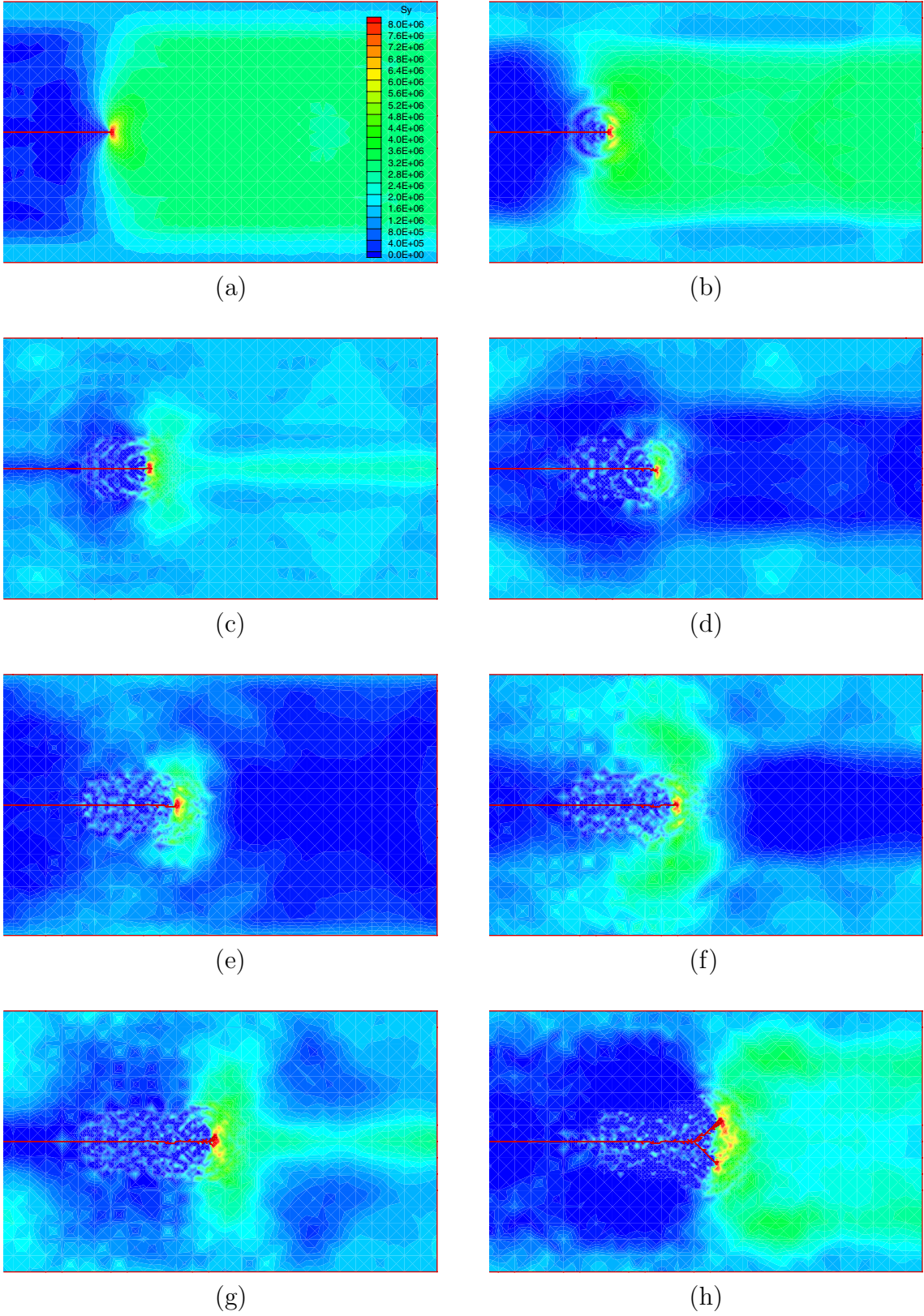
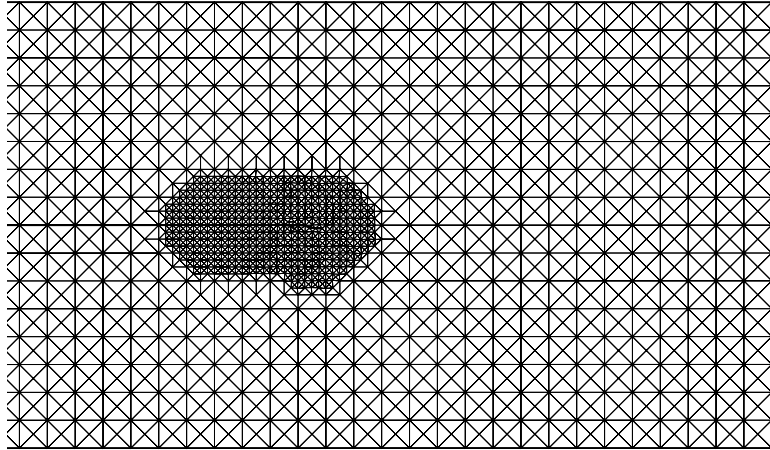
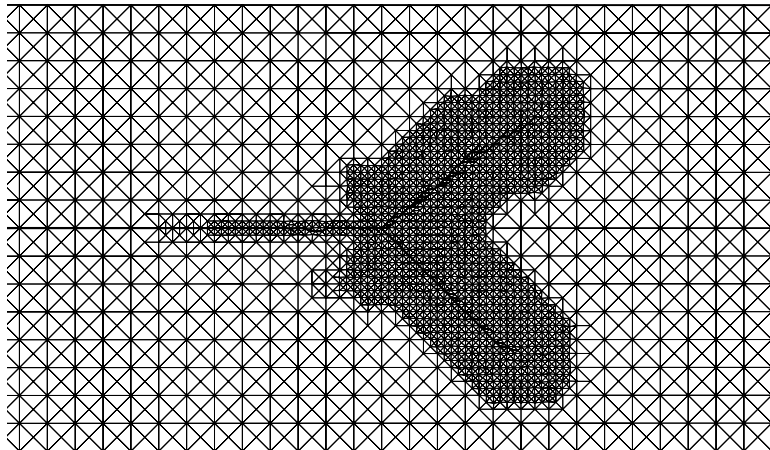


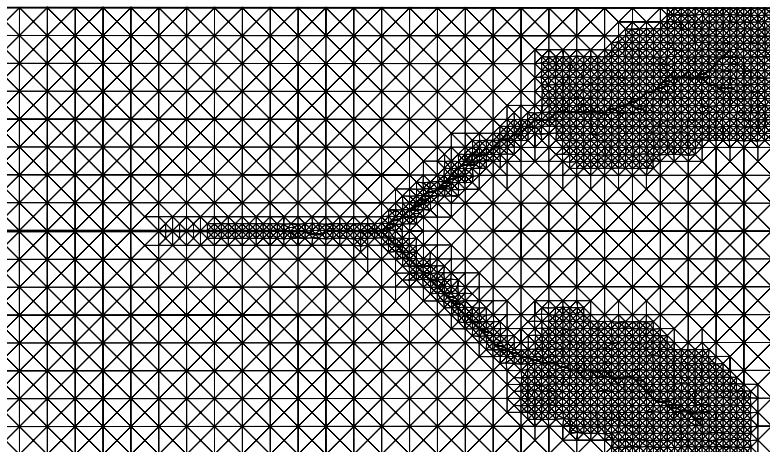
Figure 7.36: Vertical stress distribution with respect to time: (a) $10 \mu s$, (b) $13 \mu s$, (c) $16 \mu s$, (d) $19 \mu s$, (e) $22 \mu s$, (f) $25 \mu s$, (g) $28 \mu s$ and (h) $31 \mu s$.



(a)



(b)



(c)

Figure 7.37: Crack branching at different time steps: (a) time = $20\mu s$, (b) time = $40\mu s$, and (c) time = $60\mu s$.

Figure 7.37 illustrates crack patterns at different time ($20\mu s$, $40\mu s$ and $60\mu s$) with finite element mesh. While a crack propagates, crack tip regions are adaptively refined (Figure 7.37(a)). When branching occurs, two crack tip regions are refined and the outside of the two crack tip regions are coarsened on the basis of the coarsening criterion. Figure 7.38 demonstrates the zoom of the finite element mesh at time $60\mu s$. One can observe that local nodes are perturbed with the perturbation factor of 0.2, and that the edge-swap operators are utilized when they are needed.

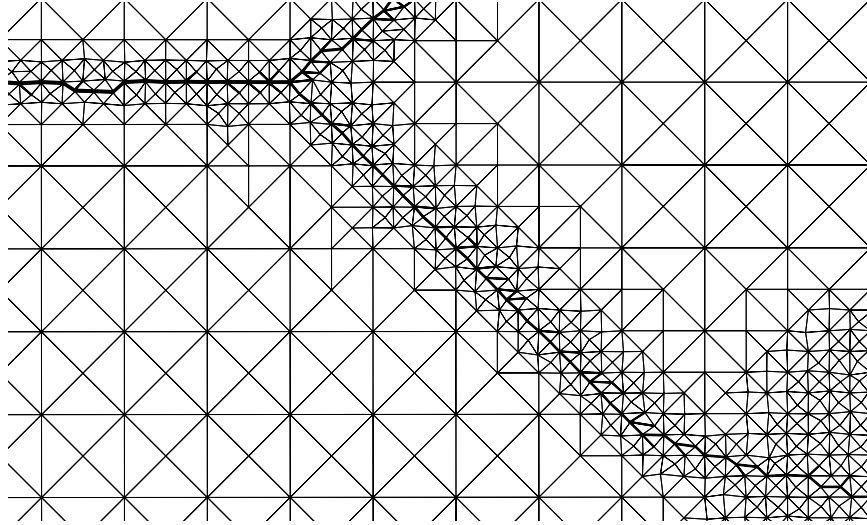


Figure 7.38: Zoom of the finite element mesh at time $60\mu s$.

7.5 Concluding Remarks

Adaptive mesh refinement and coarsening schemes are systematically developed in solving dynamic cohesive fracture problems. The adaptive mesh refinement is based on a sequence of edge-split operators while the adaptive mesh coarsening consists of a sequence of vertex-removal (or edge-collapse) operators in a $4k$ mesh. A sequence of edge-splits leads to new nodes, and nodal quantities of new nodes are interpolated using Lagrange basis shape functions. The mesh coarsening is performed on the basis of *a posteriori* coarsening criterion, i.e. the root mean square of strain error.

Three numerical examples are investigated: a mode I predefined crack path, mixed-mode crack propagation, and branching problems. The computational results of the adaptive mesh refinement and coarsening are consistent with the results of the uniform mesh refinement regarding overall crack patterns, crack velocities and energy evolutions. In a mode I dynamic fracture problem, the results demonstrate not only

convergence of extrinsic cohesive zone models but also accuracy of adaptive mesh refinement and coarsening schemes. The total energy is conserved for the adaptive mesh refinement, while it slightly decreases for the adaptive mesh coarsening because the mesh coarsening reduces a solution space. However, when the coarsening is performed outside of a crack tip region in conjunction with the coarsening criterion, the coarsening does not significantly influence the crack tip behavior. In addition, the adaptive mesh refinement and coarsening significantly reduces computational cost while capturing both global macro-crack and local micro-cracks. Furthermore, this techniques can be utilized for multiscale computation by introducing several levels of refinement.

Chapter 8

Conclusions and Future Work

Nonlinear fracture process behavior is investigated on the basis of potential-based fracture mechanics by using cohesive zone and virtual internal bond modeling. The potential-based cohesive model of mixed-mode fracture is proposed, implemented, verified and validated for quasi-static and dynamic fracture problems. For computational simulation, both intrinsic and extrinsic cohesive surface element approaches are employed in conjunction with nodal perturbation and adaptive topological operators (i.e. edge-swap, edge-split, and vertex-removal). Such operators not only improve crack patterns but also significantly reduce computational cost. In addition, the virtual internal bond model is utilized for the investigation of quasi-brittle material fracture behavior. This chapter summarizes the thesis and its contributions, and provides suggestions for the future work.

8.1 Concluding Remarks

The concept of the cohesive zone model is explained in the first chapter. Constitutive relationships of cohesive fracture (i.e. potential-based and non-potential-based models) and several computational methods (e.g. intrinsic cohesive zone model, extrinsic cohesive zone model, generalized/extended finite element methods, embedded discontinuities, microplane model, atomistic/continuum coupling, virtual internal bond model, peridynamics, etc.) are reviewed.

In Chapter 2, the original virtual internal bond model is extended to account for a relatively large fracture process zone of quasi-brittle materials, named the virtual internal pair-bond (VIPB) model. The concept of the VIPB model is that two particles are connected by two types of potentials, i.e. a steep short-range potential and a shallow long-range potential, in order to consider two fracture energies. The Morse potential function is modified for the virtual internal bond potential so that the potential is independent of a discrete lattice parameter. The VIPB model is able to capture load versus crack mouth opening displacement curves of three-point

bending tests for both plain concrete and fiber reinforced concrete. In addition, the relationship between the fracture energy and the localization zone size is addressed by using the path independent J -integral and computational simulation.

The PPR potential-based cohesive model is proposed in Chapter 3. Limitations of previous potentials are first summarized, and the PPR model is presented in conjunction with physical fracture parameters such as fracture energy, cohesive strength and shape parameters. The PPR model provides a consistent constitutive relationship for both proportional and non-proportional separation paths, and is verified by simulating the mixed-mode bending tests. The computational implementation of the PPR model is explained in Chapter 4, including the finite element formulation, time integration, topological data structure, and unloading/reloading relationships. Two unloading/reloading relationships (coupled and uncoupled) are developed in conjunction with loading history indices.

The PPR model is validated through investigations of quasi-static and dynamic fracture phenomena. For quasi-static fracture behavior, Chapter 5 studies microstructural particle/matrix debonding process. In order to obtain effective macroscopic constitutive relationships with microstructure, the extended Mori-Tanaka model is employed for micromechanics while the intrinsic cohesive zone model is utilized for the computational model. Both theoretical and computational models agree with each other in representing the macroscopic constitutive relationships for the change of volume fraction, particle sizes, and the PPR cohesive parameters. Different microscopic particle/matrix debonding processes are observed with respect to different macroscopic constitutive relationships (e.g. hardening, softening and snap-back).

Dynamic fracture, branching and fragmentation problems are investigated in Chapters 6 and 7. Chapter 6 proposes the use of nodal perturbation and edge-swap operators in conjunction with a topology-based data structure TopS. Geometrical studies demonstrate that the nodal perturbation and the edge-swap operators reduce error in crack length and angle represented by 4k finite element meshes. Three representative dynamic fracture problems are investigated: compact compression specimen tests, local branching instability, and cylindrical fragmentation. The computational results illustrate that the potential-based PPR model with TopS leads to an effective computational framework to simulate dynamic fracture, branching and fragmentation.

In Chapter 7, adaptive mesh refinement and coarsening schemes are developed by using adaptive topological operators, i.e. edge-split and vertex-removal. The adaptive mesh refinement is performed on the basis of *a priori* knowledge that mesh around a crack tip should be refined, while the adaptive mesh coarsening is performed on

the basis of *a posteriori* coarsening criterion, i.e. the root mean square of strain error. Computational simulation illustrates that the total energy is conserved for the adaptive mesh refinement while it slightly decreases for the adaptive mesh coarsening. For mixed-mode fracture and branching problems, the computational results (e.g. crack patterns and crack velocities) with the adaptive mesh refinement and coarsening are consistent with the results obtained from a uniformly refined mesh.

The major contributions of this study are summarized as follows:

- A unified potential-based model (PPR) of mixed-mode fracture is proposed, which characterizes different fracture energies and cohesive strength in each distinct fracture mode, and can be applied to various material softening responses, e.g. brittle, quasi-brittle and ductile (plateau).
- The PPR model is verified by investigating the consistency of the constitutive model and simulating mixed-mode bending tests.
- Two unloading/reloading relationships (coupled and uncoupled) are developed in order to represent the non-conservative energy of fracture.
- The macroscopic constitutive relationship of materials with microstructure is investigated by means of the PPR potential-based cohesive model for microscopic particle/matrix interfacial debonding, which integrates micromechanics (i.e. extended Mori-Tanaka method) and a computational model (i.e. finite element-based cohesive zone model).
- Dynamic crack propagation, microbranching and fragmentation phenomena are simulated utilizing the PPR potential-based cohesive zone model in conjunction with the extrinsic cohesive zone model.
- The use of nodal perturbation and edge-swap operators are proposed in order to reduce the error between the mathematical length and a length represented by edges of a finite element mesh in cohesive fracture simulation.
- Adaptive mesh refinement and coarsening schemes are developed, which provide consistent results in comparison to the uniform mesh refinement case, and reduce computational cost significantly.
- The virtual internal pair-bond model is proposed in order to represent the relatively large fracture process zone of concrete and fiber reinforced concrete in conjunction with two fracture energy quantities.

8.2 Suggestions for Future Work

Some open problems are identified below. The solution of these problems may rely on the present theoretical and computational contributions, and thus they are suggested as natural extensions of this work.

Extraction of the cohesive parameters: The PPR potential-based model contains eight fracture parameters for the intrinsic cohesive zone model and six fracture parameters for the extrinsic cohesive zone model. These fracture parameters can be estimated through the association with micromechanics and digital image correlation (DIC) techniques. For example, displacement field can be measured from DIC techniques (Sutton et al., 1983), and fracture parameters can be extracted by solving an inverse problem of a finite element model with the measured displacement field (Shen, 2009). Furthermore, microscopic fracture parameters can be estimated by using micromechanics (see Chapter 5). Notice that most previous researches have been focused on mode I fracture parameters, and that the estimation of mode II fracture parameters would be challenging. Nevertheless, Zhu et al. (2009) estimated rate-dependent traction-separation relationships in modes I and II for polyurea/steel interfaces.

Extension of the potential-based model for fatigue fracture behavior: Traditional fatigue fracture investigations have been based on linear elastic fracture mechanics using, for example, the Paris equation (Paris and Erdogan, 1963). However, materials, which demonstrate relatively large nonlinear fracture process zone, cannot be accurately analyzed by using linear elastic fracture mechanics. Thus, the PPR potential-based cohesive model can be extended to account for the nonlinear fracture process zone of fatigue cracks. The constitutive relationship of the cohesive zone can be associated with internal damage variables that describe dissipation under cyclic loadings. For instance, Nguyen et al. (2001) decreased reloading stiffness in the unloading/reloading relations with respect to the number of loading cycles. Maiti and Geubelle (2005) introduced two additional parameters for the degradation of reloading stiffness, which are calibrated by using the slope and intercept of the Paris fatigue failure curve. However, a general fatigue crack model is necessary, which accounts for arbitrary external cyclic loadings and temperature dependence.

Extension of the potential-based model for friction: The PPR potential-based model can further incorporate with frictional relationships. One can simply exploit the Coulomb friction, which is proportional to the normal force between surfaces. However, experimental observation demonstrates that friction also depends on slip rate and evolving properties of the contact of frictional surfaces (Dieterich, 1979). Therefore, friction (τ_f) on surfaces can be defined as a function of slip rate (V_f) and state variables (θ_f) (Rice and Ruina, 1983), and the constitutive equation of friction, for example, is given as

$$\tau_f = \tau_c + A \ln(V_f/V_c) - \theta_f , \quad (8.1)$$

where a state variable (θ_f) is obtained from solving a partial differential equation,

$$\frac{d\theta_f}{dt} = -\frac{V_f}{d_c} [\theta_f - B \ln(V_f/V_c)] . \quad (8.2)$$

Notice that τ_c , d_c , V_c , A and B are constants. The above frictional constitutive relationship can be integrated with the PPR potential-based model.

Parallel computation for large scale problems: Realistic three-dimensional dynamic fracture and fragmentation investigation is limited because of computational resources. In order to tackle such large-scale problems, parallel computation can be employed. As a proof of concept, a preliminary parallel computation is performed by integrating TopS (Celes et al., 2005a) and ParFUM (Parallel framework for unstruc-

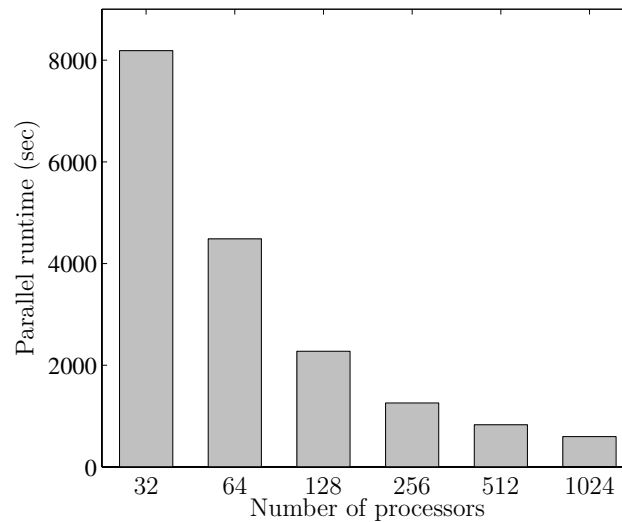


Figure 8.1: Parallel runtime performance.

tured meshes) (Lawlor et al., 2006). Intel 64 cluster Abe is utilized, located at the National Center for Supercomputing Applications (NCSA). A three-dimensional wave propagation problem is simulated. A bar is fixed at one end, and a sinusoidal load is applied on the other end. The number of elements is approximately 0.4 million, and Figure 8.1 illustrates the parallel runtime versus the number of processors. The result demonstrates promising potential for parallel computation of dynamic fracture and fragmentation. Furthermore, one can employ the parallel version of a topological data structure (ParTopS) to maintain adjacency information (Espinha et al., 2009) for simulation of dynamic crack propagation, branching and fragmentation.

Appendix A

User-defined element (UEL) subroutine of ABAQUS for the PPR potential-based cohesive zone model

```
c =====
c User-defined element (UEL) subroutine of ABAQUS
c Intrinsic cohesive element for the PPR potential-based cohesive zone
c model of mixed-mode fracture
c
c References
c K. Park, 2009, Potential-based fracture mechanics using cohesive zone
c and virtual internal bond modeling, PhD Thesis, University of Illinois
c at Urbana-Champaign.
c K. Park, G.H. Paulino, and J.R. Roesler, 2009, A unified potential-based
c cohesive model of mixed-mode fracture, Journal of the Mechanics and
c Physics of Solids 57 (6), 891-908.
c
c PPR Potential-based model
c  $\Psi := \min(GI, GII) + (\Gamma_n * (1 - y/q)^{\alpha} * (y/q + p_m/\alpha)^{p_m} + GdI)$ 
c  $*(\Gamma_t * (1 - x/p)^{\beta} * (x/p + p_n/\beta)^{p_n} + GdII)$ 
c Input type: Fracture energy, cohesive strength, shape, initial slope
c =====
      SUBROUTINE UEL (RHS, AMATRIX, SVARS, ENERGY, NDOFEL, NRHS, NSVARS,
& PROPS, NPROPS, COORDS, MCRD, NNODE, U, DU, V, A, JTYPE, TIME,
& DTIME, KSTEP, KINC, JELEM, PARAMS, NDLOAD, JDLTYP, ADLMAG,
& PREDEF, NPREDF, LFLAGS, MLVARX, DDLMAG, MDLOAD, PNEWDT, JPROPS,
& NJPRO, PERIOD)
c
      INCLUDE 'ABA_PARAM.INC'
c
      DIMENSION RHS(MLVARX,*), AMATRIX(NDOFEL,NDOFEL), PROPS(*),
& SVARS(*), ENERGY(8), COORDS(MCRD, NNODE), U(NDOFEL),
& DU(MLVARX,*), V(NDOFEL), A(NDOFEL), TIME(2), PARAMS(*),
& JDLTYP(MDLOAD,*), ADLMAG(MDLOAD,*), DDLMAG(MDLOAD,*),
& PREDEF(2, NPREDF, NNODE), LFLAGS(*), JPROPS(*)
c
      DIMENSION T(mcrd,nrhs),T_d(mcrd,mcrd),w(mcrd),P_l(ndofel,nrhs),
& P_g(ndofel,nrhs),S_l(ndofel,ndofel),S_g(ndofel,ndofel),
```

```

    & R(ndofel,ndofel),R_t(ndofel,ndofel),Shape_N(mcrd,ndofel),
    & Shape_Nt(ndofel,mcrd),coord_l(mcrd,nnode),GP(2),GP_w(2),
    & coords_m(2,mcrd), u1(mcrd), u2(mcrd),
    & store_1(ndofel,mcrd), store_2(ndofel,ndofel)
c =====
c Variables to be defined in the UEL subroutine
c   RHS : Right-Hand-Side vector
c   AMATRIX : Stiffness (Jacobian) matrix
c Variables available in the UEL subroutine
c   U : Displacement
c   COORDS : Original coordinates of the node
c   MCRD : Largest active degree of freedom (Coordinates parameter)
c   NNODE : Number of nodes
c Variables updated in the UEL subroutine
c   SVARS : Maximum separation in the element
c Constants from the ABAQUS input file: PROPS(*)
c   G_I : Mode I fracture energy
c   G_II : Mode II fracture energy
c   T_my : Mode I cohesive strength
c   T_mx : Mode II cohesive strength
c   alph : Mode I cohesive shape parameter
c   beta : Mode II cohesive shape parameter
c   ry : Mode I initial slope indicator
c   rx : Mode II initial slope indicator
c   th : Thickness of the element for 2D
c Variables during calculation
c   T : Cohesive force vector
c   T_d : Derivative of the cohesive force vector
c   w : Crack opening width vector
c   P_l : Load vector in local coordinate
c   P_g : Load vector in global coordinate
c   S_l : Stiffness matrix in local coordinate
c   S_g : Stiffness matrix in global coordinate
c   R : Coordinate transformation matrix
c   coord_l : Deformed configuration in local coordinate system
c   Shape_N : Displacement-separation relation matrix
c Constants during calculation
c   Gam_n: Energy constant in the PPR model (Gamma_n)
c   Gam_t: Energy constant in the PPR model (Gamma_t)
c   p_m : Exponent in the PPR model (m)
c   p_n : Exponent in the PPR model (n)
c   q : Characteristic length scale (delta_n)
c   p : Characteristic length scale (delta_t)
c   n_GP : Number of the Gauss Points
c   GP : Gauss points
c   GP_W : Weights at the Gauss points
c External Functions

```

```

c  x1, x2 : Shape functions
c External Subroutines
c  K_COHESIVE_PPR      : Calculate T & T_d
c  K_LOCAL_COORDINATE : Calculate R & coord_1
c  K_MATRIX_ZERO      : Matrix operation (A = 0)
c  K_MATRIX_TRANSPOSE  : Matrix operation (B = A_t)
c  K_MATRIX_PLUS_SCALAR : Matrix operation (A = A + c * B)
c  K_MATRIX_MULTIPLY   : Matrix operation (C = A * B)
c =====
c Input DATA -----
  G_I = props (1)
  G_II = props (2)
  T_my = props (3)
  T_mx = props (4)
  alph = props (5)
  beta = props (6)
  ry = props (7)
  rx = props (8)
  th = props (9)
c Initialize -----
  n_GP = 2
  data GP / 0.5773502691896 , -0.5773502691896 /
  data GP_W / 1.0 , 1.0 /
  call k_matrix_zero (rhs,ndofel,nrhs)
  call k_matrix_zero (amatrx,ndofel,ndofel)
  call k_matrix_zero (T,mcrd,nrhs)
  call k_matrix_zero (T_d,mcrd,mcrd)
  call k_matrix_zero (R,ndofel,ndofel)
  call k_matrix_zero (Shape_N,mcrd,ndofel)
c Calculate constants in the PPR model -----
  p_m = (alph-1)*alph*ry**2/(1-alph*ry**2)
  p_n = (beta-1)*beta*rx**2/(1-beta*rx**2)
  q = alph*G_I / (p_m*T_my)*(1-ry)**(alph-1)
  & * (alph/p_m*ry+1)**(p_m-1)*(alph+p_m)*ry
  p = beta*G_II/(p_n*T_mx)*(1-rx)**(beta-1)
  & * (beta/p_n*rx+1)**(p_n-1)*(beta+p_n)*rx
c
  if (G_II .GE. G_I) then
    GdI = 0
    GdII = G_II - G_I
  elseif (G_II .LT. G_I) then
    GdI = G_I - G_II
    GdII = 0
  end if
  if (G_I .EQ. G_II) then
    Gam_n = -G_II**(1)*(alph/p_m)**(p_m)
    Gam_t = (beta/p_n)**(p_n)

```

```

else
  Gam_n = (-G_I )**((GdI /(G_I-G_II))*(alph/p_m)**(p_m)
  Gam_t = (-G_II)**((GdII/(G_II-G_I))*(beta/p_n)**(p_n)
end if
c Change global coordinate into local coordinate -----
call k_local_coordinate (R,coords,coord_l,U,ndofel,nnode,mcrd)
call k_matrix_transpose (R, R_t, ndofel, ndofel)
c Element length : el_length -----
do i = 1, mcrd
  coords_m(i,1) = (coord_l(i,1)+coord_l(i,4))*0.5d0
  coords_m(i,2) = (coord_l(i,2)+coord_l(i,3))*0.5d0
end do
el_x = coords_m(1,2) - coords_m(1,1)
el_y = coords_m(2,2) - coords_m(2,1)
el_length = (el_x**2 + el_y**2)**0.5
c Opening displacement at the left and right hand side node : u1, u2
do i = 1, mcrd
  u1(i) = coord_l(i,4) - coord_l(i,1)
  u2(i) = coord_l(i,3) - coord_l(i,2)
end do
c Numerical Integration at the Gauss points
do i = 1, n_GP
c Crack opening width in tangential and normal direction : w
do j = 1, mcrd
  w(j) = x1(GP(i))*u1(j) + x2(GP(i))*u2(j)
end do
c Update the state variable for unloading/reloading: Svars
if ((Svars(n_GP*(i-1)+1) .LT. abs(w(1))) .AND.
& (abs(w(1)) .GT. rx*p)) then
  Svars(n_GP*(i-1)+1) = abs(w(1))
end if
if ((Svars(n_GP*(i-1)+2) .LT. w(2)) .AND. (w(2) .GT. ry*p)) then
  Svars(n_GP*(i-1)+2) = w(2)
end if
x_max = Svars(n_GP*(i-1)+1)
y_max = Svars(n_GP*(i-1)+2)
c Displacement-separation relation matrix
do j = 1, mcrd
  Shape_N(j,j) = x1(GP(i))
  Shape_N(j,j+2) = x2(GP(i))
  Shape_N(j,j+4) = -x2(GP(i))
  Shape_N(j,j+6) = -x1(GP(i))
end do
call k_matrix_transpose (Shape_N,Shape_Nt,mcrd,ndofel)
c Stiffness matrix & Load vector in local coordinate
call k_Cohesive_PPR (T, T_d, beta, alph, Gam_t, Gam_n, p_n, p_m,
& p, q, GdI, GdII, w, mcrd, nrhs, x_max, y_max)

```

```

        call k_matrix_multiply (Shape_Nt,T_d,store_1,ndofel,mcrd,mcrd)
        call k_matrix_multiply (store_1,Shape_N,S_l,ndofel,mcrd,ndofel)
        call k_matrix_multiply (Shape_Nt,T,P_l,ndofel,mcrd,nrhs)
c Stiffness matrix & Load vector in global coordinate
        call k_matrix_multiply (R_t,S_l,store_2,ndofel,ndofel,ndofel)
        call k_matrix_multiply (store_2,R,S_g,ndofel,ndofel,ndofel)
        call k_matrix_multiply (R_t,P_l,P_g,ndofel,ndofel,nrhs)
c Multiply element length, weight and thickness
        thick = 0.5 * el_length * GP_w(i) * th
        call k_matrix_plus_scalar (amatrx,S_g,thick,ndofel,ndofel)
        call k_matrix_plus_scalar (rhs,P_g,thick,ndofel,nrhs)
        end do
        return
        end

c =====
c = Shape Functions =====
        function x1(xi)
            INCLUDE 'ABA_PARAM.INC'
            x1 = 0.5*(1 - xi)
        end
        function x2(xi)
            INCLUDE 'ABA_PARAM.INC'
            x2 = 0.5*(1 + xi)
        end

c = Traction and Jacobian Matrix =====
        subroutine K_COHESIVE_PPR (T, T_d, beta, alph, Gam_t, Gam_n,
& p_n, p_m, p, q, GdI, GdII, w, mcrd, nrhs, x_max, y_max)
            INCLUDE 'ABA_PARAM.INC'
            dimension T(mcrd,nrhs), T_d(mcrd,mcrd), w(mcrd)
            x = abs(w(1))
            y = abs(w(2))
c Tangential component -----
            if (x .GE. x_max) then
                T_t = (Gam_t/p)*(-(1-x/p)**(beta-1)*beta*(x/p+p_n/beta)**p_n +
& (1-x/p)**beta*(x/p+p_n/beta)**(p_n-1)*p_n) *
& (Gam_n*(1-y/q)**alph*(y/q+p_m/alph)**p_m+GdI)
            else
                T_t = (Gam_t/p)*(-(1-x_max/p)**(beta-1)*beta
& *(x_max/p+p_n/beta)**p_n +
& (1-x_max/p)**beta*(x_max/p+p_n/beta)**(p_n-1)*p_n) *
& (Gam_n*(1-y/q)**alph*(y/q+p_m/alph)**p_m+GdI) * x / x_max
            end if
c Normal component -----
            if (y .GE. y_max) then
                T_n = (Gam_t*(1-x/p)**beta*(x/p+p_n/beta)**p_n+GdII) *
& Gam_n/q*(-(1-y/q)**(alph-1)*alph*(y/q+p_m/alph)**p_m +
& (1-y/q)**alph*(y/q+p_m/alph)**(p_m-1)*p_m)

```

```

else
  T_n = (Gam_t*(1-x/p)**beta*(x/p+p_n/beta)**p_n+GdII) *
& Gam_n/q*(-(1-y_max/q)**(alph-1)*alph*(y_max/q+p_m/alph)**p_m +
& (1-y_max/q)**alph*(y_max/q+p_m/alph)**(p_m-1)*p_m) * y / y_max
end if
c Tangential Component -----
c Within the tangential softening region
  if ( (x .LT. p) .AND. (w(2) .LT. q) .AND. (T_t .GE. -1.0E-5)) then
    if (w(1) .GE. 0) then
      T(1,1) = T_t
    elseif (w(1) .LT. 0) then
      T(1,1) = -T_t
    end if
c Softening condition
    if (x .GE. x_max) then
      T_d(1,1) =
& Gam_t/p**2*((1-x/p)**(beta-2)*(beta-1)*beta*(x/p+p_n/beta)**p_n -
& 2*(1-x/p)**(beta-1)*beta*(x/p+p_n/beta)**(p_n-1)*p_n +
& (1-x/p)**beta*(x/p+p_n/beta)**(p_n-2)*(p_n-1)*p_n) *
& (Gam_n*(1-y/q)**alph*(y/q+p_m/alph)**p_m+GdI)
      T_d(1,2) =
& Gam_t/p*(-(1-x/p)**(beta-1)*beta*(x/p+p_n/beta)**p_n +
& (1-x/p)**beta*(x/p+p_n/beta)**(p_n-1)*p_n) *
& Gam_n/q*(-(1-y/q)**(alph-1)*alph*(y/q+p_m/alph)**p_m +
& (1-y/q)**alph*(y/q+p_m/alph)**(p_m-1)*p_m)
      T_d(2,1) = T_d(1,2)
c Unloading/reloading condition: Uncoupled model and linear to origin
    else
      T_d(1,1) =
& (Gam_t/p)*(-(1-x_max/p)**(beta-1)*beta*(x_max/p+p_n/beta)**p_n +
& (1-x_max/p)**beta*(x_max/p+p_n/beta)**(p_n-1)*p_n) *
& (Gam_n*(1-y/q)**alph*(y/q+p_m/alph)**p_m+GdI) / x_max
      T_d(1,2) =
& Gam_t/p*(-(1-x_max/p)**(beta-1)*beta*(x_max/p+p_n/beta)**p_n +
& (1-x_max/p)**beta*(x_max/p+p_n/beta)**(p_n-1)*p_n) *
& Gam_n/q*(-(1-y/q)**(alph-1)*alph*(y/q+p_m/alph)**p_m +
& (1-y/q)**alph*(y/q+p_m/alph)**(p_m-1)*p_m) * x / x_max
    end if
c Outside the tangential softening region
c Complete separation
    else
      T(1,1) = 0
      T_d(1,1) = 0
      T_d(1,2) = 0
    end if
c Normal Component -----
    if (w(2) .GE. 0) then

```

```

c Within the tangential softening region
  if ((x .LT. p).AND.(w(2) .LT. q).AND.(T_n .GE. -1.0E-5)) then
    T(2,1) = T_n
c Softening condition
  if (y .GE. y_max) then
    T_d(2,2) =
& (Gam_t*(1-x/p)**beta*(x/p+p_n/beta)**p_n+GdII) *
& Gam_n/q**2*((1-y/q)**(alph-2)*(alph-1)*alph*(y/q+p_m/alph)**p_m -
& 2*(1-y/q)**(alph-1)*alph*(y/q+p_m/alph)**(p_m-1)*p_m +
& (1-y/q)**alph*(y/q+p_m/alph)**(p_m-2)*(p_m-1)*p_m)
    T_d(2,1) =
& Gam_t/p*(-(1-x/p)**(beta-1)*beta*(x/p+p_n/beta)**p_n +
& (1-x/p)**beta*(x/p+p_n/beta)**(p_n-1)*p_n) *
& Gam_n/q*(-(1-y/q)**(alph-1)*alph*(y/q+p_m/alph)**p_m +
& (1-y/q)**alph*(y/q+p_m/alph)**(p_m-1)*p_m)
c Unloading/reloading condition: Uncoupled model and linear to origin
  else
    T_d(2,2) =
& (Gam_t*(1-x/p)**beta*(x/p+p_n/beta)**p_n+GdII) *
& Gam_n/q*(-(1-y_max/q)**(alph-1)*alph*(y_max/q+p_m/alph)**p_m +
& (1-y_max/q)**alph*(y_max/q+p_m/alph)**(p_m-1)*p_m) / y_max
    T_d(2,1) =
& Gam_t/p*(-(1-x/p)**(beta-1)*beta*(x/p+p_n/beta)**p_n +
& (1-x/p)**beta*(x/p+p_n/beta)**(p_n-1)*p_n) *
& Gam_n/q*(-(1-y_max/q)**(alph-1)*alph*(y_max/q+p_m/alph)**p_m +
& (1-y_max/q)**alph*(y_max/q+p_m/alph)**(p_m-1)*p_m) * y / y_max
  end if
c Outside the tangential softening region
c Complete separation
  else
    T(2,1) = 0
    T_d(2,2) = 0
    T_d(2,1) = 0
  end if
c Contact condition
  elseif (w(2) .LT. 0) then
    T_d(2,2) = -Gam_n*alph*(p_m/alph)**p_m*
& (Gam_t*(p_n/beta)**p_n*p_m+a*(p_n/beta)**p_n*alph
& +GdII*p_m+GdII*alph)/q**2/p_m
    T(2,1) = T_d(2,2)*w(2)
  end if
  return
end
c = Coordinate translation =====
  subroutine K_LOCAL_COORDINATE (R,coords,coord_l,U,ndofel,nnode,
& mcrd)
  INCLUDE 'ABA_PARAM.INC'

```



```

        dimension R(ndofel,ndofel), coords(mcrd,nnode), coord_l(mcrd,nnode)
& , U(ndofel)
        dimension co_de(mcrd,nnode), co_de_m(2,2)
c Deformed configuration coordinate -----
        do i = 1, mcrd
        do j = 1, nnode
            co_de(i,j) = coords(i,j) + u(2*(j-1)+i)
        end do
        end do
c Mid point at the deformed configuration -----
        do i = 1, 2
            co_de_m(i,1) = (co_de(i,1)+co_de(i,4))*0.5
            co_de_m(i,2) = (co_de(i,2)+co_de(i,3))*0.5
        end do
c Calculate the directional cosine -----
        d_x = co_de_m(1,2) - co_de_m(1,1)
        d_y = co_de_m(2,2) - co_de_m(2,1)
        d_l = (d_x**2 + d_y**2)**0.5
        cos_a = d_x / d_l
        sin_a = d_y / d_l
c Translation(Rotational) Matrix -----
        do i = 1, nnode
            R(2*i-1,2*i-1) = cos_a
            R(2*i-1,2*i) = sin_a
            R(2*i,2*i-1) = -sin_a
            R(2*i,2*i) = cos_a
        end do
c Change global deformation into local deformation -----
        do i = 1, nnode
            coord_l(1,i) = R(1,1)*co_de(1,i) + R(1,2)*co_de(2,i)
            coord_l(2,i) = R(2,1)*co_de(1,i) + R(2,2)*co_de(2,i)
        end do
        return
        end
c = Matrix operations =====
        subroutine K_MATRIX_ZERO (A,n,m)
        INCLUDE 'ABA_PARAM.INC'
        dimension A(n,m)
        do i = 1, n
        do j = 1, m
            A(i,j) = 0.d0
        end do
        end do
        return
        end
        subroutine K_MATRIX_TRANSPOSE (A,B,n,m)
        INCLUDE 'ABA_PARAM.INC'

```

```

dimension A(n,m), B(m,n)
call k_Matrix_zero (B,m,n)
do i = 1, n
do j = 1, m
    B(j,i) = A(i,j)
end do
end do
return
end
subroutine K_MATRIX_PLUS_SCALAR (A,B,c,n,m)
    INCLUDE 'ABA_PARAM.INC'
    dimension A(n,m), B(n,m)
    do i = 1, n
    do j = 1, m
        A(i,j) = A(i,j) + c*B(i,j)
    end do
    end do
return
end
subroutine K_MATRIX_MULTIPLY (A,B,C,l,n,m)
    INCLUDE 'ABA_PARAM.INC'
    dimension A(l,n), B(n,m), C(l,m)
    call k_Matrix_zero (C,l,m)
    do i = 1, l
    do j = 1, m
    do k = 1, n
        C(i,j) = C(i,j) + A(i,k) * B (k,j)
    end do
    end do
    end do
return
end

```

c =====

Appendix B

User-defined material (UMAT) subroutine of ABAQUS for the virtual internal pair-bond (VIPB) model

```
=====
c User-defined material (UMAT) subroutine of ABAQUS
c Virtual internal pair-bond (VIPB) model
c Constraints: Lamé parameters are the same (lambda = mu)
c           Poisson's ratio is 1/3
c
c References
c K. Park, 2009, Potential-based fracture mechanics using cohesive zone
c and virtual internal bond modeling, PhD Thesis, University of Illinois
c at Urbana-Champaign.
c K. Park, G.H. Paulino, and J.R. Roesler, 2008, Virtual internal pair-bond
c model for quasi-brittle materials, Journal of Engineering Mechanics -
c ASCE 134 (10), 856-866.
=====
      SUBROUTINE UMAT (STRESS, STATEV, DDSDE, DDE, SPD, SCD,
& RPL, DDSDDT, DRPLDE, DRPLDT,
& STRAN, DSTRAN, TIME, DTIME, TEMP, DTEMP, PREDEF, DPRED, CMNAME,
& NDI, NSHR, NTENS, NSTATV, PROPS, NPROPS, COORDS, DROT, PNEWDT,
& CELENT, DFGRD0, DFGRD1, NOEL, NPT, LAYER, KSPT, KSTEP, KINC)
c
      INCLUDE 'ABA_PARAM.INC'
c
      CHARACTER*80 CMNAME
      DIMENSION STRESS(NTENS), STATEV(NSTATV),
& DDSDE(NTENS, NTENS), DDSDDT(NTENS), DRPLDE(NTENS),
& STRAN(NTENS), DSTRAN(NTENS), TIME(2), PREDEF(1), DPRED(1),
& PROPS(NPROPS), COORDS(3), DROT(3,3), DFGRD0(3,3), DFGRD1(3,3)
c
      DIMENSION F_df(2,2), F_df_t(2,2), C_gdf(2,2), E_gst(2,2),
& S_pk(2,2), S_ch(2,2), GP(10), GP_W(10), dummy(2,2)
c =====
c Variables to be defined in the UMAT subroutine
c   DDSDE : Jacobian matrix of the constitutive model
c   STRESS : Stress tensor
```

```

c Constants from the ABAQUS input file: PROPS(*)
c   E      : Elastic modulus
c   stret_l0 : Undeformed virtual bond length (Unstretched length)
c   D_ratio  : Strength ratio of the two potential
c   alph1   : parameter alpha_1 in the short-range potential
c   beta1   : parameter m_1 in the short-range potential
c   alph2   : parameter alpha_2 in the long-range potential
c   beta2   : parameter m_2 in the short-range potential
c Variables - Tensor (Matrix form)
c   F_df    : Deformation gradient
c   F_df_t  : Transpose of deformation gradient
c   C_gdf   : Green deformation tensor
c   E_gst   : Green strain tensor
c   S_pk    : 2nd Piola-Kirchhoff tensor
c   S_ch    : Cauchy stress tensor
c Variables - Scalar
c   det_F   : Determinant of Deformation gradient matrix
c   U1      : Derivative of bond potential energy : Cohesive force law
c   U2      : Second derivative of bond potential energy
c   stret   : stretch
c   stret_l : Stretched length = Unstretched length X stretch
c   D_1, D_2: Bond density
c Constants during calculation
c   po      : Poisson's ratio
c   n_GP    : Number of the Gauss points
c   GP      : Gauss points
c   GP_w    : weights at the Gauss points
c External Subroutines
c   k_Morse_Potential : Calculate U1 & U2
c   K_MATRIX_ZERO     : Matrix operation (A = 0)
c   K_MATRIX_TRANSPOSE : Matrix operation (B = A_t)
c   K_MATRIX_MULTIPLY  : Matrix operation (C = A * B)
c =====
c Input DATA -----
      E = props(1)
      stret_l0 = props (2)
      D_ratio = props (3)
      alph1 = props (4)
      beta1 = props (5)
      alph2 = props (6)
      beta2 = props (7)
c Initialize -----
      po = 0.3333333333
      pi = 3.14159265369
      n_GP = 10
      data GP /0.14887434,0.43339539,0.67940957,0.86506337,0.97390653
&      , -0.14887434, -0.43339539, -0.67940957, -0.86506337, -0.97390653/

```

```

      data GP_W /0.29552422,0.26926672,0.21908636,0.14945135,0.06667134
&      ,0.29552422,0.26926672,0.21908636,0.14945135,0.06667134/
      call k_matrix_zero (S_pk, 2, 2)
      call k_matrix_zero (DDSDDE, 3, 3)
c Calculate Bond density: D_1, D_2
      D_1 = 3*E/(2*pi*alph1**2*beta1)*D_ratio
      D_2 = 3*E/(2*pi*alph2**2*beta2)*(1-D_ratio)
c Calculate Deformation Gradient & Green strain tensor
      F_df(1,1) = DFGRD1(1,1)
      F_df(2,2) = DFGRD1(2,2)
      F_df(1,2) = DFGRD1(1,2)
      F_df(2,1) = DFGRD1(2,1)
      call k_matrix_transpose (F_df, F_df_t, 2, 2)
      call k_matrix_multiply (F_df, F_df_t, C_gdf, 2, 2, 2)
      E_gst(1,1) = (C_gdf(1,1)-1)*0.5
      E_gst(1,2) = C_gdf(1,2)*0.5
      E_gst(2,1) = C_gdf(2,1)*0.5
      E_gst(2,2) = (C_gdf(2,2)-1)*0.5
      det_F = F_df(1,1)*F_df(2,2) - F_df(1,2)*F_df(2,1)
c Calculate 2nd Piola-Kirchhoff tensor & Material tangential matrix
      do i = 1, n_GP
        phi = -(1-GP(i))/2*pi + (1+GP(i))/2*pi
        stret = (1+2*(E_gst(1,1)*(cos(phi))**2+E_gst(2,2)*(sin(phi))**2
&          + 2*E_gst(1,2)*cos(phi)*sin(phi)))*0.5
        stret_l = stret_l0 * stret
        call k_Morse_Potential (U1, U2, stret_l, stret_l0,
&          alph1, beta1, D_1, alph2, beta2, D_2)
        s0 = stret_l0/stret*U1
        c0 = U2*stret_l0**2/stret**2-U1*stret_l0/stret**3
        S_pk(1,1) = S_pk(1,1) + s0*(cos(phi))**2*GP_W(i)*pi
        S_pk(2,2) = S_pk(2,2) + s0*(sin(phi))**2*GP_W(i)*pi
        S_pk(1,2) = S_pk(1,2) + s0*cos(phi)*sin(phi)*GP_W(i)*pi
        DDSDDE(1,1)=DDSDDE(1,1)+c0*(cos(phi))**4*GP_W(i)*pi
        DDSDDE(1,2)=DDSDDE(1,2)+c0*(cos(phi))**2*(sin(phi))**2*GP_W(i)*pi
        DDSDDE(1,3)=DDSDDE(1,3)+c0*(cos(phi))**3*sin(phi)*GP_W(i)*pi
        DDSDDE(2,2)=DDSDDE(2,2)+c0*(sin(phi))**4*GP_W(i)*pi
        DDSDDE(2,3)=DDSDDE(2,3)+c0*cos(phi)*(sin(phi))**3*GP_W(i)*pi
      end do
      S_pk(2,1) = S_pk(1,2)
      DDSDDE(2,1) = DDSDDE(1,2)
      DDSDDE(3,1) = DDSDDE(1,3)
      DDSDDE(3,2) = DDSDDE(2,3)
      DDSDDE(3,3) = DDSDDE(1,2)
c Calculate Cauchy stress tensor
      call k_matrix_multiply (F_df, S_pk, dummy, 2, 2, 2)
      call k_matrix_multiply (dummy, F_df_t, S_ch, 2, 2, 2)
      stress(1) = S_ch(1,1)/det_F

```

```

stress(2) = S_ch(2,2)/det_F
stress(3) = S_ch(1,2)/det_F
return
end

c =====
c = Bond Potential energy function =====
subroutine k_Morse_Potential (U1, U2, stret_l, stret_l0,
& alph1, beta1, D_1, alph2, beta2, D_2)
INCLUDE 'ABA_PARAM.INC'
P11 = D_1*alph1*beta1/(beta1-1)/stret_l0
& *(exp(alph1*(1-stret_l/stret_l0))
& -exp(alph1*beta1*(1-stret_l/stret_l0)))
P12 = D_2*alph2*beta2/(beta2-1)/stret_l0
& *(exp(alph2*(1-stret_l/stret_l0))
& -exp(alph2*beta2*(1-stret_l/stret_l0)))
P21 = D_1*alph1**2*beta1/(beta1-1)/stret_l0**2
& *(beta1*exp(alph1*beta1*(1-stret_l/stret_l0))
& -exp(alph1*(1-stret_l/stret_l0)))
P22 = D_2*alph2**2*beta2/(beta2-1)/stret_l0**2
& *(beta2*exp(alph2*beta2*(1-stret_l/stret_l0))
& -exp(alph2*(1-stret_l/stret_l0)))
U1 = P11 + P12
U2 = P21 + P22
return
end

c = Matrix operations =====
subroutine K_MATRIX_ZERO (A,n,m)
INCLUDE 'ABA_PARAM.INC'
dimension A(n,m)
do i = 1, n
do j = 1, m
A(i,j) = 0.d0
end do
end do
return
end
subroutine K_MATRIX_TRANSPOSE (A,B,n,m)
INCLUDE 'ABA_PARAM.INC'
dimension A(n,m), B(m,n)
call k_Matrix_zero (B,m,n)
do i = 1, n
do j = 1, m
B(j,i) = A(i,j)
end do
end do
return
end

```

```
subroutine K_MATRIX_MULTIPLY (A,B,C,l,n,m)
  INCLUDE 'ABA_PARAM.INC'
  dimension A(l,n), B(n,m), C(l,m)
  call k_Matrix_zero (C,l,m)
  do i = 1, l
    do j = 1, m
      do k = 1, n
        C(i,j) = C(i,j) + A(i,k) * B (k,j)
      end do
    end do
  end do
  return
end
```

c =====

References

- Abedi, R., Petracovici, B., Haber, R. B., 2006. A space-time discontinuous Galerkin method for linearized elastodynamics with element-wise momentum balance. *Computer Methods in Applied Mechanics and Engineering* 195 (25-28), 3247–3273.
- Abraham, F. F., Brodbeck, D., Rafey, R. A., Rudge, W. E., 1994. Instability dynamics of fracture: a computer simulation investigation. *Physical Review Letters* 73 (2), 272–275.
- Ainsworth, M., Oden, J. T., 1997. A *posteriori* error estimation in finite element analysis. *Computer Methods in Applied Mechanics and Engineering* 142 (1-2), 1–88.
- Alfano, G., 2006. On the influence of the shape of the interface law on the application of cohesive-zone models. *Composites Science and Technology* 66 (6), 723–730.
- Allen, D. H., Searcy, C. R., 2001. Micromechanical model for a viscoelastic cohesive zone. *International Journal of Fracture* 107 (2), 159–176.
- Anderson, G. P., Ruggles, V. L., Stibor, G. S., 1971. Use of finite element computer programs in fracture mechanics. *International Journal of Fracture* 7 (1), 63–76.
- Anderson, T. L., 1995. *Fracture Mechanics: Fundamentals and Applications*. CRC Press, Boca Raton.
- ASTM, 2006. Standard test method for mixed mode I-mode II interlaminar fracture toughness of unidirectional fiber reinforced polymer matrix composites. Tech. Rep. ASTM D 6671/D 6671M, ASTM International.
- Babuska, I., Melenk, J. M., 1997. Partition of unity method. *International Journal for Numerical Methods in Engineering* 40 (4), 727–758.
- Babuska, I., Rheinboldt, W. C., 1978. A-*posteriori* error estimates for the finite element method. *International Journal for Numerical Methods in Engineering* 12 (10), 1597–1615.
- Banks-Sills, L., Bortman, Y., 1986. A mixed-mode fracture specimen: analysis and testing. *International Journal of Fracture* 30 (3), 181–201.

- Barenblatt, G. I., 1959. The formation of equilibrium cracks during brittle fracture: general ideas and hypotheses, axially symmetric cracks. *Applied Mathematics and Mechanics* 23 (3), 622–636.
- Batdorf, S. B., Budiansky, B., 1949. Mathematical theory of plasticity based on concept of slip. Tech. Rep. No. 1871, National Advisory Committee for Aeronautics, Washington, DC.
- Bazant, Z. P., 1984. Microplane model for strain-controlled inelastic behavior. In: Desai, C. S., Gallagher, R. H. (Eds.), *Mechanics of Engineering Materials*. John Wiley & Sons, London, pp. 45–59.
- Bazant, Z. P., 1999. Size effect on structural strength: A review. *Archive of Applied Mechanics* 69 (9-10), 703–725.
- Bazant, Z. P., 2000. Size effect. *International Journal of Solids and Structures* 37 (1), 69–80.
- Bazant, Z. P., Becq-Giraudon, E., 2002. Statistical prediction of fracture parameters of concrete and implications for choice of testing standard. *Cement and Concrete Research* 32 (4), 529–556.
- Bazant, Z. P., Caner, F. C., 2005. Microplane model M5 with kinematic and static constraints for concrete fracture and anelasticity I: Theory. *Journal of Engineering Mechanics - ASCE* 131 (1), 31–40.
- Bazant, Z. P., Caner, F. C., Carol, I., Adley, M. D., Akers, S. A., 2000. Microplane model M4 for concrete I: Formulation with work-conjugate deviatoric stress. *Journal of Engineering Mechanics - ASCE* 126 (9), 944–953.
- Bazant, Z. P., Kazemi, M. T., 1990. Determination of fracture energy, process zone length and brittleness number from size effect, with application to rock and concrete. *International Journal of Fracture* 44 (2), 111–131.
- Bazant, Z. P., Oh, B. H., 1985. Microplane model for progressive fracture of concrete and rock. *Journal of Engineering Mechanics - ASCE* 111 (4), 559–582.
- Bazant, Z. P., Planas, J., 1998. *Fracture and Size Effect in Concrete and other Quasi-brittle Materials*. CRC Press, Boca Raton.
- Bazant, Z. P., Prat, P. C., 1988. Microplane model for brittle-plastic material: I. Theory. *Journal of Engineering Mechanics - ASCE* 114 (10), 1672–1688.
- Bazant, Z. P., Xiang, Y., Prat, P. C., 1996. Microplane model for concrete. I: Stress-strain boundaries and finite strain. *Journal of Engineering Mechanics - ASCE* 122 (3), 245–254.
- Beall, M. W., Shephard, M. S., 1997. General topology-based mesh data structure. *International Journal for Numerical Methods in Engineering* 40 (9), 1573–1596.

- Beltz, G. E., Rice, J. R., 1991. Dislocation nucleation versus cleavage decohesion at crack tips. In: Lowe, T. C., Rollett, A. D., Follansbee, P. S., Daehn, G. S. (Eds.), *Modeling the Deformation of Crystalline Solids* presented. Harvard Univ, Cambridge, MA, USA, The Minerals, Metals & Materials Society (TMS), pp. 457–480.
- Belytschko, T., Chen, H., Xu, J., Zi, G., 2003. Dynamic crack propagation based on loss of hyperbolicity and a new discontinuous enrichment. *International Journal for Numerical Methods in Engineering* 58 (12), 1873–1905.
- Belytschko, T., Fish, J., Engelmann, B. E., 1988. A finite element with embedded localization zones. *Computer Methods in Applied Mechanics and Engineering* 70 (1), 59–89.
- Belytschko, T., Liu, W. K., Moran, B., 2000. *Nonlinear Finite Elements for Continua and Structures*. Wiley, New York.
- Belytschko, T., Tabbara, M., 1993. *H*-adaptive finite element methods for dynamic problems, with emphasis on localization. *International Journal for Numerical Methods in Engineering* 36 (24), 4245–4265.
- Benveniste, Y., 1987. A new approach to the application of Mori-Tanaka’s theory in composite materials. *Mechanics of Materials* 6 (2), 147–157.
- Benzeggagh, M. L., Kenane, M., 1996. Measurement of mixed-mode delamination fracture toughness of unidirectional glass/epoxy composites with mixed-mode bending apparatus. *Composites Science and Technology* 56 (4), 439–449.
- Bishop, J. E., 2009. Simulating the pervasive fracture of materials and structures using randomly close packed Voronoi tessellations. *Computational Mechanics* 44 (4), 455–471.
- Bobaru, F., 2007. Influence of van der waals forces on increasing the strength and toughness in dynamic fracture of nanofibre networks: A peridynamic approach. *Modelling and Simulation in Materials Science and Engineering* 15 (5), 397–417.
- Born, M., 1940. Stability of crystal lattices. I. *Proceedings of the Cambridge Philosophical Society* 36, 160–172.
- Bryan, G. L., 1999. Fluids in the universe: adaptive mesh refinement in cosmology. *Computing in Science & Engineering* 1 (2), 46–53.
- Budiansky, B., 1965. On the elastic moduli of some heterogeneous materials. *Journal of the Mechanics and Physics of Solids* 13 (4), 223–227.
- Camacho, G. T., Ortiz, M., 1996. Computational modelling of impact damage in brittle materials. *International Journal of Solids and Structures* 33 (20-22), 2899–2938.

- Camanho, P. P., Davila, C. G., 2002. Mixed-mode decohesion finite elements for the simulation of delamination in composite materials. Tech. Rep. NASA/TM-2002-211737, National Aeronautics and Space Administration.
- Carol, I., Bazant, Z. P., 1997. Damage and plasticity in microplane theory. *International Journal of Solids and Structures* 34 (29), 3807–3835.
- Carpinteri, A., Ferrara, G., Melchiorri, G., 1989. Single edge notched specimen subjected to four point shear: An experimental investigation. In: Shah, S. P., Swartz, S. E., Barr, B. (Eds.), *International Conference on Recent Developments in the Fracture of Concrete and Rock*. Elsevier Applied Science, pp. 605–614.
- Carpinteri, A., Paggi, M., Zavarise, G., 2005. Snap-back instability in microstructured composites and its connection with superplasticity. *Strength, Fracture and Complexity* 3 (2-4), 61–72.
- Carranza, F. L., Fang, B., Haber, R. B., 1998. An adaptive space-time finite element model for oxidation-driven fracture. *Computer Methods in Applied Mechanics and Engineering* 157 (3-4), 399–423.
- Celes, W., Paulino, G. H., Espinha, R., 2005a. A compact adjacency-based topological data structure for finite element mesh representation. *International Journal for Numerical Methods in Engineering* 64 (11), 1529–1556.
- Celes, W., Paulino, G. H., Espinha, R., 2005b. Efficient handling of implicit entities in reduced mesh representations. *Journal of Computing and Information Science in Engineering* 5 (4), 348–359.
- Christensen, R. M., Lo, K. H., 1979. Solutions for effective shear properties in three phase sphere and cylinder models. *Journal of the Mechanics and Physics of Solids* 27 (4), 315–330.
- Daux, C., Moes, N., Dolbow, J., Sukumar, N., Belytschko, T., 2000. Arbitrary branched and intersecting cracks with the extended finite element method. *International Journal for Numerical Methods in Engineering* 48 (12), 1741–1760.
- de Andres, A., Perez, J. L., Ortiz, M., 1999. Elastoplastic finite element analysis of three-dimensional fatigue crack growth in aluminum shafts subjected to axial loading. *International Journal of Solids and Structures* 36 (15), 2231–2258.
- Deshpande, V. S., Needleman, A., Van der Giessen, E., 2001. A discrete dislocation analysis of near-threshold fatigue crack growth. *Acta Materialia* 49 (16), 3189–3203.
- Deshpande, V. S., Needleman, A., Van der Giessen, E., 2002. Discrete dislocation modeling of fatigue crack propagation. *Acta Materialia* 50 (4), 831–846.
- Dieterich, J. H., 1979. Modeling of rock friction 1. Experimental results and constitutive equations. *Journal of Geophysical Research* 84 (B5), 2161–2168.

- Dijkstra, E. W., 1959. A note on two problems in connexion with graphs. *Numerische Mathematik* 1, 269–271.
- Duarte, C. A., Babuska, I., Oden, J. T., 2000. Generalized finite element methods for three-dimensional structural mechanics problems. *Computers & Structures* 77 (2), 215–232.
- Duarte, C. A., Oden, J. T., 1996. An h - p adaptive method using clouds. *Computer Methods in Applied Mechanics and Engineering* 139 (1-4), 237–262.
- Duarte, C. A., Reno, L. G., Simone, A., 2007. A high-order generalized FEM for through-the-thickness branched cracks. *International Journal for Numerical Methods in Engineering* 72 (3), 325–351.
- Dugdale, D. S., 1960. Yielding of steel sheets containing slits. *Journal of the Mechanics and Physics of Solids* 8 (2), 100–104.
- Ergodan, F., Sih, G. C., 1963. On the crack extension in plates under plane loading and transverse shear. *Journal of Basic Engineering* 85, 519–527.
- Espinha, R., Celes, W., Rodriguez, N., Paulino, G. H., 2009. ParTopS: compact topological framework for parallel fragmentation simulations. *Engineering with Computers*, in press.
- Fago, M., Hayes, R. L., Carter, E. A., Ortiz, M., 2004. Density-functional-theory-based local quasicontinuum methods: Prediction of dislocation nucleation. *Physical Review B* 70 (10), 100102–1 – 100102–4.
- Falk, M., Needleman, A., Rice, J., 2001. A critical evaluation of cohesive zone models of dynamic fracture. In: *Journal De Physique. IV : JP. Vol. 11. Delft, Netherlands*, pp. Pr5:43–50.
- Fan, R., Fish, J., 2008. The rs -method for material failure simulations. *International Journal for Numerical Methods in Engineering* 73 (11), 1607–1623.
- Field, D. A., 1988. Laplacian smoothing and Delaunay triangulations. *Communications in Applied Numerical Methods* 4 (6), 709–712.
- Finot, M., Shen, Y. L., Needleman, A., Suresh, S., 1994. Micromechanical modeling of reinforcement fracture in particle-reinforced metal-matrix composites. *Metallurgical and Materials Transactions A: Physical Metallurgy and Materials Science* 25 A (11), 2403–2420.
- Fish, J., Yuan, Z., 2005. Multiscale enrichment based on partition of unity. *International Journal for Numerical Methods in Engineering* 62 (10), 1341–1359.
- Ganguly, P., 2006. Spatial convergence of finite element cohesive interface networks. Ph.D. thesis, Cornell University.

- Ganguly, P., Vavasis, S. A., Papoulia, K. D., 2006. An algorithm for two-dimensional mesh generation based on the pinwheel tiling. *SIAM Journal of Scientific Computing* 28 (4), 1533–1562.
- Gao, H., Ji, B., 2003. Modeling fracture in nanomaterials via a virtual internal bond method. *Engineering Fracture Mechanics* 70 (14), 1777–1791.
- Gao, H., Klein, P., 1998. Numerical simulation of crack growth in an isotropic solid with randomized internal cohesive bonds. *Journal of the Mechanics and Physics of Solids* 46 (2), 187–218.
- Gerstle, W., Sau, N., Silling, S., 2007. Peridynamic modeling of concrete structures. *Nuclear Engineering and Design* 237 (12-13), 1250–1258.
- Geubelle, P. H., Baylor, J. S., 1998. Impact-induced delamination of composites: A 2D simulation. *Composites Part B:Engineering* 29 (5), 589–602.
- Girifalco, L. A., Weizer, V. G., 1959. Application of the Morse potential function to cubic metals. *Physical Review* 114 (3), 687–690.
- Gray III, G. T., Idar, D. J., Blumenthal, W. R., Cady, C. M., Peterson, P. D., 1998. High- and low-strain rate compression properties of several energetic material composites as a function of strain rate and temperature. In: Proceedings of the 11th International Detonation Symposium. pp. 76–87.
- Guibas, L. J., Knuth, D. E., Sharir, M., 1992. Randomized incremental construction of Delaunay and Voronoi diagrams. *Algorithmica* 7 (4), 381–413.
- Haber, R. B., 2009. Personal communication.
- Hill, R., 1962. Acceleration waves in solids. *Journal of the Mechanics and Physics of Solids* 10 (1), 1–16.
- Hill, R., 1965. A self-consistent mechanics of composite materials. *Journal of the Mechanics and Physics of Solids* 13 (4), 213–222.
- Hillerborg, A., 1985. The theoretical basis of a method to determine the fracture energy G_F of concrete. *Materials and Structures* 18 (4), 291–296.
- Hillerborg, A., Modeer, M., Petersson, P. E., 1976. Analysis of crack formation and crack growth in concrete by means of fracture mechanics and finite elements. *Cement and Concrete Research* 6 (6), 773–781.
- Hou, T. Y., Wu, X.-H., 1997. A multiscale finite element method for elliptic problems in composite materials and porous media. *Journal of Computational Physics* 134 (1), 169–189.

- Huang, H., Costanzo, F., 2004. On the use of space-time finite elements in the solution of elasto-dynamic fracture problems. *International Journal of Fracture* 127 (2), 119–146.
- Hughes, T. J. R., 1995. Multiscale phenomena: Green's functions, the Dirichlet-to-Neumann formulation, subgrid scale models, bubbles and the origins of stabilized methods. *Computer Methods in Applied Mechanics and Engineering* 127 (1-4), 387–401.
- Hughes, T. J. R., 2000. *The Finite Element Method: Linear Static and Dynamic Finite Element Analysis*. Dover Publications, New York.
- Hughes, T. J. R., Hulbert, G. M., 1988. Space-time finite element methods for elastodynamics: Formulations and error estimates. *Computer Methods in Applied Mechanics and Engineering* 66 (3), 339–363.
- Huttenlocher, D. P., Klanderman, G. A., Rucklidge, W. J., 1993. Comparing images using the Hausdorff distance. *IEEE Transactions on Pattern Analysis and Machine Intelligence* 15 (9), 850–863.
- Ingraffea, A. R., Gerstle, W. H., Gergely, P., Saouma, V., 1984. Fracture mechanics of bond in reinforced concrete. *Journal of Structural Engineering* 110 (4), 871–890.
- Jenq, Y. S., Shah, S. P., 1985. Two parameter fracture model for concrete. *Journal of Engineering Mechanics - ASCE* 111 (10), 1227–1241.
- Jirasek, M., 2000. Comparative study on finite elements with embedded discontinuities. *Computer Methods in Applied Mechanics and Engineering* 188 (1-3), 307–330.
- Jirasek, M., Bazant, Z. P., 1995. *Inelastic Analysis of Structures*. John Wiley & Sons, London.
- Kalthoff, J. F., Winkler, S., 1987. Failure mode transition at high rates of shear loading. *International Conference on Impact Loading and Dynamic Behavior of Materials* 1, 185–195.
- Kilic, B., Agwai, A., Madenci, E., 2009. Peridynamic theory for progressive damage prediction in center-cracked composite laminates. *Composite Structures* 90 (2), 141–151.
- Kim, J.-H., Paulino, G. H., 2004. Simulation of crack propagation in functionally graded materials under mixed-mode and non-proportional loading. *International Journal of Mechanics and Materials in Design* 1 (1), 63–94.
- Klein, P., Gao, H., 1998. Crack nucleation and growth as strain localization in a virtual-bond continuum. *Engineering Fracture Mechanics* 61 (1), 21–48.

- Klein, P. A., Foulk, J. W., Chen, E. P., Wimmer, S. A., Gao, H. J., 2001. Physics-based modeling of brittle fracture: Cohesive formulations and the application of meshfree methods. *Theoretical and Applied Fracture Mechanics* 37 (1-3), 99–166.
- Krenk, S., 2006. Energy conservation in Newmark based time integration algorithms. *Computer Methods in Applied Mechanics and Engineering* 195 (44-47), 6110–6124.
- Kulkarni, M. G., Geubelle, P. H., Matou, K., 2009. Multi-scale modeling of heterogeneous adhesives: Effect of particle decohesion. *Mechanics of Materials* 41 (5), 573–583.
- Lawlor, O. S., Chakravorty, S., Wilmarth, T. L., Choudhury, N., Dooley, I., Zheng, G., Kale, L., 2006. ParFUM: a parallel framework for unstructured meshes for scalable dynamic physics applications. *Engineering with Computers* 22 (3-4), 215–235.
- Lee, Y. J., Freund, L. B., 1990. Fracture initiation due to asymmetric impact loading of an edge cracked plate. *Transactions of the ASME. Journal of Applied Mechanics* 57 (1), 104–111.
- Levy, A. J., 1994. Separation at a circular interface under biaxial load. *Journal of the Mechanics and Physics of Solids* 42 (7), 1087–1104.
- Li, A., Li, R., Fish, J., 2008. Generalized Mathematical Homogenization: From theory to practice. *Computer Methods in Applied Mechanics and Engineering* 197 (41-42), 3225–3248.
- Linder, C., Armero, F., 2007. Finite elements with embedded strong discontinuities for the modeling of failure in solids. *International Journal for Numerical Methods in Engineering* 72 (12), 1391–1433.
- Linder, C., Armero, F., 2009. Finite elements with embedded branching. *Finite Elements in Analysis and Design* 45 (4), 280–293.
- Liu, X., Li, S., Sheng, N., 2008. A cohesive finite element for quasi-continua. *Computational Mechanics* 42 (4), 543–553.
- Lo, S. H., 1989. Generating quadrilateral elements on plane and over curved surfaces. *Computers and Structures* 31 (3), 421–426.
- Macek, R. W., Silling, S. A., 2007. Peridynamics via finite element analysis. *Finite Elements in Analysis and Design* 43 (15), 1169–1178.
- Maiti, S., Geubelle, P. H., 2005. A cohesive model for fatigue failure of polymers. *Engineering Fracture Mechanics* 72 (5), 691–708.
- Maiti, S., Ghosh, D., Subhash, G., 2009. A generalized cohesive element technique for arbitrary crack motion. *Finite Elements in Analysis and Design* 45 (8-9), 501–510.

- Matous, K., Kulkarni, M. G., Geubelle, P. H., 2008. Multiscale cohesive failure modeling of heterogeneous adhesives. *Journal of the Mechanics and Physics of Solids* 56 (4), 1511–1533.
- McMeeking, R. M., Parks, D. M., 1979. On criteria for J-dominance of crack-tip fields in large-scale yielding. In: *Elastic-Plastic Fracture* (ASTM Special Technical Publication). Vol. 668. pp. 175–194.
- Menouillard, T., Rethore, J., Moes, N., Combescure, A., Bung, H., 2008. Mass lumping strategies for X-FEM explicit dynamics: Application to crack propagation. *International Journal for Numerical Methods in Engineering* 74 (3), 447–474.
- Mi, Y., Crisfield, M. A., Davies, G. A. O., Hellweg, H. B., 1998. Progressive delamination using interface elements. *Journal of Composite Materials* 32 (14), 1246–1272.
- Miller, O., Freund, L. B., Needleman, A., 1999. Energy dissipation in dynamic fracture of brittle materials. *Modelling and Simulation in Materials Science and Engineering* 7 (4), 573–586.
- Miller, R., Tadmor, E. B., Phillips, R., Ortiz, M., 1998. Quasicontinuum simulation of fracture at the atomic scale. *Modelling and Simulation in Materials Science and Engineering* 6 (5), 607–638.
- Milstein, F., 1973. Applicability of exponentially attractive and repulsive interatomic potential functions in the description of cubic crystals. *Journal of Applied Physics* 44 (9), 3825–3832.
- Moes, N., Belytschko, T., 2002. Extended finite element method for cohesive crack growth. *Engineering Fracture Mechanics* 69 (7), 813–833.
- Mogilevskaya, S. G., Crouch, S. L., 2002. A Galerkin boundary integral method for multiple circular elastic inclusions with homogeneously imperfect interfaces. *International Journal of Solids and Structures* 39 (18), 4723–4746.
- Molinari, J. F., Ortiz, M., 2002. Three-dimensional adaptive meshing by subdivision and edge-collapse in finite-deformation dynamic-plasticity problems with application to adiabatic shear banding. *International Journal for Numerical Methods in Engineering* 53 (5), 1101–1126.
- Mooney, M., 1940. Theory of large elastic deformation. *Journal of Applied Physics* 11 (9), 582–592.
- Mori, T., Tanaka, K., 1973. Average stress in matrix and average elastic energy of materials with misfitting inclusions. *Acta Metallurgica* 21 (5), 571–574.
- Morse, P. M., 1929. Diatomic molecules according to wave mechanics. II. vibrational levels. *Physical Review* 34, 57–64.

- Mura, T., 1987. *Micromechanics of Defects in Solids*. Kluwer Academic Publishers, Norwell, MA.
- Needleman, A., 1987. A continuum model for void nucleation by inclusion debonding. *Journal of Applied Mechanics - Transactions of the ASME* 54 (3), 525–531.
- Needleman, A., 1990. An analysis of tensile decohesion along an interface. *Journal of the Mechanics and Physics of Solids* 38 (3), 289–324.
- Needleman, A., Tvergaard, V., 1984. Analysis of ductile rupture in notched bars. *Journal of the Mechanics and Physics of Solids* 32 (6), 461–490.
- Nemat-Nasser, S., Hori, M., 1999. *Micromechanics: Overall Properties of Heterogeneous Materials*. North Holland, Amsterdam, The Netherlands.
- Newmark, N. M., 1959. A method computation for structural dynamics. *Journal of Engineering Mechanics Division, ASCE* 85, 67–94.
- Nguyen, O., Repetto, E. A., Ortiz, M., Radovitzky, R. A., 2001. A cohesive model of fatigue crack growth. *International Journal of Fracture* 110 (4), 351–369.
- Nguyen, T. D., Govindjee, S., Klein, P. A., Gao, H., 2004. A rate-dependent cohesive continuum model for the study of crack dynamics. *Computer Methods in Applied Mechanics and Engineering* 193 (30-32), 3239–3265.
- Ortiz, M., Leroy, Y., Needleman, A., 1987. A finite element method for localized failure analysis. *Computer Methods in Applied Mechanics and Engineering* 61 (2), 189–214.
- Ortiz, M., Pandolfi, A., 1999. Finite-deformation irreversible cohesive elements for three-dimensional crack-propagation analysis. *International Journal for Numerical Methods in Engineering* 44 (9), 1267–1282.
- Pandolfi, A., Krysl, P., Ortiz, M., 1999. Finite element simulation of ring expansion and fragmentation: the capturing of length and time scales through cohesive models of fracture. *International Journal of Fracture* 95 (1-4), 279–297.
- Papoulia, K. D., Sam, C.-H., Vavasis, S. A., 2003. Time continuity in cohesive finite element modeling. *International Journal for Numerical Methods in Engineering* 58 (5), 679–701.
- Papoulia, K. D., Vavasis, S. A., Ganguly, P., 2006. Spatial convergence of crack nucleation using a cohesive finite-element model on a pinwheel-based mesh. *International Journal for Numerical Methods in Engineering* 67 (1), 1–16.
- Paris, P. C., Erdogan, F., 1963. A critical analysis of crack propagation laws. *Journal of Basic Engineering - ASME* 85, 528–534.

- Park, K., 2005. Concrete fracture mechanics and size effect using a specialized cohesive zone model. Master's thesis, University of Illinois at Urbana-Champaign.
- Park, K., Paulino, G. H., Roesler, J. R., 2008a. Determination of the kink point in the bilinear softening model for concrete. *Engineering Fracture Mechanics* 75 (13), 3806–3818.
- Park, K., Paulino, G. H., Roesler, J. R., 2008b. Virtual internal pair-bond (VIPB) model for quasi-brittle materials. *Journal of Engineering Mechanics - ASCE* 134 (10), 856–866.
- Park, K., Paulino, G. H., Roesler, J. R., 2009a. A unified potential-based cohesive model of mixed-mode fracture. *Journal of the Mechanics and Physics of Solids* 57 (6), 891–908.
- Park, K., Pereira, J. P., Duarte, C. A., Paulino, G. H., 2009b. Integration of singular enrichment functions in the generalized/extended finite element method for three-dimensional problems. *International Journal for Numerical Methods in Engineering* 78 (10), 1220–1257.
- Parks, M. L., Lehoucq, R. B., Plimpton, S. J., Silling, S. A., 2008. Implementing peridynamics within a molecular dynamics code. *Computer Physics Communications* 179 (11), 777–783.
- Paulino, G. H., Celes, W., Espinha, R., Zhang, Z. J., 2008. A general topology-based framework for adaptive insertion of cohesive elements in finite element meshes. *Engineering with Computers* 24 (1), 59–78.
- Paulino, G. H., Menezes, I. F. M., Cavalcante Neto, J. B., Martha, L. F., 1999. A methodology for adaptive finite element analysis: towards an integrated computational environment. *Computational Mechanics* 23 (5), 361–388.
- Paulino, G. H., Yin, H. M., Sun, L. Z., 2006. Micromechanics-based interfacial debonding model for damage of functionally graded materials with particle interactions. *International Journal of Damage Mechanics* 15 (3), 267–288.
- Rabczuk, T., Belytschko, T., 2004. Cracking particles: A simplified meshfree method for arbitrary evolving cracks. *International Journal for Numerical Methods in Engineering* 61 (13), 2316–2343.
- Radin, C., Sadun, L., 1996. The isoperimetric problem for pinwheel tilings. *Communications in Mathematical Physics* 177 (1), 255–263.
- Rae, P. J., Palmer, S. J. P., Goldrein, H. T., Field, J. E., Lewis, A. L., 2002. Quasi-static studies of the deformation and failure of PBX 9501. *Proceedings of the Royal Society of London, Series A (Mathematical, Physical and Engineering Sciences)* 458 (2025), 2227–2242.

- Reeder, J. R., Crews Jr., J. H., 1990. Mixed-mode bending method for delamination testing. *AIAA Journal* 28 (7), 1270–1276.
- Rice, J. R., 1968a. Mathematical analysis in the mechanics of fracture. In: Liebowitz, H. (Ed.), *Fracture: An Advanced Treatise*. Vol. 2. Academic Press, New York, pp. 191–311.
- Rice, J. R., 1968b. A path independent integral and the approximate analysis of strain concentration by notches and cracks. *Journal of Applied Mechanics - ASME* 35, 379–386.
- Rice, J. R., 1992. Dislocation nucleation from a crack tip: An analysis based on the Peierls concept. *Journal of the Mechanics and Physics of Solids* 40 (2), 239–271.
- Rice, J. R., Ruina, A. L., 1983. Stability of steady frictional slipping. *Journal of Applied Mechanics - ASME* 50 (2), 343–349.
- Rittel, D., Maigre, H., 1996. An investigation of dynamic crack initiation in PMMA. *Mechanics of Materials* 23 (3), 229–239.
- Rivara, M.-C., 1997. New longest-edge algorithms for the refinement and/or improvement of unstructured triangulations. *International Journal for Numerical Methods in Engineering* 40 (18), 3313–3324.
- Roe, K. L., Siegmund, T., 2003. An irreversible cohesive zone model for interface fatigue crack growth simulation. *Engineering Fracture Mechanics* 70, 209–232.
- Roesler, J., Paulino, G. H., Gaedicke, C., Bordelon, A., Park, K., 2007a. Fracture behavior of functionally graded concrete materials for rigid pavements. *Transportation Research Record* 2037, 40–49.
- Roesler, J., Paulino, G. H., Park, K., Gaedicke, C., 2007b. Concrete fracture prediction using bilinear softening. *Cement & Concrete Composites* 29 (4), 300–312.
- Rose, J. H., Ferrante, J., Smith, J. R., 1981. Universal binding energy curves for metals and bimetallic interfaces. *Physical Review Letters* 47 (9), 675–678.
- Shah, S. P., Swartz, S. E., Ouyang, C., 1995. *Fracture Mechanics of Concrete: Applications of Fracture Mechanics to Concrete, Rock and Other Quasi-Brittle Materials*. Wiley-Interscience, New York.
- Sharon, E., Fineberg, J., 1996. Microbranching instability and the dynamic fracture of brittle materials. *Physical Review B (Condensed Matter)* 54 (10), 7128–7139.
- Sharon, E., Gross, S. P., Fineberg, J., 1995. Local crack branching as a mechanism for instability in dynamic fracture. *Physical Review Letters* 74 (25), 5096–5099.

- Shen, B., 2009. Functionally graded fiber-reinforced cementitious composites – Manufacturing and extraction of cohesive fracture properties using finite elements and digital image correlation. Ph.D. thesis, University of Illinois at Urbana-Champaign.
- Shen, Y. L., Finot, M., Needleman, A., Suresh, S., 1994. Effective elastic response of two-phase composites. *Acta Metallurgica et Materialia* 42 (1), 77–97.
- Shen, Y. L., Finot, M., Needleman, A., Suresh, S., 1995. Effective plastic response of two-phase composites. *Acta Metallurgica et Materialia* 43 (4), 1701–1722.
- Shilkrot, L. E., Curtin, W. A., Miller, R. E., 2002. A coupled atomistic/continuum model of defects in solids. *Journal of the Mechanics and Physics of Solids* 50 (10), 2085–2106.
- Shim, D.-J., Paulino, G. H., Dodds Jr., R. H., 2006. J resistance behavior in functionally graded materials using cohesive zone and modified boundary layer models. *International Journal of Fracture* 139 (1), 91–117.
- Siegmund, T., Brocks, W., 1999. Prediction of the work separation and implications to modeling. *International Journal of Fracture* 99 (1-2), 97–116.
- Sih, G. C., 1974. Strain-energy-density factor applied to mixed mode crack problems. *International Journal of Fracture* 10 (3), 305–321.
- Silling, S. A., 1998. Reformation of elasticity theory for discontinuous and long-range forces. Tech. Rep. SAND98-2176, Sandia National Laboratories.
- Silling, S. A., 2000. Reformulation of elasticity theory for discontinuities and long-range forces. *Journal of the Mechanics and Physics of Solids* 48 (1), 175–209.
- Silling, S. A., Askari, E., 2005. A meshfree method based on the peridynamic model of solid mechanics. *Computers & Structures* 83 (17-18), 1526–1535.
- Simo, J. C., Oliver, J., Armero, F., 1993. An analysis of strong discontinuities induced by strain-softening in rate-independent inelastic solids. *Computational Mechanics* 12 (5), 277–296.
- Song, J.-H., Belytschko, T., 2009. Cracking node method for dynamic fracture with finite elements. *International Journal for Numerical Methods in Engineering* 77 (3), 360–385.
- Song, S. H., Paulino, G. H., Buttlar, W. G., 2006. Simulation of crack propagation in asphalt concrete using an intrinsic cohesive zone model. *Journal of Engineering Mechanics - ASCE* 132 (11), 1215–1223.
- Song, S. H., Paulino, G. H., Buttlar, W. G., 2008. Influence of the cohesive zone model shape parameter on asphalt concrete fracture behavior. In: Paulino, G. H., Pindera, M.-J., Dodds Jr., R. H., Rochinha, F. A., Dave, E., Chen, L. (Eds.), Multiscale and Functionally Graded Material 2006 (M&FGM 2006). AIP Conference Proceedings, pp. 730–735.

- Sutton, M., Wolters, W., Peters, W., Ranson, W., McNeill, S., 1983. Determination of displacements using an improved digital correlation method. *Image and Vision Computing* 1 (3), 133–139.
- Swenson, D. V., Ingraffea, A. R., 1988. Modeling mixed-mode dynamic crack propagation using finite elements: Theory and applications. *Computational Mechanics* 3 (6), 381–397.
- Tadmor, E. B., Ortiz, M., Phillips, R., 1996. Quasicontinuum analysis of defects in solids. *Philosophical Magazine A* 73 (6), 1529–1563.
- Tan, H., Huang, Y., Liu, C., Geubelle, P. H., 2005a. The Mori-Tanaka method for composite materials with nonlinear interface debonding. *International Journal of Plasticity* 21 (10), 1890–1918.
- Tan, H., Huang, Y., Liu, C., Ravichandran, G., Paulino, G. H., 2007. Constitutive behaviors of composites with interface debonding: The extended Mori-Tanaka method for uniaxial tension. *International Journal of Fracture* 146 (3), 139–148.
- Tan, H., Liu, C., Huang, Y., Geubelle, P. H., 2005b. The cohesive law for the particle/matrix interfaces in high explosives. *Journal of the Mechanics and Physics of Solids* 53 (8), 1892–1917.
- Taya, M., Chou, T.-W., 1981. On two kinds of ellipsoidal inhomogeneities in an infinite elastic body: an application to a hybrid composite. *International Journal of Solids and Structures* 17 (6), 553–563.
- Taylor, G. I., 1938. Plastic strain in metals. *Journal of the Institute of Metals* 62 (1), 307–324.
- Thiagarajan, G., Hsia, K. J., Huang, Y., 2004. Finite element implementation of virtual internal bond model for simulating crack behavior. *Engineering Fracture Mechanics* 71 (3), 401–423.
- Trangenstein, J. A., 2002. Multi-scale iterative techniques and adaptive mesh refinement for flow in porous media. *Advances in Water Resources* 25 (8-12), 1175–1213.
- Tvergaard, V., Hutchinson, J. W., 1992. The relation between crack growth resistance and fracture process parameters in elastic-plastic solids. *Journal of the Mechanics and Physics of Solids* 40 (6), 1377–1397.
- Tvergaard, V., Hutchinson, J. W., 1993. The influence of plasticity on mixed mode interface toughness. *Journal of the Mechanics and Physics of Solids* 41 (6), 1119–1135.
- van den Bosch, M., Schreurs, P. J. G., Geers, M. G. D., 2006. An improved description of the exponential Xu and Needleman cohesive zone law for mixed-mode decohesion. *Engineering Fracture Mechanics* 73 (9), 1220–1234.

- van Mier, J. G. M., 1996. *Fracture Processes of Concrete: Assessment of Material Parameters for Fracture Models*. CRC Press, Boca Raton.
- Velho, L., 2001. Mesh simplification using four-face clusters. In: *Shape Modeling and Applications*. SMI 2001 International Conference, Genova, Italy, pp. 200–208.
- Velho, L., Gomes, J., 2000. Variable resolution 4-k meshes: concepts and applications. *Computer Graphics Forum* 19 (4), 195 – 212.
- Volokh, K. Y., 2004. Comparison between cohesive zone models. *Communications in Numerical Methods in Engineering* 20 (11), 845–856.
- Volokh, K. Y., Gao, H., 2005. On the modified virtual internal bond method. *Journal of Applied Mechanics - Transactions of the ASME* 72 (6), 969–971.
- Wawrzynek, P. A., Ingraffea, A. R., 1991. Discrete modeling of crack propagation: theoretical aspects and implementation issues in two and three dimensions. Tech. Rep. 91-5, School of Civil Engineering and Environmental Engineering, Cornell University.
- Wells, G. N., Sluys, L. J., 2001. A new method for modelling cohesive cracks using finite elements. *International Journal for Numerical Methods in Engineering* 50 (12), 2667–2682.
- Weng, G. J., 1990. The overall elastoplastic stress-strain relations of dual-phase metals. *Journal of the Mechanics and Physics of Solids* 38 (3), 419–441.
- Xu, X. P., Needleman, A., 1993. Void nucleation by inclusion debonding in a crystal matrix. *Modelling and Simulation in Materials Science and Engineering* 1 (2), 111–132.
- Xu, X. P., Needleman, A., 1994. Numerical simulations of fast crack growth in brittle solids. *Journal of the Mechanics and Physics of Solids* 42 (9), 1397–1434.
- Yang, B., Ravi-Chandar, K., 1996. On the role of the process zone in dynamic fracture. *Journal of the Mechanics and Physics of Solids* 44 (12), 1955–1976.
- Yang, Q. D., Thouless, M. D., 2001. Mixed-mode fracture analyses of plastically-deforming adhesive joints. *International Journal of Fracture* 110 (2), 175–187.
- Yin, H. M., Paulino, G. H., Buttlar, W. G., Sun, L. Z., 2007. Micromechanics-based thermoelastic model for functionally graded particulate materials with particle interactions. *Journal of the Mechanics and Physics of Solids* 55 (1), 132–160.
- Yin, H. M., Sun, L. Z., Paulino, G. H., 2004. Micromechanics-based elastic model for functionally graded materials with particle interactions. *Acta Materialia* 52 (12), 3535–3543.

- Zhang, P., Klein, P., Huang, Y., Gao, H., Wu, P. D., 2002. Numerical simulation of cohesive fracture by the virtual-internal-bond model. *Computer Modeling in Engineering & Sciences* 3 (2), 263–278.
- Zhang, Z., 2007. Extrinsic cohesive modeling of dynamic fracture and microbranching instability using a topological data structure. Ph.D. thesis, University of Illinois at Urbana-Champaign.
- Zhang, Z., Paulino, G. H., 2005. Cohesive zone modeling of dynamic failure in homogeneous and functionally graded materials. *International Journal of Plasticity* 21 (6), 1195–1254.
- Zhang, Z., Paulino, G. H., Celes, W., 2007. Extrinsic cohesive modelling of dynamic fracture and microbranching instability in brittle materials. *International Journal for Numerical Methods in Engineering* 72 (8), 893–923.
- Zhou, F., Molinari, J. F., 2004. Dynamic crack propagation with cohesive elements: A methodology to address mesh dependency. *International Journal for Numerical Methods in Engineering* 59 (1), 1–24.
- Zhou, F., Molinari, J.-F., Ramesh, K. T., 2005. A cohesive model based fragmentation analysis: Effects of strain rate and initial defects distribution. *International Journal of Solids and Structures* 42 (18-19), 5181–5207.
- Zhu, Y., Liechti, K. M., Ravi-Chandar, K., 2009. Direct extraction of rate-dependent traction-separation laws for polyurea/steel interfaces. *International Journal of Solids and Structures* 46 (1), 31–51.
- Zienkiewicz, O. C., Taylor, R. L., Zhu, J. Z., 2005. *The Finite Element Method: Its Basis & Fundamentals*. Butterworth-Heinemann, Oxford, UK.
- Zienkiewicz, O. C., Zhu, J. Z., 1987. A simple error estimator and adaptive procedure for practical engineering analysis. *International Journal for Numerical Methods in Engineering* 24 (2), 337–357.

Curriculum Vitae

EDUCATION

- **Ph.D.**, Structural Engineering (Civil and Environmental Engineering)
Computational Science & Engineering (CSE) program
University of Illinois at Urbana-Champaign (Aug. 2005 – Oct. 2009)
- Advisor: Glaucio H. Paulino / Co-advisor: Jeffery R. Roesler
- Thesis: Potential-based fracture mechanics using cohesive zone and virtual internal bond modeling
- **M.S.**, Structural Engineering (Civil and Environmental Engineering)
University of Illinois at Urbana-Champaign (Aug. 2003 – Aug. 2005)
- Advisor: Glaucio H. Paulino / Co-advisor: Jeffery R. Roesler
- Thesis: Concrete fracture mechanics and size effect using a specialized cohesive zone model
- **B.S.**, Civil Engineering
Hanyang University, Seoul, S. Korea (Mar. 1996 - Feb. 2003)

JOURNAL PUBLICATIONS (PUBLISHED)

- K. Park, G.H. Paulino, and J.R. Roesler, 2009, A unified potential-based cohesive model of mixed-mode fracture, *Journal of the Mechanics and Physics of Solids* 57 (6), 891–908.
- K. Park, J.P. Pereira, C.A. Duarte, and G.H. Paulino, 2009, Integration of singular enrichment functions in the generalized/extended finite element method for three-dimensional problems, *International Journal for Numerical Methods in Engineering* 78 (10), 1220–1257.
- K. Park, G.H. Paulino, and J.R. Roesler, 2008, Virtual internal pair-bond model for quasi-brittle materials, *Journal of Engineering Mechanics-ASCE* 134 (10), 856–866.
- K. Park, G.H. Paulino, and J.R. Roesler, 2008, Determination of the kink point in the bilinear softening model for concrete, *Engineering Fracture Mechanics* 75 (13), 3806–3818.

- J.R. Roesler, G.H. Paulino, K. Park, and C. Gaedicke, 2007, Concrete fracture prediction using bilinear softening, *Cement & Concrete Composites* 29 (4), 300–312.
- J.R. Roesler, G.H. Paulino, C. Gaedicke, A. Bordelon, and K. Park, 2007, Fracture behavior of functionally graded concrete materials (FGCM) for rigid pavements, *Transportation Research Record* 2037, 40–49.

JOURNAL PUBLICATIONS (SUBMITTED OR IN PREPARATION)

- K. Park, G.H. Paulino, W. Celes, and R. Espinha, 2009, Adaptive dynamic cohesive fracture simulation using edge-swap and nodal perturbation operators, (submitted).
- D. Ngo, K. Park, G.H. Paulino, and Y. Huang, 2009, On the constitutive relation of materials with microstructure using the PPR potential-based cohesive model for interface interaction, (submitted).
- K. Park, G.H. Paulino, and J.R. Roesler, 2009, Cohesive fracture modeling of functionally graded fiber reinforced concrete composite, (submitted).
- K. Park, G.H. Paulino, W. Celes, and R. Espinha, 2009, Adaptive mesh refinement and coarsening for cohesive dynamic fracture, (in preparation).

CONFERENCE PRESENTATIONS

- K. Park, G.H. Paulino, W. Celes, and R. Espinha, 2009, Potential-based dynamic fracture simulation with adaptive topological operators, *10th US National Congress on Computational Mechanics (USNCCM10)*, Columbus, Ohio.
- K. Park, G.H. Paulino, and J.R. Roesler, 2009, A novel potential-based approach for mixed-mode cohesive fracture simulation, *12th International Conference on Fracture (ICF12)*, Ottawa, Canada.
- K. Park, G.H. Paulino, and W. Celes, 2008, Adaptive dynamic cohesive fracture simulation using edge-swap and node perturbation operators, *8th World Congress on Computational Mechanics (WCCM8)*, Venice, Italy.
- K. Park, G.H. Paulino, and J.R. Roesler, 2008, Potential-based cohesive constitutive model of mixed-mode fracture, *Inaugural International Conference of the Engineering Mechanics Institute (EM08)*, Minneapolis, Minnesota.
- K. Park, 2008, Parallel wave propagation and topological operators for simulating microbranching and fragmentation, *Computational Science and Engineering Annual Research Symposium*, University of Illinois at Urbana-Champaign.

- K. Park, G.H. Paulino, and J.R. Roesler, 2006, Concrete fracture predictions using the virtual internal bond model with a modified Morse functional potential, *Multiscale & Functionally Graded Materials Conference*, Oahu Island, Hawaii.
- K. Park, G.H. Paulino, and J.R. Roesler, 2005, Prediction of concrete fracture mechanics behavior and size effect using cohesive zone modeling, *Workshop on Fracture Mechanics for Concrete Pavements: Theory to Practice*, Copper Mountain, Colorado.

CONFERENCE PROCEEDINGS

- K. Park, G.H. Paulino, and J.R. Roesler, 2008, Concrete fracture predictions using the virtual internal bond model with a modified Morse functional potential, *Multiscale & Functionally Graded Materials Conference 2006*, American Institute of Physics, Oahu Island, Hawaii, 724–729.
- J. Roesler, A. Bordelon, C. Gaedicke, K. Park, and G.H. Paulino, 2008, Fracture behavior and properties of functionally graded fiber-reinforced concrete, *Multiscale & Functionally Graded Materials Conference 2006*, American Institute of Physics, Oahu Island, Hawaii, 513–518.

ACADEMIC HONORS

- Computational Science & Engineering (CSE) Fellow, 2007 - 2008
University of Illinois at Urbana-Champaign
- Graduate Study Abroad Scholarship, 2003
Korea Science and Engineering Foundation (KOSEF), S. Korea
- Honor Degree in Civil Engineering, 2003
Hanyang University, Seoul, S. Korea
- Conference Awards
10th U.S. National Congress on Computational Mechanics (USNCCM-10)
Inaugural International Conference of the Engineering Mechanics Institute (EM08)
USACM fellowship for 8th World Congress on Computational Mechanics (WCCM8)